Defense Special Weapons Agency
Alexandria, VA 22310-3398

Dynamic Failure of Materials
Volume 1–Experiments and Analyses

Tarabay H. Antoun
Lynn Seaman
Donald R. Curran
SRI International
333 Ravenswood Avenue
Menlo Park, CA 94025-3434

November 1998

Technical Report

19990510 001

CONTRACT No. DNA 001-93-C-0104

DESTRUCTION NOTICE:

Destroy this report when it is no longer needed.
Do not return to sender.

PLEASE NOTIFY THE DEFENSE SPECIAL WEAPONS
AGENCY, ATTN: CSTI, 6801TELEGRAPH ROAD,
ALEXANDRIA, VA 22310-3398, IF YOUR ADDRESS IS
INCORRECT, IF YOU WISH IT DELETED FROM THE
DISTRIBUTION LIST, OR IF THE ADDRESSEE IS NO
LONGER EMPLOYED BY YOUR ORGANIZATION.

REPORT DOCUMENTATION PAGE

Public reporting burden for this collection of information is estimated to average 1 hour per response including the time for reviewing instructions, searching existing data sources, gathering and maintaining the data needed, and completing and reviewing the collection of information. Send comments regarding this burden estimate or any other aspect of this collection of information, including suggestions for reducing this burden, to Washington Headquarters Services Directorate for information Operations and Reports, 1215 Jefferson Davis Highway, Suite 1204, Arlington, VA 22202-4302, and to the Office of Management and Budget, Paperwork Reduction Project (0704-0188), Washington, DC 20503.

1. AGENCY USE ONLY (Leave blank)	2. REPORT DATE 981101	3. REPORT TYPE AND DATES COVERED Technical 930520 - 960920

4. TITLE AND SUBTITLE
Dynamic Failure of Materials
Volume 1–Experiments and Analyses

5. FUNDING NUMBERS
C-DNA 001-93-C-0104
PE-63216C and 63214C
PR-SB, AJ
TA-AE, AF
WU-DH00002 and DH00012

6. AUTHOR(S)
Tarabay H. Antoun, Lynn Seaman, and Donald R. Curran

7. PERFORMING ORGANIZATION NAME(S) AND ADDRESS(ES)
SRI International
333 Ravenswood Avenue
Menlo Park, CA 94025-3434

8. PERFORMING ORGANIZATION REPORT NUMBER
PYU-4727

9. SPONSORING/MONITORING AGENCY NAME(S) AND ADDRESS(ES)
Defense Special Weapons Agency
6801 Telegraph Road
Alexandria, VA 22310-3398
WEL/Bishop

10. SPONSORING/MONITORING AGENCY REPORT NUMBER
DSWA-TR-96-77-V1

11. SUPPLEMENTARY NOTES
This work was sponsored by the Ballistic Missile Defense Office (BMDO), managed and executed by the Defense Special Weapons Agency under RDT&E RMC Codes B7668D SB AE 00002 7010A AJ 25904D, B7668D AJ AE 00002 7010A and B7666D AJ AF 00012 7010A 25904D.

12a. DISTRIBUTION/AVAILABILITY STATEMENT

Approved for public release: distribution unlimited.

12b. DISTRIBUTION CODE

13. ABSTRACT (Maximum 200 words)

Over the past three decades, scientist in the Former Soviet Union (FSU) and in the West have developed innovative experimental techniques, measurement diagnostics, and constitutive models of the Spall Process. Extensive literature has been built up over the years in Western publications. However, much of the FSU work was not available in English and was largely inaccessible to Western readers. Improved communication between Western and FSU scientists since the end of the Cold War now allows the parallel FSU and Western work to be collected, compared, cross-correlated, and examined for new insights and ideas for future directions. The goal of this project was to make formerly inaccessible FSU results available to Western readers and to create a handy reference source for fracture kinetics data, experimental techniques, measurement diagnostics, interpretation methods, constitutive modeling approaches, and numerical computation approaches and results. We hope this work will be useful to investigators and engineers dealing with fast load and fracture as well as to investigators working in the field of physics of strength.

14. SUBJECT TERMS

Spall Fracture	Spall Data	Shock Wave Loading
Spall Experiment	Nucleation and Growth	Numerical Simulation
Dynamic Fracture	Dynamic Fracture Data	Constitutive Modeling

15. NUMBER OF PAGES
342

16. PRICE CODE

17. SECURITY CLASSIFICATION OF REPORT UNCLASSIFIED	18. SECURITY CLASSIFICATION OF THIS PAGE UNCLASSIFIED	19. SECURITY CLASSIFICATION OF ABSTRACT UNCLASSIFIED	20. LIMITATION OF ABSTRACT SAR

NSN 7540-280-5500

CLASSIFIED BY:

N/A since Unclassified.

DECLASSIFY ON:

N/A since Unclassified.

PREFACE

This Volume 1 describes experiments and analyses performed in the United States and the Former Soviet Union (FSU), Volume 2 gives a compilation of FSU spall data.

CONVERSION TABLE

Conversion factors for U. S. Customary to metric (SI) units of measurement

MULTIPLY ——————→ BY ——————————→ TO GET
TO GET ◄—————— BY ◄—————— DIVIDE

	BY		TO GET / DIVIDE
angstrom	1.000 000	X E -10	meters (m)
atmosphere (normal)	1.013 25	X E +2	kilo pascal (kPa)
bar	1.000 000	X E +2	kilo pascal (kPa)
barn	1.000 000	X E -28	meter^2 (m^2)
British thermal unit (thermochemical)	1.054 350	X E +3	joule (J)
calorie (thermochemical)	4.184 000		joule (J)
cal (thermochemical)/cm^2	4.184 000	X E -2	mega joule/m^2 (MJ/m^2)
curie	3.700 000	X E +1	*giga becquerel (GBq)
degree (angle)	1.745 329	X E -2	radian (rad)
degree Fahrenheit	$T_K = (T\,°F + 459.67)/1.8$		degree kelvin (K)
electron volt	1.602 19	X E -19	joule (J)
erg	1.000 000	X E -7	joule (J)
erg/second	1.000 000	X E -7	watt (W)
foot	3.048 000	X E -1	meter (m)
foot-pound-force	1.355 818		joule (J)
gallon (U.S. liquid)	3.785 412	X E -3	meter^3 (m^3)
inch	2.540 000	X E -2	meter (m)
jerk	1.000 000	X E +9	joule (J)
joule/kilogram (J/kg) (radiation dose absorbed)	1.000 000		Gray (Gy)
kilotons	4.183		terajoules
kip (1000 lbf)	4.448 222	X E +3	newton (N)
kip/inch^2 (ksi)	6.894 757	X E +3	kilo pascal (kPa)
ktap	1.000 000	X E +2	newton-second/m^2 (N-s/m^2)
micron	1.000 000	X E -6	meter (m)
mil	2.540 000	X E -5	meter (m)
mile (international)	1.609 344	X E +3	meter (m)
ounce	2.834 952	X E -2	kilogram (kg)
pound-force (lbs avoirdupois)	4.448 222		newton (N)
pound-force inch	1.129 848	X E -1	newton/meter (N · m)
pound-force/inch	1.751 268	X E +2	newton-meter (N/m)
pound-force/foot^2	4.788 026	X E -2	kilo pascal (kPa)
pound-force/inch^2 (psi)	6.894 757		kilo pascal (kPa)
pound-mass (lbm avoirdupois)	4.535 924	X E -1	kilogram (kg)
pound-mass-foot^2 (moment of inertia)	4.214 011	X E -2	kilogram-meter^2 (kg·m^2)
pound-mass-foot^3	1.601 846	X E +1	kilogram/meter^3 (kg/m^3)
rad (radiation dose absorbed)	1.000 000	X E -2	**Gray (Gy)
roentgen	2.579 760	X E -4	coulomb/kilogram (C/kg)
shake	1.000 000	X E -8	second (s)
slug	1.459 390	X E +1	kilogram (kg)
torr (mm Hg, 0° C)	1.333 22	X E -1	kilo pascal (kPa)

*The becquerel (Bq) is the SI unit of radioactivity; 1 Bq = 1 event/s.
**The Gray (Gy) is the SI unit of absorbed radiation.

iv

TABLE OF CONTENTS

TABLE OF CONTENTS (Continued)

FIGURES

TABLES

SECTION 1

INTRODUCTION

1.1 HISTORICAL BACKGROUND.

The strength of solids has been the subject of steadfast interest throughout history. However, the scientific basis for studying the mechanics of fracture was not founded until the twentieth century. Griffith (1921, 1925) first explained the brittle fracture phenomenon in glass through consideration of the elastic energy necessary for the propagation of a crack. He postulated that a crack will propagate if the energy released by the crack growth process is enough to provide all the energy necessary for crack propagation. This postulation led to the well known Griffith criterion, which characterizes the failure of brittle solids in terms of a single parameter, G_{Ic}—the critical energy release rate in the material.

Since the early pioneering work of Griffith, numerous experimental and theoretical investigations have contributed new fundamental information and provided new insight into the physical and mechanical aspects of the strength and fracture of solids. In spite of outstanding progress in this field, more work is needed. The strength of solids is significantly influenced by the discreteness of the atomic structure of real materials as well as submicroscopic irregularities of this structure due to microscopic defects, distinctions between laboratory samples and real components in size and form, and differences between testing conditions. To account for all these factors in a generalized theory of fracture and strength would render such a theory too complicated to be constructed solely based on first principles. Such a theory, if developed, would not be of great practical value. Consequently, quantitative fracture models in use today are based primarily on empirical or semiempirical relationships.

Fracture is not an instantaneous event. It is an evolution process controlled by the stress state, load history, temperature, environment, and other conditions. The failure mode varies depending on these conditions. As a result, the strength, measured under a particular set of conditions, is not a material constant or a similitude parameter. Many tests are used to characterize the resistance of materials to fracture under operational, or close to operational, conditions. To better understand the physical nature of elementary fracture events, it is desirable to quantify the resistance to fracture in the simplest modes of behavior, such as pure tension or pure shear, but these modes cover only a small portion of the parameter space that must be explored as part of a thorough understanding of the material response. To better understand the contributions of different damage micromechanisms to the fracture event, we need testing and examination of the material in various ranges of load duration, temperature, and plastic strain as well as experiments with samples of different microstructures.

1

Tensile strength in the microsecond load duration range can be studied by analyzing spall phenomena under shock pulse action. Spalling is the process of internal rupture of a body due to tensile stresses generated as a result of compression pulse reflection from the surface. Beside short load duration, spalling conditions are characterized by pure one-dimensional deformation and stressed states close to three-dimensional tension. An important feature of this kind of test is that neither the surface of the body nor the environment contributes to the development of the spall fracture.

The discipline of dynamic fracture mechanics has a rich history, particularly since World War II. The first description of the phenomenon of dynamic fracture belongs to Hopkinson (1914), and the first quantitative data on the resistance of materials to fracture under dynamic loading conditions were, apparently, obtained by Rinehart (1951a, 1951b), who applied the modified Hopkinson bar method to determine the fracturing stresses in steel, aluminum alloy, brass, and copper. Further development of experimental techniques provided the opportunity of making more informative measurements. An essential step in developing our present understanding of the micromechanisms of dynamic fracture was the careful examination of samples recovered from spall tests. Numerous papers discuss different methods and results of quantitative investigations of the spall fracture of metals, polymers, rocks, ceramics, and liquids. Much of the work was driven by military applications, and during the Cold War significant efforts were performed in parallel in the West and Former Soviet Union (FSU).

Experiments with plane shock waves provide a unique base of information about the strength of solids under one-dimensional tension. Large overstresses near the ultimate tensile strength can be reached under these conditions due to the high rate of stress application. As discussed later, we define such tensile failure at high rates with the term "spall."

Spall fracture can be induced, measured, and characterized with length scales ranging from micrometers to centimeters, with the possibility of varying the strain rate, temperature, and load orientation. Different classes of materials, ranging from armor steels to water, can be tested with this method. Thus, spall tests are promising tools for characterizing material failure under a wide range of testing conditions unattainable in conventional testing methods. Spall test results therefore complement conventional test results and provide a powerful tool that can be used to attain a better understanding of fracture and failure in a wide range of applications.

All methods of measuring the dynamic tensile stress in materials during spalling are indirect. It is impossible to introduce a sensor into a sample without influencing the resistance of the sample to tensile stresses. Because of this lack of a direct spall strength measurement technique, several indirect methods have evolved. Each of the methods uses a different approach to determine the dynamic tensile stress, and sometimes large discrepancies are apparent between the results obtained using different methods. Choosing the method of investigation that can provide the most complete and valid information as well as an understanding of the abilities and limitations of each method is very important.

Fracturing stresses obtained from spall experiments exceed the tensile strength value measured under quasi-static conditions. The time required for spall fracture to develop is comparable to the shock wave duration, and depending on the duration of the load, various stages of fracture can be observed ranging from the absence of visible damage to the nucleation, growth, and then coalescence of microcracks and micropores, culminating in macrocrack formation and complete rupture. This failure process is time-dependent. As such, time-dependent failure criteria are needed to describe it adequately. These criteria range in complexity from the relatively simple empirical formulations to the more complex physically based microstatistical formulations. Empirical criteria (e.g., Butcher et al., 1964; Cohen and Berkowitz, 1971; Ivanov, 1975) are based on macroscopic observations and measurements; they tend to be easy to use, but they do not provide any insight about the micromechanisms that underlie the development of fracture damage. Typically, these criteria depend on both the magnitude and duration of the applied load, with fitting parameters determined from experimental data. Microstatistical formulations (e.g., Seaman et al., 1976), however, attempt to describe spall damage in terms of the microphysical mechanisms of damage nucleation and growth. Models based on the microstatistical approach, although more complex, provide added insight into the damage process; and because the model is based on physical processes, the material parameters are identifiable from experimental data and the results can be extrapolated with higher confidence outside the domain for which the model is calibrated.

Since much of the FSU and Western dynamic fracture work was motivated by defense applications, it took a rather different direction from classical "dynamic fracture mechanics" associated with the initiation, propagation, and arrest of single macrocracks. Rather, the defense work focused on the kinetics of spall, in which many microvoids and microcracks more or less simultaneously undergo nucleation, growth, and coalescence in a volume of material to form a failed or spalled region. Later work showed that these processes also occur in the process zone at a macrocrack tip, thereby providing an important link between the fracture mechanics approach and the microstatistical approach.

Both the FSU and Western workers developed innovative experimental techniques, measurement diagnostics, and constitutive models of the spall process. An extensive literature has been built up over the years in Western publications. However, much of the FSU work was not available in English and was largely inaccessible to Western readers. Improved communication between Western and FSU scientists since the end of the Cold War now allows the parallel FSU and Western work to be collected, compared, cross-correlated, and examined for new insights and ideas for future directions. This report is an attempt to do so. Our goal was not only to make formerly inaccessible FSU results available to Western readers but will also to create a handy reference source for fracture kinetics data, experimental techniques, measurement diagnostics, interpretation methods, constitutive modeling approaches, and numerical computation approaches and results. We hope this work will be useful to investigators and engineers dealing with fast load and fracture as well as to investigators working in the field of physics of strength.

3

1.2   THE DYNAMIC FAILURE PROCESS.

A 1987 review paper by some of the present authors (Curran et al., 1987) gives a thorough review of the experimental and constitutive modeling approaches of dynamic failure. This review paper is the source of much of the information presented in this and the following section.

All failure is dynamic; it is a rate process in which material bonds are broken and voids are created in previously intact material. Characteristic times range from nanoseconds to years; successful material models must handle all rates. We, thus, do not distinguish in general between dynamic and static failure—it is all dynamic. The key is to understand the interaction between load histories and damage histories. However, in this document, we concentrate on "spall," tensile failure at high rates.

The purpose of reviewing the experiments described in this report is to compile data that form the basis for development of constitutive relations that describe the evolution of microscopic fracture in a "material element" (ME) from an undamaged state to a final damaged state that has no strength. The constitutive relations use continuum or "average" stresses and strains to describe the forces on the material element and its deformation, but it is understood that the microscopic stresses and strains inside the material element may be highly anisotropic and nonhomogeneous. The concept of a material element thus introduces a characteristic size or "nonlocality" into the constitutive relations (as discussed by Curran et al., 1987), and a key experimental challenge is to provide data regarding the anisotropic, nonhomogeneous microscopic failure processes inside the material element.

In short, we emphasize at the outset that the constitutive relations, although couched in the mathematics of continuum mechanics, will be based on a description of the actual, observed microscopic failure kinetics. Direct observation and quantification of these kinetics were the goals of the experiments to be described and summarized in this report.

Our approach is thus to be distinguished from the more common approach of inventing various functional forms for "damage evolution" and then testing these forms against continuum data. Our approach is bottom-up rather than top-down. We believe that our bottom-up approach is much more efficient in the long run, because basing the damage evolution relations on microscopic reality strongly restricts the functional forms to be considered and adds confidence to extrapolations outside the data base used to develop the constitutive relations. The experiments reviewed in this report were aimed at revealing and measuring this microscopic reality.

Table 1-1 lists the main microscopic nucleation sites in solids or liquids, and Figures 1-1 through 1-7 provide examples of the nucleation mechanisms. Once microscopic damage nucleates, it can grow in three main geometric modes:

> (1)   As ductile, roughly equiaxed voids that produce void volume by plastic flow (see Figure 1-8).

4

Table 1-1. Experimentally observed microscopic fracture nucleation processes.[1]

Nucleation Site	Nucleation Mechanism	Governing Continuum Load Parameters	Figure Reference
Preexisting flaws (voids or cracks)	• Growth of flaw	• Tensile stress • Plastic strain	1-1 and 1-2
Inclusions and second phase particles	• Cracking of inclusion • Debonding at interface • Fracture of matrix material near the inclusion . .	• Tensile stress • Plastic strain	1-3, 1-4, and 1-6
Grain boundaries	• Vacancy clustering • Grain boundary sliding • Mechanical separation (Solids only)	• Tensile stress • Plastic strain	1-7
Subgrain structure	• Dislocation pilups (Solids only)	• Shear strain	1-8

[1]Reproduced from Curran et al. (1987).

500 µm
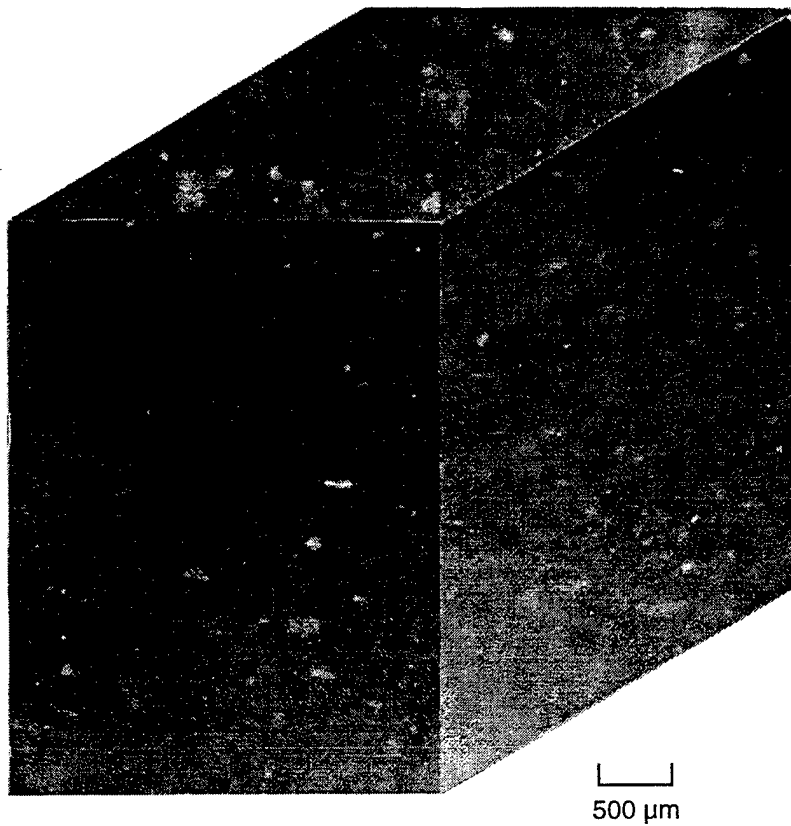
Figure 1-1. Composite micrograph of a block of Arkansas novaculite
showing the preferred orientation of the inherent flaws
(Curran et al., 1987).

6
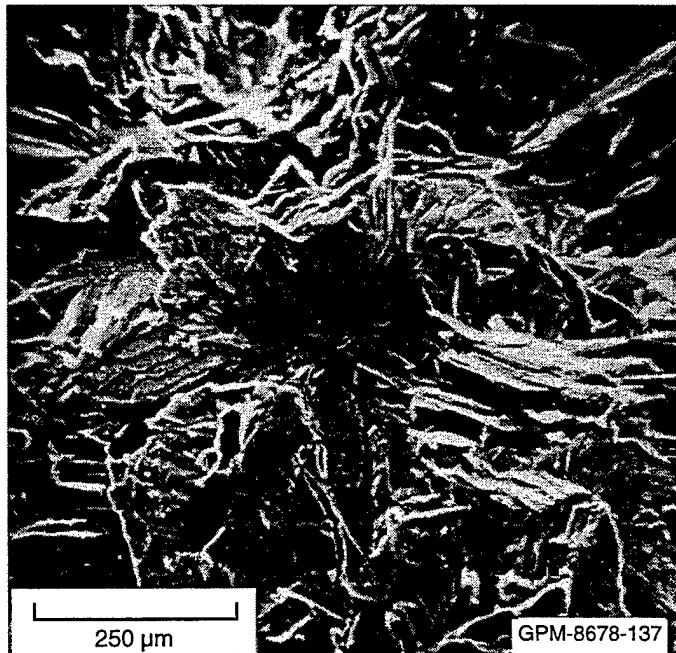
(a)
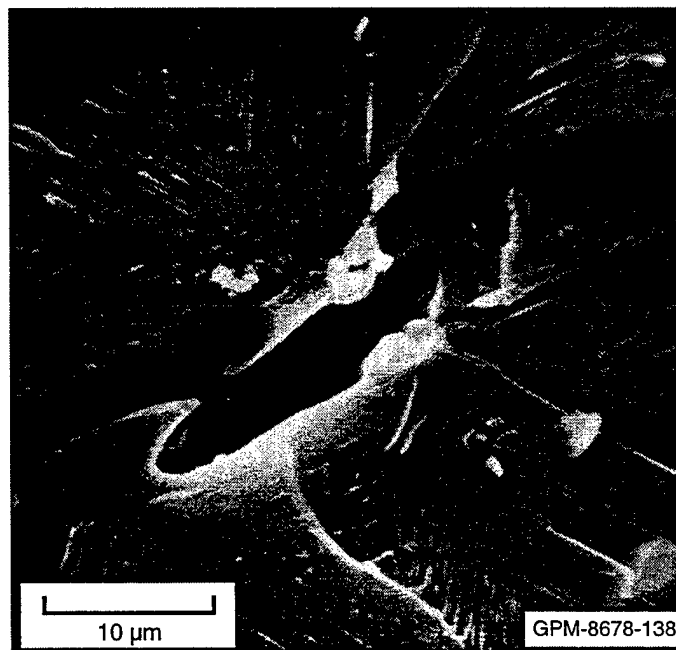
(b)

Figure 1-2. Crack nucleation at void. (a) Low magnification view
of the fracture surface of high purity beryllium
showing fracture steps radiating from a center.
(b) High magnification of center region revealing
the presence of a flattened void (Curran et al., 1987).

20 µm
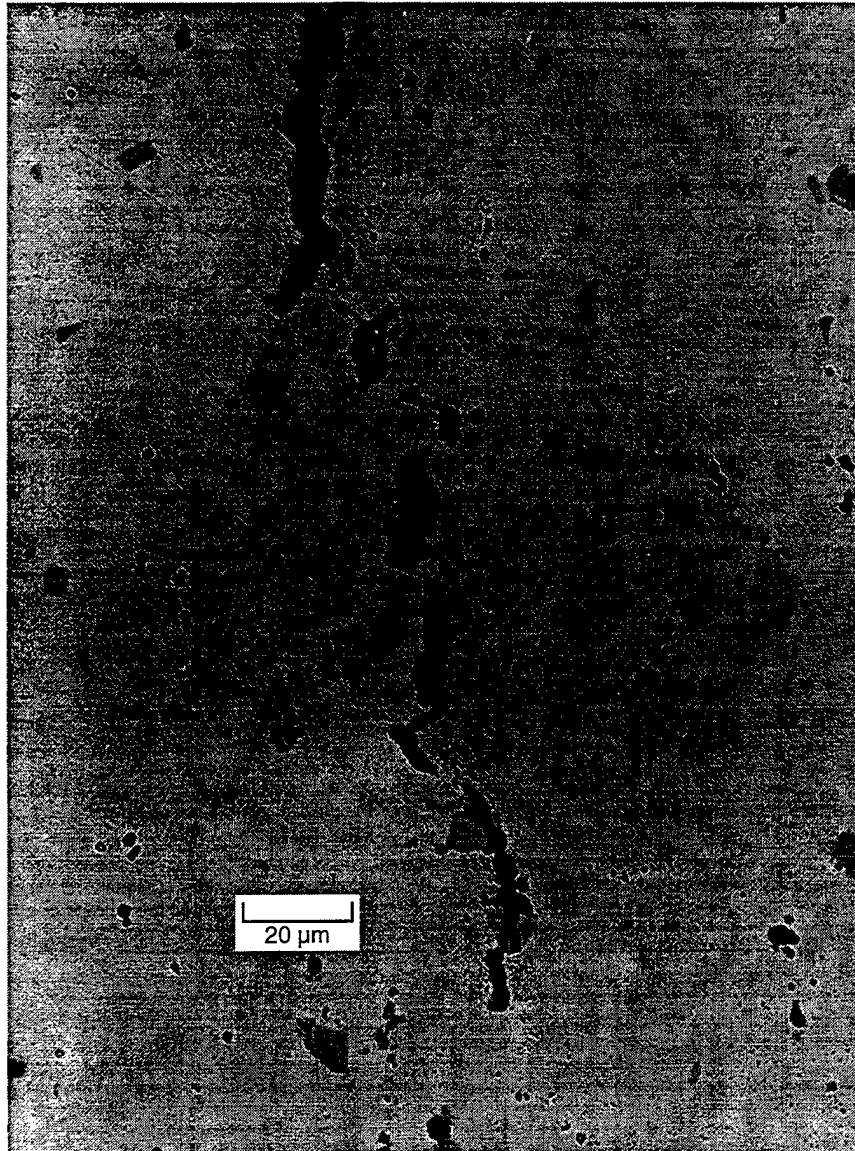
Figure 1-3. Cracking of inclusions in 2024-T81 Al (Curran et al., 1987).
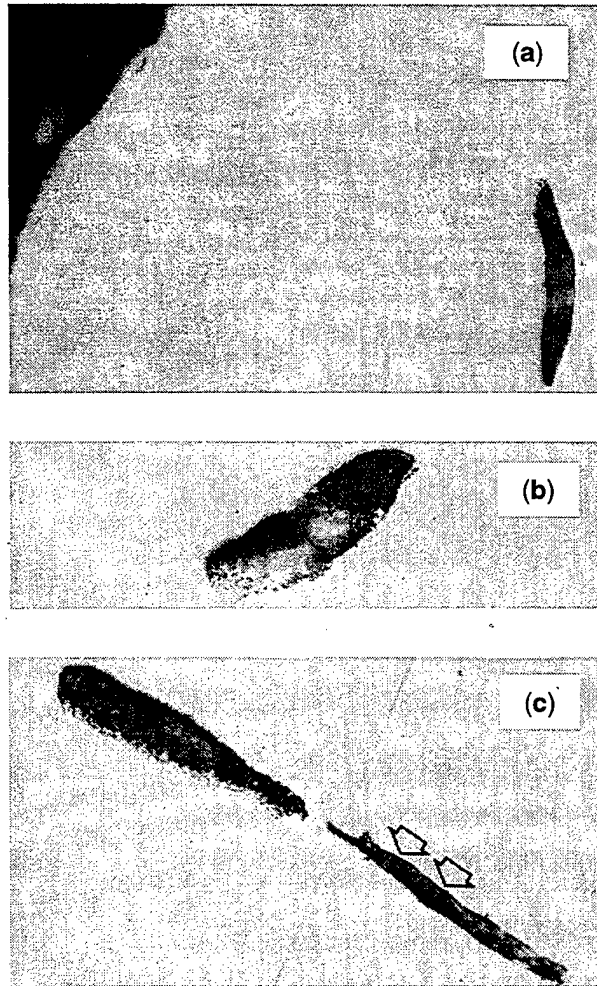
Figure 1-4. MnS inclusions in quasi-statically loaded
Charpy specimen. (a) Unbroken MnS
inclusions in relatively strain-free area
near notch flank. (b) Broken MnS
inclusion in highly strained region below
the notch showing the void remaining
where a portion of the solid inclusion
has dropped out. (c) MnS inclusion in
highly strained region below the notch,
one of which has acquired several
fractures (arrows), whereas the other
has dropped out (Curran et al., 1987).

300 µm

GPM-8678-143
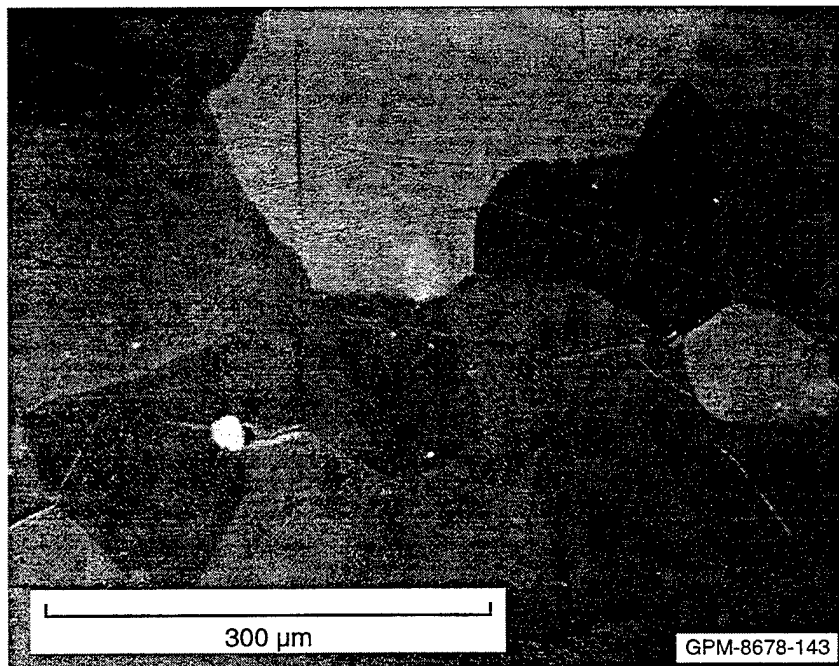
Figure 1-5. Nucleation of cracks and twins at oxide inclusions in high purity beryllium (Curran et al., 1987).
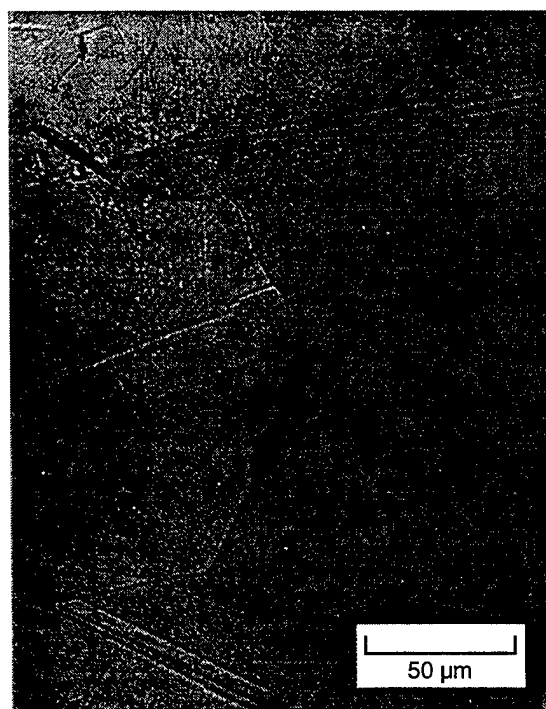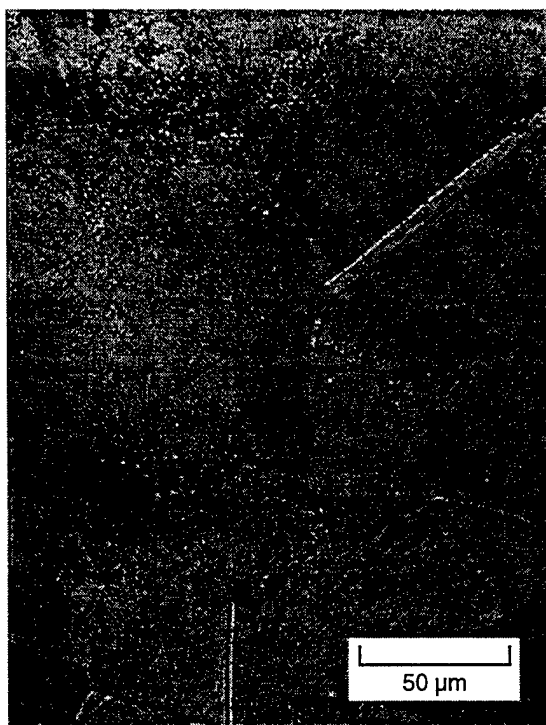
Figure 1-6. Void nucleation at grain boundaries
and triple points in OFHC copper
(Curran et al., 1987).
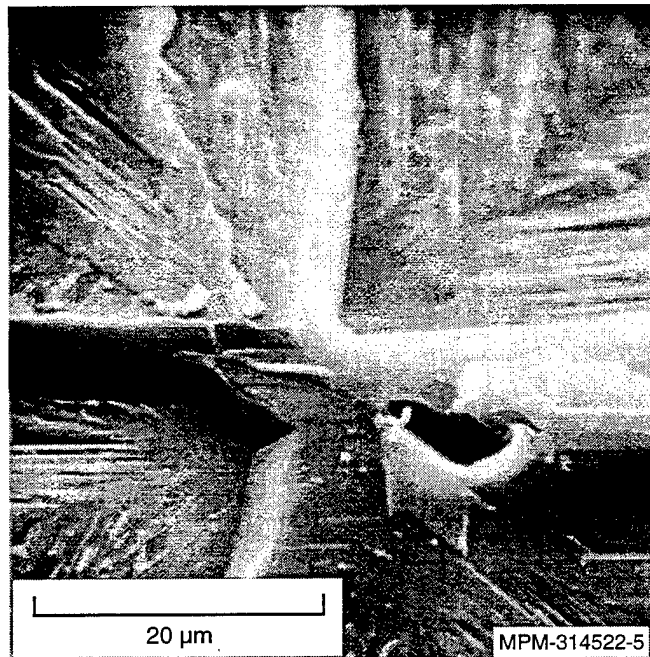
Figure 1-7. Crack nucleation site in beryllium where
a plastic flow-mechanism probably operated
(Curran et al., 1987).
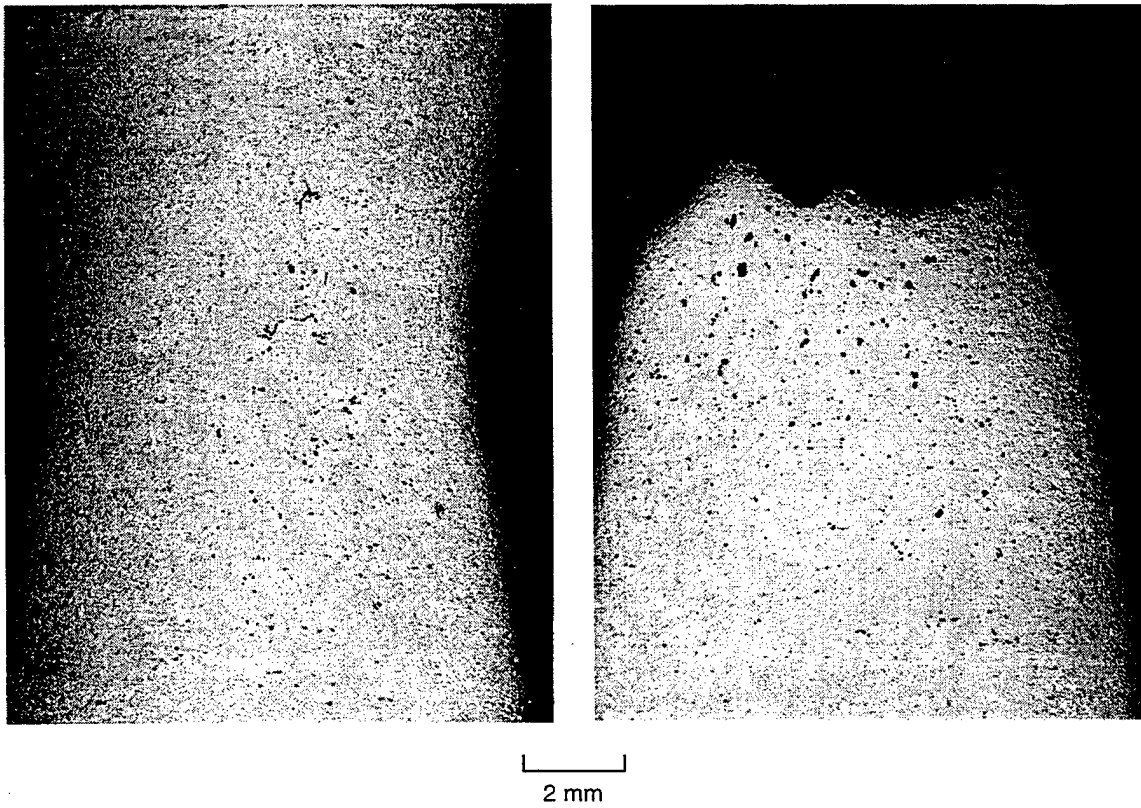
Figure 1-8. Photomicrographs of microscopic voids in sectioned specimens of A533B pressure
vessel steel (Curran et al., 1987).

(2) As brittle cleavage cracks that produce void volume by crack opening (see Figure 1-9).

(3) As shear cracks or bands that produce localized slip (see Figure 1-10). The shear cracks can be of two types: brittle shear cracks or regions of localized plastic flow often called "adiabatic shear bands."

1.3 EXPERIMENTAL METHODS AND ANALYSES.

Many of the experiments discussed in this report provide insightful information about the kinetics of the various modes of damage nucleation and growth described above. To achieve this objective, the experiments must be designed to provide well-controlled and measured stress and strain histories. The samples must be large enough to contain a statistical number of the microcracks or voids in material volume elements (MEs) that experience uniform stress and strain histories. That is, it must be possible to divide the sample into MEs, each of which has experienced a known load history, which implies that the load gradients must be small across each ME. In the language of computer modeling, the cell size must be big enough to contain many microcracks and small enough to experience a uniform load history.

Figure 1-11 shows several of the tests that can be used to study the mechanisms of dynamic fracture at various stresses, strains, and strain rates. The plate impact test is the most heavily used of the "high rate" experiments, both in the West and in the Former Soviet Union. In this test, a flat "flyer plate" is caused to nearly simultaneously impact on a flat "target plate", as diagrammed in Figure 1-12. The loading conditions are then especially simple: uniaxial strain. At later times unloading waves from the specimen edges relax the uniaxial strain condition, but by that time the reverberating stress waves in the specimen have produced the microdamage to be measured.

As shown in Figure 1-12, the flyer plate is launched by a gas gun, the technique most favored in the West. As discussed later, most of the analogous FSU experiments used high explosive techniques to launch the flyer plate. In plate impact tests, reverberating stress waves produce a series of tensile pulses in the target plate whose amplitudes and durations vary with position in the sample. The pulse amplitude is varied by varying the impact velocity, and the duration is varied by varying the specimen dimensions.

If the first tensile pulse is enough to nucleate and grow microdamage, the effect of the evolving damage is usually to damp the second tensile pulse enough to confine all the damage formation to that occurring under the influence of the first pulse. However, in some high amplitude cases, the second and successive pulses can also cause damage, usually refocused to adjacent "spall planes."

Figure 1-12 shows no target diagnostics, but a laser interferometer (e.g., VISAR) could be used in this configuration to measure the free surface velocity of the sample. In such tests, the impact velocities are measured and the sample is softly recovered for posttest microscopic evaluation. The recovered
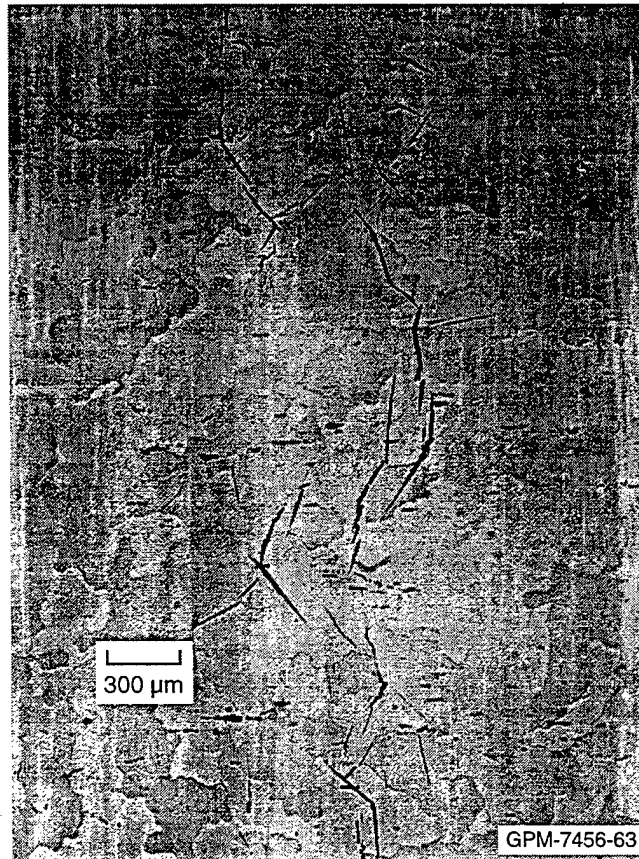
Figure 1-9. Photomicrograph of microcracks in Armco
iron (Curran et al., 1987).
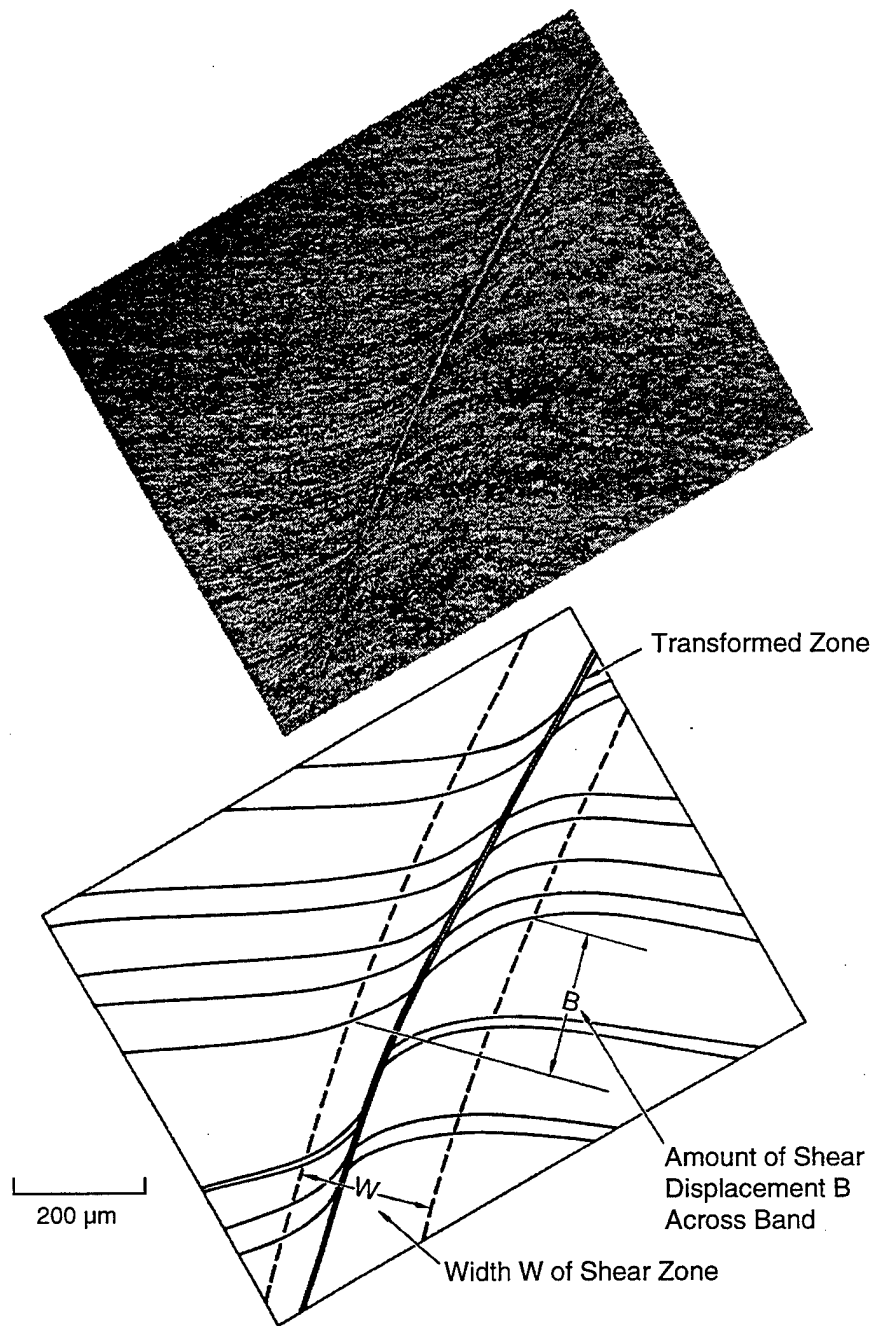
Figure 1-10. Micrograph and schematic of shear band in a plate
of rolled steel (Curran et al., 1987).

Labels in figure:
- Transformed Zone
- B
- Amount of Shear Displacement B Across Band
- W
- Width W of Shear Zone
- 200 μm
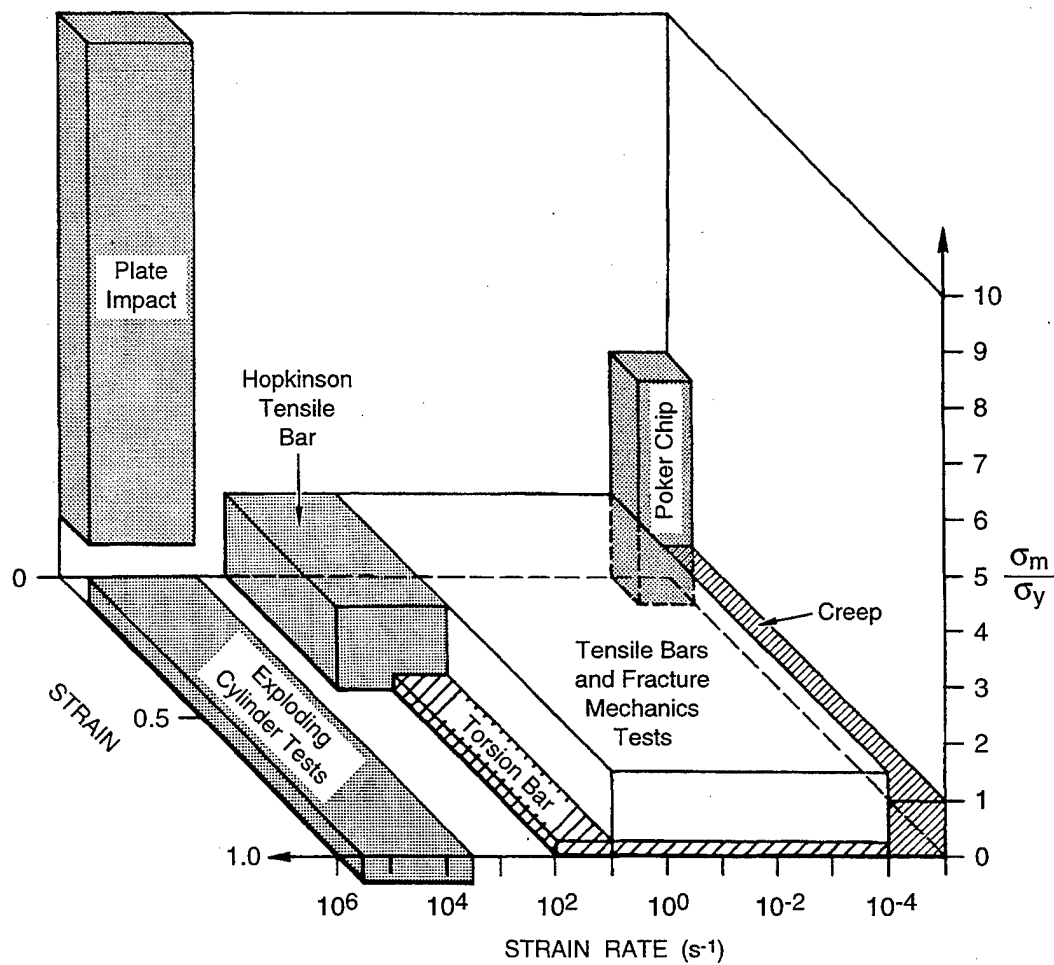
Figure 1-11. Regions of stress, strain, and strain rate attained by various mechanical tests (Curran et al., 1987).
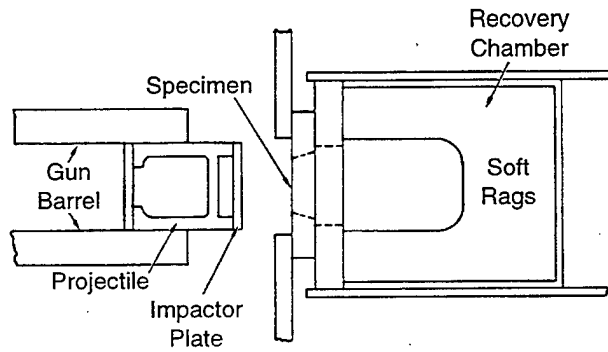
(a) Plate impact experiments for studies of dynamic fracture
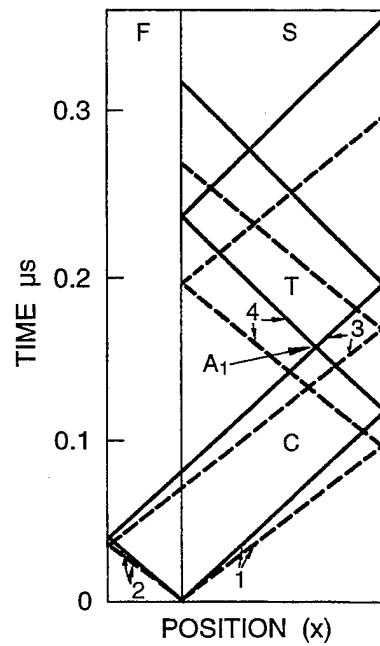
(b) Distance-time plot showing wave paths and compressive (C) and tensile (T) regions in a one-dimensional impact

Figure 1-12.   Schematic and wave dynamics of the plate impact test configuration used in the study of dynamic fracture (Curran et al., 1987).

samples are then sectioned and polished to reveal the microscopic damage, which is quantified by carefully measuring the number and size distributions of the microscopic cracks, voids, or bands. In an iterative manner to be described later (and more thoroughly in Curran et al., 1987), these distributions are then correlated with calculated load histories.

In other variations of the plate impact test, a material of lower shock impedance than that of the target material is placed at the rear surface, and particle velocity or stress history measurements are made of the "transmitted wave" in this "buffer" material. Figure 1-13 shows a schematic of the evolution of the stress pulse in this kind of experiment. Very many plate impact experiments like those shown in Figures 1-12 and 1-13 have been performed by both Western and FSU workers. As discussed later in detail, much information regarding the microdamage evolution kinetics is contained in the shape of the transmitted wave in the case of experiments with a buffer and in the shape of the free surface velocity profile in the case of experiments without a buffer.

Much of this report will be devoted to reporting and interpreting experiments of this type. Among the experiments discussed will be recent results in which the target plate is a single crystal, and the "impactor" is not a flyer plate, but an ion beam-driven plasma.

As discussed by Curran et al. (1987), creep tests and tensile round and notched bar tests also fulfill the above criteria for providing useful microdamage kinetics data at the other extreme of the strain rate spectrum. Intermediate strain rates are attained with Hopkinson tension and torsion bar experiments.

Figure 1-14 shows results for the evolution of ductile void damage in a round bar tensile test. This detailed picture of damage evolution is a good example of the kind of information we wish to obtain from posttest examinations of dynamically loaded plate impact samples.

Figures 1-15 and 1-16 show an experimental technique for obtaining similar data for the microscopic damage mode of "adiabatic shear banding," a type of plastic instability in which the plastic strain localizes into microscopic patches of concentrated slip.

In summary, in all the experiments shown in Figure 1-11, a key diagnostic technique is the posttest sectioning of the specimens to reveal and quantify the microscopic damage in various stages of evolution. The microstructural damage characterizations thus obtained can be correlated with measurements of the wave profiles recorded during the experiments to provide a powerful tool for understanding, quantifying, and modeling damage evolution and fracture.

1.4 CONSTITUTIVE RELATIONS FOR THE EVOLUTION OF DAMAGE.

The ultimate use of the experimental data reviewed here is to develop, validate, and calibrate mesomechanical constitutive relations for describing the behavior of materials undergoing damage and
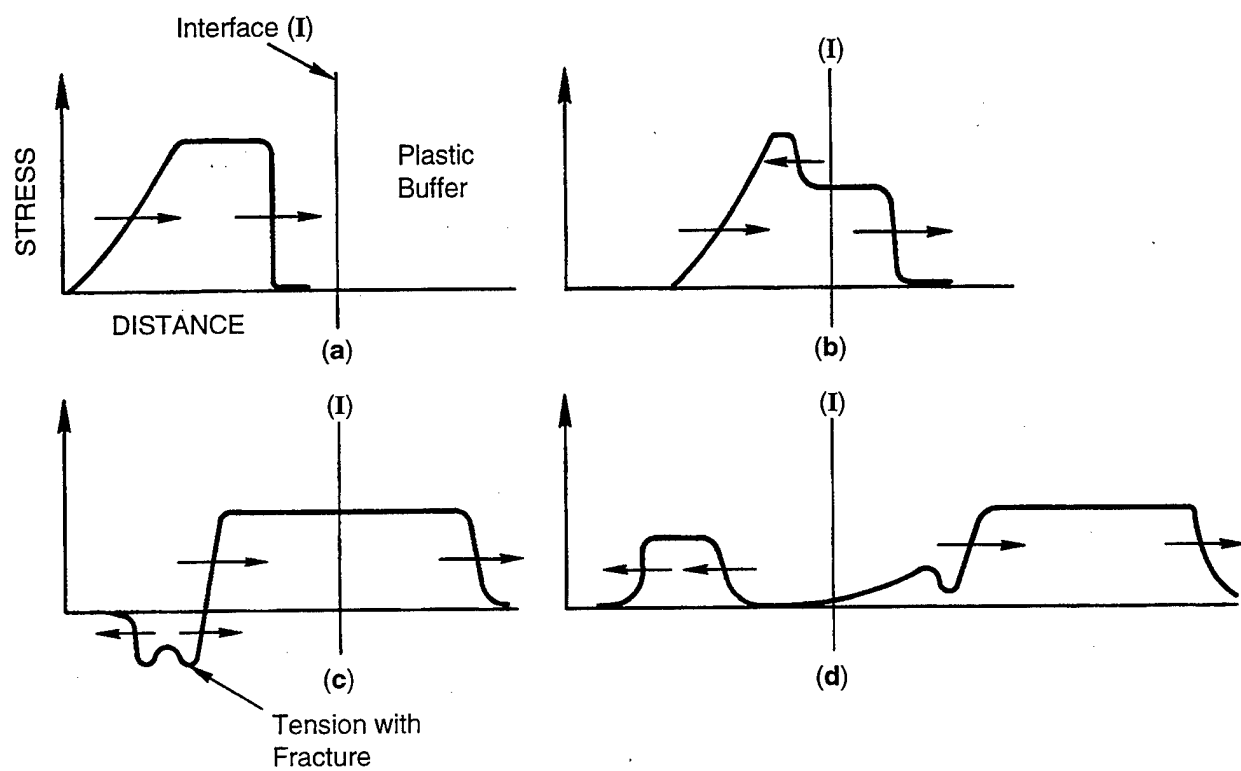
Figure 1-13. Development of fracture signal (Curran et al., 1987).
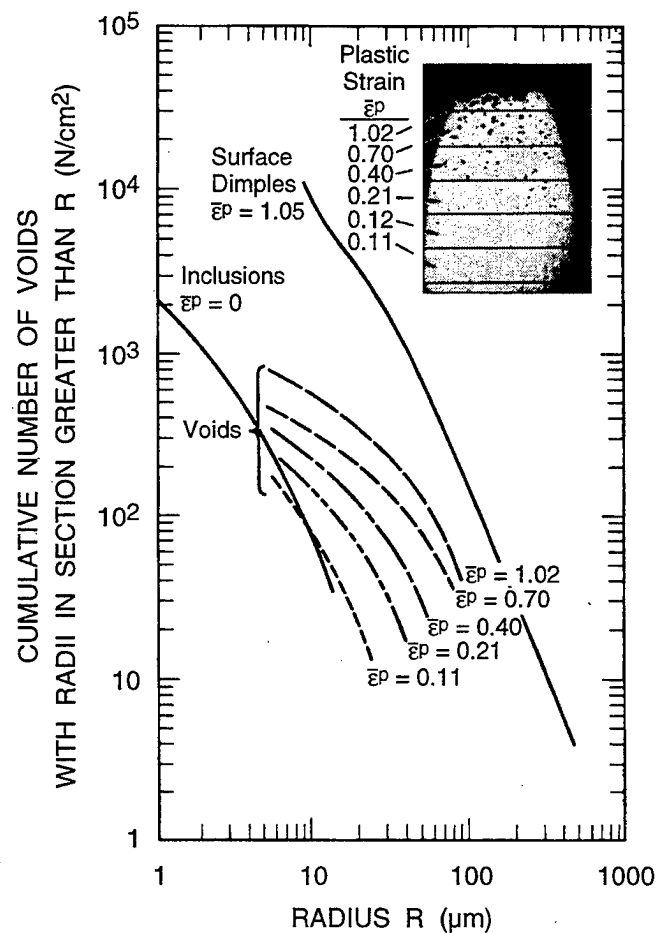
Figure 1-14. Size distributions of inclusions, voids, and surface dimples in a smooth tensile bar of A533B steel, heat CBD, at various plastic strains (Curran et al., 1987).

21
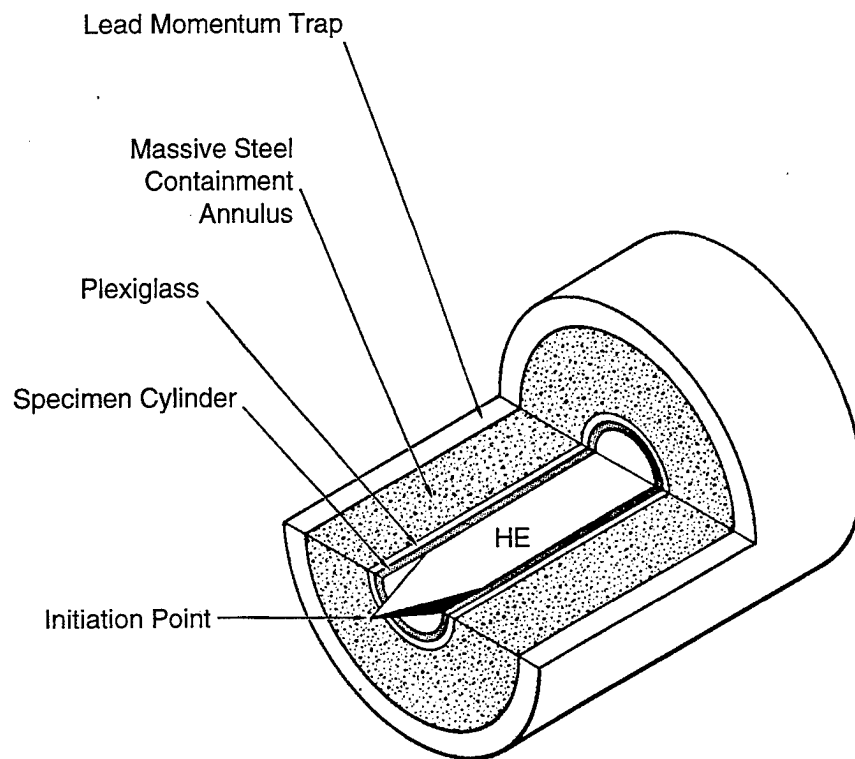
Figure 1-15. Contained fragmenting cylinder experiments for studying shear band kinetics (Curran et al., 1987).

Shear Bands

(a) Cross section of cylinder with damage

(b) Surface data

(c) Volume data
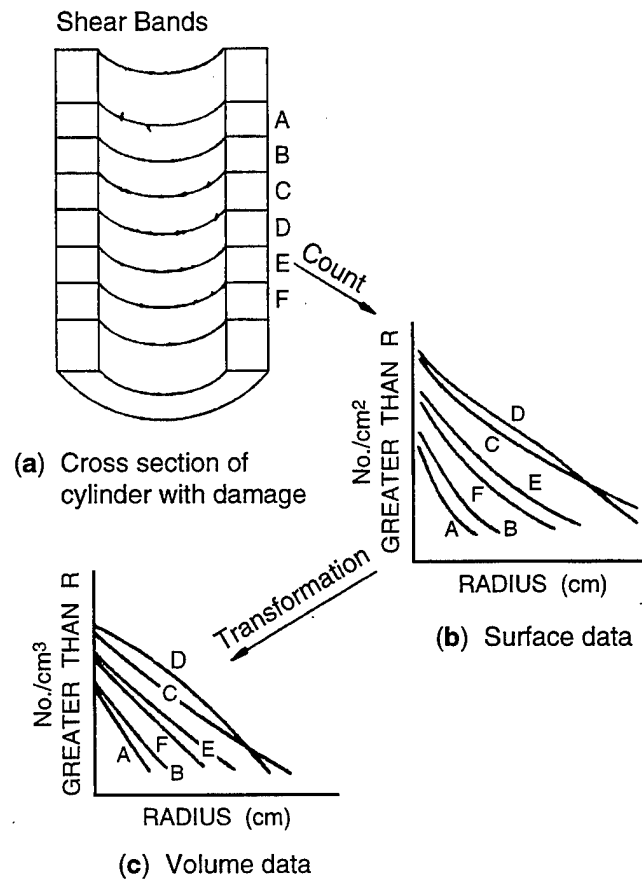
Figure 1-16. Steps in obtaining cumulative shear band distributions from contained fragmenting cylinder data (Curran et al., 1987).

23

fracture. Such constitutive relations are reviewed by Curran et al. (1987) and will be discussed in later chapters in detail in connection with the experimental data.

The discussion focuses on the nucleation and growth (NAG) modeling approach, but we also discuss a second, simplified type of material model, one that is based on empirical damage evolution relations. Such empirical models, developed by both Western and FSU scientists, are useful in experimental design and in preliminary interpretation of data.

As mentioned briefly above, "classical fracture mechanics" is a discipline that deals with the conditions for instability (initiation), propagation, and arrest of a single large crack, where "large" means that the crack is large compared with the microstructure. The link between the mesomechanical approach and the classical approach is that the former can be used to model the evolution of microscopic damage in the "process zone" at the tip of the macroscopic crack. We will not discuss this link further, but we wish to emphasize that the experimental data presented here is applicable to classical fracture mechanics insofar as macrocrack propagation is related to the nucleation and growth of microscopic damage.

1.5 OBJECTIVES AND REPORT ORGANIZATION.

The objectives of this report are to

- Describe and analyze the techniques and physical aspects of the spall test methods.

- Describe the microstatistical mechanics and kinetic aspects of fracture under shock-wave loading.

- Analyze the constitutive factors of dynamic fracture (such as load duration and amplitude, orientation, temperature).

- Describe FSU and Western experiments used to generate the reported data.

- Show how the experimental data are interpreted with the use of the models.

- Provide a library of data and constitutive model parameters for many engineering materials.

The remainder of this document is organized as follows. Section 2 provides a qualitative description of the spall process including information about the nature of spall fracture, measurements to quantify the spall process, and means of representing damage in constitutive fracture models.

Section 3 presents the theoretical background for wave propagation. The treatment is not comprehensive, but the laws of one-dimensional motion of compressible continuous media are described in enough detail to introduce the discussions of dynamic experiments in Section 4. Section 3 summarizes the conservation

laws for wave propagation, the theory of characteristics, analysis of the shock front, temperature in shock and rarefaction waves, elastic-plastic material response, and the methods used in computer simulations.

Section 4 describes the experimental techniques used in the study of dynamic fracture. The discussion covers the experimental means of producing controllable shock wave loads suitable for the study of spall fracture, the techniques used to measure particle velocity and stress histories during the experiment, and the procedures used to characterize fracture damage in shock loaded samples.

Section 5 describes the methods used to estimate the fracture stress based on free surface velocity histories measurements or particle velocity measurements at the interface between a spall sample and a buffer plate of lower impedance. The section also includes an overview of other methods used over the years to determine the fracture stress during spall.

Section 6 examines the influence of damage kinetics on wave dynamics, using the theory of characteristics and the linear acoustic approximation. Here, we examine the evolution of the spall pulse as we attempt to relate the features typically observed in experimental records to the damage kinetics in the interior of the sample.

Section 7 describes the spall fracture phenomenon in relation to materials of various classes. Experimental data for metals and metallic alloys, metal single crystals, ceramics, glasses, polymers, and elastomers are examined in this chapter, and the trends in the data are discussed. The effects of temperature, strain rate, heat treatment, and anisotropy on the spall strength of the various materials investigated are also examined. Connected with this section are two appendices given in Volume 2: Appendix A, which provides correlations between Russian metals and alloys and their counterparts in the Western literature, and Appendix B, which includes experimental records from 148 spall experiments performed by the present FSU authors and their colleagues at the Russian Academy of Sciences. Enough detail is provided with each of the experimental records to allow the interested reader to computationally simulate the experiment.

Section 8 presents a simple empirical model for describing the kinetics of spall fracture. The model is based solely on measurements of free surface velocity profiles. The model parameters are determined for an aluminum alloy, and numerical simulations with the model are compared with measured free surface velocity histories.

Section 9 provides a detailed description of the nucleation and growth (NAG) microstatistical modeling approach. The chapter describes the experimental aspects of ductile and brittle fracture, and in each case, the experimental discussions is followed by an analytical treatment and model development. Two models: DFRACT (for Ductile FRACTure) and BFRACT (for Brittle FRACTure) are described in detail. The section concludes with a section on the application of the NAG fracture method, discussing response characteristics, model parameters, and simulations results are discussed for a variety of materials of practical interest including metals, ceramics, plastics, and geologic materials.

Section 10 provides concluding remarks, promising applications, and speculations regarding future directions.

SECTION 2

DESCRIPTION OF FAILURE PROCESSES

2.1 BACKGROUND AND SCOPE.

This qualitative description of spall processes is based on our current view of fracture and is not necessarily applicable to all situations and all materials. Spall processes are examined in more details in later sections, where the features associated with spall of materials of various classes are also discussed.

Spall damage occurs when rarefaction (expansion) waves within a material interact in such a manner as to produce tensile stresses in excess of the threshold required for damage initiation. Favorable conditions for spall can be produced (1) by impacts, (2) by lasers or other thermal radiation sources, and (3) by explosions. In each case, the spall-producing rarefaction waves are preceded by compression waves generated in the specimen by the initial impact, by the thermomechanical stresses associated with energy deposition, or by the detonation wave generated by the explosives. Figures 2-1 through 2-4 show examples of each of these three kinds of loadings.

Figure 2-1(a) shows a typical plate impact experimental configuration in which a 1.14-mm-thick Armco iron flyer plate is made to impact a target assembly consisting a 3.16-mm-thick Armco iron plate and a 4.80-mm-thick PMMA buffer plate with a stress gage sandwiched between the Armco iron and the PMMA plates to provide diagnostic measurements during the experiment. The configuration shown in this figure was used in a series of spall experiments in Armco iron (Seaman et al., 1971; Barbee et al., 1972), and the data from the experiments were used to calibrate the BFRACT (Brittle FRACTure) model used in the simulations presented later in this section. The relatively low impact velocity of 50 m/s was intentionally chosen in this case to ensure elastic response throughout, so that the basic features of wave propagation in a typical spall experiment could be identified without the additional complications associated with plastic yielding or spall fracture.

The stress histories at several locations within the Armco iron target, simulated using SRI PUFF (Seaman and Curran, 1978), are shown in Figure 2-1(b). As shown, the impact causes a square wave to propagate into the sample away from the impact plane. The amplitude and duration of this stress wave can be controlled by varying the impact velocity and the thickness of the flyer plate, respectively. A wave of the same amplitude also propagates into the flyer plate. The compression waves in the flyer and target plates have uniform amplitudes of stress and particle velocity. These outward-facing compression waves are reflected from the back free-surface of the impactor and from the interface between the Armco iron and

27
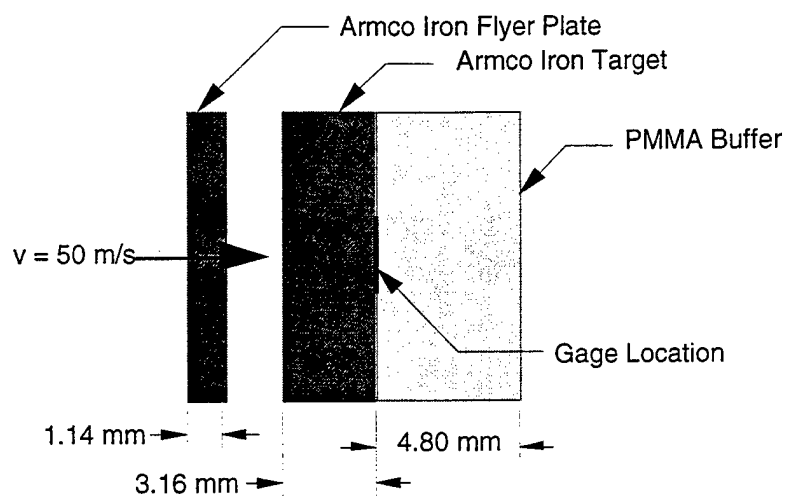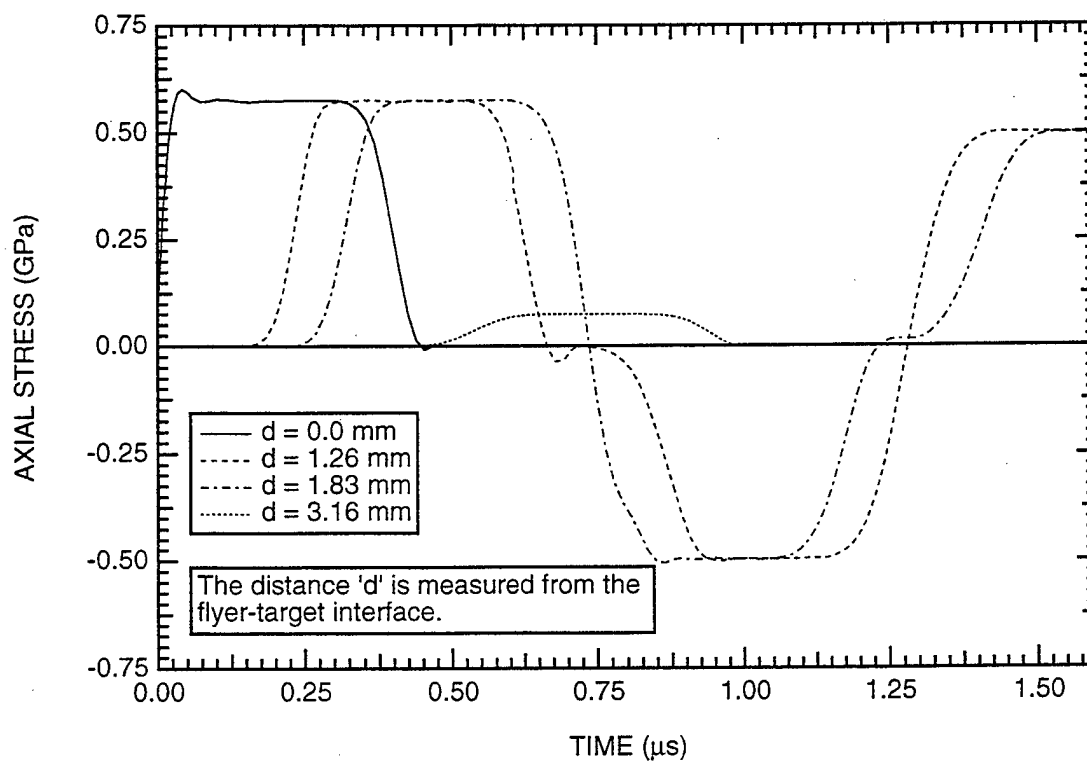
(a) Configuration.

(b) Stress histories at various locations within the target.

Figure 2-1.   Configuration for a low-impact plate impact test in Armco iron and typical stress histories simulated using SRI PUFF.
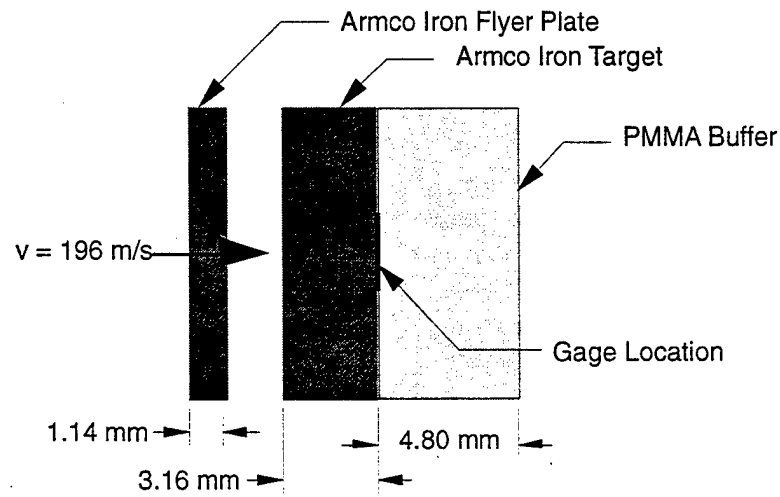
(a) Configuration.
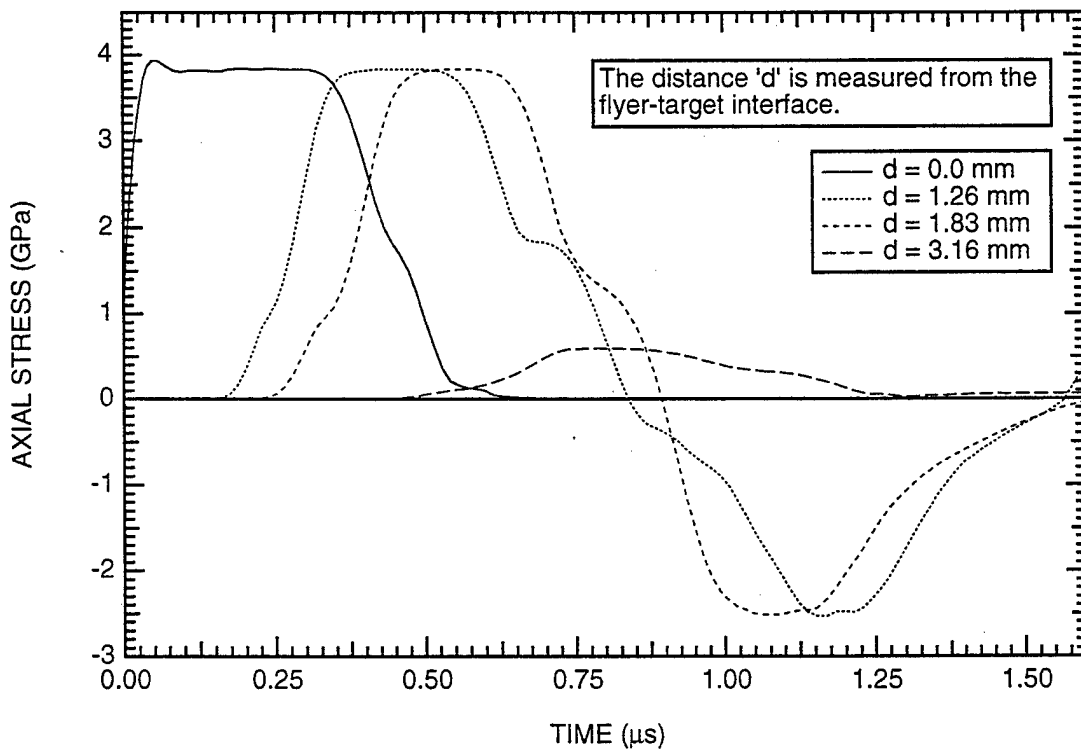
(b) Stress histories at various locations within the target.

Figure 2-2.   Configuration for a high-impact plate impact test in Armco iron
and typical stress histories simulated using SRI PUFF and the
BFRACT fracture model for Armco iron.

29
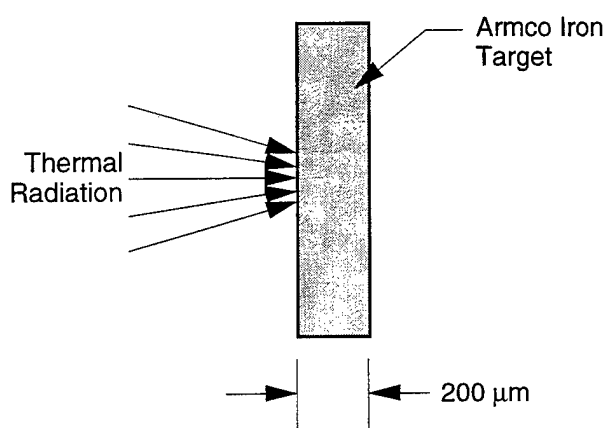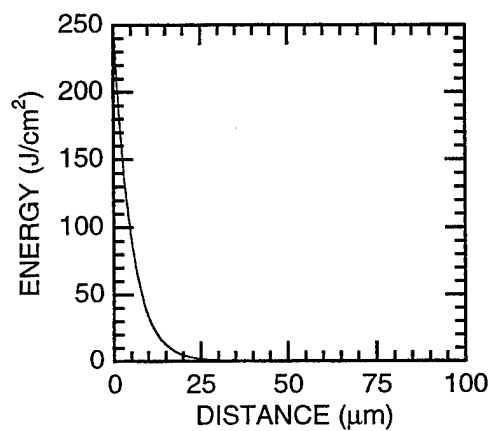
(a) Configuration.

(b) Energy deposition profile.

The distance 'd' is measured from the irradiated surface of the specimen.

d = 15.62 μm
d = 43.99 μm
d = 72.61 μm
d = 119.2 μm
d = 152.6 μm
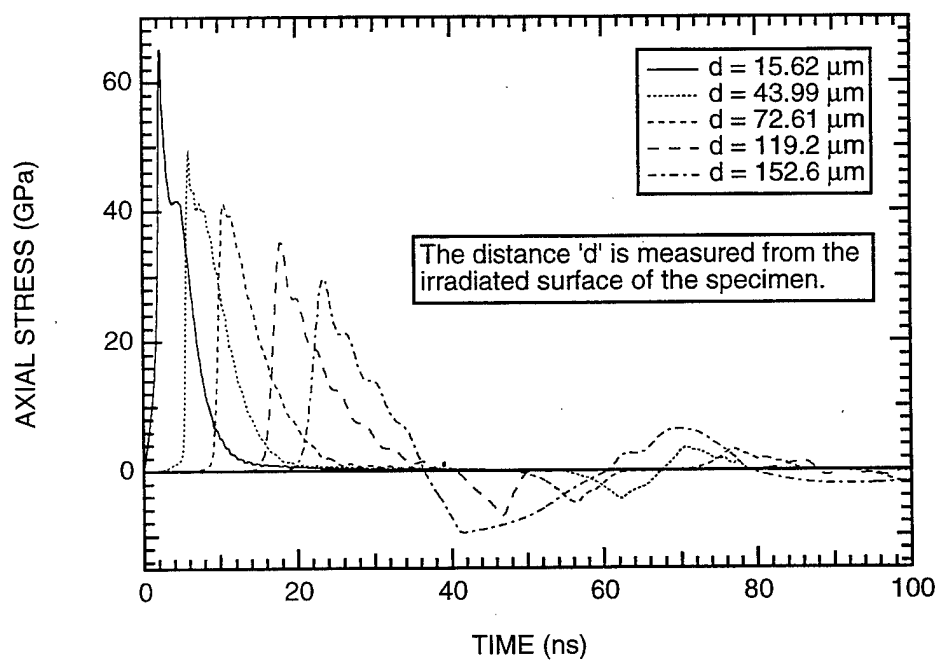
(c) Stress histories at various locations within the target.

Figure 2-3. Configuration for a thermal radiation test and typical stress history in the target simulated using BFRACT.

30
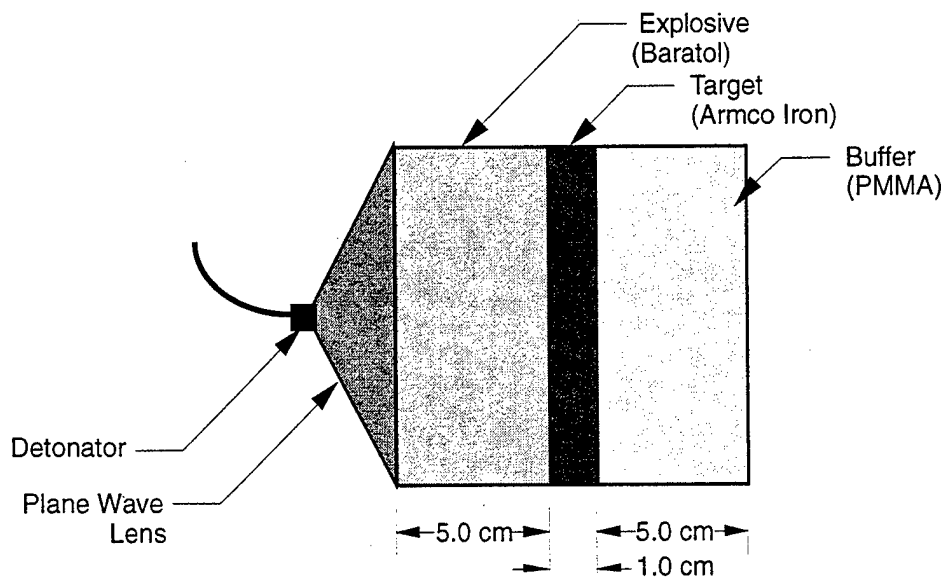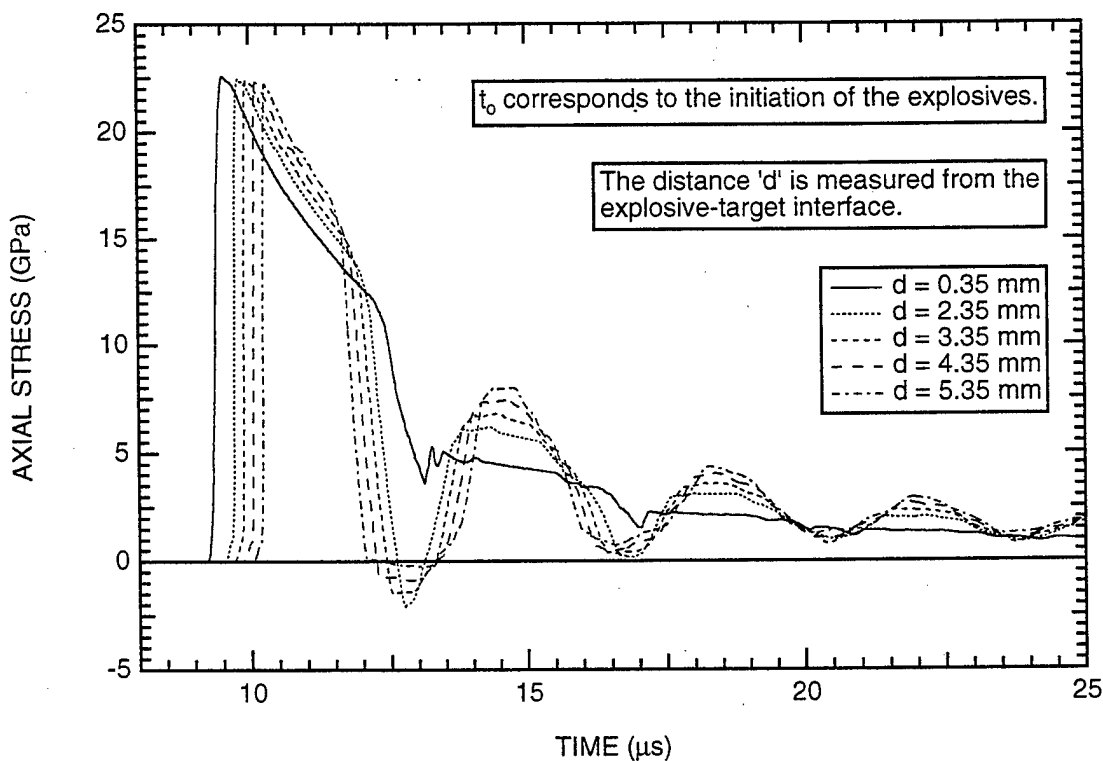
(a) Configuration.

(b) Stress histories at various locations within the target.

Figure 2-4.   Configuration for an explosive loading test in Armco iron and typical stress histories in the target simulated using BFRACT.

31

PMMA plates as inward facing rarefaction waves. The relief waves propagate toward the interior of the target plate, where they interact to produce states of tensile stress as shown in Figure 2-1(b). Tensile fracture damage occurs in the specimen if the tensile stress magnitude exceeds the threshold for spall damage.

In the foregoing example, the tensile stress wave in the target did not have a high enough amplitude to cause spall damage. In the next example, shown in Figure 2-2, the peak stress is increased to a level that causes spall damage by increasing the impact velocity from 50 m/s to 196 m/s. The stress histories shown in this figure were simulated using SRI PUFF. Spall damage was treated in the simulation by using the BFRACT fracture model, with the model parameters determined from a series of spall experiments like the one shown in Figure 2-2(b). BFRACT is described in detail in Section 8, but we simply use the model here to show the effect of spall on the wave structure. As in the elastic case, stress wave interactions lead to tensile stresses in the specimen. Unlike the elastic case however, the stresses in the present example are high enough to cause spall damage under tension as well as yielding under compression, as illustrated by the kink in the stress history at a stress level of about 1 GPa. The effect of spall on the wave structure is evident in this figure. Details of the stress wave profiles in the interior of the specimen and on the gage plane will be discussed further in later sections.

Figure 2-3 shows an example in which spall damage is induced by deposition of thermal radiation (e.g., lasers, x-rays) into a semitransparent sample. Here a bipolar stress pulse develops in the sample, and there is a possibility of either front surface (left) or rear surface (right) spall depending on the parameters that affect wave interactions (i.e., Grüneisen coefficient and absorption depth of the sample material, and wavelength, pulse width, and fluence of the laser). Front surface spall may occur when the rarefaction waves originating at the front surface of the specimen overtake the initial compression wave, attenuate it, and produce a tensile stress state of enough magnitude to cause fracture near the front surface. The triangular-shaped compression wave travels toward the rear surface of the specimen. When it reaches the stress-free back surface boundary, the stress wave reflects back into the specimen as a rarefaction wave. The interaction of the rarefaction wave with the compressed state could lead to tensile stresses of sufficient magnitude to cause fracture. Figure 2-3 shows a scenario in which the Armco iron plate experienced rear surface spall.

Figure 2-4 shows an explosive in contact with the sample. This case is somewhat like the impact case, except that the explosive loading provides a compressive wave with a decaying stress amplitude. The decay rate of the peak stress is rather slow; hence, the rarefaction wave reflected from the front interacts with a compressed state of essentially the same magnitude, thus providing a very small tensile stress. Therefore, the main region for spall is near the center where the rarefaction waves from the front and back surfaces intersect. The periodic oscillations in the stress profiles shown in Figure 2-4 are due to wave reverberations within the sample plate.

2.2 SPALL FRACTURE.

The focus of our investigation is spall fracture under one-dimensional uniaxial strain conditions. Under these conditions, the material undergoes relatively large volumetric strain and comparatively little shearing strain, a situation that is very different from the more usual one in structural analysis, where there may be large shear strains but little volumetric strain. Also under these conditions there are no free boundaries for most of the material, so the stresses are not limited to the yield strength, and stresses many times the yield strength are often reached.

The loading rates are 10^4 to 10^5 per second under tension and sometimes higher under compression. The durations of loading and therefore the time during which fracture occurs in samples with dimensions of about 1 centimeter (laboratory-scale tests) are about 1 μs, and often the tests are arranged so that the loading duration is only a few nanoseconds.

2.2.1 Observations of Fracture.

Figures 2.5 through 2.8 show cross sections of disk-shaped target plates that were impacted by another flyer plate. The sections were made along a diameter of the disk, and most photomicrographs were made of regions near the center of the disk where the material was under a state of uniaxial strain during most of the period of damage. The targets in Figures 2-5 and 2-6 were impacted from the top with enough velocity to produce an intermediate level of damage.

The target plate in Figure 2-5 was 6.313-mm-thick commercially pure aluminum, impacted by a 2.27-mm-thick flyer plate traveling at 145 m/s, and it was heated to 400°C before the impact. The lines drawn on the photo were used for a quantitative analysis, which is discussed in Section 4.3. The appearance of the fracture is that of nearly spherical voids in regions of low damage. The odd-shaped voids in the heavier damage areas in a central plane in the target were probably formed by coalescence of many smaller voids. About 40% of the plate thickness is shown in the figure, so we see that the fracture is spread over the central 20% of the plate.

The impacted aluminum target from a 251-m/s impact is shown in Figure 2-6. The impact was from the left side in the figure and a epoxy buffer plate was on the right. The photomicrograph was made near a cylindrical edge of the target disk (down and out of the photo) where the flow is not uniaxial for the entire period of damage. Near this edge of the target plate, full separation has occurred, whereas the center is heavily damaged but not separated. The macroscopic appearance is that of a running crack with a very rough surface, but in fact the damage occurred mostly simultaneously along the damage plane and the running crack represents only the completion of separation for a portion of the distance.

Figure 2-7 shows a similar cross section through a target plate of Armco iron. In this case, microcracks cut through the iron grains (the grain boundaries are not visible in the photo). The zig-zags nature of the

33
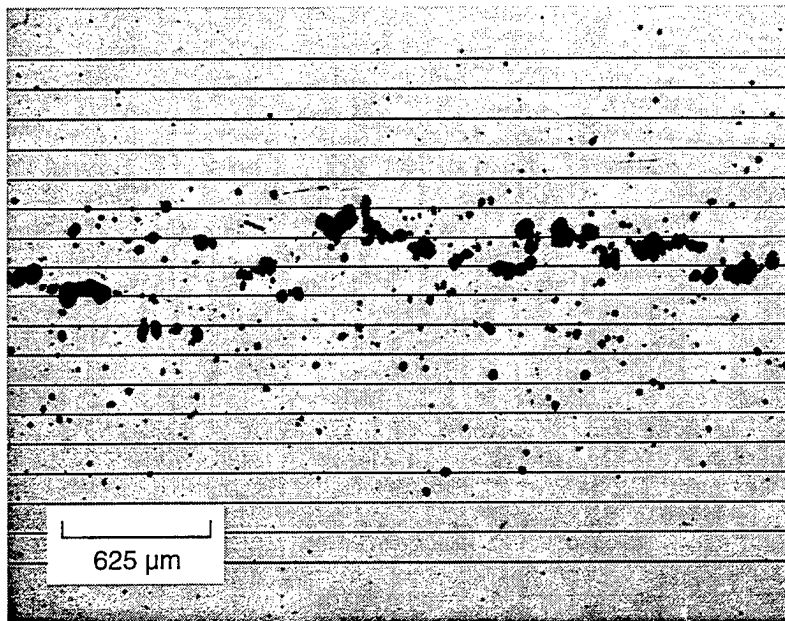
Figure 2-5.   Impingement of voids and cracks in impact-loaded
specimens of 1145 aluminum.

500 μm

(a)

50 μm

(b)
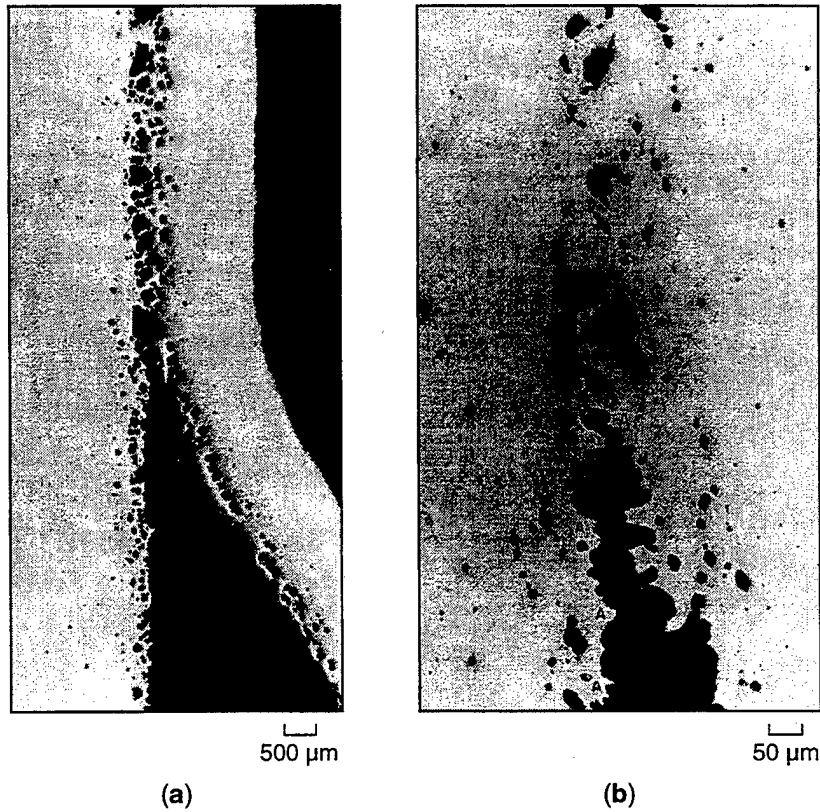
Figure 2-6. Ductile cracks.

(a) Ductile crack propagation by void coalescence. (b) Tip
of ductile crack shown in (a) at higher magnification.
Material failure by void coalescence due to necking of the
regions separating the voids is apparent near points A
(Barbee et al., 1970).

35
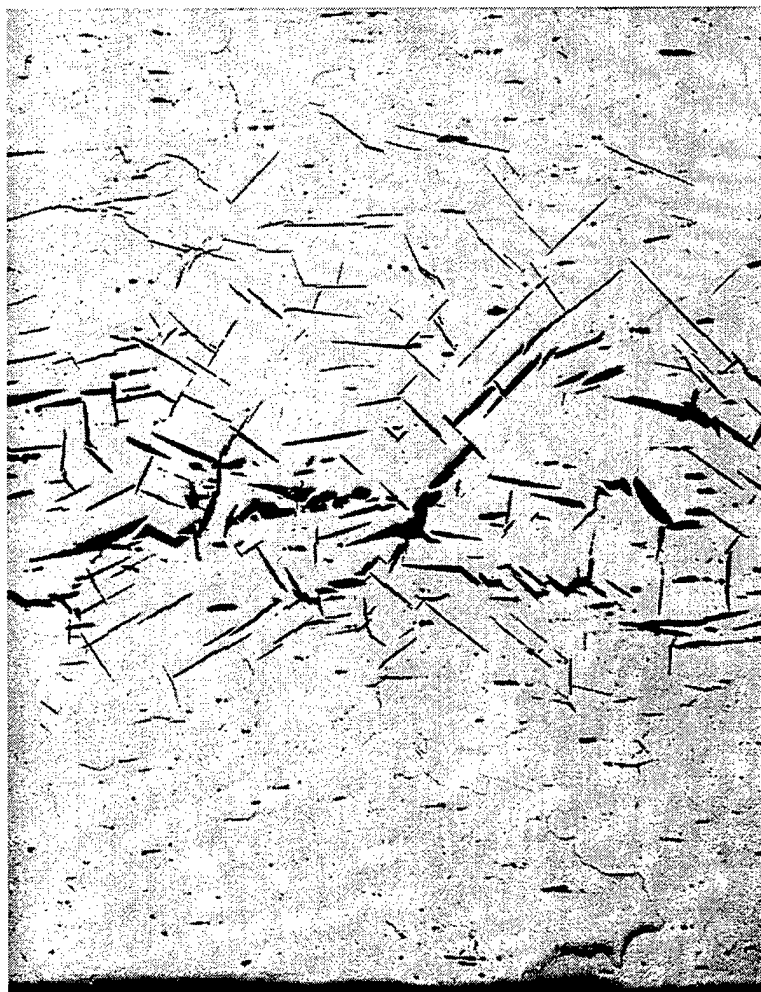
Figure 2-7. Impingement of voids and cracks in impact-loaded
specimens of Armco iron (Curran et al., 1987).

0.5 mm

Figure 2-8.   Coalesced microcracks in Armco iron (Curran et al., 1987).

cracks have occurred because the cracks follow preferred directions in each grain and then change direction as they cross grain boundaries. A great many microcracks have formed, and they have interacted strongly so that they are almost to the point of producing separate fragments. No fracture plane has formed, but there is a central region along which there is a maximum of damage; this region would have become the fracture plane if the impact velocity had been higher.

Another Armco iron target with somewhat higher damage is shown in Figure 2-8. The 6.35-mm-thick target was struck at 149 m/s by a 2.39-mm-thick flyer. Again, we see a broad region of damage nearly a millimeter, wide, and coalescence of the microcracks has proceeded to the point of roughly defining a fracture plane. This figure is typical in illustrating that no actual spall "plane" occurs. Rather a surface of separation wanders through a field of partially fragmented material. An etchant has been used on the target so we can faintly see some of the grain boundaries.

2.2.2 The Fracture Processes.

Under the very rapid loading conditions that prevail during spall, fracture usually produces very many microcracks or microvoids: 10^6 or more per cubic centimeter. With so many damage sites, nucleation is a very important aspect of damage and may lead almost directly to fragmentation or shattering of the material. Here "nucleation" means the initial formation of the microcrack or microvoid by decohesion of an inclusion from the matrix material, initiation of a void or crack at a triple point between grains, or activation of a dormant crack or void or flaw. This aspect of dynamic fracture is different from fracture under quasi-static loading, where a single crack or a few cracks usually dominate the material response. Thus, nucleation plays a lesser role under static loading. Furthermore, in the static case surface imperfections are significant because fracture usually initiates at a surface or boundary where a small flaw already exists. In contrast, spall fracture occurs in the midst of the body; hence, it is a bulk material behavior unaffected by surface defects.

Growth of microcracks or microvoids under dynamic loading conditions is different from that in ordinary fracture mechanics in that there are myriads of damage sites, each of which grows a small amount, rather than one crack that grows from a microscopic size to the size of the structure. The crack surfaces formed under quasi-static loading and under spall conditions often look very similar in spite of these differences and the difference in the rates of loading. The surfaces are generally very rough under both fast and slow rate loading, because each larger crack is actually formed by the joining of many smaller cracks.

Fracture may occur under conditions of pure tension or a combination of shear and tension across the potential spall plane. Here, we focus on conditions in which tension is the primary driver for the fracture, but shear may still be present.

38

2.2.3 Definitions of Terms.

"Spall fracture" means fracture that occurs simultaneously over an area, not by growth of a single macrocrack, but by the nucleation and growth of a many cracks, or voids at essentially the same time. Suitable conditions for such fracture occur only during wave propagation; hence, spall fracture refers to damage caused by tensile wave(s) that have reflected from a boundary.

In describing spall fracture, the term "damage" may have many meanings, depending on the observations and the point of view of the researcher. One definition is relative void volume or relative crack volume. The following parameter is useful for characterizing spall damage in cases where fracture occurs by nucleation, growth, and coalescence of a large number of cracks:

$$\tau = T_F \sum_{i=1}^{n} \Delta N_i R_i^3 \qquad (2.1)$$

where T_F is a dimensionless constant associated with the shape of fragments and ΔN_i are the numbers of cracks per unit volume with radii R_i. The use of ΔN_i and R_i to describe a distribution of crack sizes is described more fully in Section 8. The τ factor is dimensionless, varies from 0 to 1, and controls the gradual reduction of stiffness of the material as damage increases. The term damage has often been used by other authors to describe a more qualitative factor, which describes the progress from intact to full separation, but without an explicit relationship to observed fractures.

"Spall strength" is a term used loosely to indicate the relative resistance of material to spallation under a specific set of conditions. The stress-strain path followed by Armco iron in Figure 2-9 illustrates several stress levels that may be associated with "spall strength": the beginning of nucleation, the peak tensile stress, and the beginning of coalescence. The path certainly depends on the strain rate, stress level in the impact, and the temperature. Because the stress path does not have a square top and the peak depends on so many factors including the conditions of the test, the "spall strength," "tensile strength," and "fracture stress" have various interpretations. However, we will usually use the term "spall strength" to denote the peak tensile stress attained under the specific loading conditions considered.

2.3 MEASUREMENTS TO QUANTIFY THE SPALL PROCESS.

Both active and passive measurements can be used to assist us in quantifying the damage that occurs during the spall process and in determining the fracture rate processes. Active measurements are dynamic time-dependent measurements of stress or particle velocity histories that occur at some points in the test specimen. Passive measurements include posttest examinations of the recovered sample. Measurements of both types provide valuable information that can be used to aid in the understanding of spall processes.

39
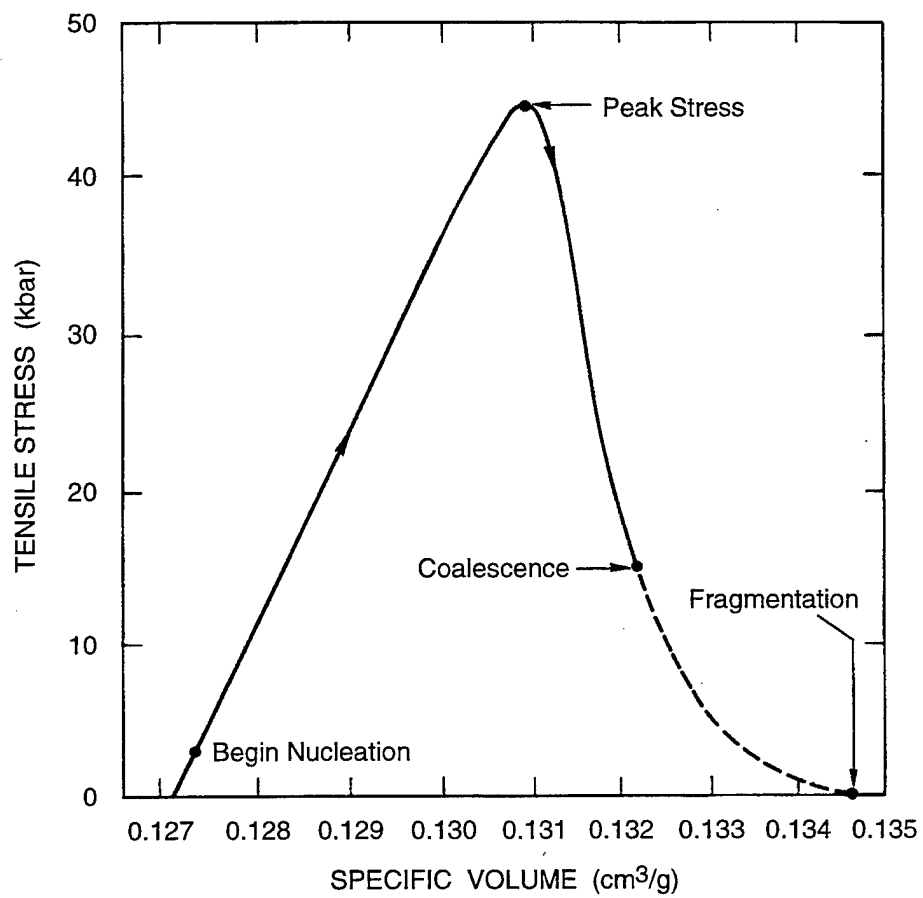
Figure 2-9. Stress-volume path for constant strain-rate loading
of Armco iron to fragmentation (Shockey et al., 1973a).

However, neither active nor passive measurements provide a direct means for determining either the stress history at the spall plane or the rates at which the damage has occurred. For these reasons, all determination of this stress history and of the damage rates are indirect. A detailed analysis of the fracture event is required, using all our knowledge of the wave propagation processes, other material processes, assumed forms for the fracture processes, the gage records during the event, and the state of damage after the event. By combining the experiments and computations, we expect to obtain fracture descriptions that represent at least averages of the actual processes.

2.3.1   Time-Dependent Measurements.

Dynamic measurements of the stress and particle velocity can be made during the fracture event. For stress measurements, a piezoelectric or piezoresistive gage is used to obtain an electric signal that is approximately proportional to the stress experienced by the gage. A piezoelectric stress gage, such as a quartz gage, may be placed as in Figure 2-10, behind the target plate as the buffer material. Because of their relatively high impedance, quartz gages are not normally used in spall experiments. A piezoresistive stress gage is a thin foil embedded within the target, either within layers of a material or at the interface between different materials (such foils are indicated in Figure 2-10 on the impact plane, between layers of the target, and between the target and the buffer).

Particle velocity measurements can be made using metal foil gages (generally copper) and a magnetic field around the sample; a current (or voltage) is induced in the foil by its motion in the magnetic field and is proportional to the velocity. Both stress and particle velocity measurements are made during the fracture event at various locations in the sample. Calibration is based on prior tests with the same material under known stress or velocity conditions, or on measurements of the magnetic field, or on a combination of these procedures. These measurement devices are explored more fully in Section 4, which also describes methods of measuring free surface velocity histories of material samples subjected to impact.

The purpose of making time-dependent measurements in spall tests is to determine the stress state at the plane of fracture. We wish to make the measurement in such a manner that the presence of the gage does not disturb the stress waves, so that the measured stress history closely approximates the stress history that would have occurred at the gage plane in the absence of the gage. Because these conditions cannot be achieved directly, our effort is aimed toward finding optimum indirect methods.

In-material stress or particle velocity measurements are possible only outside the region of spall fracture. The placement of a gage within the damage region would perturb both the stress waves and damage evolution to the extent that the measured variable could not be reliably related to its counterpart in the free field. For this reason and because in-material stress gages cannot be used to measure tensile stress

41
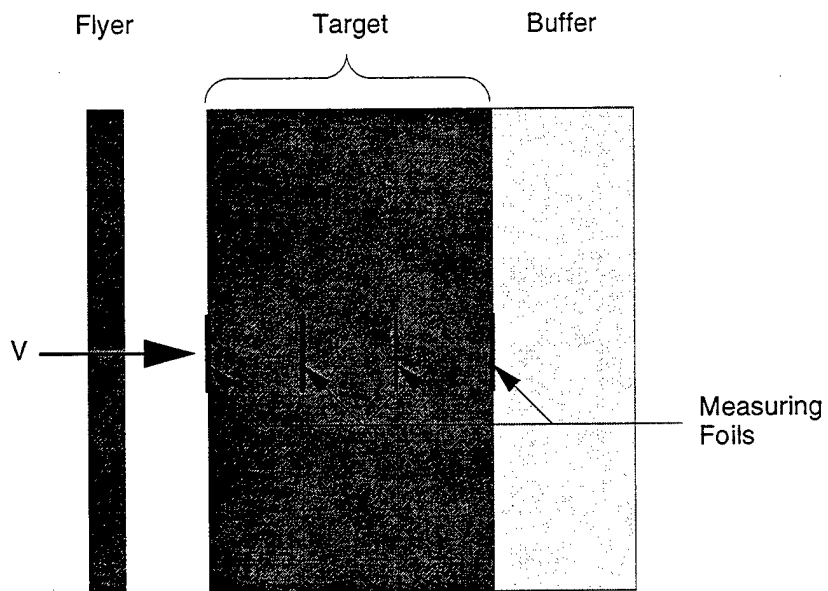
Figure 2-10. Schematic of a plate impact experiment showing some of the gage configurations that can be used to measure stress and/or particle velocity.

states such as those on or near the spall plane, gages are usually emplaced outside the fracture region. The gage usually records the information carried by stress waves from the region of fracture to the gage plane. The character of these waves is determined by the damage at the site of maximum damage and by the lesser damage in adjacent regions through which the waves must propagate. The computed stress histories in Figure 2-11 illustrate the nature of the stress records that may be obtained at the interface with a low impedance buffer plate. Such records are used (as described in later sections) to deduce the character of the stress histories at the spall plane.

The interpretation of gage histories is much more complex during fracture than during elastic behavior. For example, the distance between any two original points in the material (and hence the distance that waves must travel) changes during fracture in an inelastic manner. Also the wave velocities (C), densities (ρ), and hence the impedance (ρC) are altered by the presence of damage. As noted in Section 3, the impedance governs the amplitude of stresses and material velocities following wave interactions. In elastic wave propagation, the waves may travel completely through the sample and interact only with the boundaries. But after damage, the waves travel through layers of slightly different material because different levels of damage cause different sound velocities and densities and hence impedance (see Figure 3-5 in Section 3 for a sample of these wave interactions arising because of the changing damage and properties within the target). Hence, the region of fracture in the sample is a field of continuous wave interaction. No simple analytical treatment is possible for describing, in closed form, these waves and the resulting stress or velocity histories.

In the study of material behavior, it is usual to perform experiments in which a large region of the sample is at essentially the same state of stress and strain—as in a quasi-static tension test. But spall fracture is an unstable process during which there are no large regions of nearly uniform behavior. Figure 2-12 shows the variation of void volume fraction with distance through an aluminum target plate. The amplitude of damage increases with impact velocity and becomes concentrated near a single plane at higher impact velocities and higher damage. This figure illustrates the phenomenon of "localization" in which regions that are partially damaged tend to attract further damage and thereby protect their less-damaged neighbors.

From these observations, we see that our measurements are appropriate only for specific locations in the specimen; they are not values that may be approximately true over a large region of the sample. Therefore, because measurements in the fracture region are not possible, and because the states are not uniform in the sample, we can obtain only peripheral and circumstantial evidence of the occurrence of fracture and especially of the rates at which fracture occurs.
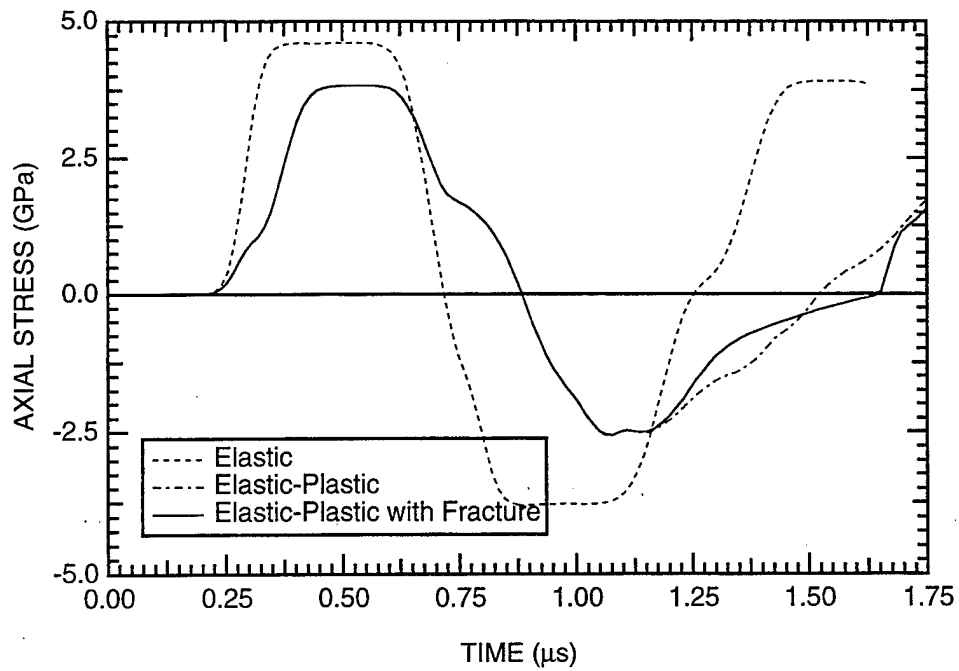
(a) Stress histories on the spall plane.
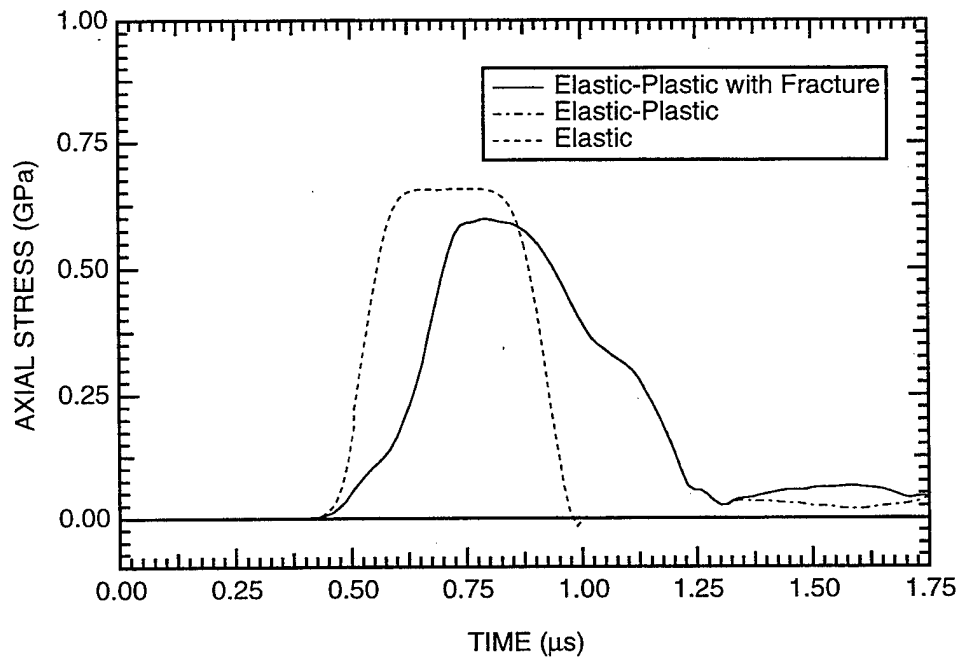
(b) Stress histories on the gage plane.

Figure 2-11.   Comparison of stress histories computed at the fracture plane and at a nearby gage plane assuming elastic behavior, elastic-plastic behavior, and elastic-plastic behavior with fracture.

44
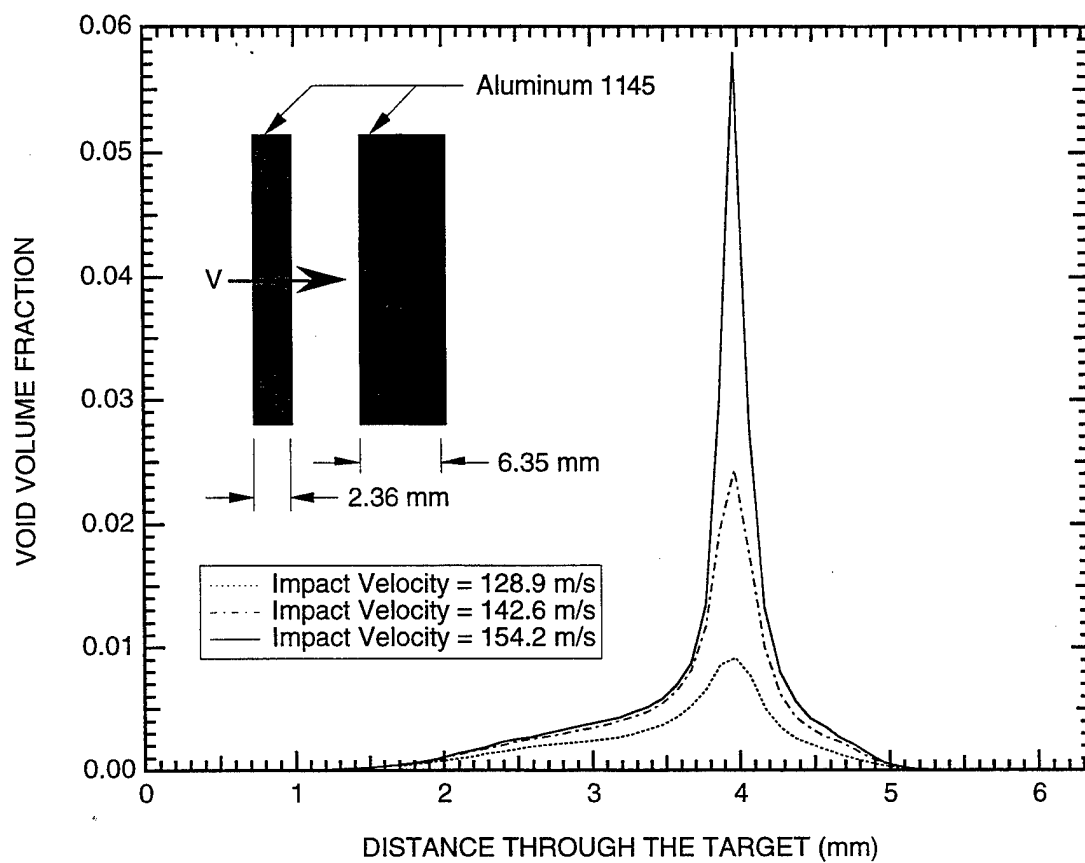
Figure 2-12. Simulated damage distributions in an aluminum 1145 target plate subjected to symmetric impact at varying impact velocitries.

2.3.2 Posttest Examination.

Posttest measurements of the recovered fracture sample are made to locate and quantify the cracks, voids, shear bands, and other evidence of fracture. For these observations, we section, polish, and etch the sample, then we examine the cross section under a microscope. Figure 2-5 above showed a cross section of an aluminum target that was polished to reveal the microvoids. The lines were drawn on the photograph to separate the sample into zones for counting the voids.

A void count made on another aluminum sample that was radiated with a laser is shown in Figure 2-13. Following counting in five successive zones, the numbers were summed to provide a cumulative size distribution. We see that the plane of maximum damage is within the second zone 50 to 100 μm from the rear of the target, where both the size and number of voids reached their maximum values. Lesser amounts of damage occurred on either side of this plane.

Posttest observations such as those described above provide only circumstantial knowledge about the processes that led to the observed damage. Questions like 'did the damage occur during the passage of the first tensile wave or a later one?' and 'what were the damage nucleation and growth rates?' cannot be answered solely on the basis of posttest observations. However, these nucleation and growth processes and the rates at which they occur are the fundamental processes that must be understood to develop methodologies for predicting the occurrence of damage under other circumstances.

2.4 CONSTITUTIVE MODELS OF DAMAGE.

The purpose of formulating constitutive models for spall fracture is to be able to represent damage in the material over a wide range of conditions. For example, we would like a spall model to be able to treat damage under plate impact loading, explosive loading, and x-ray radiation; under stress levels from 1 to 10 GPa; and for loading durations from 10 ns to 10 μs. For a model to provide an accurate description of the material response in such a wide range of loading environments, the underlying physics of the fracture processes must be understood and incorporated into the model. To formulate such a model, we have found it necessary to divide the solution procedure for wave propagation into several parts. First, we isolate the wave propagation equations into the conservation relations (for mass, momentum, and energy) and the constitutive relations. Then, we separate the constitutive relations into behavior for intact material plus fracturing processes.

This separation of the damage processes from other processes is often very difficult. During the spall event, we have simultaneous processes of yielding, work hardening, heating and thermal softening, nucleation and growth of damage, and wave propagation. All these affect the stress level and some affect the material strength. Our view requires isolating the damage from the others—at least approximately and

46

Laser Beam Parameters:

Power = 1038 GW/cm^2
Energy = 81.5 J
Duration = 2.5 ns

Aluminum Target

900 μm

(a) Configuration.

Legend:
- 0 < d < 50 μm
- 50 < d < 100 μm
- 100 < d < 150 μm
- 150 < d < 200 μm
- 200 < d < 250 μm

The distance 'd' is measured from the back surface of the target.

CUMULATIVE NUMBER OF VOIDS

VOID RADIUS (μm)
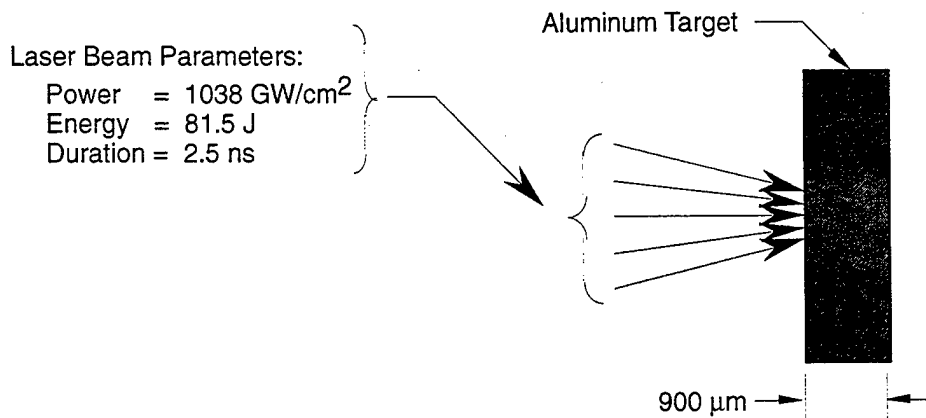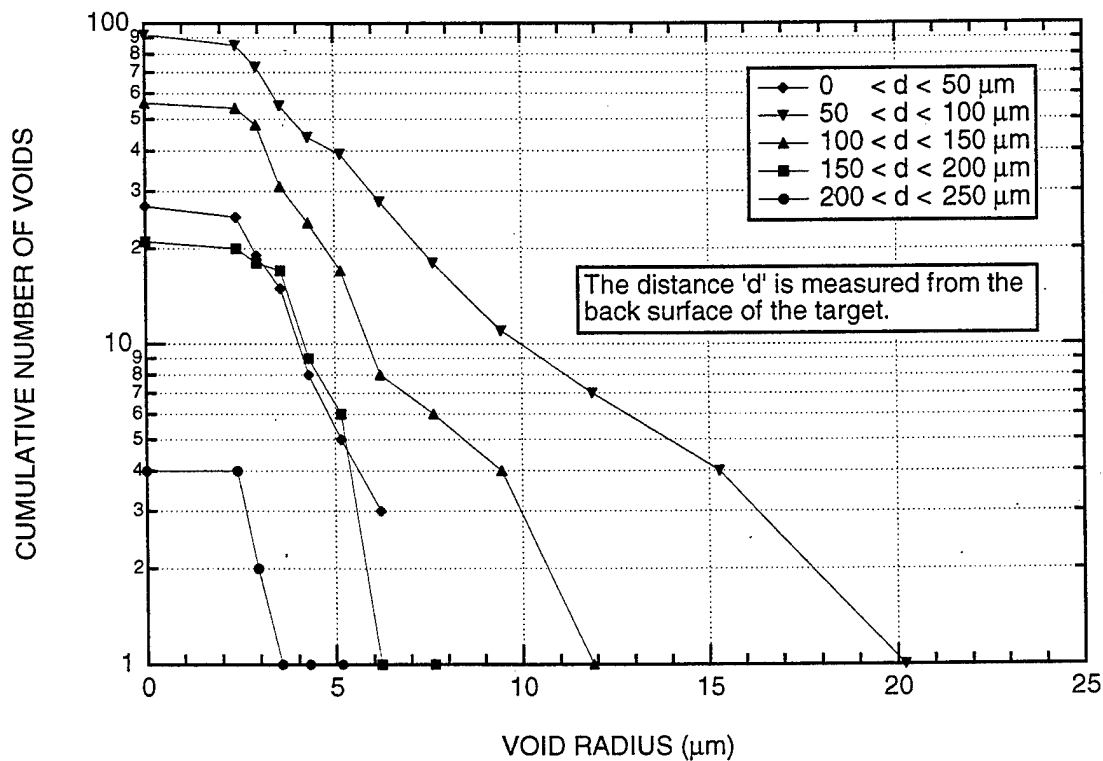
(b) Cumulative void size distributions.

Figure 2-13. Cumulative void size distributions in the vicinity of the spall plane near the rear surface of a soft aluminum specimen subjected to laser deposition.

47

conceptually. This separation is difficult because all these can be rate dependent and time dependent, so a large amount of precise data is required to provide the physical basis for this separation. However, the separation effort is worthwhile because the damage is permanent and has different effects on later waves than the other variables. Also, the time-dependent nature of fracture is generally different from that of the other processes; hence, for accurate predictions of damage under a range of different durations and stress levels, we need to define accurately the damage processes.

Because we explicitly describe the fracture processes in the model in terms of quantifiable variables, the resulting computed damage features can then be directly compared with experimental observations of the damage. Also we have no need for a new constitutive relation, because the standard one is used for the intact material between the damage sites. The further theoretical advantage is that the new constitutive relation including the damage processes is likely to be both stable and consistent with general thermodynamic and mechanical requirements because it is based on observed physical processes.

SECTION 3

WAVE PROPAGATION

This section presents the laws of one-dimensional motion of compressible continuous media to the extent necessary for the discussion of dynamic experiments in Section 4. A comprehensive account of the fundamentals of the mechanics of continuous media can be found, for example, in the texts of Courant and Friedrichs (1948) and Zel'dovich and Raizer (1967). The volume edited by Chou and Hopkins (1972) provides yet another useful reference for wave propagation theory and computations. In that volume, contributions from several authors cover a wide range of experimental and analytical topics including shock waves, the method of characteristics, constitutive relations, and finite-difference computational procedures. Other wave propagation references that emphasize material properties and constitutive relations are those of Rice et al. (1958) and of Duval and Fowles (1963).

3.1 CONSERVATION RELATIONS FOR WAVE PROPAGATION.

The theoretical analysis of stress wave and shock wave propagation begins with the conservation equations, which underlie all solutions. Here, we consider these conservation relations only in one-dimensional planar form. This simplified description is sufficient for the study of the wave propagation problems of interest here. The plate impact experiments, explosive loading experiments, and energy deposition experiments considered here are all planned to be primarily uniaxial strain tests. Under these conditions, the one-dimensional planar form of the conservation equations can be used, and in Lagrangian coordinates, these equations can be written in the following differential form,

Conservation of mass
$$\left(\frac{\partial x}{\partial h}\right)_t = \frac{\rho_o}{\rho} \tag{3.1}$$

Conservation of momentum
$$\left(\frac{\partial u}{\partial t}\right)_h = -\frac{1}{\rho_o}\left(\frac{\partial \sigma}{\partial h}\right)_t \tag{3.2}$$

Conservation of energy
$$\left(\frac{\partial E}{\partial t}\right)_h = -\sigma\left(\frac{\partial (1/\rho)}{\partial t}\right)_h \tag{3.3}$$

where x is the Eulerian position (i.e., x changes with particle motion), h is the Lagrangian position (i.e., h retains its initial value and travels with the particle), t is time, ρ and ρ_o are the current and initial values of the density, u is particle velocity, σ is the mechanical stress in the direction of wave

49

propagation, and E is the internal energy. The sign convention used in Eqs. (3.1) through (3.3), and throughout the remainder of this section, is that stress is positive in tension.

Stress and particle velocity measurements in shock wave experiments are normally performed in Lagrangian coordinates (i.e., the position of the sensor relative to the material particles is fixed). Therefore, it is more convenient to perform the analysis of wave dynamics in Lagrangian coordinates than in Eulerian coordinates. For this reason, Eqs. (3.1) through (3.3) were given in Lagrangian form.

The equations of motion, or conservation equations, are universal equations that apply to all materials that satisfy the underlying assumptions of continuum mechanics. However, by themselves, these equations do not provide solutions to wave propagation problems. The number of unknown independent variables in the problem (u, ρ, σ, and E) exceeds the number of available equations by one variable, and an additional equation is required to render the mathematical problem well-posed. This additional equation is the equation of state.

Strictly speaking, the equation of state is a unique relation between the five state variables: pressure, internal energy, density or volume, temperature, and entropy. For most computational purposes, the equation of state is reduced to a relation between the pressure, density, and internal energy. Only when temperature is required is a more complete equation of state specified.

The equation of state is unique in the sense that the state is independent of the path taken to reach it. Hence, we expect to reach the same state by an impact followed by heating or by heating followed by an impact.

When strength effects are significant, the equation of state is supplemented with a constitutive relation for the deviatoric stresses (the equation of state provides only the mean stress or pressure). Deviatoric stress is defined in Section 3.5. A constitutive relation is like an equation of state, but has a looser definition. A stress-strain path for a material undergoing yielding is a simple example of a constitutive relation. It is not necessarily unique because the state may depend on the path, and only a small subset of the state variables may actually be specified.

3.2   THEORY OF CHARACTERISTICS.

Two standard solution procedures are available for solving problems in wave propagation: the method of characteristics and the finite difference or finite element method. Here, we give a brief discussion of the method of characteristics because its mathematical procedure is closely related to the wave motion and aids in understanding the interaction of waves. The finite element and finite difference computational procedures are discussed in Section 9.

For discussing the method of characteristics, we consider the flow field developed during one-dimensional wave motion as illustrated in Figures 3-1 through 3-5 for a variety of one-dimensional flow situations ranging in complexity from the simple wave shown in Figure 3-1 to the plate impact experiment with spall damage shown in Figure 3-5. The coordinates are time and the Lagrangian distance; because the Lagrangian position is fixed with the material, the boundaries and interfaces do not shift with time.

In this flow field, there are so-called "characteristic" lines, special paths in the time-distance space along which an ordinary differential equation holds, rather than the usual set of coupled partial differential equations. For wave propagation, characteristics are especially interesting because wave motion occurs along these directions. In one-dimensional flow, waves generally propagate forward and backward in space, giving rise to C_+ and C_- characteristics, as shown in these figures. An additional characteristic line follows the particle path in case the material is modified during the flow, thereby becoming different from its neighbors. Work-hardening, fracture, and phase changes are modifications that cause the material to differ from point to point (see Figure 3-5 for such a particle path).

Waves move in the characteristic directions with the Lagrangian sound velocity a, which is related to the velocity c in the laboratory coordinate system, by the formula

$$a = \frac{\rho}{\rho_o} c = \frac{\rho}{\rho_o} \sqrt{\left(\frac{\partial p}{\partial \rho}\right)_S} \tag{3.4}$$

where p is the pressure, S is the entropy, and the notation $(\ )_S$ indicates that the derivative is taken along the isentrope (i.e., path of constant entropy). Thus, a is the wave velocity with respect to the moving material. For isentropic flow, the two sets of characteristics, C_+ and C_-, show trajectories of perturbations in positive and negative directions:

$$\frac{\partial h}{\partial t} = a \qquad \text{and} \qquad \frac{\partial h}{\partial t} = -a \tag{3.5}$$

The variation of the material state along these characteristics in the time-distance plane is described by the following set of ordinary differential equations:

$$\frac{du}{ds} + \frac{1}{\rho_o a} \frac{d\sigma}{ds} = o \qquad \text{along } C_+ \tag{3.6a}$$

and

$$\frac{du}{ds} - \frac{1}{\rho_o a} \frac{d\sigma}{ds} = o \qquad \text{along } C_- \tag{3.6b}$$

51
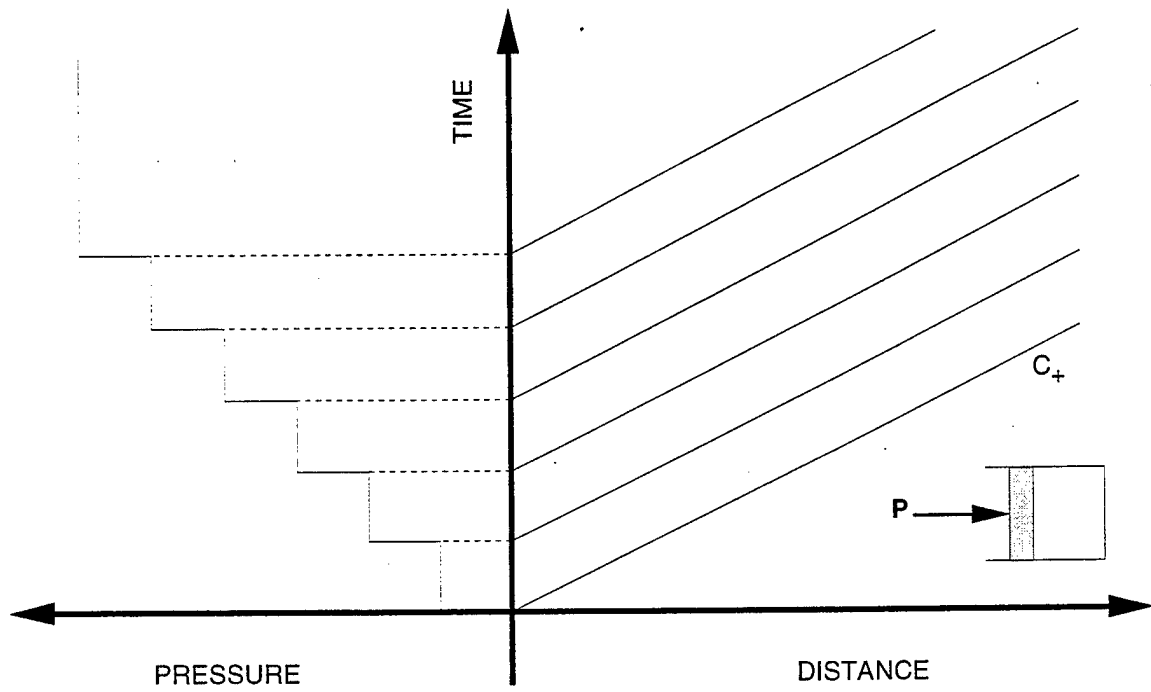
Figure 3-1.   Simple wave in elastic material.

52
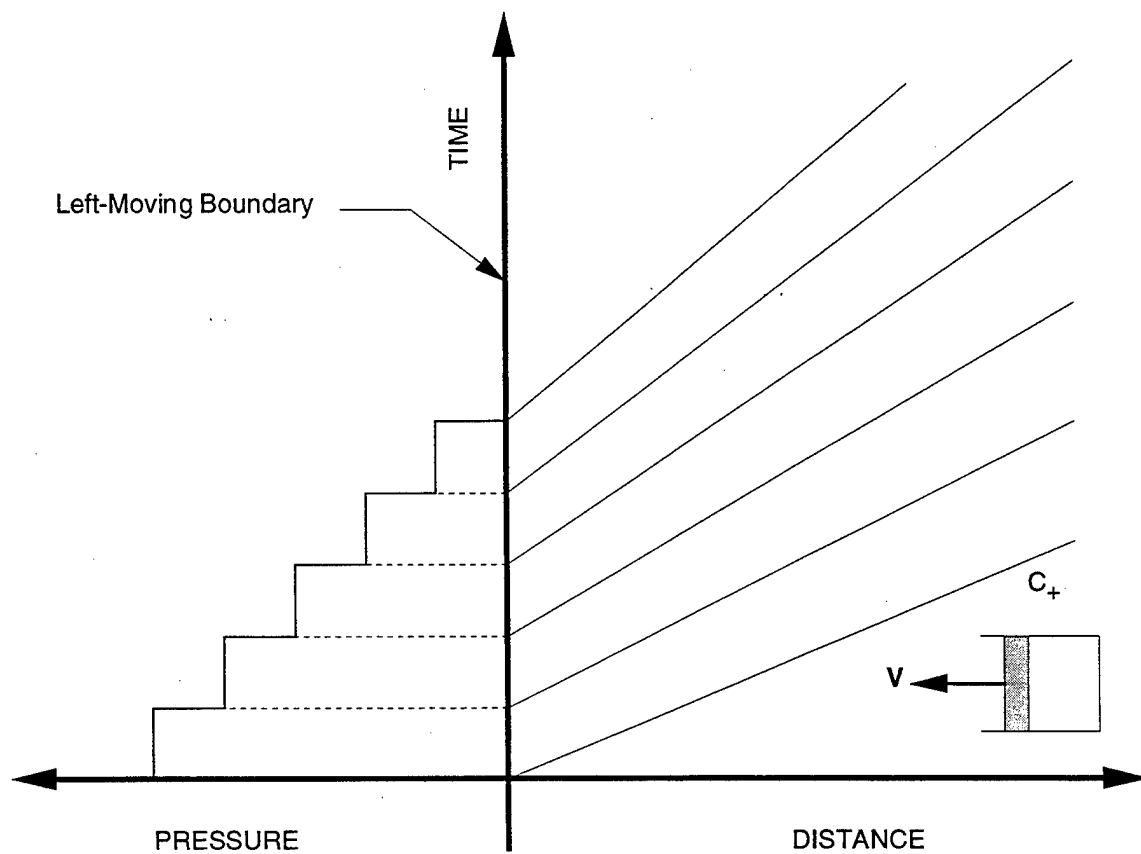
Figure 3-2. Rarefaction fan caused by a piston moving away from compressed material.
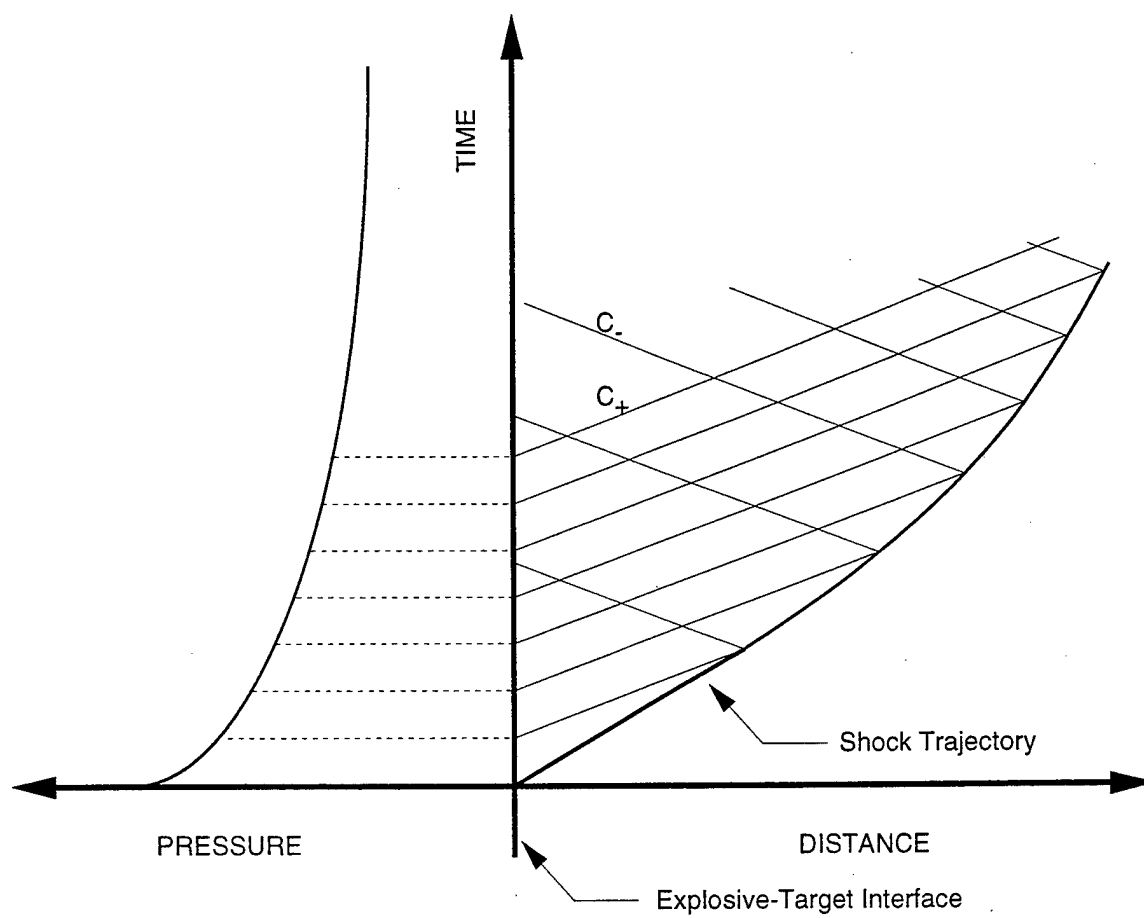
Figure 3-3.   Rarefaction behind a shock, causing attenuation.
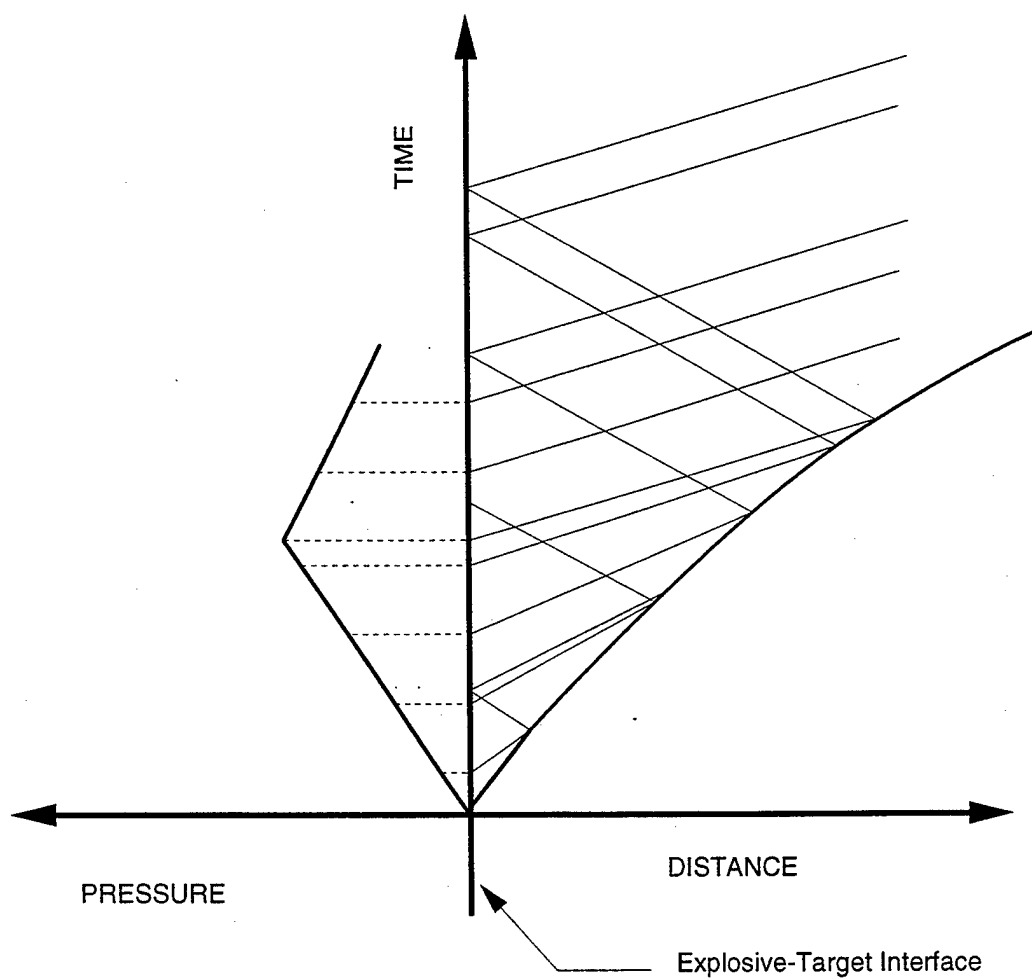
Figure 3-4. Shock formation for a gradually rising wave.
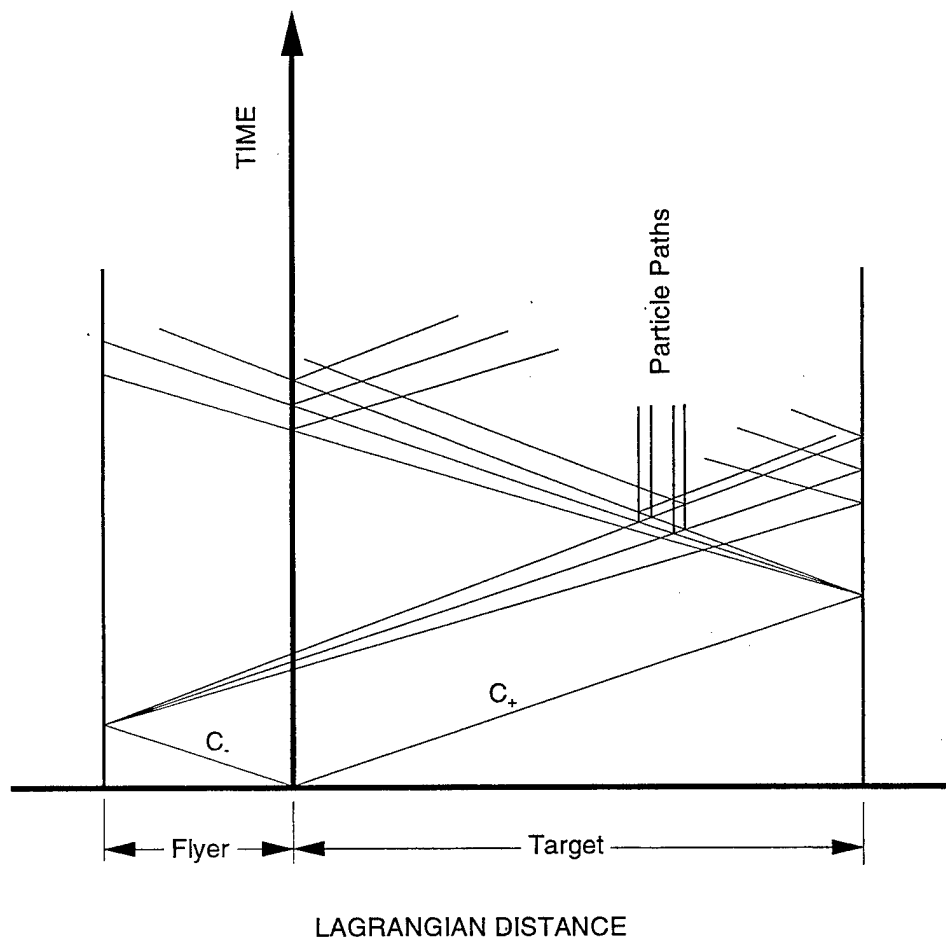
Figure 3-5. Impact of a flyer plate onto a target plate with resultant fracture damage.

The integrals of these equations are the Riemann integrals:

$$u = u_0 - \int_{\sigma_o}^{\sigma} \frac{d\sigma}{\rho_o a} \qquad \text{along } C_+ \qquad\qquad (3.7a)$$

and

$$u = u_0 + \int_{\sigma_o}^{\sigma} \frac{d\sigma}{\rho_o a} \qquad \text{along } C_- \qquad\qquad (3.7b)$$

where u_0 and σ_0 are integration constants.

A simple or progressive wave is a disturbance in a flow field in which all disturbances propagate in the same direction. In this simple wave, the states along the characteristic pointing in the direction of wave propagation remain constant, while all states along any other path in the $x - t$ plane are described by the function $u(\sigma)$ or $\sigma(u)$ corresponding to the Riemann integral.

A simple wave moving into an elastic medium is shown in Figure 3-1. The stress is rising in steps and the C_+ characteristics each correspond to one of these steps. Another example of a simple wave is the rarefaction in a uniformly compressed medium shown in Figure 3-2. Here, the material has been compressed to some stress state, and now the left boundary begins to move left at time zero. The C_+ characteristics each have constant wave velocities, but successive characteristics have lower velocities because the stress is decreasing and the velocity is stress dependent.

We will refer to the trajectory that describes states in a simple wave in $\sigma - u$ coordinates as the rarefaction or Riemann isentrope. This rarefaction path is generally called an isentrope, although some nonisentropic processes (yielding, for example) may be occurring. When all characteristics originate at a single point in the $x - t$ plane, the wave is referred to as a centered wave. The slope of the Riemann isentrope,

$$\frac{d\sigma}{du} = \pm \rho_o a \qquad\qquad (3.8)$$

is the dynamic impedance of the material.

In normal media, the sound velocity increases with pressure. Therefore, rarefaction waves are diverged during propagation, as illustrated in Figure 3-2. Compression waves, however, become steeper and steeper during propagation and gradually become discontinuities or shock waves, as indicated in Figure 3-4.

The pressure history in Figure 3-3 is typical for explosives: a shock front followed by an attenuating pressure. The attenuation of pressure gives rise to right-moving C_+ characteristics (we show only a few C_+ characteristics as if attenuation occurs in steps rather than continuously, as it actually does). When these C_+ characteristics intersect the shock front, C_- characteristics are generated, and they travel

back toward the explosive-target interface. Each intersection of characteristic lines gives rise to new characteristic lines: the intersections of interest here are those of C_+ with C_-, of C_- with the left boundary, and of C_+ with the shock trajectory. The wave velocities (and slopes of the lines) generally depend on the stress levels. Therefore, the new characteristic lines generated at an intersection will have essentially the same slope as the intersecting characteristics. The shock trajectory, however, represents an attenuating stress level so its wave velocity decreases gradually, causing an upward curvature in the shock trajectory.

Figure 3-4 illustrates the waves caused by a gradually rising stress wave (possibly caused by an explosion that is building up to detonation) in a material that stiffens with compression (the usual case). As the pressure rises, the corresponding characteristic lines increase in velocity so the C_+ characteristics are not parallel. When the C_+ characteristics intersect, they produce a rearward-facing C_- characteristic and a forward-moving shock with a velocity that is intermediate to the velocities of the interacting characteristics. The shock front thus formed is concave downward, showing a gradually increasing velocity as it travels.

Figure 3-5 shows the characteristics for a plate impact configuration that produces fracture damage. Here, one shock wave is initially moving into each material after impact (no elastic precursor is shown—see Section 3.6 for such precursors). When these initial C_+ and C_- characteristics are reflected at the outer free boundaries, rarefaction fans are generated (the fan or continuous range of characteristics is shown by just three lines indicating the fastest, slowest, and an intermediate velocity). When these rarefaction fans intersect, they cause tensile stresses to arise. Here, we indicate that damage also occurs at some intersections: damage changes the materials condition and leads to generation of a particle path characteristic in addition to the usual C_+ and C_- characteristics. At later times, the characteristics calculation must account for intersections of each C_+, C_-, and particle path. Clearly, the computation as well as the diagram becomes very complex.

3.3 ANALYSIS OF THE SHOCK FRONT.

A shock wave occurs as a rapid change in stress, density, and particle velocity in the flow. The usual conservation equations for mass, momentum, and energy still govern the flow field, but the discontinuous nature of the shock wave leads to the following special forms for these equations:

Conservation of mass $\qquad\qquad \rho_o U = \rho(U - u)$ $\qquad\qquad\qquad\qquad$ (3.9)

Conservation of momentum $\qquad \sigma = \sigma_o - \rho_o U u$ $\qquad\qquad\qquad\qquad$ (3.10)

Conservation of energy $\qquad \rho_o(E - E_o) = \dfrac{1}{2}(\sigma + \sigma_o)\left(\dfrac{\rho_o}{\rho} - 1\right)$ $\qquad\qquad$ (3.11)

where ρ_o and ρ are the initial and current values of the density, U is the shock velocity, u is particle velocity, σ_o and σ are the total mechanical stress in the direction of propagation before and after the shock, and E_o and E are the internal energy before and after the shock. The sign convention used here is that stress is positive in tension. Collectively, Eqs. (3.9), (3.10), and (3.11) are known as the Rankine-Hugoniot jump conditions, they named after the two men who independently derived them.

3.3.1 The Hugoniot, the Isentrope, and the Isotherm.

Because of their importance in shock wave work, we discuss here three important paths taken by state points across the equation-of-state surface: the Hugoniot, the isentrope, and the isotherm as shown in Figure 3.6. The Rankine-Hugoniot curve, also known as the Hugoniot or shock adiabat, is the locus of end states achieved through a steady shock wave transition. Such a curve is usually shown in stress-volume or stress-particle velocity space. Usually, the initial state of the material is at rest and with zero stress, but Hugoniot curves can also be defined for other initial conditions.

Under moderate compressions (less than 1 Mbar or 10^5 GPa), Hugoniots of condensed media are usually described by linear relationships of the form

$$U = c_o + su \qquad (3.12)$$

where the material constant c_o is the sound velocity corresponding to the initial equilibrium bulk compressibility of the medium and s is a dimensionless material constant with values usually in the range of 1.0 to 1.5. Other useful forms of the Hugoniot equation can be obtained by combining Eq. (3.12) with the Rankine-Hugoniot jump conditions.

An isentrope is a series of states (of stress, energy, density, temperature, and entropy) along which the entropy is constant. Such a path is useful for reference because it includes no exchange of heat with the surroundings, no dissipation, and is reversible. Loading paths such as a Hugoniot may approximate an isentrope for weak shocks (low stress amplitude). Figure 3.6 shows two isentropes: one corresponding to the initial or reference state (S_o), and another (S_1) that is a possible unloading path for material that was shock-loaded to the intersection of the Hugoniot and the isentrope corresponding to the shock-loaded state (Point G in Figure 3-6). Note that during unloading the material may pass the liquid and even reach the mixed liquid-vapor state. If the material were shock loaded to a higher stress state, the isentrope could lie above the critical point and the material could vaporize on unloading.

An isotherm is a series of states along which the temperature remains constant. Such a loading path as the isotherm is common in quasi-static loading, where the material may remain at constant temperature throughout the whole loading regime. A reference isotherm is shown in Figure 3.6.
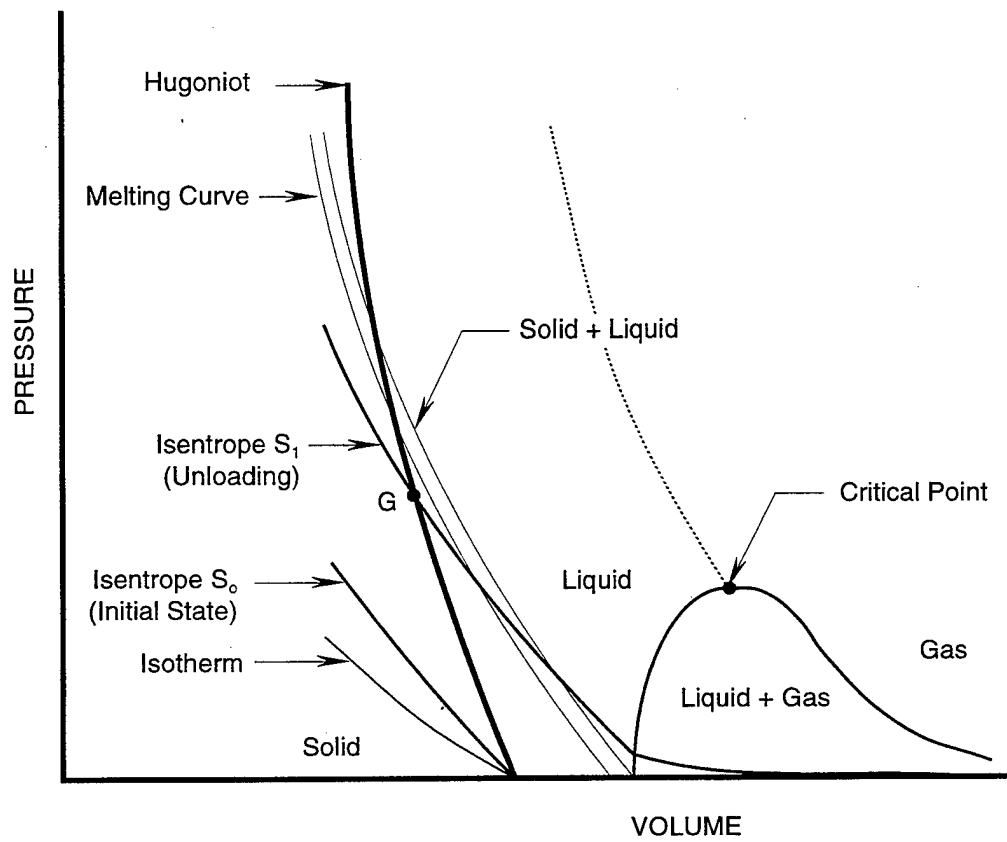
Figure 3-6. Schematic phase diagram of matter in pressure-volume space. The diagram also shows the relative positions of the Hugoniot, isotherm, isentrope, and melting curve.

3.3.2 Estimating the Lagrangian Sound Velocity from Experimental Data.

Experiments have shown that, in the pressure-particle velocity plane, the release isentrope of many materials deviates from the Hugoniot by not more than 3% for pressures up to at least 50 GPa. If we assume that the Hugoniot and the rarefaction isentrope coincide on the p-u plane, we find that

$$\left(\frac{dp}{du}\right)_S = \pm\rho_o a = \pm\left(\frac{dp}{du}\right)_H = \pm\rho_o(c_o + 2su) \tag{3.13}$$

where the derivatives $(dp/du)_S$ and $(dp/du)_H$ are evaluated along the isentrope and Hugoniot, respectively. The Lagrangian sound velocity in shock-compressed matter can now be estimated using the results in Eq. (3.13) in combination with the Hugoniot equation, Eq. (3.12), and the momentum conservation law, Eq. (3.10),

$$a = c_o + 2su = \sqrt{c_o^2 + \frac{4s\sigma}{\rho_o}} \tag{3.14}$$

When the Hugoniot deviates from the isentrope by only a small amount, the quasi-acoustic approach for treating the shock wave velocity (Landau and Lifshitz, 1959) is satisfactory. According to this approach, the velocity of the shock wave is the average between the sound velocities ahead of the shock discontinuity, c_o, and behind it, a:

$$U \approx \frac{1}{2}(c_o + a) \approx \frac{1}{2}(c_o + c_o + 2su) = c_o + su \tag{3.15}$$

Hence, we have an estimation procedure for the Lagrangian sound velocity, Eq. (3.14), that is consistent with the quasi-acoustic approach for shock wave computations.

3.4 TEMPERATURE IN SHOCK AND RAREFACTION WAVES.

Processes that occur in shock or rarefaction waves (e.g., plastic flow, phase changes, chemical reactions, evolution of damage) are in general rate processes that depend on the temperature of the material. In many cases such temperature dependence can be neglected, but in others (notably chemical reactions), computational simulations must calculate the temperature. A specific and important example is the case in which burning occurs on microscopic crack surfaces in the propellant in a rocket motor, thereby leading to unstable burning rates and potential detonation. Although the initial nucleation and growth of the fractures may be to a first approximation temperature-independent, the burning rate depends strongly on the temperature. Furthermore, in fracturing material the fracture mode and kinetics are also typically

temperature-dependent, so if the material is being heated by radiation, plastic flow, or exothermic reactions, the fracturing process may change significantly with time.

Unfortunately, standard computer "hydrocodes" generally use an equation of state that depends only on pressure, volume, and internal energy (a $p - v - E$ equation of state). Such an equation of state is called "incomplete." Knowledge of the specific heats as functions of stress, deformation, and internal energy is needed to calculate the temperature. Assuming such knowledge, various numerical procedures for calculating temperature are used in working hydrocodes, but they tend to be *ad hoc* and nonrigorous.

A thermodynamically rigorous way to calculate temperature in materials that are undergoing rate processes was reported in 1967 in an important paper by Coleman and Gurtin (1967). In their internal state variable formulation, all dissipation is described by evolution equations for internal state variables, α_n :

$$\dot{\alpha}_n = f_n(\theta, F_{iJ}, \theta_{,i}, \alpha_n) \tag{3.16}$$

where θ is the temperature, $\theta_{,i}$ is the temperature gradient, and $F_{iJ} = \partial x_i / \partial X_J$ are the components of the deformation gradient tensor $\mathbf{F}$. The subscript n in Eq. (3.16) represents the total number of internal state variables α. All other subscripts refer to coordinate directions. Capital letter indices like J in Eq. (3.16) are referenced back to the original configuration, whereas small letter indices, like i in Eq. (3.16), are referenced to the current configuration. The usual summation conventions (i.e., Malvern, 1969) are used whenever indices appear in an equation.

Examples of processes that can be represented as internal state variables within the framework of the Coleman and Gurtin thermomechanical approach include microcrack nucleation and growth in an elastic matrix material, which would result in inelastic behavior on the continuum level. In this case, one of the α_n values would be chosen to represent the crack deformation strain. A second example is the case of an elastic-plastic material, where the internal state variable would be selected to represent some measure of the plastic deformation. Finally, for a reacting propellant, we could select α_n values to represent relative amounts of various chemical species.

In general, the vector α_n refers to the complete set of internal state variables used in the specific application, and the set of Eq. (3.16) completely describes their rate dependencies and associated dissipations in the constitutive model. Note that, depending on the process represented by any one of the internal state variables, the state variable can be a scalar, a vector, or a higher order tensor.

In the following developments, we choose two internal state variables: α_{ij}^c, which represents the cracking strain tensor, and α_{ij}^p, which represents the plastic strain tensor. In this case then, the symbol α_n refers to the two internal state variables α_{ij}^c and α_{ij}^p.

The internal energy per unit mass, E, obeys the conservation of energy equation:

$$\rho \dot{E} = T_{ij}L_{ij} + \rho r - q_{i,i} \qquad (3.17)$$

where ρ is the mass density, T_{ij} are the components of the Cauchy stress tensor $\mathbf{T}$, L_{ij} are the components of the particle velocity gradient $\mathbf{L}$, r is the heat supply absorbed by the material from radiation from the external world, and q_i are the components of the heat flux vector $\mathbf{q}$. Respectable hydrocodes all use Eq. (3-17). Thus, increments in the internal energy E in the hydrocode should be calculated from the above formula. In many standard applications, both q_i and r are zero, but x-ray effects codes routinely account for r, and increasingly they include heat flow as well. Note that the term $T_{ij}L_{ij}$ in Eq. (3.17) represents the total mechanical work done on a material element and thus includes the work producing shear as well as the volumetric deformations and includes plastic as well as elastic work.

Coleman and Gurtin developed general representations for constitutive relations that are thermodynamically consistent (obey the second law). One such representation that may be useful for us is the following set of equations:

$$\theta = \hat{\theta}\left(F_{iJ}, E, \alpha_n\right) \qquad (3.18)$$

$$S_{iJ} = \hat{S}_{iJ}\left(F_{iJ}, E, \alpha_n\right) \qquad (3.19)$$

$$q_i = \hat{q}_i\left(F_{iJ}, E, \theta_{,i}, \alpha_n\right) \qquad (3.20)$$

$$\alpha_n = \hat{\alpha}_n\left(F_{iJ}, E, \theta_{,i}, \alpha_n\right) \qquad (3.21)$$

where a new stress tensor $\mathbf{S}$, with components S_{iJ}, has been introduced for mathematical convenience. This new stress tensor is closely related to the first Piola-Kirkhoff stress tensor[1] and is given in terms of the Cauchy stress tensor as

$$\mathbf{S} = \frac{1}{\rho}\mathbf{T}\mathbf{F}^{-\mathbf{T}} \qquad (3.22)$$

In terms of the components of $\mathbf{S}$, Eq. (3.17) becomes:

$$\rho \dot{E} = \rho S_{iJ}\dot{F}_{iJ} + \rho r - q_{i,i} \qquad (3.23)$$

Coleman and Gurtin show that, within this framework, the entropy, η, can be expressed as

$$\eta = \hat{\eta}\left(F_{iJ}, E, \alpha_n\right) \qquad (3.24)$$

---

[1]First Piola-Kirkhoff stress tensor = $\rho_o{}^*\mathbf{S}$.

Furthermore, the stress and temperature can be derived from Eq. (3.24) as follows:

$$\theta = \left\{ \frac{\partial \hat{\eta}(F_{iJ}, E, \alpha_n)}{\partial E} \right\}^{-1} \tag{3.25}$$

$$S_{iJ} = -\theta \frac{\partial \hat{\eta}(F_{iJ}, E, \alpha_n)}{\partial F_{iJ}} \tag{3.26}$$

Thus, if we can define an entropy function $\hat{\eta}(F_{iJ}, E, \alpha_n)$ such that Eq. (3.26) produces realistic constitutive relations, we can calculate the temperature from Eq. (3.25).

To illustrate how the approach described above can be used to compute temperature in hydrocode calculations, we consider the following equation of state:

$$\hat{\eta}(F_{iJ}, E, \alpha_n) = C \ln \left\{ \left\{ \frac{\left[E - H(F_{iJ}, \alpha_n) \right]}{E_o} \right\} \left\{ 1 + g \left\{ \varepsilon_{ij} - \alpha_{ij}^c \right\} \delta_{ij} \right\} \right\} \tag{3.27}$$

where C is a constant with the dimensions of specific heat, $E_o = C\theta_o$ is an arbitrary reference energy (θ_o is a reference initial temperature), g is a dimensionless constant, ε_{ij} is the strain tensor (see Section 3.6), and δ_{ij} is the kronecker delta and has a value of either 0 or 1 depending on whether $i = j$ or $i \neq j$. The ( ) brackets are reserved to indicate functional dependence, and repeated indices denote summation.

We define $H(F_{iJ}, \alpha_n)$ as the elastic mechanical work done on a reference isotherm associated with the reference temperature θ_o:

$$H(F_{iJ}, \alpha_n, \theta_o) = \int S_{iJ}(\theta_o) d\varepsilon_{iJ}^e = \int S_{iJ}(\theta_o) \left[d\varepsilon_{iJ} - d\alpha_{iJ}^c - d\alpha_{iJ}^c \right] \tag{3.28}$$

where $S_{iJ}(\theta_o)$ is the stress on the isotherm. Note that we are using the Piola-Kirkhoff stresses, and corresponding measures of strains, in this expression for the work, consistent with Eq. (3.19). Note also that $H(F_{iJ}, \alpha_n, \theta_o)$ is not a simple reference function, but depends on the complete elastic strain tensor.

Using Eqs. (3.25) and (3.27), we can now obtain the temperature as

$$\theta = \frac{E - H(F_{iJ}, \alpha_n, \theta_o)}{C} \tag{3.29}$$

Similarly, the stress can be computed from Eqs. (3.26) and (3.27) as follows

$$S_{iJ} = S_{iJ}(\theta_o) - \frac{g \left\{ E - H(F_{iJ}, \alpha_n, \theta_o) \right\}}{1 + g \left\{ \varepsilon_{kL} - \alpha_{kL}^c \right\} \delta_{kL}} \delta_{iJ} \tag{3.30}$$

Note that θ_0 is a reference temperature for the unstrained case when $H = 0$. The temperature increase over θ_0 from Eq. (3.29) is intuitively obvious: it is the excess of internal energy over that on the reference isotherm divided by a specific heat.

Equation (3.30) is similar to the usual Mie-Grüneisen pressure-volume and elastic deviator formulations, except that the familiar "ΓE" thermal term is a weak function of volumetric strain.

In a hydrocode application, the above method of calculating temperature has a computational burden, because significant computational storage is required to continually update the value of $H(F_{iJ}, \alpha_n)$ in each computational cell. Furthermore, it is not trivial to fit experimental constitutive relation data to a $\hat{\eta}(F_{iJ}, E, \alpha_n)$ function. (The example $\hat{\eta}(F, e, \alpha)$ function of Eq. (3.27) will fit available Hugoniot and shear moduli data in many cases, but not when the specific heat is a strong function of temperature.) Nevertheless, Coleman and Gurtin's approach provides a rigorous method for calculating the temperature in materials experiencing rate-dependent failure.

3.5   ELASTIC-PLASTIC RESPONSE.

In the range of pressures and temperatures typical for spall experiments, the elastic-plastic properties of solids have a significant effect on the shock-wave structure. The state of solids in this case is described by two tensors: the stress tensor σ_{ij} and the strain tensor ε_{ij}, where subscripts i and j represent the coordinate directions x, y, and z of the orthogonal Cartesian coordinate system. The stress σ_{ij} is the force per unit area in the body along the direction i, acting on an area with a normal oriented along the j axis. The components σ_{xx}, σ_{yy}, and σ_{zz} are the normal stress components and $\sigma_{xy} = \sigma_{yx}$, $\sigma_{yz} = \sigma_{zy}$, $\sigma_{xz} = \sigma_{zx}$ are the tangential or shear stress components. The normal stresses are also represented by the singly subscripted symbols $\sigma_x = \sigma_{xx}$, $\sigma_y = \sigma_{yy}$, and $\sigma_z = \sigma_{zz}$; and the shear stresses by $\tau_{ij} = \sigma_{ij}$. The strain components ε_{xx}, ε_{yy}, and ε_{zz} are the normal strains describing elongations along the coordinate axes. Tangential or shear strains are represented by $\varepsilon_{xy} = \varepsilon_{yx}$, $\varepsilon_{yz} = \varepsilon_{zy}$, and $\varepsilon_{xz} = \varepsilon_{zx}$. For shearing strains, the notation $\gamma_{ij} = 2\varepsilon_{ij}$ is also used and γ_{ij} is referred to as engineering strain.

At each point and for every admissible state of stress in the solid, three mutually perpendicular planes exist on which the shear stresses are identically zero. The stress components acting on these planes are known as the principal stresses, and the orientations along which the principal stresses act are known as the principal directions. The principal stresses are designated by the symbols σ_1, σ_2, and σ_3 where $\sigma_1 \geq \sigma_2 \geq \sigma_3$. At least two of the principal stresses have maximum and minimum magnitudes for all possible normal stresses in all orientations. The maximum shear stress, τ_{max}, acts on the plane with a normal vector that bisects the angle between the maximum and minimum principal stresses. The

65

magnitude of the maximum shear stress is equal to half the difference between the maximum and minimum principal stresses and is therefore given by the relation

$$\tau_{max} = \frac{1}{2}\left(\sigma_1 - \sigma_2\right) \tag{3.31}$$

The normal strains $\varepsilon_1 \geq \varepsilon_2 \geq \varepsilon_3$ acting along the principal directions also have maximum and minimum magnitudes in one-dimensional problems. Filaments lying along the principal axes of stress and strain can change their lengths, but they cannot rotate. The maximum shearing strain occurs in the direction intermediate between the directions of the maximum and minimum normal strains and is given by

$$\gamma_{max} = \varepsilon_1 - \varepsilon_3 \tag{3.32}$$

Small relative changes in the specific volume V are equal to the sum of the relative elongations in any three orthogonal directions:

$$\frac{dV}{V} = d\varepsilon_{xx} + d\varepsilon_{yy} + d\varepsilon_{zz} \tag{3.33}$$

For isotropic material, it is useful to divide the stress and strain tensors into spherical (or hydrostatic) and deviatoric (or distortional) components so that the volumetric and shearing aspects of the material behavior can be treated separately. The spherical component of the stress tensor is the hydrostatic pressure p (with the sign reversed):

$$p = -\frac{1}{3}\left(\sigma_{xx} + \sigma_{yy} + \sigma_{zz}\right) \tag{3.34}$$

The negative sign reflects the common convention that stresses are positive in tension, whereas pressure is positive in compression. The deviatoric components of the stress tensor σ'_{ij} are computed by subtracting the mean stress or pressure from the stress tensor:

Normal Components $\qquad \sigma'_{ij} = \sigma_{ij} + p\delta_{ij} \qquad i = j \qquad$ (3.35a)

Shearing Components $\qquad \sigma'_{ij} = \sigma_{ij} \qquad\qquad i \neq j \qquad$ (3.35b)

where δ_{ij} is the kronecker delta and has a value of either 0 or 1 depending on whether $i = j$ or $i \neq j$. The deviatoric stress components are concerned primarily with shear behavior and with yield phenomena. The spherical component is more closely related to hydrostatic phenomena.

The components of the deviatoric strain tensor, ε'_{ij}, are related to the components of the strain tensor by the equation

$$\varepsilon'_{ij} = \varepsilon_{ij} - \frac{1}{3}e_v \qquad (3.36)$$

where $e_v = \varepsilon_{11} + \varepsilon_{22} + \varepsilon_{33}$ is the volumetric strain, or dilatation, and it represents the change in volume of an element. The deviatoric strain components, however, represent the change in shape of the element.

In the linear theory of elasticity, the stress and strain increments are related by Hooke's law, which can be expressed in the following incremental form:

Normal
$$d\left(\sigma_{ij} + p\delta_{ij}\right) = d\sigma'_{ij} = 2G\left(d\varepsilon_{ij} - \frac{1}{3}\frac{dV}{V}\delta_{ij}\right) \qquad i = j \qquad (3.37a)$$

Shear
$$d\tau_{ij} = d\sigma_{ij} = d\sigma'_{ij} = Gd\gamma_{ij} = 2Gd\varepsilon_{ij} \qquad i \neq j \qquad (3.37b)$$

where G is the shear modulus. The increments in the spherical components of stress and strain are related as follows:

$$dp = -K\frac{dV}{V} \qquad (3.38)$$

where K is the bulk modulus.

The yield condition or limiting elastic state may be defined by many criteria. The purpose of these criteria is to use a standard test to define the conditions under which plastic flow occurs for given load conditions. For example, according to the criterion of Coulomb and Guest, the yield condition is reached when the maximum shear stress reaches the value corresponding to the yield strength, Y, in simple tension:

$$|\tau_{max}| = \frac{Y}{2} \qquad (3.39)$$

Another commonly used criterion is that of von Mises, in which the yield limit is reached when the so-called equivalent stress, $\overline{\sigma}$, is equal to the yield strength. The equivalent stress, an invariant of the deviatoric stress tensor, is defined by

$$\overline{\sigma}^2 = \frac{3}{2}\sigma'_{ij}\sigma'_{ij}$$
$$= \frac{3}{2}\left\{\left(\sigma'_{xx}\right)^2 + \left(\sigma'_{yy}\right)^2 + \left(\sigma'_{zz}\right)^2\right\} + 3\left\{\left(\sigma'_{xy}\right)^2 + \left(\sigma'_{yz}\right)^2 + \left(\sigma'_{xz}\right)^2\right\} \qquad (3.40)$$

In terms of the effective stress, the von Mises yield condition is simply

$$\overline{\sigma} = Y \qquad (3.41)$$

Fortunately, for uniaxial strain conditions, as in planar one-dimensional wave propagation, these two yield conditions agree identically.

During deformation in the plastic region, the increment of strain along each axis is the sum of elastic and plastic components:

$$d\varepsilon_{ij} = d\varepsilon_{ij}^{el} + d\varepsilon_{ij}^{pl} \qquad (3.42)$$

In metal plasticity, it is usual to assume that the material is incompressible during plastic flow; hence,

$$d\varepsilon_{xx}^{pl} + d\varepsilon_{yy}^{pl} + d\varepsilon_{zz}^{pl} = 0 \qquad (3.43)$$

The yield strength of materials is usually determined in standard tension tests under uniaxial stress conditions. Figure 3-7 shows the idealized stress-strain diagram of standard tests under uniaxial stress, the usual test condition for quasi-static loading. In this case,

$$-Y \le \sigma_{xx} \le Y \qquad \sigma_{yy} = \sigma_{zz} = 0 \qquad \text{and } \varepsilon_{yy} = \varepsilon_{zz} \ne 0 \qquad (3.44)$$

Until the yield strength Y is reached, the material responds elastically to the loading and obeys Hooke's law, which can be expressed by the following relationship:

$$\sigma_{xx} = E\varepsilon_{xx}, \text{ where } E = \frac{3G}{1 + \dfrac{G}{3K}} \qquad (3.45)$$

where E is the Young's modulus of elasticity. The stress-strain relationship is governed by Hooke's law until the yield strength of the material is reached (i.e., $\sigma_{xx} = Y$). Further straining beyond the yield point does not cause an increase in stress. Upon unloading, the material again behaves elastically until reverse yielding occurs at the stress level $\sigma_{xx} = -Y$. After reverse yielding, the stress in the material remains constant with further straining. In later loading cycles, each reversal in the loading direction causes an initial elastic response that persists until the stress is equal to the yield strength; thereafter, the stress remains constant.
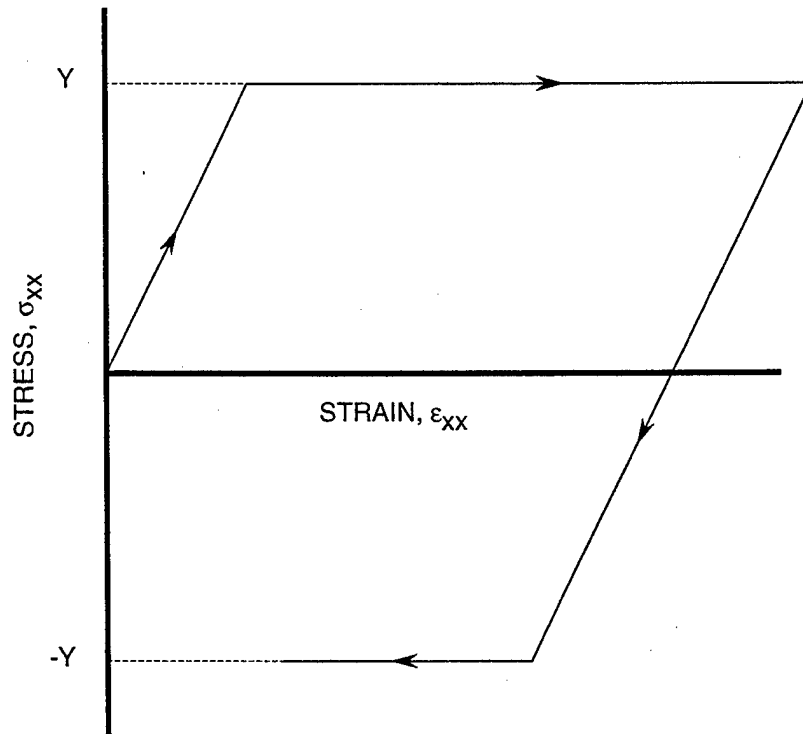
Figure 3-7.   Idealized uniaxial stress-strain diagram in an elastic-plastic
material under uniaxial stress loading conditions.

In both compression and rarefaction waves, the boundary conditions are uniaxial strain where $\varepsilon_{yy} = \varepsilon_{zz} = 0$ and $\sigma_{yy} = \sigma_{zz} \neq 0$. Figure 3-8(b) shows the stress-strain diagram for a solid body under one-dimensional compression during both loading and unloading. In the elastic region, the longitudinal modulus of the material is

$$\frac{d\sigma_{xx}}{d\varepsilon_{xx}} = V\frac{d\sigma_{xx}}{dV} = K + \frac{4}{3}G \tag{3.46}$$

This uniaxial strain modulus is larger than the bulk stiffness

$$-V\frac{dp}{dV} = K \tag{3.47}$$

which approximately represents the material stiffness during yielding.

The yield condition under uniaxial strain conditions is satisfied when

$$|\sigma_{xx} + p| = |\sigma'_{xx}| = \frac{2}{3}Y \tag{3.48}$$

Thus, the longitudinal stress in an elastic-plastic body deviates from the hydrostatic curve $p(V)$ by not more than $2Y/3$. The longitudinal stiffness during plastic deformation is approximately the bulk stiffness. Combining the yield condition with the longitudinal stiffness relation, we obtain the longitudinal stress at initial yield:

$$\sigma_{xx} = -Y\left(\frac{K}{2G} + \frac{2}{3}\right) \tag{3.49}$$

This initial yield value for the longitudinal stress under shock wave loading is called the Hugoniot elastic limit (HEL) and is indicated by point A in Figure 3-8(b).

During unloading under planar wave propagation conditions, the stress σ_{xx} initially decreases elastically, as from point B to point C in Figure 3-8(b). Reverse yielding at point C occurs after the deviator stress σ'_{xx} passes through zero and increases to yielding again [again meeting the criterion in Eq. (3.48)]. The decrease in the stress σ_{xx} to reach reverse yielding is approximately twice the HEL.

With this background on the yield process in ideal plasticity (only a rough approximation for most materials), let us now examine the wave processes illustrated in Figure 3-8 for a typical plate impact experiment. Figure 3-8(a) shows the configuration for the impact. An impactor on the left strikes a target
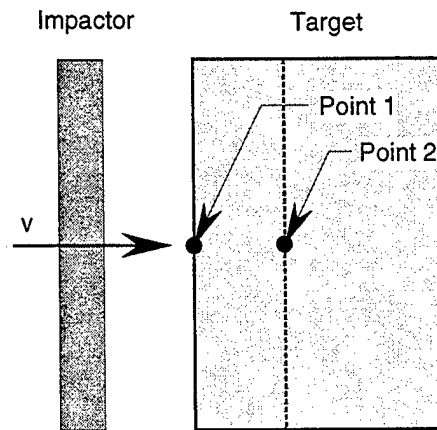
(a) Impact configuration.
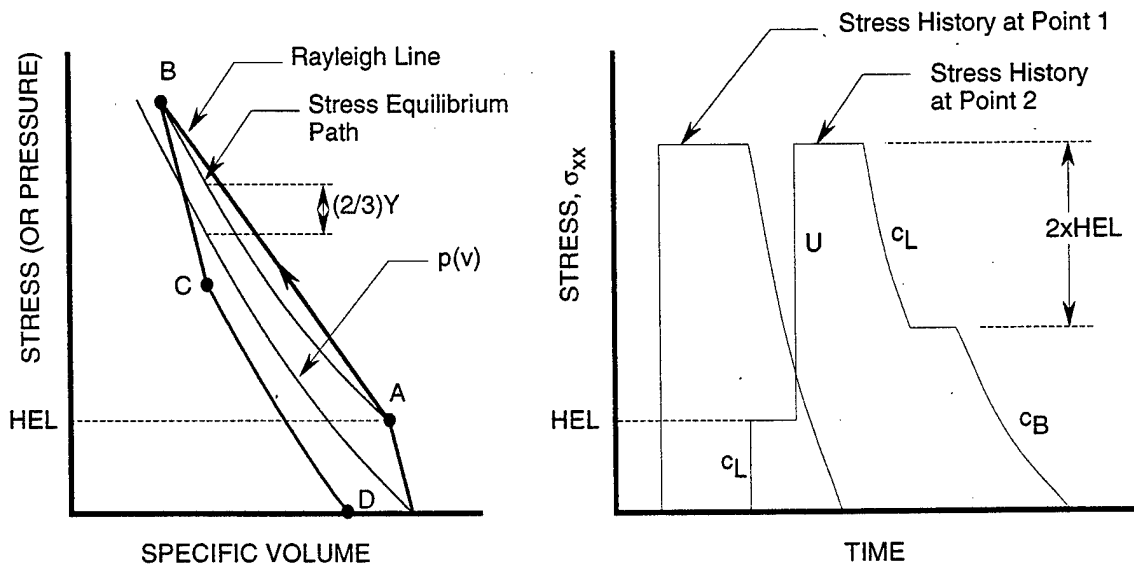
(b) Shock and rarefaction paths under uniaxial strain.

(c) Stress histories at two points in the target.

Figure 3-8.   Evolution of a typical stress pulse in an elastic-plastic material subjected to uniaxial strain impact loading.

plate with a velocity v, and we examine the resulting stress wave as it passes two points in the target. The stress wave histories at these points are shown in Figure 3-8(c). At point 1, we see a rapid rise to a stress plateau and then a gradual decrease in stress corresponding with the rarefaction fan proceeding from the rear of the impact plate (a time-history diagram appropriate for this impact is shown in Figure 3-5). The impactor in this case has responded in either a purely elastic case or as a material with a negligible yield strength so that no yield process is observed in the rarefaction fan at this time.

After the wave has passed through some of the elastic-plastic target material, considerable structure has developed. At point 2, the wave front shows the arrival of an elastic precursor with an amplitude corresponding to the HEL. The wave velocity of the precursor corresponds to the elastic wave velocity in the target [the equation for the longitudinal elastic wave velocity is given in below in Eq. (3.50)].

The remainder of the compressional wave arrives with the shock velocity U. This velocity corresponds with the slope of the Rayleigh line connecting points A and B in part (b) of Figure 3-8. As indicated in this figure, the stress path during the shock loading is along the Rayleigh line, not along the quasi-static equilibrium path (i.e., the curved line between A and B). This curved line is parallel to the pressure-volume path with an offset of $2Y/3$ as noted above.

Following the plateau on the second wave history in part (c) of the figure, the stress decreases by twice the HEL, then reverse yielding occurs. Following this reverse yielding, the remainder of the wave travels at a slower range of velocities—a rarefaction fan corresponding with the bulk sound speed, which is a function of the stress level.

Parts (b) and (c) of Figure 3-8 show the usual wave processes for the conditions under which the elastic longitudinal wave velocity is greater than the shock velocity; that is, the slope of the stress path up to A in part (b) is steeper than the Rayleigh line. If the stress level is high, the shock wave may be overdriven—the slope of the Rayleigh line then becomes steeper than the elastic slope connecting the initial state to point A. In this latter case, loading proceeds along a Rayleigh line that connects the initial state to the final state at B and no precursor appears in the wave front.

Let us examine approximate relations for the wave speeds illustrated in Figure 3-8(c). Because the longitudinal compressibility is different in the elastic and plastic regions, elastic precursors appear in both compression and rarefaction waves. Elastic precursors propagate with the velocity c_L of longitudinal elastic waves

$$c_L = \sqrt{\frac{K + \frac{4}{3}G}{\rho}} \tag{3.50}$$

Here K is, in general, the bulk stiffness at the current stress level. For the initial precursor, the appropriate value of K is the zero- or low-pressure bulk modulus. But for unloading from the peak stress at point B in part (b), we should use the bulk stiffness at that stress level. The curvature of the pressure-volume path indicates that this stiffness increases with increasing stress. The velocity of wave propagation in the plastic region is the "bulk" sound velocity c_B:

$$c_B = \sqrt{\frac{K}{\rho}} \tag{3.51}$$

The bulk sound velocity is often treated as a fixed number, but it certainly varies throughout a rarefaction fan as shown in Figure 3-8(c). When we use the zero-pressure bulk modulus, we obtain the velocity associated with the foot of the wave.

The longitudinal and bulk sound velocities are related through the Poisson's ratio ν:

$$\frac{c_L}{c_B} = \sqrt{\frac{3(1-\nu)}{1+\nu}} \tag{3.52}$$

It has been shown that Poisson's ratio is almost independent of pressure, so a constant ratio of the longitudinal and bulk sound velocities is a good approximation for treating most wave propagation problems.

The elastic-perfectly plastic idealization of material behavior is relatively simple, is mathematically tractable, and serves the useful purpose of illustrating some of the important processes that take place in solid materials during stress wave propagation. However, real materials rarely exhibit such simple response. In most instances, real materials exhibit a hardening behavior in which the yield stress increases with increasing strain. Yielding in real materials is further complicated by the influence of several other variables including pressure, temperature, and strain rate. Some of these effects will be discussed in more detail in later sections.

3.6 COMPUTER SIMULATION METHODS.

A computational simulation of an event (impact, explosion, thermal radiation) is conducted by representing the geometry and materials of all the objects in the event and the initial conditions of the event. The material behavior represented can include standard stress-strain relations, detonation, melting, yielding, and fracture. The most common solution procedures are the methods of characteristics and the finite element or finite difference methods.[2] Both the method of characteristics and the finite element method

---

[2] The term finite element will be used throughout the remainder of this section to represent both finite element and finite difference methods because their differences in the present context are mainly in nomenclature and in the history of their development.

73

involve discretization of the domain of the problem. The solution is performed in such a manner as to determine successive states of equilibrium in the material at a sequence of times and at many points distributed over the objects participating in the event. With the solution known at these discrete points in time and space, we can interpolate to determine a complete solution over all locations in the objects and throughout the time of interest.

Both the method of characteristics and the finite element method are based on the simultaneous solution of the differential equations representing the conservation of mass, momentum, and energy, plus the constitutive relations. The solution procedure consists of determining the particle velocity, stress, strain, internal energy, temperature, fracture damage, and other quantities at each selected point in time and space. With these quantities known at one time, we can step forward to the next time and solve again for new values of these quantities, using the conservation laws and the constitutive relations.

The laws for the conservation of mass, momentum, and energy are fully prescribed by mechanics principles, but the constitutive relations must be provided by the user for each material participating in the event. Hence, the development of the constitutive relations is a crucial step in the solution of problems with these computational methods. For the spall or fracture problems discussed here, the constitutive relations generally begin with standard elastic or elastic-plastic relations for the intact material. Then when a criterion is met, fracture processes are added to the standard sets of relations. We present below some of the requirements for an appropriate constitutive relation, then we present some requirements for the computational subroutine containing the constitutive relation. The comments are intended to provide a quick overview of the methods available for performing computational simulations for fracture problems and particularly in the use of constitutive relations including fracture in finite-element codes.

3.6.1 Requirements for Constitutive Relations.

Certain restrictions must be imposed to provide physically reasonable and mathematically consistent constitutive relations for the fracture of materials. These restrictions stem from a variety of considerations including frame invariance, material symmetry, and thermodynamic restrictions. Generalized, thermomechanically consistent constitutive models usually conform to the following criteria:

(1) The material must not produce energy during cyclic loading. This requirement conforms with our accepted notions of energy conservation (first law of thermodynamics) and of entropy production (second law of thermodynamics).

(2) The constitutive relations must be independent of the orientation of the object (the "frame-indifference" requirement). This requirement means that for isotropic material, for example, the x, y, and z coordinates can be interchanged without changing the constitutive processes.

(3) A third requirement concerning the "local" nature of mechanical processes is treated in various ways, so we present two possible approaches:

- The "local" approach takes the viewpoint of the material particles and requires that the constitutive relations involve only quantities local to those particles. For example, the particle knows mainly its current stress state, strain increments, and strain rates, but sees no overall wave shapes, has a limited memory of its own past, and has no knowledge of the future. The particle cannot tell if the loading is sinusoidal nor can it tell the period or frequency of loading. The knowledge of the past is limited to the prior stress state, plastic strain, damage, and similar current quantities that may be stored, but there is no history of stress, for example.

  In fracture problems the particle does not have an overall knowledge of the damage, such as the crack length and orientation, but knows only the motion of its own boundaries and the stress within. Hence the particle cannot know the stress intensity factor K_I, for example, which would require a knowledge of the crack length, orientation, and an appropriate far-field stress normal to the crack plane.

- The second approach allows the computation to proceed with a broad knowledge of the past and present, but not of the future. In this procedure, the program can compute global quantities such as the stress intensity factor and compare this factor with the fracture toughness, then decide whether an element does or does not fracture. This second approach allows computational simulations to represent some analytical approaches taken in fracture.

3.6.2 Connection to a Finite-Element Code.

The finite element code provides a solution for the three conservation relations and the constitutive relations for points throughout the object of interest and the time of interest. The part of the solution procedure that pertains to the conservation relations is built into the code because the conservation relations are always the same regardless of the material involved. But a variety of constitutive relations may be used, depending on the problem and materials at hand, the desired results, and the requirements of the user. Therefore, the constitutive relation is a separable feature of the code and, in this section, we are concerned with how to distinguish between the part of the code dealing with the solution of the conservation equations and the part dealing with the solution of the constitutive relations and how to pass data between them.

Here, we discuss how data are stored and shared between the main program—the wave propagation code—and the constitutive routine. For our constitutive routines, we require that they can be fully tested separately from the wave propagation code; hence, these routines stand as complete units. Because of this independence, they can also be readily connected to other finite-element codes. The subroutine (or subroutines) containing the constitutive relations provide a solution for the stresses in the finite elements. In our strategy, the constitutive routine is given the old values of the stress tensor, the old historical variables, the material properties, and the increments of strain and time for an element. The routine then computes the new stress state, updates the historical variables, and passes these data back to the calling code. The constitutive routine is called once for each finite element and time step (vectorization or pipelining may alter this simple pattern for speed of execution, but the concept is not changed).

An example of the layout of a constitutive model for microfracture is given below. This pattern has been followed in much of our work and can be a general pattern for providing complex constitutive relations for finite-element codes. The pattern contains four major subroutines and possibly several subsidiary routines. The four main routines are

(1) UMAT, a user routine called by the finite-element code. Many large finite-element codes have open call statements for connecting constitutive relations to be provided by the user. This routine organizes the data (material and historical data) to a form usable by the fracture routine and checks a criterion to determine whether fracture is occurring. If fracture is occurring, UMAT then calls the fracture routine for the stress and damage computations. If no fracture is occurring, UMAT calls routines to compute the pressure and the deviator stresses.

(2) BFRACT, a microfracture routine for computing damage and stresses in material undergoing brittle fracture. BFRACT calls the same pressure and deviator stress subroutines as UMAT does, thereby ensuring continuity between the damaged and undamaged states.

(3) PRESSURE, a subroutine for computing the pressure from a Mie-Grüneisen relation.

(4) EPLAS, a subroutine that provides an elastic-plastic computation for the deviator stresses.

Next, we determine how to pass the data between the main code and these subroutines. We wish the constitutive routines to stand as an independent entity both for testing and so that they can be readily connected to any finite element code. For satisfactory testing, there can be no changes in these routines as they proceed from tests of a single element to connection to one-, two-, or three-dimensional finite-element codes. Therefore, our procedure is to let all the data pass through the calling statements. Thus, all the information needed by the routines and produced by the routines appears in the formal parameters of the constitutive routines.

This strategy facilitates the use of EPLAS, for example, as a routine that can be called to provide the deviator stresses. These stresses computed by EPLAS are not the stresses in the main element arrays of the calling code. Thus, EPLAS may be called by UMAT to provide deviator stresses that UMAT sends back to the code for the main arrays, or EPLAS may be called iteratively by BFRACT and then its deviator stresses are used as part of the stress sent back to the code. During these iterations, the stress quantities in the main arrays are left intact.

Many other issues must be dealt with in connecting a constitutive relation to a finite-element code. For example, where shall the computation of internal energy occur? The energy computation is actually simultaneous with the stress computation in the standard solution procedure, so the energy may be computed within the constitutive routine or it may be provided by the main code as an estimate before the call to the constitutive relation and a completion computation after the call. Also, where shall the rotational transformations of stress and strain quantities be handled? These transformations are required so that the

76

constitutive results are indifferent to the location of the reference frame. Generally, these rotational transformations are handled by the main code so that the constitutive relation deals with a finite element that appears not to be rotating.

SECTION 4

EXPERIMENTAL TECHNIQUES

Investigating the strength of condensed matter under shock wave loading requires the ability to create plane shock pulses in laboratory samples and to measure the evolution of these pulses inside the samples. This section discusses methods of producing and recording intense load pulses in condensed media. Although shock wave techniques are well documented in technical papers, monographs (e.g., Caldirola and Knoepfel, 1971; Graham, 1993), and reviews (e.g., Al'tshuler, 1965; Graham and Asay, 1978; Chhabildas and Graham, 1987), a summary of methods will be useful here for better understanding of the experimental results that will be presented in later sections.

4.1 TECHNIQUES USED TO GENERATE SHOCK WAVE LOADS.

Plane shock waves for spall strength measurements are usually generated by impacting the sample of interest with a flyer plate or by detonating an explosive plane wave generator in contact with the sample. These shock wave generation schemes produce loading pulses with durations on the order of a microsecond. Radiation energy from a laser or particle beam can be used to produce stress pulses with much shorter durations. To properly design and correctly interpret the results of shock wave experiments, we need to understand the details of the loading history in the specimen for each of the wave generation schemes used in the experiments.

4.1.1 Graphical Analysis of Experimental Designs.

A particularly useful approach for analyzing shock wave propagation problems relies on graphical techniques. In place of the conservation and constitutive equations normally used in analytical solutions (see Section 3), this approach uses a distance-time diagram (or $x - t$ diagram), and a stress-particle velocity diagram (or $\sigma - u$ diagram) to provide graphical solution to stress wave propagation problems. The distance-time diagram is used to display the relative positions, in space and time, of the materials involved in a given problem. This $x - t$ diagram is also used to keep track of the type and relative position of the stress waves, as well as their interactions. The stress-particle velocity diagram is used to find new equilibrium states, in the $\sigma - u$ space, after the impact of two materials or after the interaction of waves with one another or with material boundaries. In locating new equilibrium states, we use the fact that, at any point in a solid material, both the stress and the particle velocity must remain continuous at all times. We also invoke the definition of the Hugoniot curve as the locus of all possible equilibrium states in a material attainable behind a shock front.

Let us now apply this graphical analysis technique to study wave dynamics under plate impact loading conditions. The experimental configuration of a typical plate impact experiment is shown in Figure 4-1(a). A flyer plate approaches a target plate from the left with velocity u_i. Figure 4-1(b) shows the distance-time diagram of the wave process after impact of the flyer plate upon the plane target. The origin of the $x - t$ diagram corresponds to the moment in time the impact event is initiated. This impact causes shock waves to propagate in the impactor and target plates away from the impact face as shown in Figure 4-1(b).

To determine the equilibrium states in the flyer and target plates after impact, we use the $\sigma - u$ diagram shown in Figure 4-1(c). By definition, all attainable equilibrium states in the shock compressed target must lie on the target Hugoniot. The state of the target before impact defines the point at which the target Hugoniot is centered. In our example, the point $(0, 0)$ in $\sigma - u$ space defines the initial state of the target; therefore, the target Hugoniot passes through the point $(0, 0)$. The direction of wave propagation in the target determines whether the Hugoniot faces to the right or to the left. In our example, the shock wave in the target travels from left to right. Therefore, the target Hugoniot shown in Figure 4-1(c) faces to the right. Using the same reasoning, we find that the Hugoniot of the flyer must pass through the point $(0, u_i)$ and must be facing to the left.

Continuity of stress and particle velocity at the interface between the flyer and target plates requires that they both reach the same postimpact state. This common state is represented by the intersection of the two Hugoniots representing the target and flyer plates and is labeled state 'p' in Figures 4-1(b) and (c). When the target and flyer are made of the same material, then due to symmetry, the particle velocity of the shock compressed matter is exactly one-half of the initial impactor velocity. This, in fact, is the situation shown in Figure 4-1.

When the shock wave reaches the back surface of the impactor, it is reflected as a centered rarefaction wave, which propagates toward the target. The material behind this rarefaction fan is at rest and in a stress-free state. While the stress wave reverberates in the impactor, the impact surface and the target remain at constant stress. Because the rarefaction front, which propagates with the sound velocity in shock compressed matter, is faster than the initial shock front, the rarefaction front eventually overtakes the shock front and causes a decay in peak stress. If the impactor and target are made of the same material, the distance x where the rarefaction front overtakes the shock front can be calculated by using the following equation derived using the quasi-acoustic approach:

$$x = \delta\left(1 + \frac{2U}{su}\right) = \delta\left(1 + \frac{4U}{su_i}\right) \approx \delta\left(1 + \frac{4c_o}{su_i}\right) \tag{4.1}$$
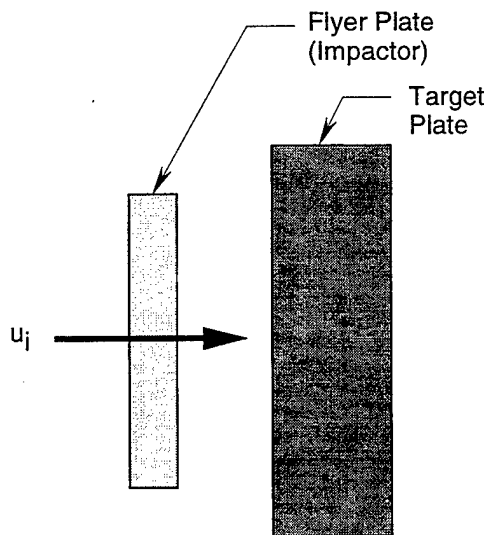
(a) Impact configuration.
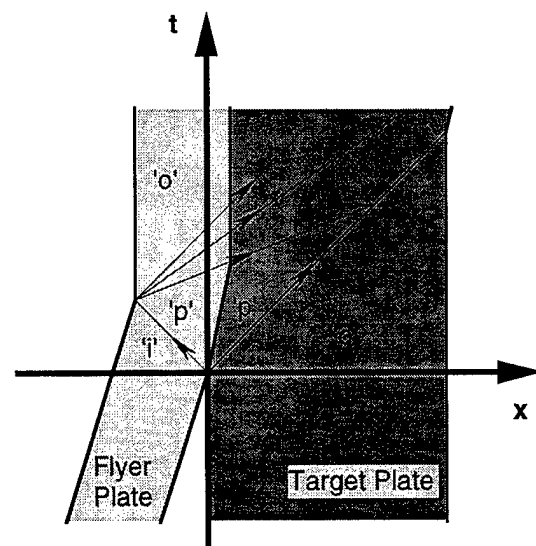
(b) Distance-time diagram.
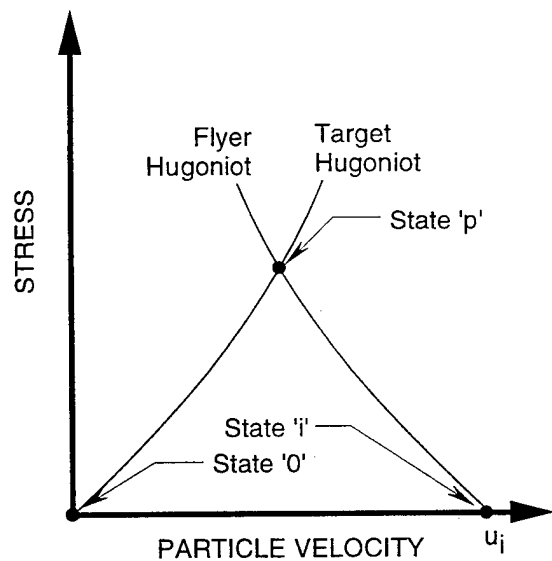
(c) Stress-particle velocity diagram.

(d) Edge effects.
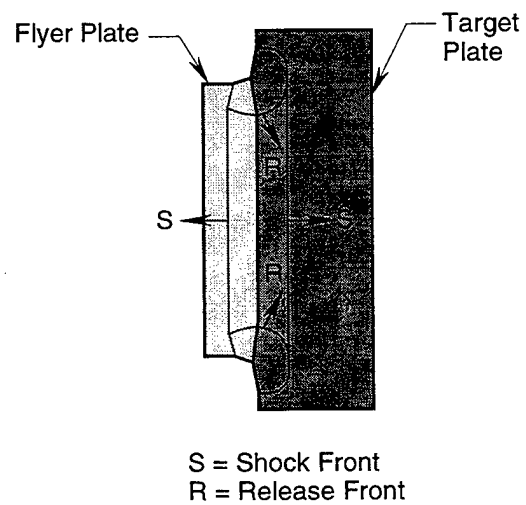
S = Shock Front
R = Release Front

Figure 4-1. Generation of a compression pulse by the impact of a flyer plate.

where δ is the impactor thickness, and c_o and s are the coefficients defining the intercept and slope of the linear relationship between the shock front velocity U and the particle velocity u [Eq. (3.12)]. Thus, stronger shock waves begin to decay earlier than weaker shock waves. In the case of elastic-plastic materials with Poisson's ratio independent of pressure, the distance x can be estimated as

$$x = \delta \frac{U(c_l + c_o) + c_l su}{U(c_l - c_o) + c_l su} \approx \delta \frac{c_l + c_o}{c_l - c_o + \frac{c_l}{2c_o} su}_i \qquad (4.2)$$

where c_l is the longitudinal wave velocity and all other parameters are as previously defined. The value of the distance x computed from Eq. (4.2) is actually an upper bound estimate, and it decreases if we take into account the elastic precursor of the shock wave in the impactor.

An important factor in the design of experimental configurations for shock wave propagation experiments is the ratio of the axial to transverse dimensions of the impactor and target plates. The transverse dimensions must be large enough to ensure one-dimensional motion throughout the time period required for the measurements. The dimensions of the experiment should be chosen such that the release waves emanating from the edges of the impactor and target plates [see Figure 4-1(d)] do not interfere with the one-dimensional flow in the central region of the specimen during the experiment. Thus, longer recording times can be achieved by using impactor and target plates with large diameter-to-thickness ratios.

Figure 4-2 illustrates the wave dynamics for the impact of a flyer plate with high dynamic impedance upon a softer target. The impact configuration shown in Figure 4-2(a) is essentially the same as in the previous case. As before, the impact causes compressive shock waves to propagate in the impactor and target plates away from the impact face. These waves are shown in Figure 4-2(b), where several later wave reverberations are also shown. The $\sigma - u$ diagram for this impact configuration is shown in Figure 4-2(c). As before, this diagram is used to determine the equilibrium stress and particle velocity states in the impactor and target. Those equilibrium states are labeled with the letters A through E, while the initial states in the impactor and target before impact are designated with 'i' and '0', respectively.

The stress-particle velocity state in both the target and projectile just after impact is designated by the letter A in Figure 4-2. As the initial shock wave reaches the back surface of the impactor, it reflects as a release fan, which unloads the impactor to a state of zero stress. This state is designated by the letter B in Figures 4-2(b) and (c). The interaction of this release fan with the impactor-target interface produces a new equilibrium state in both the impactor and the target. This state is indicated by the letter C in Figure 4-2. In the target, the new equilibrium state is reached through an unloading wave that transforms the material from state A to state C. In the impactor, the new equilibrium state is reached through a compression wave that transforms the material from state B to state C. Several such wave reverberations
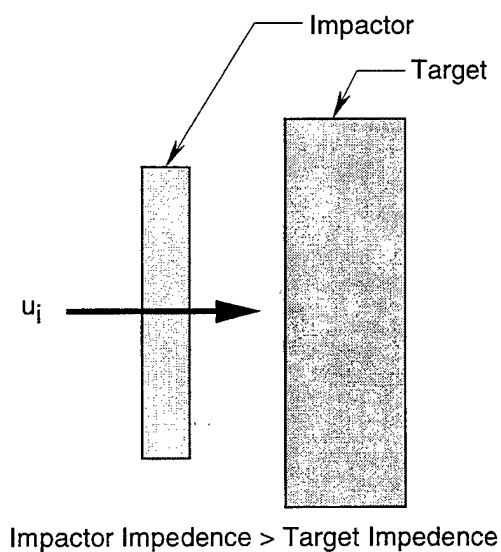
(a) Impact configuration.
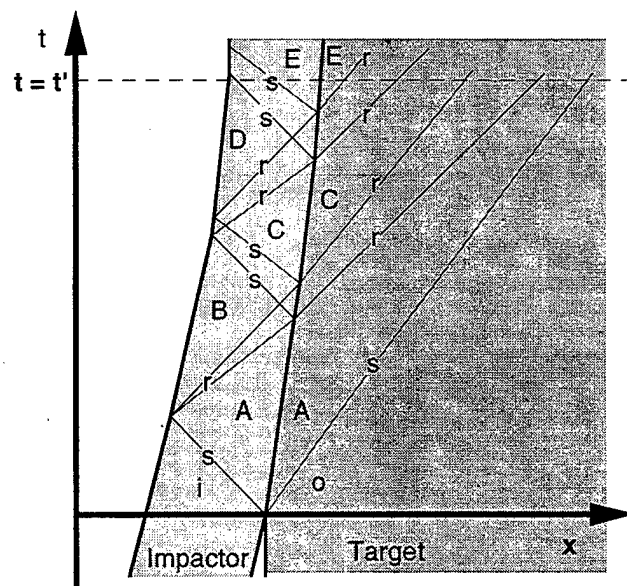
(b) Distance-time diagram.
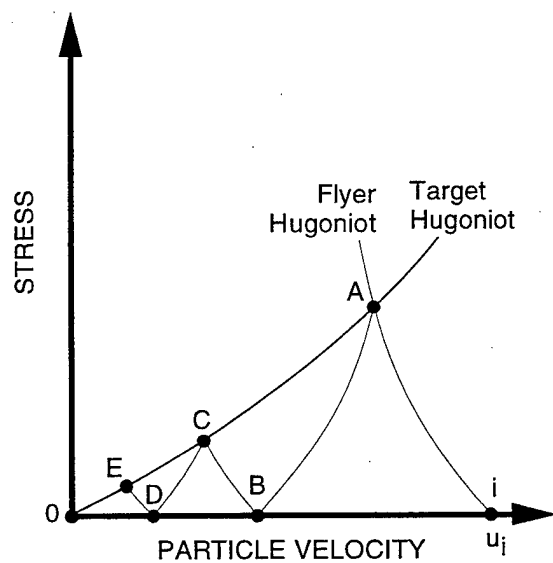
(c) Stress-particle velocity diagram.
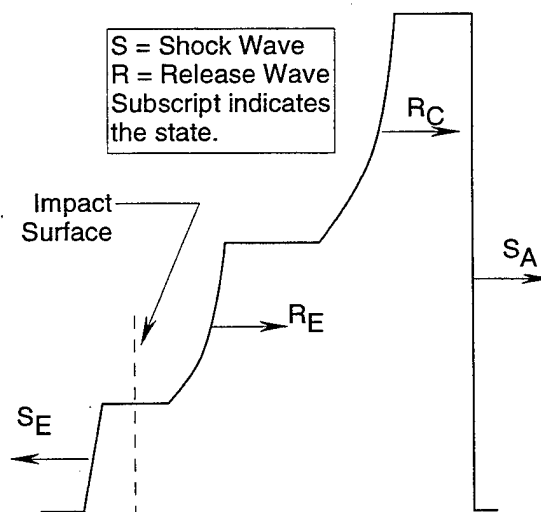
(d) Wave structure at time t = t'.

Figure 4-2. Wave interactions for the impact of a relatively rigid flyer plate upon a softer target.

occur between the impact surface and the back surface of the impactor. Each reverberation produces a release wave that propagates into the target material. Thus unloading of the target occurs in several successive steps, each lower in magnitude than the previous one. The resulting wave structure after two reverberations is shown in Figure 4-2(c).

The progressive unloading of the target noted in the case just discussed cannot be achieved if the impactor material is softer than the target material. The wave dynamics for this case are illustrated in Figure 4-3. On impact, the stress and particle velocity in the impactor change from state 'i' to state 'A' whereas the target material the stress and particle velocity change from state '0' to state 'A'. Interaction of the shock wave with the rear surface of the impactor causes a release fan to emerge. Behind this release fan, the impactor material is in a state of zero stress and negative particle velocity. This state is indicated by the letter B in Figure 4-3.

Wave interactions resulting from the interaction of the release fan with the impactor-target interface lead to a new equilibrium state. The continuity condition requires that both the impactor and target reach the same new equilibrium state indicated by point C in Figure 4-3. However, this is physically impossible because the interface cannot support tensile stresses. For this reason, the target separates from the projectile at the interface, and the target material unloads to a stress-free state.

Next, we examine a case involving generation of a stress pulse in a material using a laser beam, particle beam, or other radiation sources. In this case, the energy is deposited in a thin layer of material near the front surface. The deposition profile is nearly exponential for lasers and x-ray sources.[3] The deposition depth depends on the light absorption characteristics of the target material and on the characteristics of the light source. The nearly instantaneous deposition of energy in a thin layer of material causes local heating at constant volume, which in turns causes the stress to increase. The highest stress magnitude occurs near the irradiated surface.

Since a free surface cannot sustain compressive stresses, a rarefaction wave forms at the irradiated surface and propagates toward the interior of the sample. Meanwhile, the compression wave that forms during energy deposition also propagates into the cold interior of the sample, ahead of the rarefaction wave. Thus, a bipolar stress pulse forms as shown in Figure 4-4. The stress profile in the irradiated material at the instant of deposition is directly related to the deposited energy profile through the Grüniesen coefficient, Γ. For this reason, the thermomechanical stress that develops as a result of energy deposition is also known as Grüniesen stress.

Figure 4-5 illustrates the wave dynamics for instantaneous bulk energy deposition. The analysis assumes that the deposited energy profile has its maximum near the surface, as shown earlier in Figure 4-4. If the deposited energy is not great enough to cause vaporization, the process can be analyzed, at least

---

[3]Stress profiles caused by radiation from a particle beam are more complex.
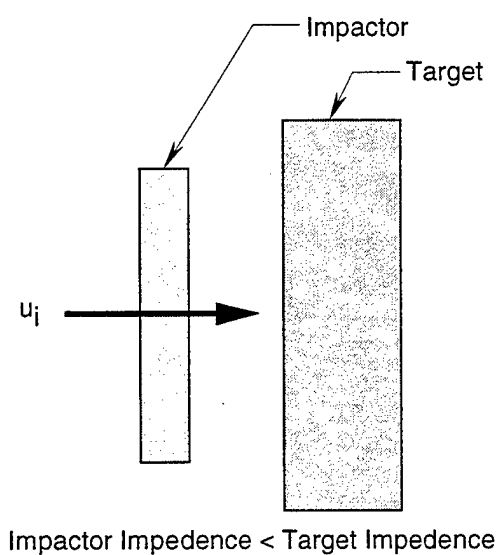
(a) Impact configuration.
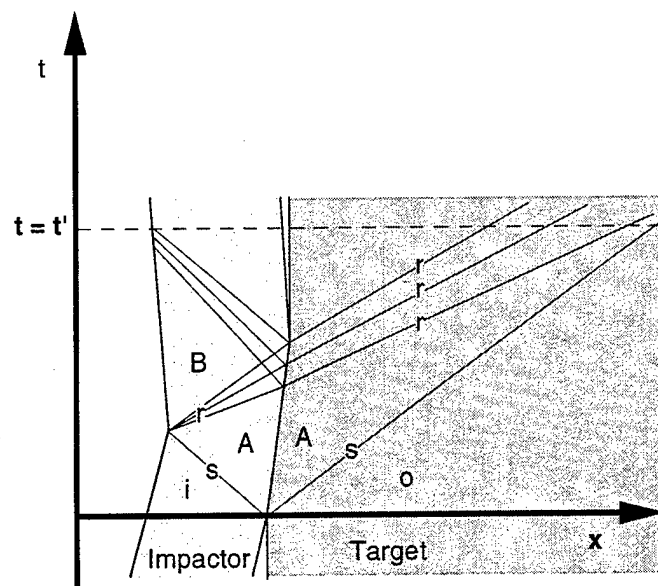
Impactor Impedence < Target Impedence

(b) Distance-time diagram.
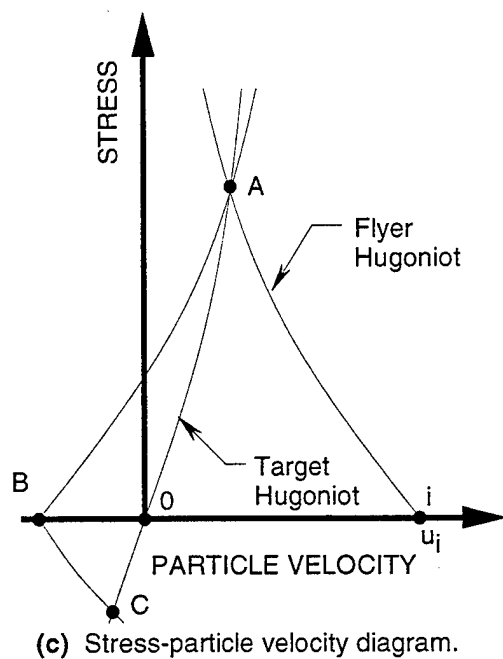
(c) Stress-particle velocity diagram.
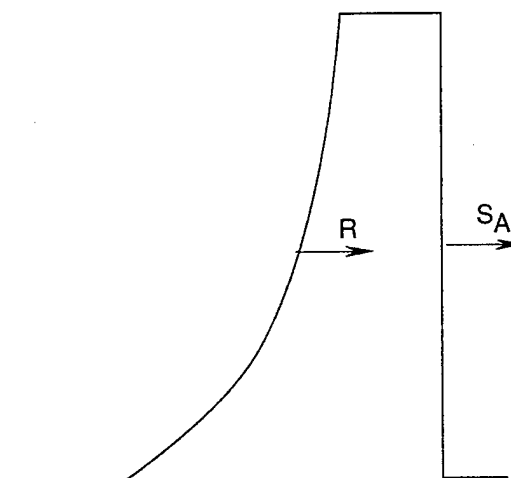
(d) Wave structure at time t = t'.

Figure 4-3. Wave interactions for the impact of a relatively soft flyer plate upon a hard target.

84

STRESS, ENERGY

Energy Profile at t = 0

Stress Profile at t = 0
$\sigma(0, x) = \rho\Gamma E(0, x)$

DISTANCE

Stress Profile at t > 0
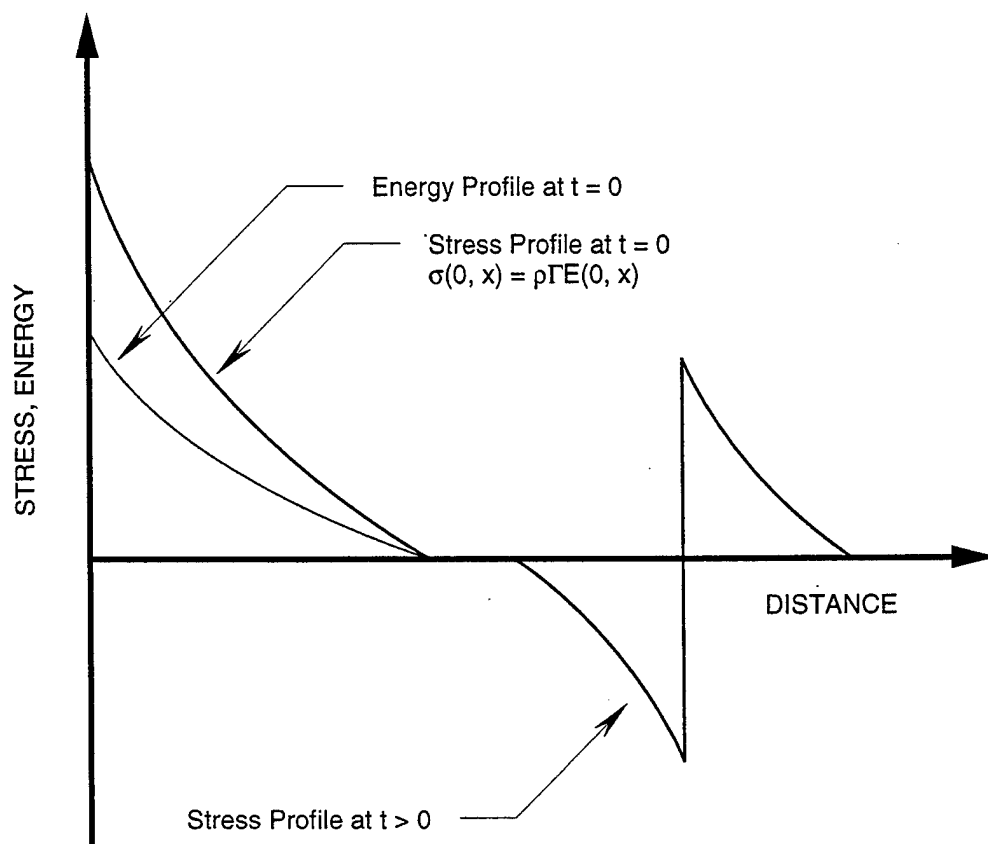
Figure 4-4. Generation of a stress pulse by instantaneous energy
deposition and the evolution of a bipolar stress wave.
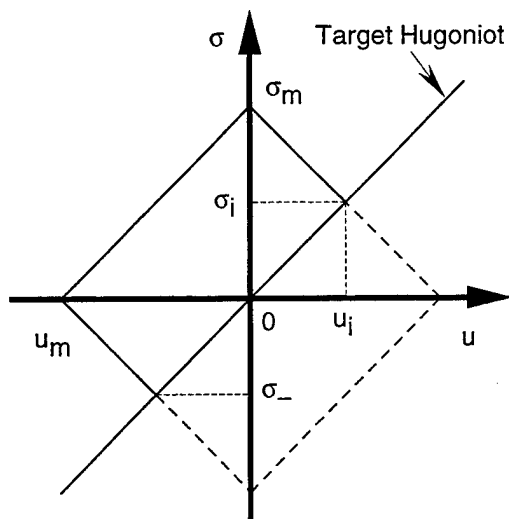
(a) Stress-particle velocity diagram.
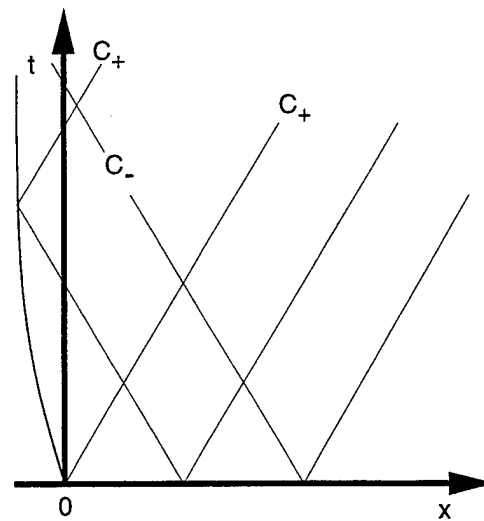
(b) Distance-time diagram.
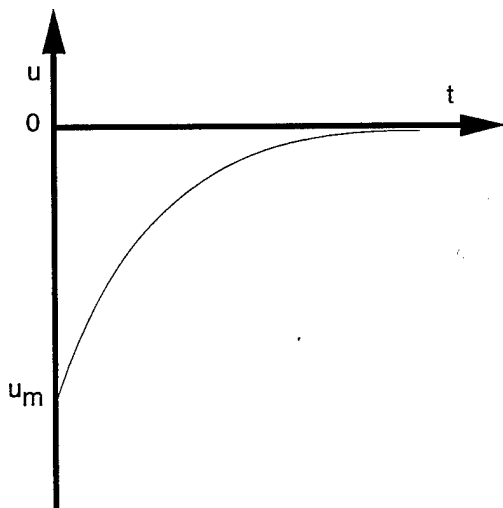
(c) Free-surface velocity profile on irradiated side.
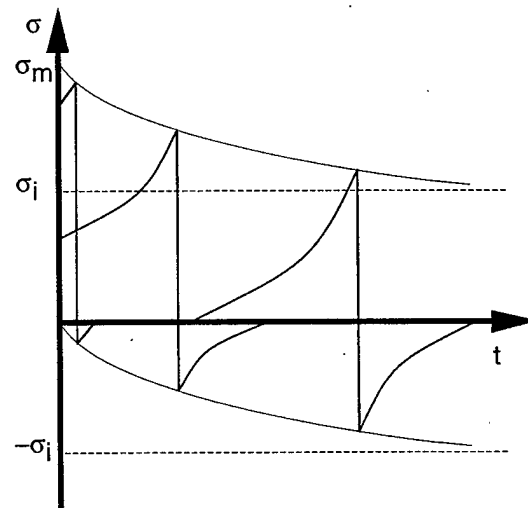
(d) Evolution of the bipolar stress pulse.

Figure 4-5. Wave dynamics for problems involving instantaneous bulk energy deposition.

86

qualitatively, by using the acoustic approach. Immediately after the instantaneous irradiation of the target, the particle velocity is identically zero throughout the deposition region as well as in the rest of the target. States of particles on the $\sigma - u$ diagram [see Figure 4-5(a)] are described by points along the stress axis.

Information about changes in state of each point is propagated by sound perturbations both into the body and toward its irradiated surface. For each point x at time t, the stress and particle velocity in the new state are located on intersections of Riemann's isentropes describing the changing states along C_+ and C_- characteristics, which pass through the point x, as shown in Figure 4-5(b). Thus maximum pressure and particle velocity magnitudes at points far from the irradiated region (i.e., where deposited energy is equal to zero) correspond on the $\sigma - u$ diagram to intersections of the lines

$$\sigma = \rho c u \qquad (4.3)$$

describing states along a C_- characteristic that originates from a undisturbed area, and the lines

$$\sigma = \sigma_m - \rho c u \qquad (4.4)$$

describing states along a C_+ characteristic that originates from the point of maximum stress, σ_m. Thus,

$$u = \frac{\sigma_m}{2\rho c}, \qquad \text{and} \qquad \sigma = \frac{\sigma_m}{2} \qquad (4.5)$$

The values of u and σ obtained from Eq. (4.5) are indicated by u_i and σ_i in Figure 4-5(a). The maximum free-surface velocity toward the radiation source is

$$u_s = u_m = -\frac{\sigma_m}{\rho c} \qquad (4.6)$$

where u_m is the maximum particle velocity (with a negative sign). Thus, the maximum particle velocity is reached at the free surface of the irradiated side of the target. The free-surface velocity begins to decay almost instantaneously with the arrival of perturbations from internal layers of the targets. The resulting free-surface velocity profile is shown in Figure 4-5(c).

Expansion of the target material is accompanied by the appearance of negative stress (i.e., tension) inside the target. The tensile stress magnitudes can be obtained from the intersection of Riemann's isentropes for perturbations coming from deep layers of the target toward the irradiated surface with Riemann's isentropes for perturbations reflected by the surface. On the time-distance diagram of Figure 4-5(b), the negative pressure area is situated above the C_+ characteristic emanating from the origin.

The tensile stress in the target increases gradually until the ultimate maximum value is reached during propagation of the reflected wave into the cold region of the target. The magnitude of the maximum tensile stress is given by the relation

$$\sigma_- = \frac{\rho c u_m}{2} = -\frac{\sigma_m}{2}$$ (4.7)

This maximum tensile stress is reached on cross sections in the cold region of the specimen, where initially the deposited energy and stress are both zero.

The evolution of the stress pulse is shown in Figure 4-5(d), which show stress histories at several successive locations in the target. As shown, a bipolar stress pulse develops in the target. Initially, the compressive component of the pulse dominates the stress history. However, as noted in Figure 4-5(d), the pulse baseline continually shifts downward while the magnitude of the difference between the maximum tensile stress and the maximum compressive stress remains constant. This trend continues until the peak compressive stress is equal in magnitude to the peak tensile stress.

4.1.2 Experimental Procedures Used to Produce Shock Waves.

4.1.2.1 Explosive Devices. The simplest method of producing a shock wave with a peak pressure of a few tens of gigapascals is to detonate a chemical explosive charge on the surface of the sample. Various explosive lenses have been designed to create plane shock and detonation waves with lateral dimensions up to few tens of centimeters.

Detonation of an explosive in contact with the sample creates a triangular stress history because, in detonation waves, the pressure begins to fall immediately after the shock as a result of expansion of the detonation products. Often, well controlled stress wave propagation experiments require a square stress pulse (i.e., a stress pulse with constant amplitude) rather than the triangular pulse produced using in-contact explosives. Such a stress pulse is usually generated by using the flyer plate impact configuration in which a flyer plate, or impactor, is made to collide with the target in a planar fashion and at a well controlled impact velocity. Then the peak stress in the target is controlled by the impact velocity and by the dynamic impedances of the impactor and target materials. The duration of the stress plateau behind the shock front is controlled by the thickness of the impactor. Experimentally, plane impactors are projected using explosive detonation facilities or ballistic devices—known as "guns."

Figure 4-6 shows a typical arrangement of an explosive launching device. Such a device can accelerate metal or plastic impactors, 1 to 10 mm thick, to velocities of 1 to 6 km/s. The central region of the impactor remains flat even though the radial expansion of the detonation products leads to a pressure gradient that causes the pressure in the explosive gases to decrease with distance away from the center of the explosive charge. The guard ring shown in Figure 4-6 is placed around the impactor to compensate
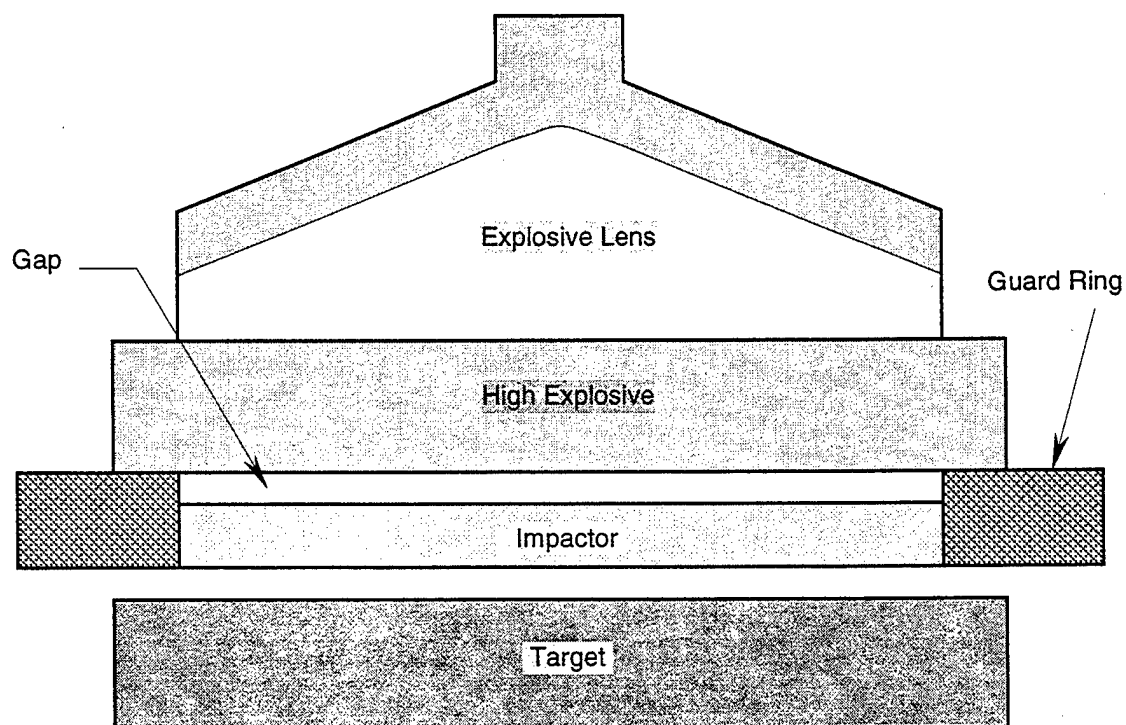
Figure 4-6. Experimental configuration for using explosives to launch a flyer plate at high velocity .

for the effect of this pressure gradient. The reflection of the detonation wave from the guard ring causes a momentary increase in pressure around the periphery of the impactor, which in turn produces additional inflow of the detonation products into the gap above the impactor. This gap also serves to "softens" the impact and prevent fracture in the flyer plate.

It is difficult to attain impactor velocities below 1 km/s using the launching scheme shown in Figure 4-6. An alternative explosive launching technique that produces low impact velocities is shown in Figure 4-7. With this technique, an intermediate or attenuator plate with a high dynamic impedance is placed between the explosive charge and the flyer plate. Detonation of the explosive charge produces a plane shock wave in the attenuator. The flyer plate, which has a dynamic impedance lower than that of the attenuator, is accelerated by the shock wave and it acquires a velocity higher than that of the attenuator. This velocity difference causes the flyer plate to separate from the intermediate plate. A soft polyethylene gasket is inserted between the attenuator and impactor to prevent damage to the impactor as a result of rarefaction wave reflection from the rigid attenuator. This launching technique is also suitable for accelerating very thin impactors, such as foils or films, which are normally used to produce very short shock pulses.

Explosive launching techniques have been used to perform shock wave experiments since World War II, primarily because explosive facilities are compact and inexpensive. The impactor velocity can be easily varied over a wide range by varying the composition and density of the high explosives and the material and thickness of the flyer plate. However, the use of explosive materials is destructive and highly hazardous, thus requiring the deployment of safety measures. The experiments must be contained in specially designed containment chambers or performed at remote test areas. The explosives must be stored in specially designed bunkers where accidental detonations can be harmlessly contained. Furthermore, experiments with explosives require the availability of the technology to manufacture suitably shaped high-grade explosive charges. These constraints make it impractical in some cases to use explosive launch facilities.

4.1.2.2 Gas and Powder Guns. A popular U.S. alternative to the use of explosives for performing shock wave experiments is the use smooth-bore ballistic installations such as gas guns or powder guns. The single-stage gas (or powder) gun produces planar stress waves. With these smooth-bored guns, it is possible to vary the impactor velocity over a wide range in a reproducible and controllable fashion. Figure 4-8 shows a schematic of a typical gas gun. This gas gun is 14 m long and 101.6 mm in diameter. These dimensions are usually chosen to optimize the performance of the gas gun in terms of attainable projectile velocity, which is controlled by the length of the barrel as well as the volume and pressure of the gas, and recording time, which is controlled by the diameter of the gun (i.e., the lateral dimensions of the specimen). Gas gun dimensions vary greatly from one facility to another, but generally the bore diameter varies from 20 to 150 mm and the length of the barrel varies from 3 to 30 m (e.g., Fowles et al., 1970).
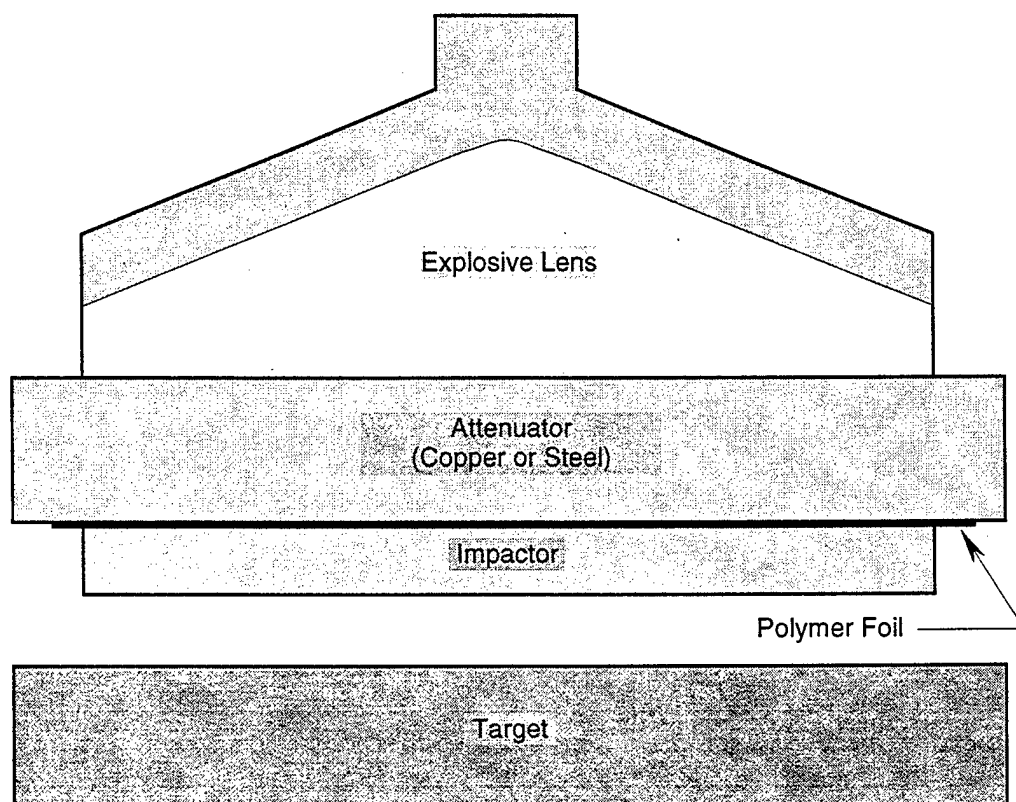
Figure 4-7. Experimental configuration for using explosives to launch a flyer plate at low velocity .

91

Breech

Shock Absorbers
and Positioning
Mechanism

Target Chamber

Catcher Tank
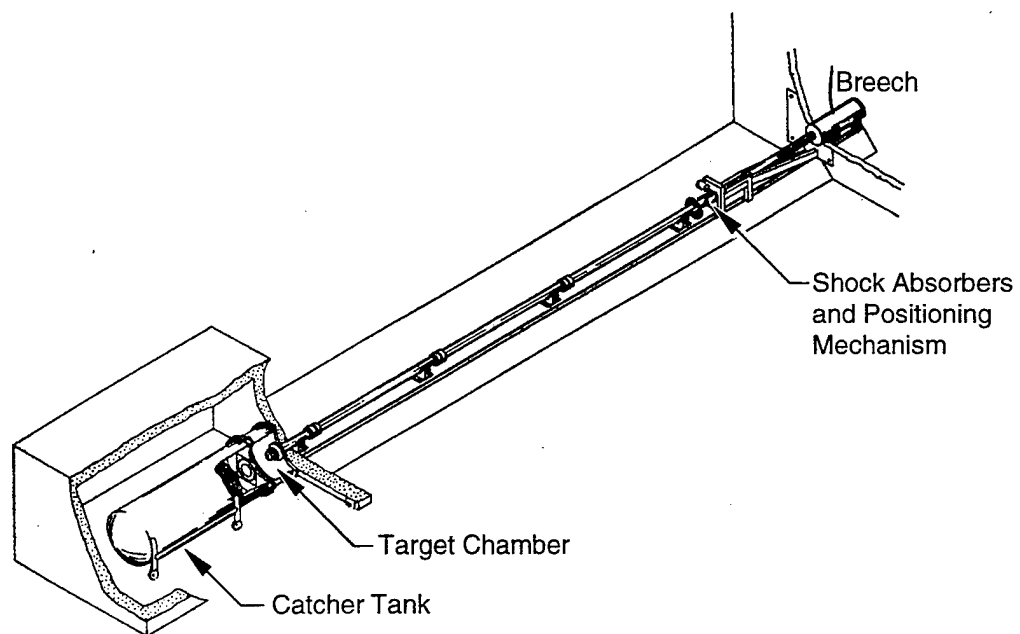
Figure 4-8.   Overall view of the gas gun facility at Washington State University
             (Fowles et al., 1970).

With a barrel up to 14 m long and initial compressed gas (nitrogen or helium) pressure of up to 15 MPa, a propulsion velocity of 100-1500 m/s can be produced.

At low impact velocities (below 100 m/s), frictional effects in the gun barrel become nonreproducible. For this reason, gas guns are not reliable in terms of generating reproducible low impact velocities. To overcome this inherent deficiency, the 101.6-mm-diameter gas gun at SRI International has been equipped with a "monkey's fist" that grips the projectile and holds it close to the target, thereby minimizing friction and enabling reproducible experiments at impact velocities below 100 m/s.

The flyer plate in a gas gun experiment is usually attached to a hollow projectile, which holds the plate normal to the axis of the gun barrel. To ensure planar impact and thereby minimize impactor tilt with respect to the target plate, impact is often arranged with the projectile still partly in the barrel, as shown schematically in Figure 4-9. The gun barrel and target chamber are usually tightly sealed and evacuated before each experiment to minimize the effect of the air cushion that would otherwise develop as the projectile travels down the gun barrel and compresses the air column in its path.

The target in Figure 4-9 is configured for soft recovery. The tapered edges of the specimen allow it to easily separate from the remainder of the target plate after the impact event. The specimen is then softly recovered in the rag-filled catcher box for posttest microstructural examination.

4.1.2.3 Electro-Explosive Devices (Electric Guns). The desire to extend the range of parameter values attainable in shock wave propagation experiments has led to the development of novel shock wave generators. Promising sources of high dynamic pressure include electro-explosive devices (electric guns) and high-power pulsed laser and particle beams.

In the electric gun, the explosion of an electrically heated metal foil and the accompanying magnetic forces drive a thin flyer plate up a short barrel (Osher et al., 1989). Such a device is diagrammed in Figure 4-10. The electric gun uses the energy initially stored in a fast-rise-time capacitor bank to ohmically heat and explode a bridge foil. The dense plasma produced by the electrical explosion of the foil pushes a cover polymer film, which can then be used as an impactor. In a later stage, the magnetic field of the expanding current-carrying circuit contributes to the acceleration of both the partially expanded plasma and the flyer.

The energy density of the electro-explosive plasma may exceed the energy density achieved with chemical explosives by one or two orders of magnitude. The flyer velocity can thus be varied from ~100 m/s to 10 km/s or higher. Lateral dimensions of the accelerated film can be varied from ~1 mm to ~10 cm. Thus electric gun is an effective tool for studying the dynamic strength of materials for short duration loads.
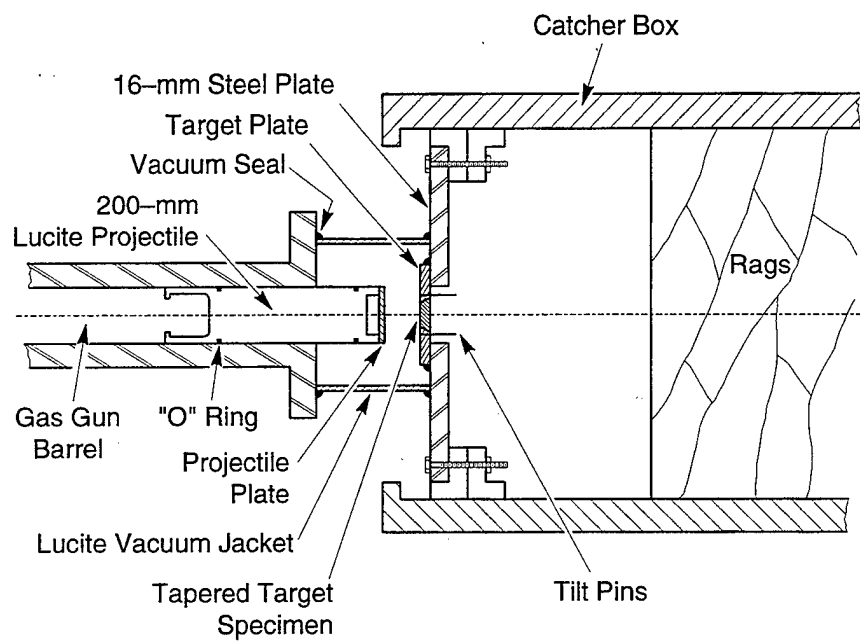
Figure 4-9. Schematic of the target area in a typical plate impact experiment (Barbee et al., 1970).

Top View

Side View

Bottom View

Aluminum Foil

Flyer Plate

L

Switch

Insulator   R

Copper
Transmission Line
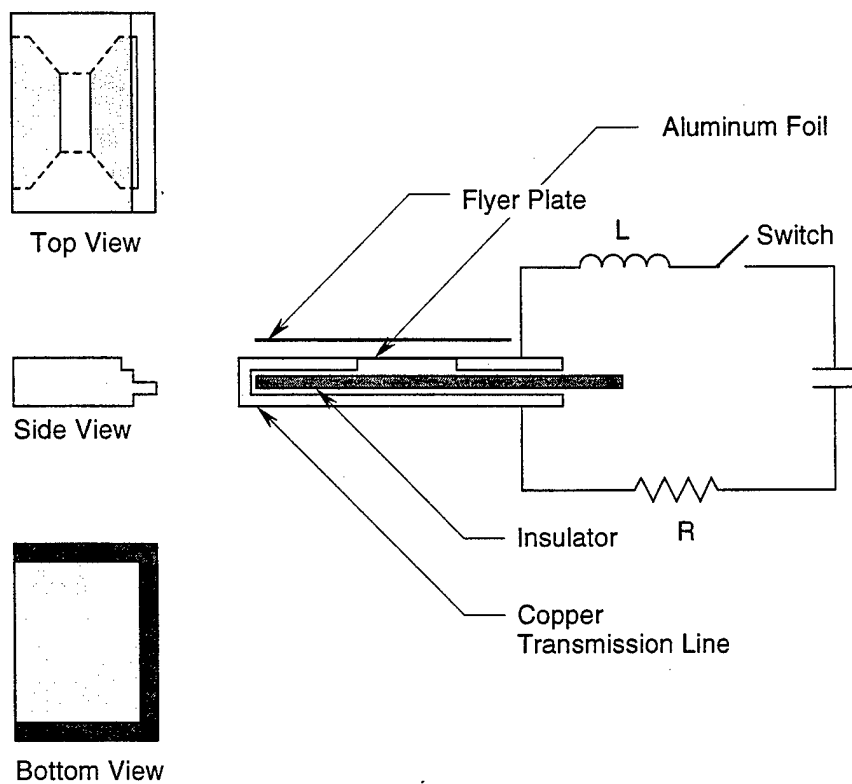
Figuire 4-10. Schematic of the electric gun.

4.1.2.4 Radiation. High energy concentration in a sample can be achieved by focusing a powerful laser beam on a small area of the sample. Since the early 1960s, lasers have been used to generate shock waves in condensed matter by directing a short ($\sim10^{-9}$-10^{-8} s) high-power laser pulse onto the open surface of a material. The surface layer is vaporized, and the resulting pressure in the ablation plasma produces a shock wave in the target. Only a small fraction of the energy is coupled into the target in this case. In another configuration, the ablative pressure is used to launch a thin (~1 to 10 μm) flyer plate. The maximum free-foil velocities can be modeled adequately by a rocket propulsion model, which predicts that the velocity is inversely proportional to the foil thickness.

Sheffield and Fisk (1984) transmitted laser pulses through a transparent substrate optically coupled to a launched foil, as shown in Figure 4-11(a). Their results show that water-confined foils attained peak velocities about three times higher than free foils due to tamping of the laser-induced plasma.

Figure 4-11(b) shows an advanced scheme developed by Paisley et al. (1992) to perform miniature plate impact experiments for material property studies. A plate to be launched, 0.2 to 20 μm thick, is placed on the output end of an optical fiber. Fiber diameters are typically 0.4 to 2 mm, and the flyer diameter is that of the optical fiber. A laser pulse is transmitted through the fiber and vaporizes a small amount of the flyer plate at the interface between the output end of the fiber and the flyer plate. The optical fiber provides a spatially uniform energy profile through the cross section. The laser-pulse temporal profile, the optical properties of materials, and the power density determine the optical coupling efficiency of the laser energy to the kinetic energy of the launched plate. This miniature plate-launch technique gives any laboratory with an Nd:YAG laser and subnanosecond shock wave diagnostics the ability to study mechanical properties of materials for nanosecond load durations.

The powerful pulsed sources of electron and ion beams, developed for controlled thermonuclear fusion and other applied physics problems, are now being used as shock wave generators. Pulse accelerators with power from a gigawatt to several terrawatts or more are operated in laboratories around the world to drive intense particle beams. In shock wave applications, the particle beam extracted by the high voltage pulse from a diode is focused on a target spot with a diameter of a few millimeters. The high-energy particles are absorbed in a thin surface layer of the target, and the kinetic energy of the particles is transformed into heat (see Figure 4-12). The depth of the energy deposition zone depends on the energy and kind of particles and on the target properties. The rapid heating of the finite material layer produces a compression wave inside the target. If the beam energy is high enough to vaporize the target matter in the deposition zone, the ablation pressure from the particle beam source can be used to launch thin foil flyer plates by the same mechanisms as those discussed earlier in connection with laser beams.
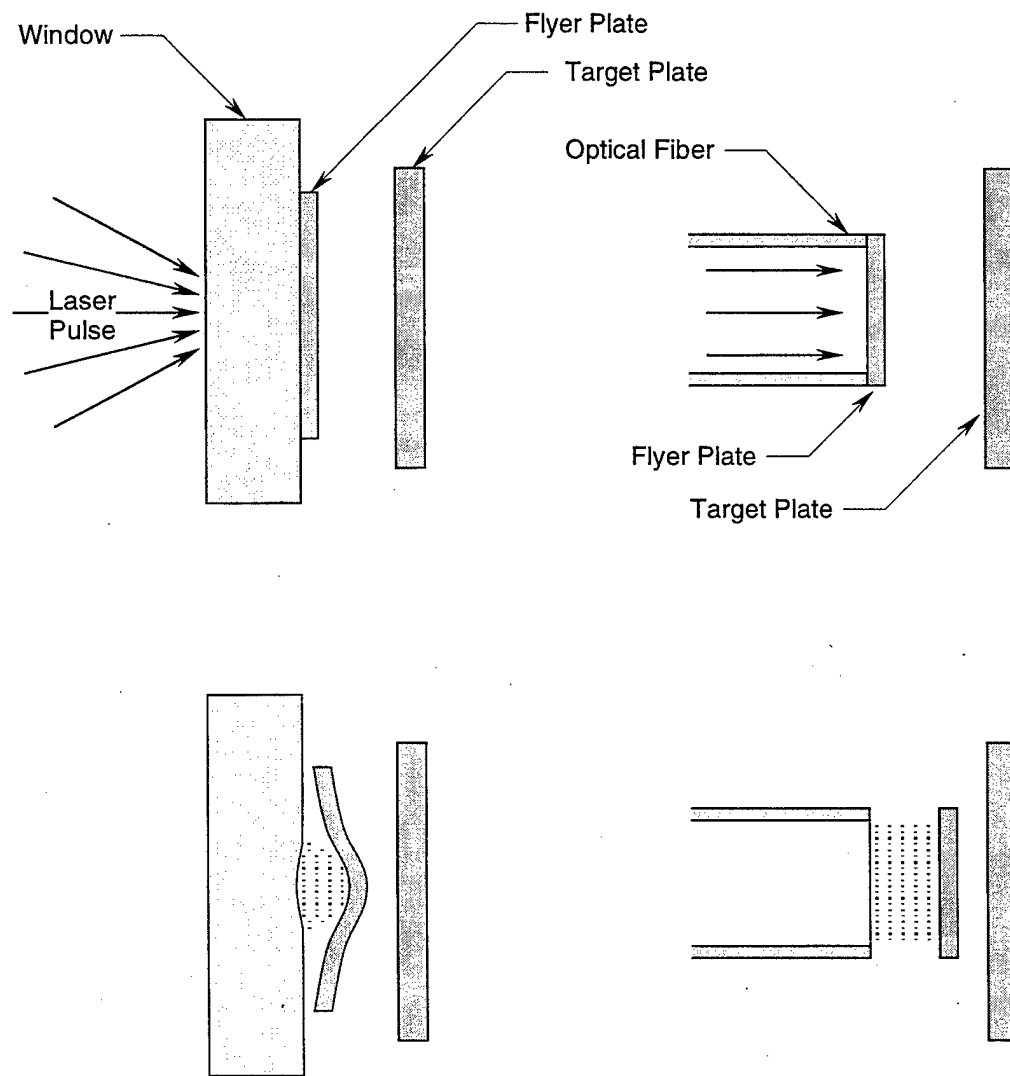
(a) Flyer plate backed by a transparent window.

(b) Flyer plate attached to the output end of an optical fiber.

Figure 4-11. The acceleration of foils by laser-induced plasma.
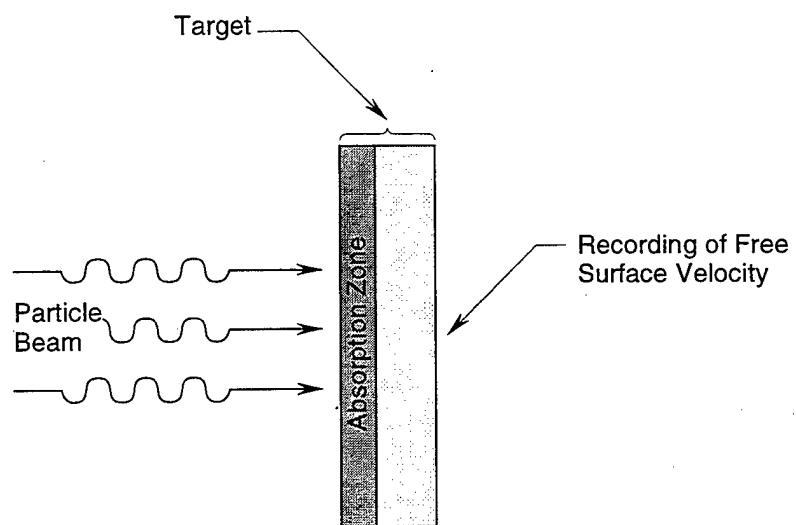
Figure 4-12. The acceleration of thin foils by electron or ion beams.

4.2 TECHNIQUES USED TO MEASURE SHOCK PARAMETERS.

Continuous measurements of the wave evolution inside a sample are needed to quantitatively characterize the mechanical properties of matter under shock wave loading conditions. Several techniques, using various physical principles, were developed during the early 1960s to provide direct time-resolved measurements of particle velocity or stress. This survey of these measurement techniques is not exhaustive, but it is comprehensive enough to provide a general view of the overall characteristics and the advantages and disadvantages of the methods currently used for shock wave diagnostics. Emphasis in this survey is placed on methods of measuring stress and particle velocity histories in shock-loaded specimens.

4.2.1 Methods for Measuring Particle Velocity Histories.

Methods for measuring particle velocity histories in shock wave experiments are based on fundamental physical laws. For this reason, these measurements have the advantage of not relying on any sensor calibrations. Modern methods of continuous time-resolved measurements of particle velocity include the capacitor gage, the electromagnetic gage, and laser Doppler techniques.

4.2.1.1 Capacitor Gage. The capacitor gage is used to record the motion of electrically conducting surfaces. This method of measuring free-surface velocity is illustrated in Figure 4-13. The measuring capacitor C_m consists of two parallel surfaces: the sample surface and a flat electrode with a distance x_o between them. An external voltage is applied to the capacitor via the resistor R_i, whose resistance is low enough to ensure that the time constant $R_i C_m$ is much less than the characteristic time of measurement. The guard ring ensures that the electric field is uniform over the region of the measuring electrode.

Motion of the free surface of the sample causes the capacitance of the gage to vary, and an electric current begins to flow through the gage circuit. This current is proportional to the rate of change of the capacitance, and ultimately, to the velocity of the free surface of the specimen, u_{fs}:

$$i(t) = U\frac{dC_m}{dt} = \frac{\varepsilon A U}{4\pi x^2(t)}\frac{dx}{dt} = \frac{\varepsilon A U}{4\pi x^2(t)}u_{fs} \qquad (4.8)$$

where U is the applied external voltage, ε is the dielectric constant, A is the area of the measuring electrode, and x, the distance between the plane electrodes at time t, is determined by integrating the current oscillogram $i(t)$. An example of a current oscillogram measured using a capacitor gage and the resulting particle velocity history are shown in Figure 4-14.

The capacitor gage method provides a noncontact measurement so that, in principle, its time resolution is limited only by the tilt of the shock wave with respect to the sample surface in the sensor-monitored
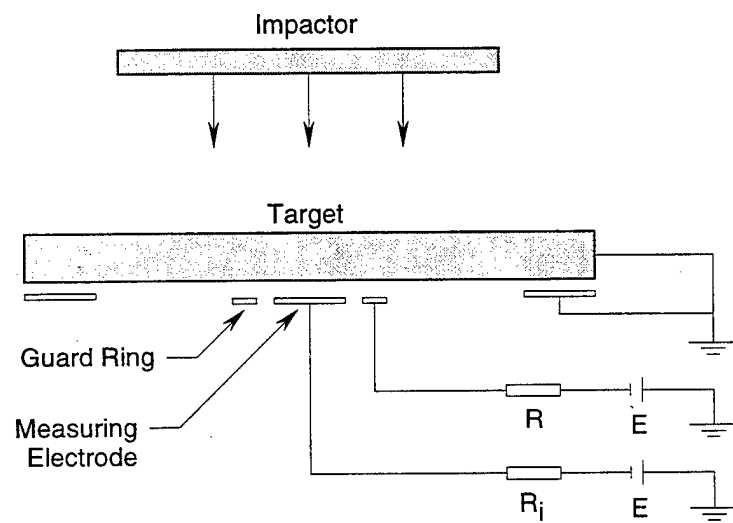
Figure 4-13. Capacitor gage for measuring free-surface velocity histories. The signal is recorded as a current in the resistor R.
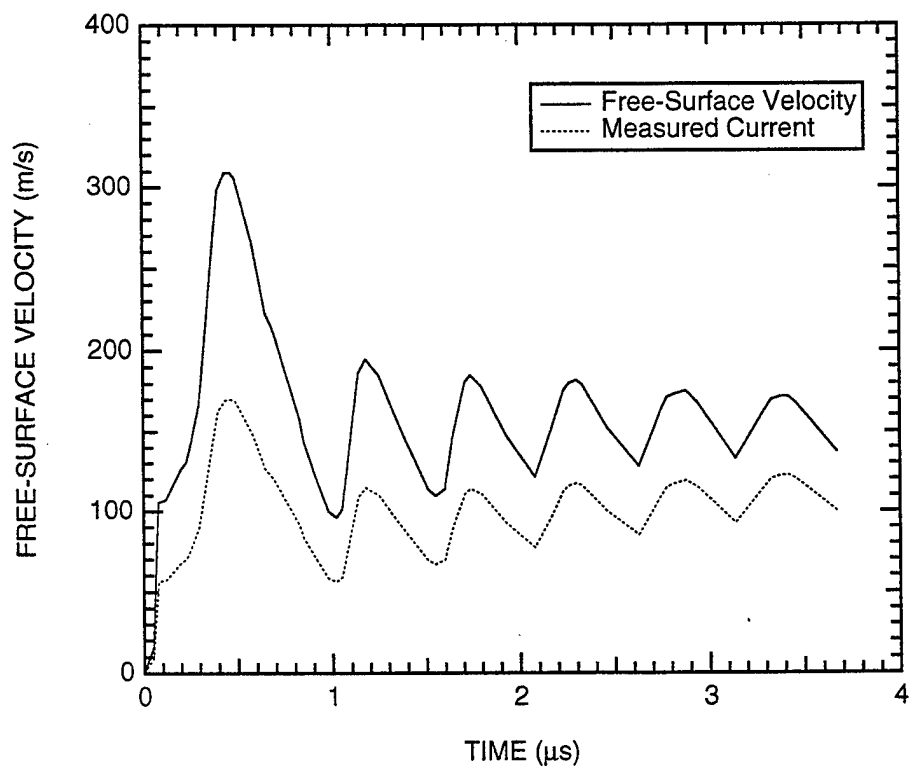
Figure 4-14.   An example application of the capacitor gage.

region. Depending on the required resolution and the duration of the event, the gage diameter and its initial distance from the sample surface, x_o, can be varied within 5 to 25 mm and 1 to 6 mm, respectively. The actual time resolution of a capacitor gage with a 5-mm electrode diameter is ~10 to 20 ns.

With a supply voltage of 3 kV, the signal typically is 1 to 100 mV. Because of this relatively low output, the capacitor gage is susceptible to electrical noise, which restricts its applications. Another limiting factor in the use of capacitor gages is that the nonlinearity of the registration causes the accuracy of the measurement to decrease at a large shift of the sample surface in the capacitor gap.

4.2.1.2 Electromagnetic Gage. The electromagnetic gage is used to record particle velocity profiles in dielectric materials. The technique is based on Faraday's law of induction, which asserts that the motion of a conductor of length $\vec{l}$, when placed in a magnetic field of intensity $\vec{B}$, generates an EMF, E, that is proportional to the velocity of the conductor $\vec{u}$, as given by relation

$$E = \vec{l} \cdot \left(\vec{u} \times \vec{B} \right) \tag{4.9}$$

The gate-shaped electromagnetic gage made of thin aluminum or copper foil is embedded in the interior of the sample. The whole experimental assembly is placed in a constant uniform magnetic field, such that the sensitive element of the gage is perpendicular to the magnetic lines and parallel to the shock wave front, as shown in Figure 4-15. Since the gage is embedded within the specimen, the velocity of the sensing element of the gage is equal to the particle velocity in the sample at the location of the gage. This velocity is simply given by,

$$u(t) = \frac{E(t)}{lB} \tag{4.10}$$

4.2.1.3 Laser Velocimeter. The spatial resolution of the two velocity measurement techniques described above is limited by the size of the sensing element of the gage. At best, this amounts to a few millimeters in the plane of the wave front. Since some tilt between the shock front and the gage plane almost always exists, the finite dimensions of the gage sensor also limit the time resolution of measurements. Laser methods of recording the motion of free and contact surfaces offer much higher resolution in space and in time.

Laser velocimeters use Doppler-shifted light reflected from the target surface. Since the Doppler shift is very small for velocities of ~1000 m/s (the wavelength shift is ~10^{-2} è), it must be recorded using two-beam or multiple-beam interferometry. The measurements thus become differential, and this provides a significant increase in their accuracy. Interferometers have become standard devices used by shock
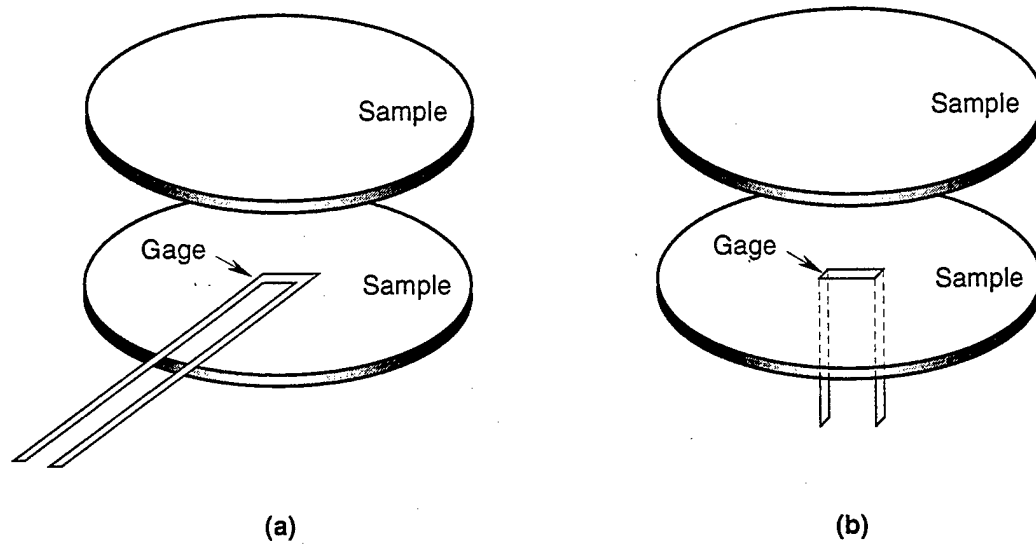
Figure 4-15. Typical electromagnetic particle velocity gage configurations.

wave physicists to measure velocity histories. The laser techniques have such high space resolution because the laser beam is focused down to a spot ~0.1 mm in diameter on the target surface.

Figure 4-16 illustrates the two-beam laser Doppler velocimeter VISAR (Barker and Hollenbach, 1972; Asay and Barker, 1974). In this system, the reflected beam is split equally into two beams to form the two legs of a wide-angle Michelson interferometer. In the interferometer, one leg is delayed in time by a period, Δt, with respect to the other. The operation relies on the periodic variation in time (fringes) of the radiation intensity due to interference between two light beams of slightly different wavelengths. In the velocimeter, interference fringes result from the interaction between light beams reflected from a moving surface at different instants of time. If the velocity of the reflecting surface varies with a time, the Doppler shift for the two beams will be different because of the time difference. The frequency of the fringes recorded by photodetectors is proportional to the acceleration of the reflecting surface and the delay time Δt.

Glass etalons or a lens system can be used to introduce a temporal delay in the delay leg of the interferometer. The apparent optical path length of the two legs is maintained the same, whereas the geometric paths are different. In the case of a solid etalon, the geometrical difference is given by

$$\Delta l = l_d(1 - 1/n) \tag{4.11}$$

where l_d and n are the length and refractive index of the delay line. The delay time is then given by

$$\Delta t = \frac{2l_d}{c}(n - 1/n) \tag{4.12}$$

where c is the velocity of light under vacuum.

When the lens combination is used for delay, the delay time Δt is given by the following relation:

$$\Delta t = 2l_d / c \tag{4.13}$$

Because of the apparent optical symmetry of the interferometer, a coincidence of wave fronts of superimposed beams is reached, and as a result, the technique can operate with both specular and diffuse reflecting surfaces.

When two beams are superimposed, fringes, $F(t)$, are produced in the interferometer and are related to the change in velocity of the reflecting surface, $u(t)$, by the following relation (Barker and Hollenbach, 1970; Barker and Schuler, 1974):

$$u(t - \Delta t/2) = \frac{\lambda}{2\Delta t} \frac{F(t)}{(1 + \delta)(1 + \Delta v/v)} \tag{4.14}$$
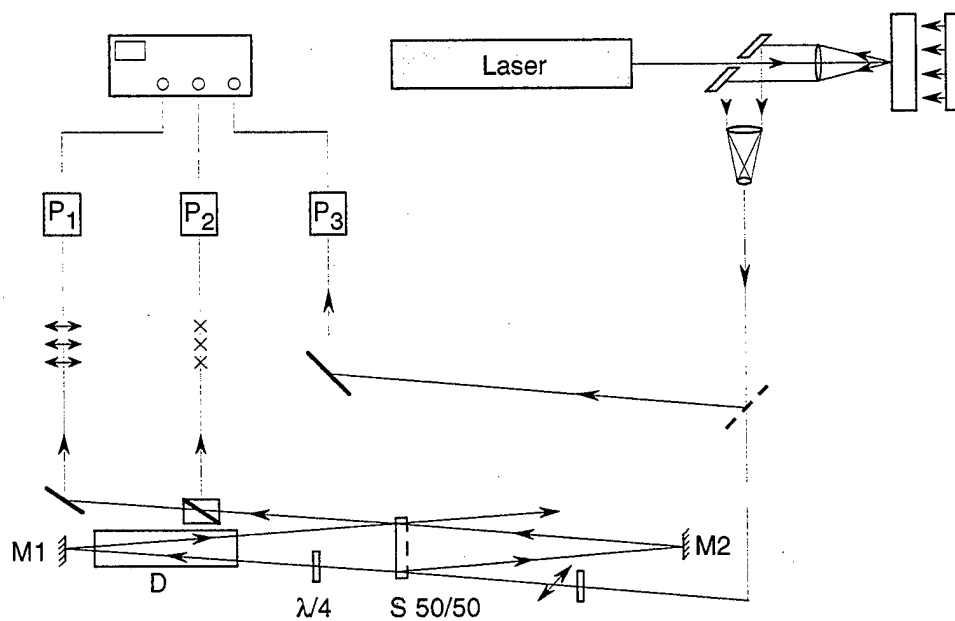
Figure 4-16. Schematic of a two-beam laser Doppler velocimeter (VISAR).

where λ is the wavelength of the light used, and δ is a correction term that accounts for the dependence of the refractive index of the etalon material on wavelength, given by

$$\delta = \begin{cases} \dfrac{n}{n^2-1}\lambda\dfrac{dn}{d\lambda} & \text{for the etalon} \\ \\ 0 & \text{for the lens combination} \end{cases} \tag{4.15}$$

The optical correction term $\Delta v / v$ is incorporated in Eq. (4.14) for measurement at an interface between the target and transparent window. The correction results from the change in refractive index of the window material with shock stress (Barker and Hollenbach, 1970).

In the VISAR, quadrature coding has been included to distinguish between acceleration and deceleration and to improve fringe resolution. This coding is accomplished by adding a quarter-wave retardation plate and a polarization beam splitter to provide a 90° out-of-phase shift between the two fringe signals. Two independent detectors are used to record the fringes in the two polarization components. Any change in the sign of acceleration will thus be recorded by at least one of the photodetectors as a "turn point" of oscillations in the interferogram. Fringes in the interferograms are related to the velocity of the reflecting surface by a simple sine expression. The instantaneous velocity therefore can be found from experimental interferograms, either discretely (by counting the number of fringes) or by measuring within individual fringes. The complete analysis of VISAR data for many time points is sophisticated and usually requires computer. The accuracy of the velocity measurements with VISAR is ~1%-2% or less; the time resolution can reach ~2 ns.

Limitations on the time resolution of VISAR measurements are associated mainly with a limited bandwidth of the oscilloscope, photodetectors, and other recording equipment. The optically recording velocity interferometer system (ORVIS) uses a high-speed electronic streak camera to record interference fringes, which improves the time resolution of the measurement to ~200 ps (Bloomquist and Sheffield, 1983). Compared with the VISAR, the ORVIS system is adjusted so that the recombining beams are at a small angle φ to each other, and the resulting pattern has a fringe separation $d = \lambda / \sin\varphi$. When the reflecting surface is at rest, the phase difference of the two beams is constant and hence the fringes are at rest. As the surface moves, the Doppler shift causes the phase difference to change and thus the fringes to shift. A streak record of the fringe pattern that is changing position in time directly yields the time history of the surface velocity. The shift is proportional to the velocity so that shift value d corresponds, as before, to the velocity increment $u_0 = \lambda / 2\Delta t (1 + \delta)(1 + \Delta v / v)$. Compared with VISAR, ORVIS provides a higher temporal resolution, but a slightly less accurate velocity measurement.

Standard multibeam Fabry-Perot interferometers are also used as an element of the laser Doppler velocimeter (Johnson and Burgess, 1968; Durand et al., 1977). A fringe pattern in this case is also

106

recorded by the streak camera. As the frequency of the light from the moving target surface changes, the fringe diameter changes from its incident static value, D_1, to a new value, D_1'. The velocity of the moving surface is then calculated using the relation

$$u(t) = \frac{c\lambda}{4L}\left(\frac{(D_1'^2 - D_1^2)}{(D_2^2 - D_1^2)} + m\right)$$

(4.16)

where L is the distance between the plates of the Fabry-Perot interferometer, D_2 is the static diameter of the next fringe, and m is an integer. The precision of the system can be varied over the range of 0.1% to 2% and is determined by the spacing between the Fabry-Perot plates, the number of fringe jumps inserted, and the lens system. The time resolution of such velocimeters is determined by the photon fill time of the Fabry-Perot plates and is typically lower than that of VISAR and ORVIS.

In 1986, Gidon and Behar used a Fabry-Perot interferometer to measure velocity over an entire surface. In this modification, the velocity at many points for a single time is measured instead of the velocity history at a single point. Mathews et al. (1992) developed the experimental and analytical methods to make this full-field Fabry-Perot interferometer a practical diagnostic tool. Using a framing camera provides a time history of a velocity over a moving surface. A line-imaging VISAR was constructed by Hemsing et al. (1992) to measure many velocity histories simultaneously along the line on the target surface. Both versions (Mathews et al., 1992, and Hemsing et al., 1992) use a dye amplifier that provides 600-W single-frequency power starting from a standard argon-ion laser. Baumung et al. (1994) modified the optical scheme of the VISAR/ORVIS velocimeter to allow for illumination of a line on the target surface and for measurement of the velocity history along this line with a standard argon ion laser and streak camera.

4.2.2 Methods for Measuring Stress Histories.

Sensors used to measure stress histories in shock loaded specimens include manganin, ytterbium, and carbon piezoresistance gages; dielectric gages; and quartz and $PVDF_2$ ferroelectric gages. Unlike particle velocity gages, which do not require sensor calibration, all stress gages require calibration so that their output can be related to stress in the specimen. The subject of stress sensor calibration for shock wave studies has received significant attention over the past three decades. Here, we limit our discussion to manganin gages, the most widely used gages for performing in-material stress measurements in planar shock wave studies.

The use of manganin gages in uniaxial strain shock wave experiments is illustrated in Figure 4-17. The gage consists of a 10- to 30-μm-thick grid arranged in a zigzagging pattern. The gage is embedded in the specimen such that the active gage element is normal to the direction of wave propagation. The gage

107
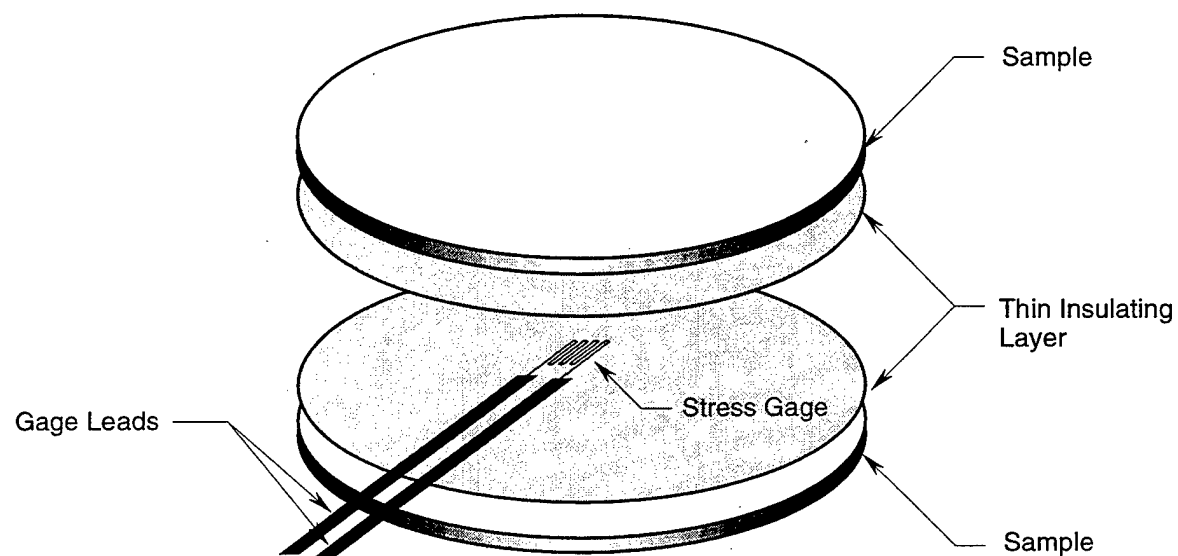
Figuire 4-17.   Typical manganin stress gage configuration.

is electrically isolated from the specimen by a thin layer of Kapton, Mylar, Teflon, or mica. A constant electrical current is passed through the gage. When a shock pulse passes through the gage plane, the recorded voltage increases with pressure applied to the gage. To increase the precision of the pressure measurements, a resistance bridge is used to eliminate the d.c. component of the signal, defined by the initial resistance of the sensor.

Manganin was first used by Bridgman (1911, 1940) as a pressure sensor under static loading conditions. Bridgman found that the resistivity of the manganin alloy increases with increasing pressure and is relatively insensitive to changes in ambient temperature. Fuller and Price (1964) and Bernstein and Keough (1964) used manganin gages for pressure measurements in plane shock wave experiments. Since then, several investigators have contributed to the understanding and calibration of the piezoresistance response of manganin under shock wave loading conditions, including Chen et al. (1984), DeCarli (1976), Gupta and Gupta (1987), Kanel et al. (1978), Lee (1973), and Postnov (1980).

The intended purpose of a manganin stress gage is to measure the stress normal to the direction of shock wave propagation. In reality, piezoresistive materials like manganin are also sensitive to straining. Thus, the sensor responds to both stress as well as strain, and it is important to be able to separate the stress component of the measured resistivity change from the strain component to obtain accurate stress measurements. For this reason, independent strain measurements are necessary when dimensional changes in the gage are not negligible (e.g., Dremin et al., 1972; Kanel and Molodets, 1976), such as might be expected in divergent flow situations. Simultaneous stress and strain measurements are now routinely used in the flatpack series of armored stress gages used for measuring stresses in large-scale dynamic experiments in geologic materials (e.g., Keough et al., 1993).

If the change in resistivity and the strain in a manganin gage are both measured, the stress normal to the gage can be determined uniquely and accurately by using a generalized calibration model for manganin such as that proposed by Gupta (1983), provided that the model parameters are calibrated for the particular grade of manganin used in the stress sensor and that the strain contribution is smaller than the stress contribution. In practice, it is desirable to maximize the stress contribution and minimize the strain contribution of the sensor.

A simpler approach can be used to calibrate manganin sensors for shock wave experiments. In this case, one takes advantage of the fact that the experiments are conducted under uniaxial strain conditions. Thus, the calibration of the gage becomes a one-dimensional problem involving only the stress component normal to the sensing element of the gage. The procedure for calibrating the manganin gage in this case involves measuring the fractional change in resistance of the active gage element, $\Delta R / R_0$, in a well-controlled uniaxial strain shock wave experiment and correlating the measured resistance change to the stress in the material at the location of the gage, determined through some other means. Repeating

this procedure at several stress levels shows a relationship between the change in resistance of the gage and the stress component normal to the gage. For manganin, this relationship is shown in Figure 4-18.

Special measurements (Kanel et al., 1978) have shown that, at pressures above 7-10 GPa, the change in the resistivity of manganin is reversible and does not depend on whether dynamic compression occurs by single or multiple shocks (i.e., quasi-isentropic behavior). Chen et al. (1984) also found the resistivity of manganin to be history-independent. These findings are important because they imply that the resistivity of manganin can be uniquely related to stress at any instant during shock deformation, regardless of the history of deformation. Therefore, the manganin gage can be used to measure stress in experiments involving multiple wave structures such as those encountered during plastic flow, phase transition, or fracture.

The release to zero pressure from a shock compressed state produces slight hysteresis in the gage resistance. This irreversible component is attributed to dimensional changes and strain hardening of the gage during shock compression and possibly to residual stresses in the matrix material. The residual resistance is small, usually 2%-2.5%. Below 7 GPa, the residual increment of the resistance is nearly proportional to the peak pressure and can easily be taken into account during interpretation of low-pressure measurements.

4.3 FRACTURE EXPERIMENTAL PROCEDURES.

Flyer plate impact tests have been conducted (e.g., Barbee et al., 1972; Curran et al., 1987) with targets of a ductile metal such as aluminum or copper to obtain incipient spall damage at approximately the midplane of the target plate. Two types of data are taken from the impacts. First, the targets are recovered and examined metallographically for damage. Second, stress measurements are made to determine the shape of the stress waves that have been modified by the development of damage. The experimental arrangement is outlined first below, then typical results of the metallographic examination are given, and finally some stress gage records are examined.

4.3.1 Experimental Techniques.

A light-gas gun is used to accelerate projectile plates to desired velocities. The experimental arrangement with the projectile and flyer at the muzzle of the gun near the point of impact with a target was shown earlier in Figure 4-9. Spallation experiments are usually performed with the projectile plate (flyer) of the same material as the target specimen: this symmetry helps ensure an accurate stress calculation. To achieve tensile pulses on the order of one microsecond, projectile plates are about 0.5 to 5 mm thick and target plates are about twice as thick. Projectile and target plates are ground to a surface finish of 5 μm rms and parallel to within about 1 μm to provide appropriate simultaneity of impact over
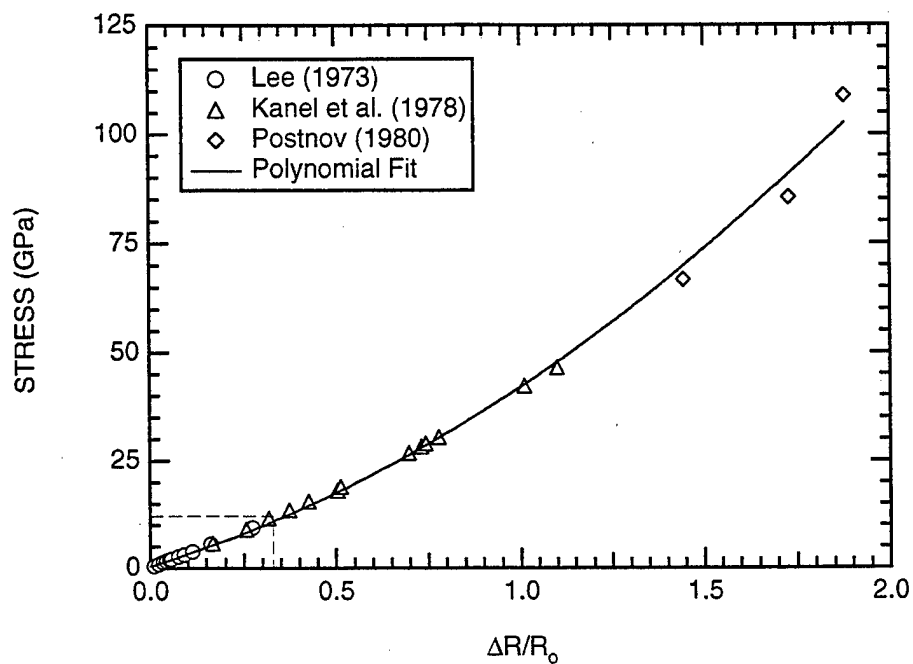
(a) Calibration curve up to 125 GPa.
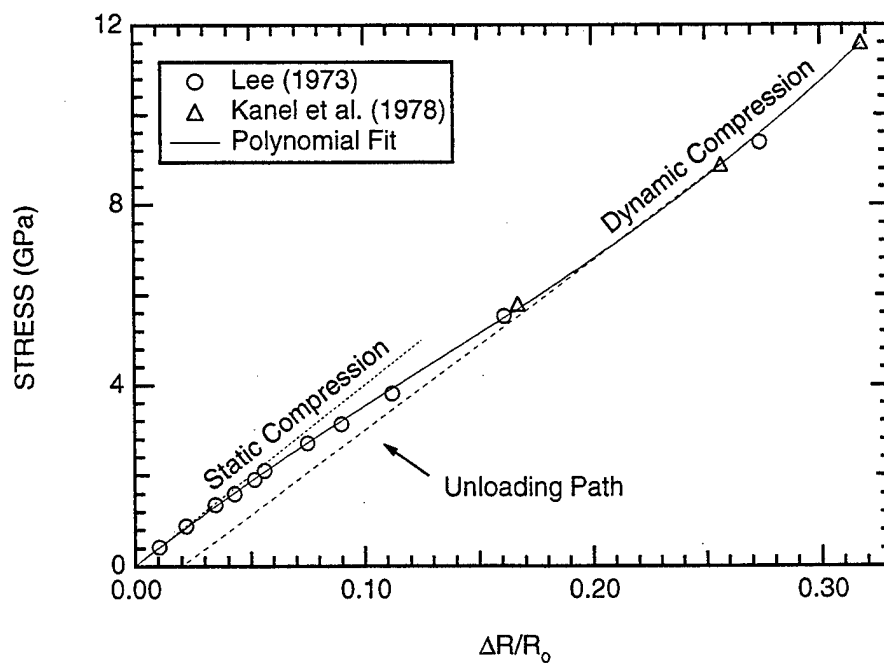
(b) Calibration curve up to 12 GPa.

Figure 4-18. Calibration curves for the manganin stress gage.

the faces of the two plates. The flyer and target thicknesses may be varied to provide a range of stress durations in the targets.

Two target designs used in these measurements are shown in Figure 4-19. In both designs, a plug with a taper (8 degrees is appropriate) is fitted into the rest of the target plate as shown. Following the initial compressive pulse during the impact, this plug separates from the rest of the target and is caught in a soft material to avoid further damage. The target plugs are then sectioned along a diameter, and the cut surface is polished and etched for metallographic examination.

Stress measurements are made using manganin or ytterbium piezoresistive stress gages (or other well-calibrated gages) mounted in a buffer material such as epoxy at the back surface of the target samples.

4.3.2 Metallographic Observations of Shocked Specimens.

Metallographic observations are made on the polished and etched cross sections of the target samples. A collection of photomicrographs of such cross sections is shown in Figure 4-20 for samples of 1145 aluminum tested with the same plate thicknesses—only the impact velocity was varied. The samples are arranged in order of increasing velocity (and therefore, increasing tensile stress) and also evidently in order of increasing damage. Damage is in the form of individually nucleated spherical voids which grow and coalesce to induce failure.

Four characteristics are apparent from these photomicrographs. First, the observed microdamage features (voids) have a circular cross section in the plane view. These cross sections are, in fact, sections through spherical voids. That the voids were spherical was verified by sectioning the samples normal to the direction of shock propagation. Circular cross sections were observed on these normal planes also. Second, the voids are distributed over some central region of the plate: there is no narrowly defined spall plane. Rather there is a narrow vertical region of maximum damage; then the numbers and sizes of voids decrease with distance away from this region on either side. From simulations of these experiments with a simple elastic-plastic model, we determined that the expected location of the spall plane (location for first occurrence of tensile stress) falls in the region of maximum damage. Third, there is a range of sizes of voids within regions with the same shock history. Fourth, at higher damage levels the interaction of the growing voids leads to the formation of large crack-like defects and finally to full separation (as seen in Figure 4-21).

Observations of full-spall samples have supplied further insights into the failure of these ductile materials. The opening of a crack resulting from void coalescence is shown in Figure 4-21(a). The tip domain [Figure 4-21(b)] shows the region of the material corresponding to full failure or approaching full failure. Near points labeled A in Figure 4-21(b), separation has occurred by elongation of voids and

REAR VIEW   **SIDE VIEW**

(a) Instrumented assembly

Manganin Pressure Transducer (or Optical Prism)

102 mm

25 mm

6 mm

Tilt Pins

(b) Uninstrumented assembly

38 mm

102 mm

6 mm
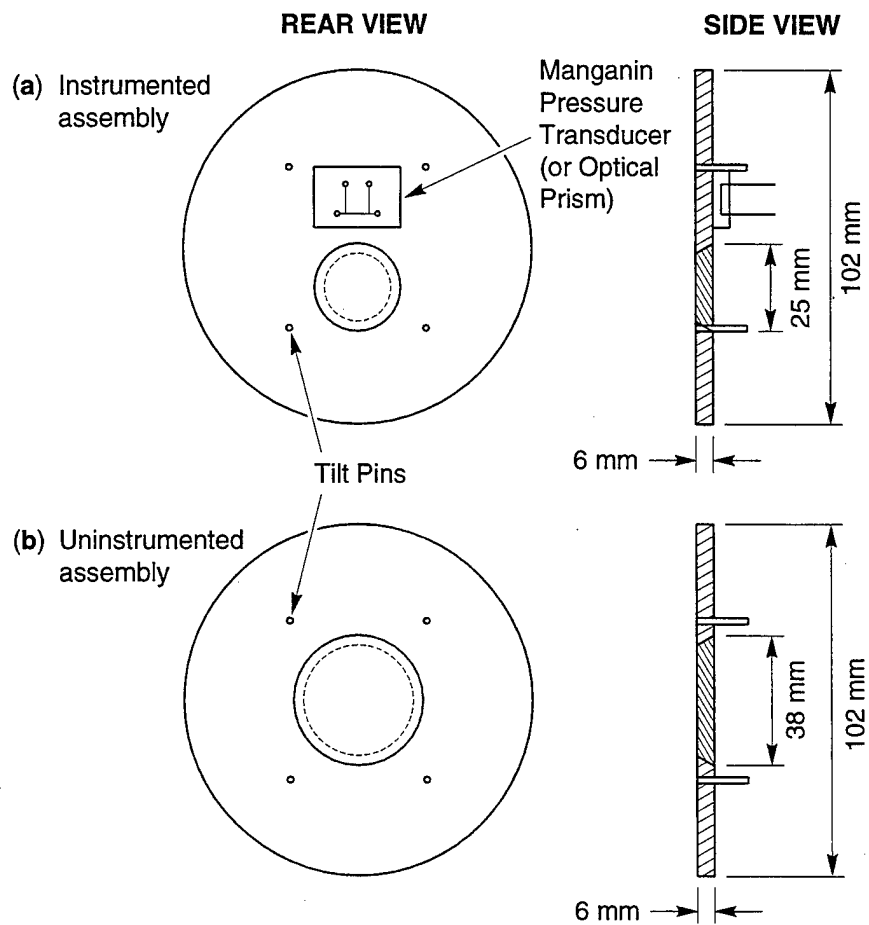
Figure 4-19. Target plate assembly showing tapered specimen (Barbee et al., 1970).

113
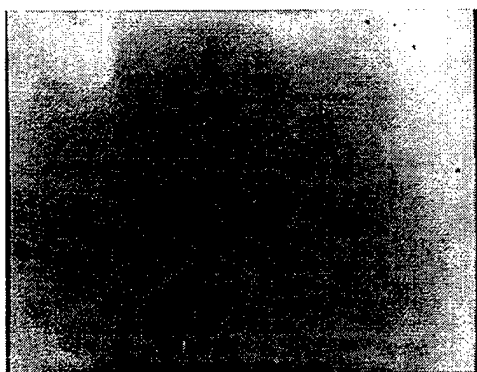
Impact Velocity — 128.9 m/s
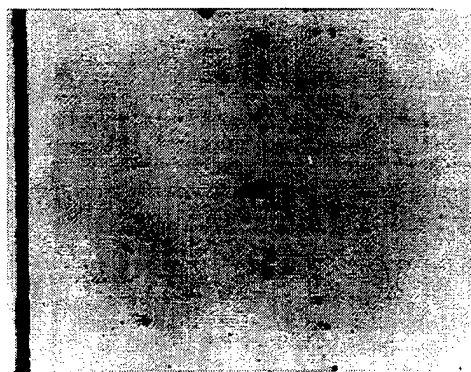
Impact Velocity — 132.0 m/s
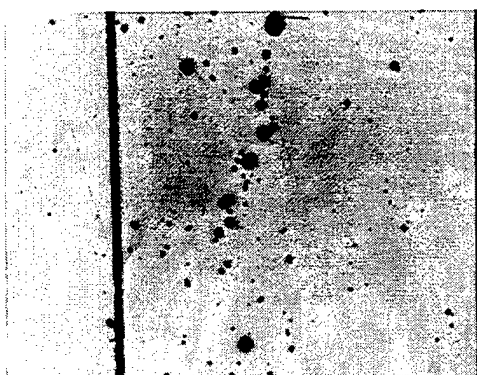
Impact Velocity — 142.7 m/s
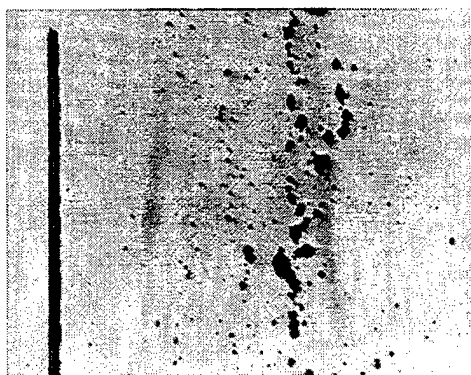
Impact Velocity — 154.2 m/s

200 μm
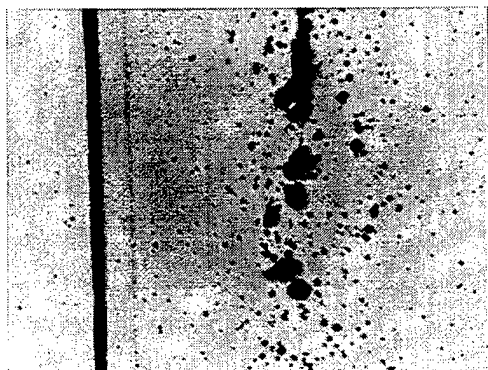
Impact Velocity — 203.6 m/s

Figure 4-20. Damage observed in 1145 aluminum for a constant shot geometry
(i.e., time at stress) for increasing impact velocities (i.e., stress).

More voids and larger sizes result from increasing impact velocities.
Projectile thickness is 0.236 cm, sample thickness is 0.635 cm
(Barbee et al., 1970).

114

500 μm

(a)

50 μm

(b)
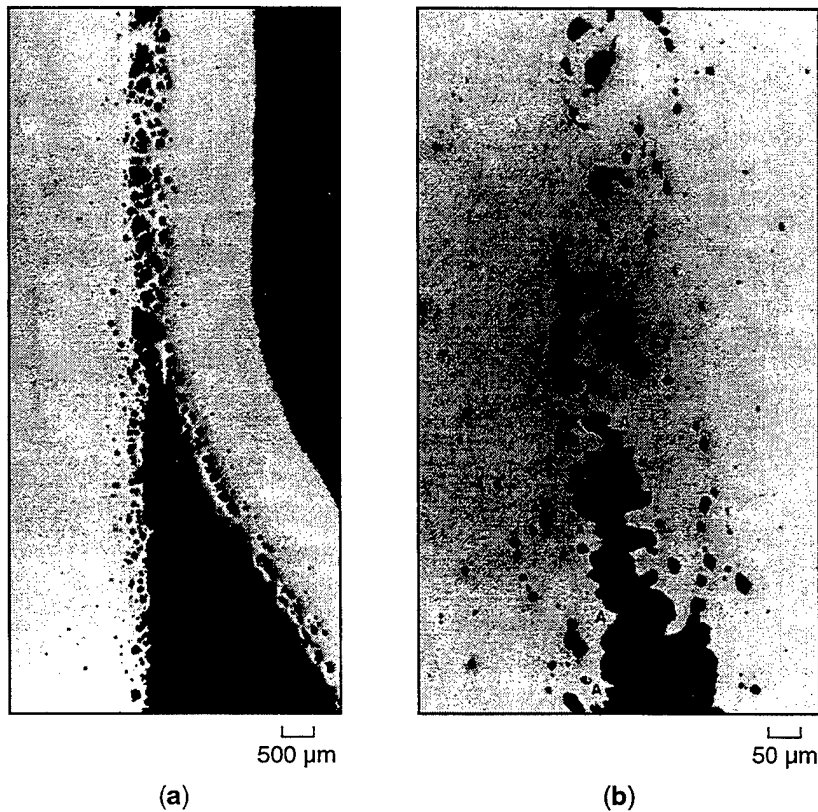
Figure 4-21. Ductile cracks.

(a) Ductile crack propagation by void coalescence. (b) Tip of ductile crack shown in (a) at higher magnification. Material failure by void coalescence due to necking of the regions separating the voids is apparent near points A (Barbee et al., 1970).

115

necking of the regions separating them. The necked regions have failed by fully ductile, knife-edge fracture under essentially uniaxial stress conditions.

4.3.3 Stress Measurements Behind Fracturing Samples.

The objective of stress measurements in the impact experiments is to detect the recompression wave (or fracture signal) resulting from the development of damage. Some manganin gage records from impacts in 1145 aluminum are presented in Figure 4-22. The important parts of these records are the recompression pulses (indicated with arrows) observed before the full release of the initial compression wave is attained.

The occurrence of the fracture signal can be explained qualitatively with the aid of the distance-time diagram in Figure 4-23(a). Along the distance (x) coordinate are the three plates: flyer, target, and epoxy buffer. The lines show the propagation of waves within these plates as a function of position and time. Initially, compression waves leave point 0 traveling left into the flyer and right into the target, creating a compressive stress level C. At point 6 at the free surface of the flyer, the wave (0-6) is fully reflected as a rarefaction, which moves along the path 6-2-3.

The compression wave (0-1) propagating into the target is partially transmitted into the epoxy (the epoxy has lower impedance than the aluminum) and partially reflected as a rarefaction wave back into the target. The transmitted wave has an amplitude C_1, which is less than C. The rarefaction from point 1 proceeds along 1-2, meeting the rarefaction from point 6, and causing tensile stresses in the region above the broken line 7-2-3. Point 2 then defines the plane of first tension and therefore the x-location of the spall plane.

When the rarefaction from point 6 reaches the epoxy at point 3, a partial rarefaction is transmitted back into the target, reducing the stress to a level C_2. For this diagram, we presume that the developing damage first becomes important at point 4 (at the same position as 2, but at some later time). The tensile stress reduction caused by the developing damage produces recompression waves propagating along the lines 4-8 and 4-5. At point 5, the recompression wave is partially transmitted into the epoxy, bringing the stress up to C_3.

The history of these stresses at the target-epoxy interface is shown in Figure 4-23(b). The amplitude of the fracture signal (the difference between stress levels C_3 and C_2) depends on the strength of the recompression wave and hence on the amount of damage. The time between the main wave and the fracture signal is governed by the rate at which the damage develops in the target.
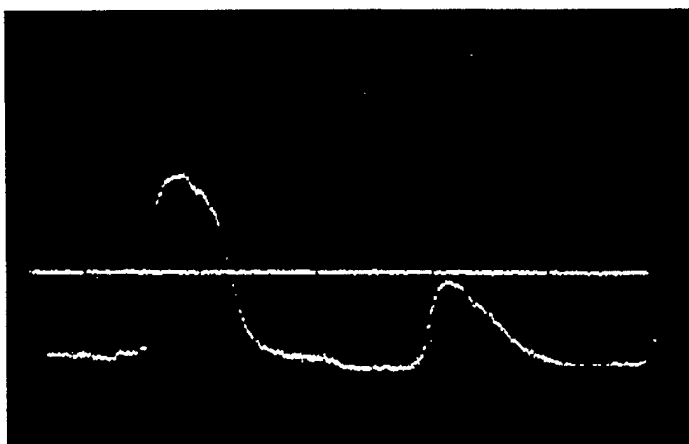
(a) Manganin gage records for typical low-damage or no damage response.
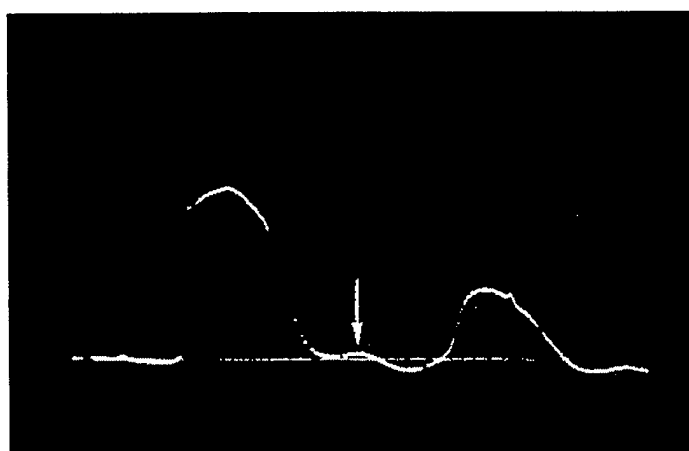
(b) Manganin gage record showing for fracture signal (arrow) arising from damage at spall plane.
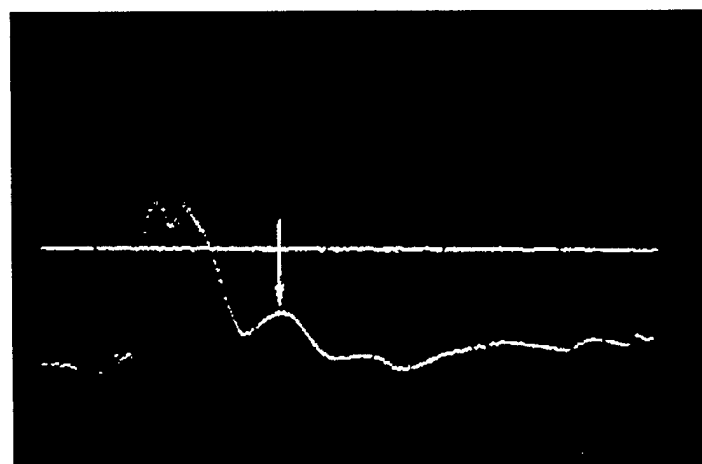
(c) Manganin gage records showing a strong fracture signal (arrow), indicating high damage. No ringing is observed, indicating fracture has suppressed later loading.

Figure 4-22. Fracture signals observed in manganin gage records (Barbee et al., 1970).
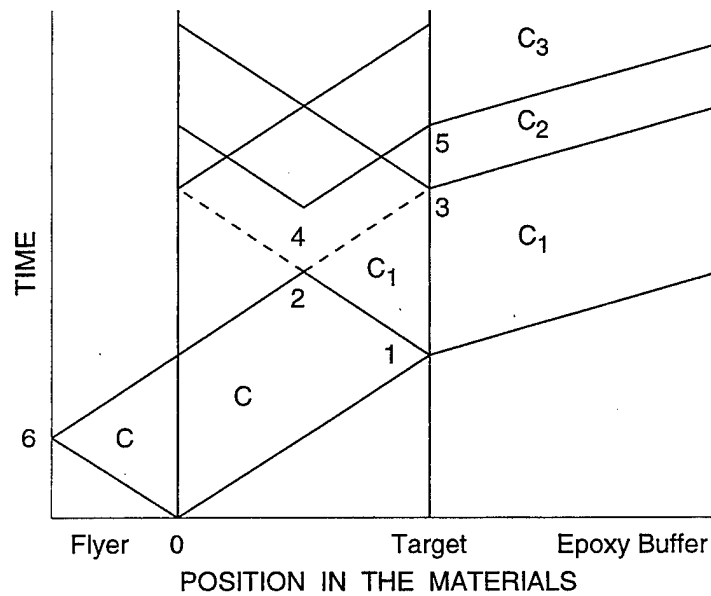
(a) Distance–time diagram for waves resulting from impacting an aluminum flyer onto an aluminum target backed by a thick epoxy plate.
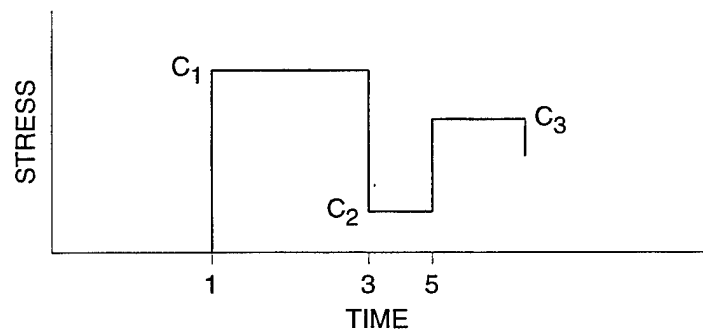
(b) Stress history at the interface of the aluminum target and epoxy buffer.

Figure 4-23. Effect of damage on stress history at spall plane (C_1 = 820 MPa) (Barbee et al., 1970).

118

Hence, the fracture signal can be used to guide us in understanding several aspects of the damage process. Measured fracture signals are important for verifying models developed to account for the effect of void or crack growth on the applied stress history because these signals are directly related to the rates at which the fracture processes are occurring.

SECTION 5

ESTIMATING SPALL STRESSES FROM EXPERIMENTAL DATA

All methods of measuring the dynamic tensile stress in materials during spalling are indirect, because it is impossible to introduce a sensor into a sample without influencing the resistance of the sample to tensile stresses. Each of the indirect methods uses a different approach to determine the dynamic tensile stress, and sometimes large discrepancies are obtained using different methods. This section describes the various methods for determining the spall threshold and explores the advantages and limitations of each method. Emphasis is placed on fracture stress determination using measurements of the free-surface velocity histories, with and without soft barriers. These methods are emphasized because they were used in obtaining most of the spall data presented later in this report.

5.1 WAVE INTERACTIONS DURING SPALL.

Measurements of spall strength are based on analysis of the one-dimensional motion of compressible, continuous, condensed media following the reflection of a shock pulse from the surface of the body. Figure 5-1 illustrates the dynamics of wave interactions during the reflection of a triangular shock pulse from the free surface of a body under uniaxial strain conditions. Figure 5-1(a) shows the triangular loading stress history. This stress history is typical of what might be expected when an explosive is detonated in contact with the front surface of the specimen. This stress history comprises an initial peak, associated with the detonation pressure (also known as the Chapman-Jouguet or CJ pressure), followed by a gradual decay caused by the release wave emanating from the expanding explosive gases. This release wave is commonly known as the "Taylor wave" after G. I. Taylor (1950), who first developed a theory to describe the flow that connects the CJ point to the final state in the expanded reacted gases.

In the x-t diagram of Figure 5-1(b), the shock front trajectory is described by the line oo'. A family of C_+ characteristics represents the unloading wave overtaking the shock front. One of these characteristics is shown to intersect the shock trajectory at point o'. Note that, in Figure 5-1(b), each unloading wavelet is represented by a single characteristic line that is a member of a fan of characteristics. When the shock front reaches the free surface at o', the free-surface velocity undergoes a jump from zero up to $u_o = 2u_s$, where u_s is the particle velocity behind the shock front. The unloading wave behind the shock front causes a decay in the free-surface velocity as shown in Figure 5-1(d). Thus, initially (i.e., before fracture), the particle velocity history has the same triangular shape as the stress history.

120
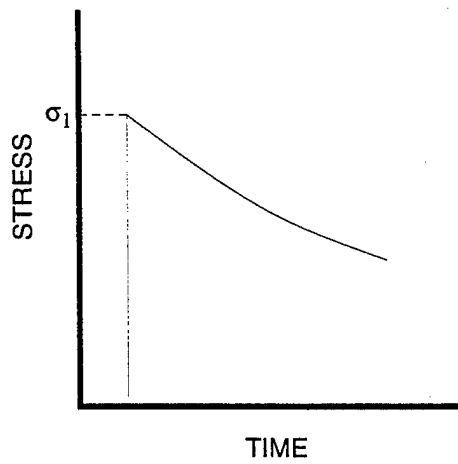
(a) Loading stress history.
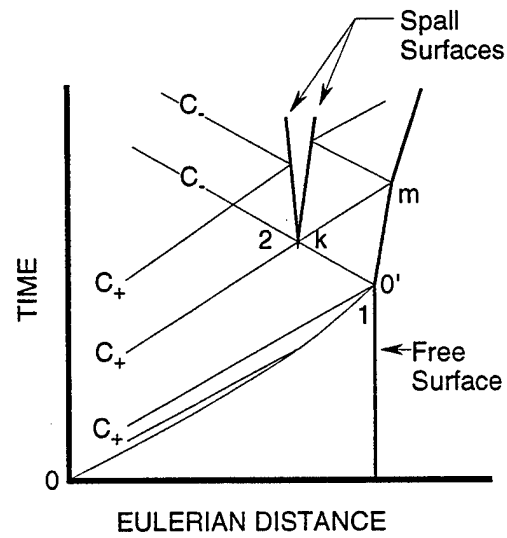
(b) Distance-time diagram showing trajectories of loading and unloading waves.
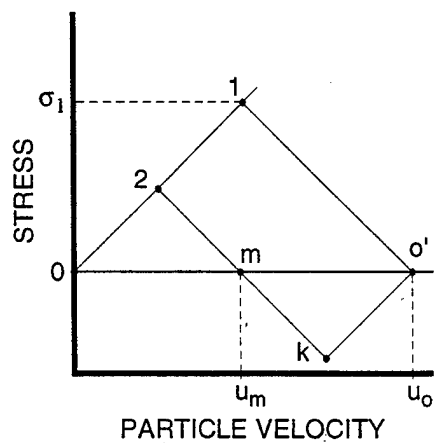
(c) Stress-particle velocity diagram.
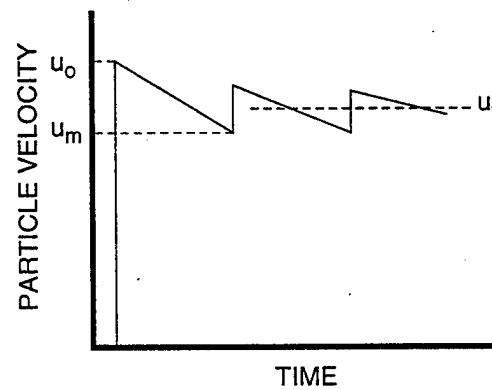
(d) Free-surface velocity history.

Figure 5-1.   Wave interaction diagrams for the reflection of a triangular shock pulse (like that caused by an explosion) from a free-surface and formation of a fracture plane.

121

At the free surface of the specimen, the shock wave is reflected as a centered unloading wave that travels backward toward the interior of the sample. This rarefaction wave is represented by the left-going C_- characteristic emanating from point o'. Here too each C_- characteristic is a member of a rarefaction fan centered at o'. The state of particles must satisfy conditions on both the C_+ and C_- characteristics and is determined in the σ-u diagram of Figure 5-1(c) by the intersection of Riemann trajectories describing states of matter along the C_+ and C_- characteristics that pass through the particle at any given time.

The maximum tensile stress is reached at each particle position as it is traversed by the terminal C_- characteristic of the centered rarefaction wave emanating from point o' on the back surface of the specimen. Therefore, the peak tensile stress at the spall plane just before fracture corresponds to the intersection of trajectories $o'k$ and $2k$ in the σ-u plane of Figure 5-1(c). Line $o'k$ describes the change of state along the tail C_- characteristic of the centered rarefaction wave; line $2k$ represents the trajectory of the change of state along the last of the C_+ characteristics of the incident wave crossing the spall plane before the fracture.

Fracture of the material at the spall plane causes the tensile stress to decrease rapidly to zero. As a result, a compression wave forms in the material adjacent to the spall plane. This wave propagates to the left and right away from the spall zone. At the rear surface of the specimen, where the free-surface velocity, u_{fs}, is usually measured, this compression wave is manifested as a jump in velocity from u_m to some higher velocity. This signature of spall damage is referred to as the spall pulse. When the material spalls, a stress wave becomes trapped between the spall plane and the rear surface of the specimen. Later reverberations of this stress wave lead to the damped oscillations observed in the particle velocity record in Figure 5-1(d). The period of these oscillations can be used to determine the thickness of the spalled layer.

5.2 DETERMINING FRACTURING STRESS USING MEASUREMENTS OF THE FREE-SURFACE VELOCITY HISTORY.

The available methods for measuring the free-surface velocity of the sample during a spall experiment were discussed in Section 4. Here, we focus attention on the analysis techniques used to determine the dynamic fracture stress based on the measurement of free-surface velocity histories.

The peak free-surface velocity, u_o, and the free-surface velocity just before the arrival of the spall pulse, u_m, are determined directly from the free-surface velocity profile. The tensile stress value just before spalling, σ^*, is then determined by the intersection of Riemann trajectories passing through the points $(\sigma = 0,\ u = u_o)$ for C_- and $(\sigma = 0,\ u = u_m)$ for C_+. Within the acoustic approach, the following linear approximation (e.g., Novikov et al., 1966) is used

122

$$\sigma^* = \frac{1}{2}\rho_o c_o \Delta u_{fs} \tag{5.1}$$

where $\Delta u_{fs} = u_o - u_m$ is the so-called "velocity pullback." Dynamic measurements of the spall strength are based on measurements of the velocity pullback. Equation (5.1) provides reasonable estimates of the fracture stress as long as the density and wave speed in the material are close to their original values, ρ_o and c_o. With increasing tensile stress, this condition becomes less and less accurate, and a knowledge of the compressibility of the material under tension becomes necessary. Generally, however, we have no direct knowledge of the pressure-volume curve in the tensile region except by extrapolation from quasi-static data or by extrapolation from compressed states under dynamic loading. If we extrapolate the pressure-volume relationship from the compression region, we neglect the effect of the developing damage on the compressibility of the material. Extrapolation in the p-u space provides more realistic estimates. If we extrapolate the material isentrope (in the p-u plane) into the negative pressure (i.e., tension) region, we find that the correction for nonlinear compressibility is no more than 10% for most practical cases.

Figure 5-2 shows examples of measurements of free-surface velocity profiles for the titanium alloy VT6 (Kanel and Petrova, 1981). VT6 is a designation for a Russian titanium alloy with the following composition: Ti-6%Al-4%V. The stress in the material at the lowest impact velocity (450 ± 20 m/s) shown in Figure 5-2 is below the spall threshold. As a result, the free-surface velocity profile practically replicates the form of the compression pulse in the sample. The elastic-plastic compression wave and the unloading wave are both recorded. The small hysteresis in the free-surface velocity profile is due to irreversible plastic deformation during the loading-unloading cycle.

The magnitude of the tensile stresses that develop in the body after the reflection of the compression pulse at the free surface increases with increasing shock intensity. When the peak tensile stress reaches the spall threshold, damage begins to accumulate. The tensile stress in the damage accumulation zone decreases as the fracture develops. As a result, a compressive disturbance called a "spall pulse" appears on the free-surface velocity profile. Thereafter, wave reverberation is observed within the material layer between the free surface and the damage zone. The period of velocity oscillation is a measure of the thickness of this material layer. As discussed above, the velocity pullback, Δu_{fs}, is a measure of incipient fracture strength of the material. Experiments on many materials show that increasing the shock amplitude does not influence the magnitude of Δu_{fs} as indicated in Figure 5-2 for titanium VT6.

For most solids, the free-surface velocity profiles exhibit elastic-plastic properties. There are several wave propagation velocities in a body undergoing elastic-plastic deformation. For one-dimensional flow, weak perturbations propagate with the longitudinal sound velocity, c_l, if the deformation is elastic, and with the
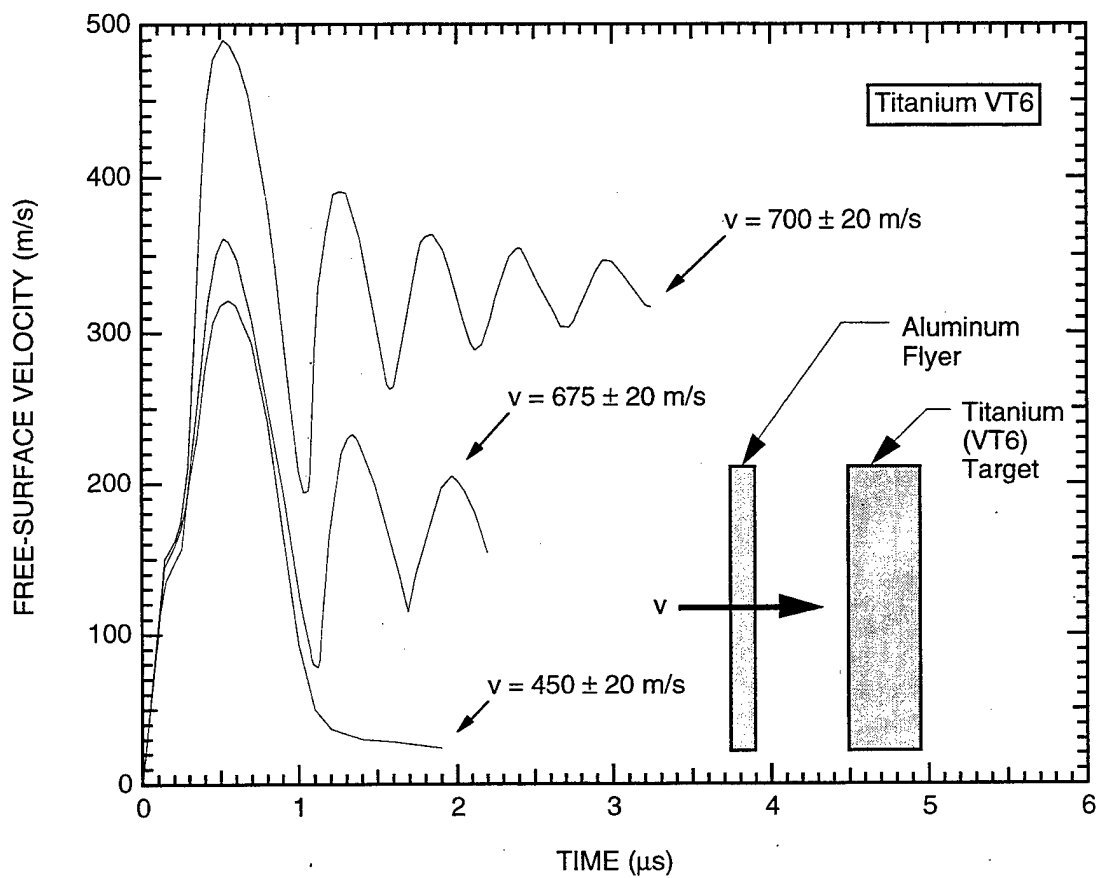
Figure 5-2.   Free-surface velocity profiles for the VT6 titanium alloy at three shock wave intensities.

bulk sound velocity, $c_b < c_l$, in the plastic deformation region. As discussed below, this propagation has a direct bearing on the procedure of calculating the tensile stress at the spall plane.

Figure 5-3 shows an axial stress-particle velocity (σ_x, u) diagram for wave interactions when a plane square compressive pulse is reflected off the free surface of an elastic-plastic body. The process of uniaxial compression is elastic until the stress reaches the Hugoniot elastic limit (HEL). The slope of the initial elastic part of Hugoniot below the HEL in these coordinates is $d\sigma/du = \rho c_l$. The slope in the plastic deformation region above the HEL is equal to ρc_b. Unloading from a shock-compressed state is initially elastic in both the incident and reflected waves. The elastic part of the unloading wave has a stress magnitude equal to twice the HEL. Thereafter, all expansion processes occur in the plastic region.

Thus, if the shock wave amplitude exceeds twice the HEL, tension produced under interaction of rarefaction waves takes place in the plastic deformation region. This means that Riemann's trajectories in the tension region have slopes defined by the bulk compressibility, and we must use the bulk sound velocity for calculation of stress using Eq. (5.1). However, the spall pulse is a compression wave that propagates through the extended material and, therefore, must have an elastic precursor. Thus, the spall pulse front propagates with the longitudinal sound velocity, whereas the rarefaction plastic wave ahead of it propagates with the bulk sound velocity (Figure 5-4). As a result, the compression wave, which appears due to the stress relaxation at fracture, overtakes the release part of the incident shock pulse and causes the measured minimum velocity before the spall pulse, u_{fs}, to exceed the value that should be used in Eq. (5.1) for calculating the fracture stress.

To compensate for this effect, we introduce the following expression for calculating the tensile stress just before spalling:

$$\sigma^* = \frac{1}{2}\rho_o c_b \left(\Delta u_{fs} + \delta\right) \tag{5.2}$$

where δ is a correction for the profile distortion due to the elastic-plastic properties of the material. Taking into account the velocity gradients ahead of the spall pulse, $\dot{u}_1$, and the gradient in its front, $\dot{u}_2$, the correction magnitude is estimated as

$$\delta = \left(\frac{h}{c_b} - \frac{h}{c_l}\right) \frac{|\dot{u}_1 \dot{u}_2|}{|\dot{u}_1| + \dot{u}_2} \tag{5.3}$$

where h is the thickness of the spall plate.

The computation of σ^* and δ in these equations assumes that fracture is instantaneous and that damage only occurs on the spall plane. These assumptions are most likely to be satisfactory for very brittle material in which the imposed tensile stress is well above the threshold for spalling. For more ductile
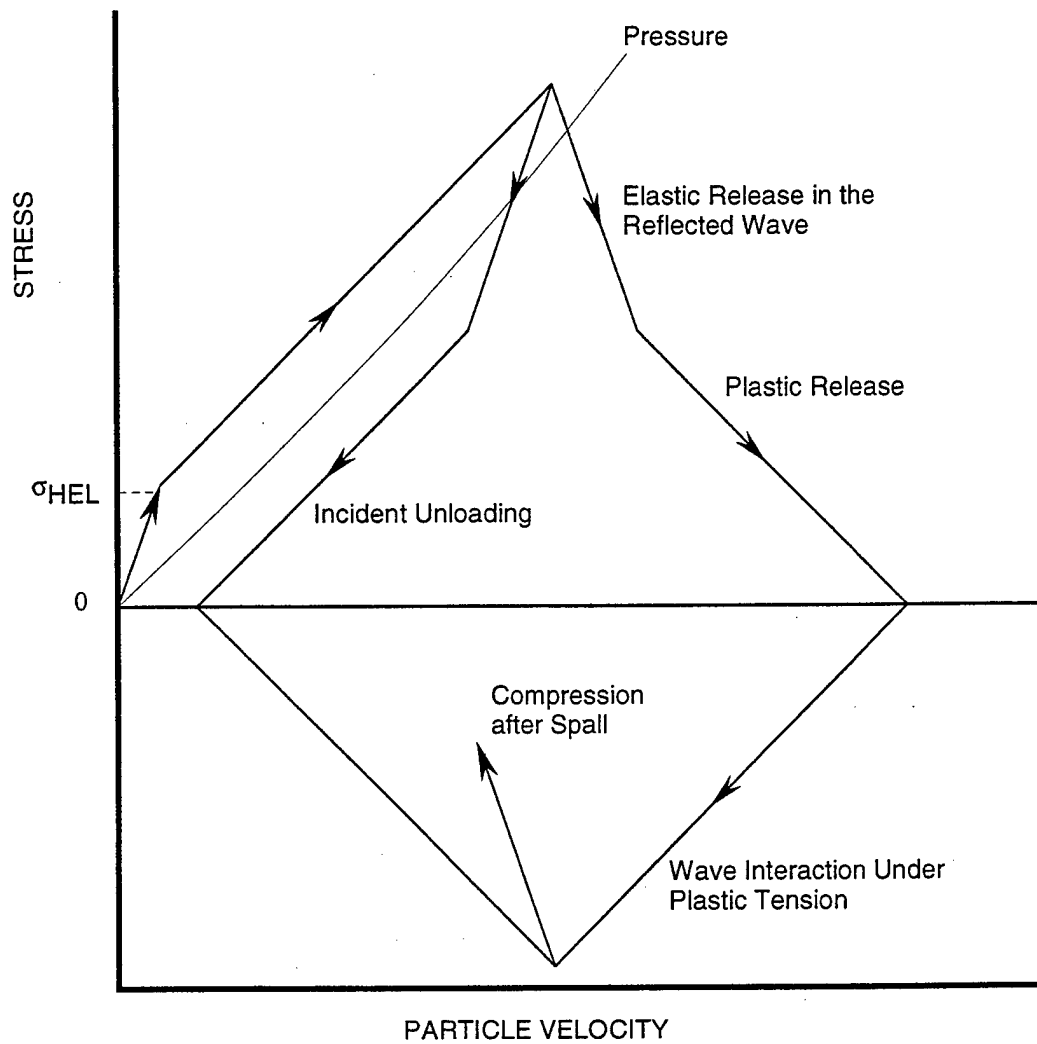
Figure 5-3.   Stress-particle velocity diagram for wave interactions during the reflection of a triangular shock pulse from the free-surface of an elastic-plastic body.
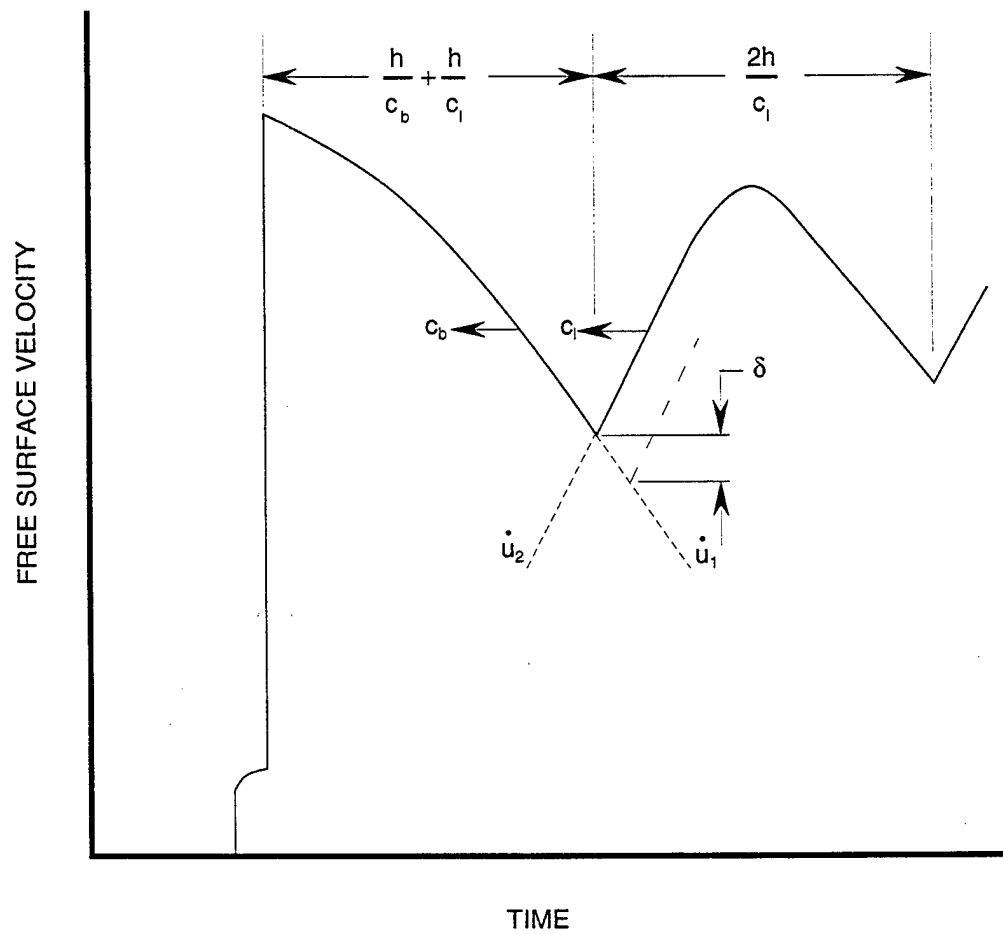
Figure 5-4.   Determination of the corrected expression for calculating the tensile stress before spalling.

materials, the evolution of fracture affects the shape of the "spall pulse", and measurement of the shape of the pulse provides information about the spall kinetics. Therefore, a more complicated analysis is required as described by Curran et al. (1987) and in later sections.

In fact, Eq. (5.2) for computing σ^* and Eq. (5.3) for estimating the correction factor δ can only be approximate. It is impossible to be sure that the extrapolation used for $u_{fs}(t)$ is accurate. Actually, an undistorted profile can contain a smooth minimum near the measured value of u_m as well as a sharp minimum near its corrected counterpart with the same effect on the real free-surface velocity profile. This means that experiments must be carefully designed to provide the smallest correction possible. To this end, it can be shown that δ is about 10% of Δu_{fs} for an incident load pulse of triangular form and reaches 50% or more of Δu_{fs} for a pulse of rectangular form.

Many spall experiments are performed using the flyer plate impact configuration. In this case, the stress and particle velocity profiles remain approximately rectangular until the distance of propagation reaches about five impactor thicknesses. After that, the unloading wave overtakes the shock front and the load pulse begins to take on a triangular shape.[4] Thus, the optimal ratio of sample thickness to impactor thickness must exceed 5 to have the smallest correction and smallest possible error of the spall strength value.

The validity of determining the fracturing stress using the free-surface velocity profiles as outlined above has been confirmed by many experiments with shock load intensities close to the spall strength magnitude. A spall pulse was not recorded in these experiments when the peak stress was below the spall strength, but it appeared in the velocity profiles with increasing stress above the spall strength. Then, the velocity pullback value remained practically unchanged as the shock intensity was increased. Careful comparison of free-surface velocity measurements with results of microscopic examination of impacted and recovered samples shows that the fracture nucleation threshold correlates well with a stress magnitude equal to σ^*.

5.3 EXPERIMENTS WITH A SOFT BUFFER PLATE BEHIND THE TARGET.

Tensile stresses can be created inside a body not only by the intersection of Taylor waves and reflections of a compression pulse from the free surface of the body, but when the stress pulse reflects from an interface with a material of lower shock impedance. In this case, measurements of the spall strength can be based on the stress or particle velocity profiles at the interface between the sample under investigation and the lower impedance buffer plate. The experimental configuration and the stress-particle velocity

---

[4]Strictly speaking, the shock propagation distance required for the pulse to evolve from rectangular to triangular shape is a function of stress amplitude and material properties. The rule of thumb of having the target thickness exceed five times the impactor thickness is based on the experience of some of the present authors with many materials subjected to a wide range of stress amplitudes.

diagram for this case are shown in Figure 5-5. The choice of a test configuration for use in a particular spall experiment depends on the available techniques of recording the wave profile. For example, the experimental configuration shown in Figure 5-5 is normally used when stress history measurements are desired. In this case, PMMA is most often used as the buffer material because PMMA has an impedance that closely matches the impedance of the epoxy in the stress gage package. This minimizes the rise time of the gage and optimizes the resolution of the stress history measurement.

Replacement of the free surface by a low impedance buffer leads to an increase in the distance between the spall plane and the plane at which measurements are made. As a result, the potential for distortion of the wave profile also increases. An additional source of error in this case is in the equations of state used for the sample and buffer materials.

Dynamics of the fracture zone in experiments with a low impedance buffer are more complicated than in experiments without a buffer and have some specific characteristic properties due to the effect of a counterpressure from the soft barrier side. This effect was analyzed by Kanel and Utkin (1991), who used the acoustic approach to analyze cavitation in an inviscid liquid with zero strength during the reflection of a triangular compression pulse from the interface between the liquid and a low impedance material. The process is illustrated by the distance-time and the stress-particle velocity diagrams of Figures 5-6 and 5-7. The objective of the analysis is to determine how the boundary of the cavitation zone is moving and how this motion influences the velocity (and stress) history at the interface between the liquid and the softer buffer.

Let $i_1 = \rho_1 c_1$ and $i_2 = \rho_2 c_2$ be the dynamic impedances of the liquid and soft buffer, respectively. In Figure 5-6, the incident triangular compression pulse propagates to the right along C_+ characteristics. This compression pulse is reflected at the liquid-buffer interface as a centered rarefaction fan that propagates to the left along C_- characteristics. Let the velocity distribution in the incident pulse be

$$u = u_o - k(c_1 t - h + H) \tag{5.4}$$

Cavitation occurs at $h = 0$, where the stress first reaches zero as a result of interaction between the incident compression pulse and the reflected rarefaction waves. This occurs at $t = \tau$, where τ is given by the relation

$$\tau = \frac{H}{c_1} = \frac{u_o}{k c_1} \frac{i_2}{i_1 + i_2} \tag{5.5}$$

The right boundary of the cavitation zone (curve AR in Figure 5-6) continually shifts to the left (i.e., moves through the material) because the recompression wave approaching the boundary from the soft buffer side causes the stress to increase above zero. The particle velocity and specific volume in the
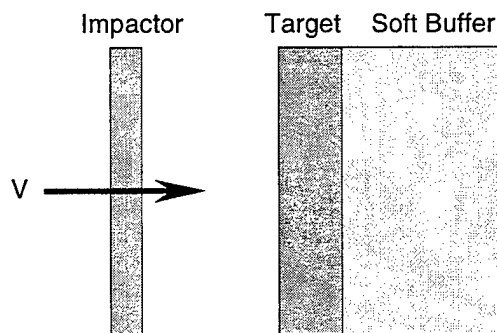
(a) Configuration of an experiment with a soft buffer behind the target.
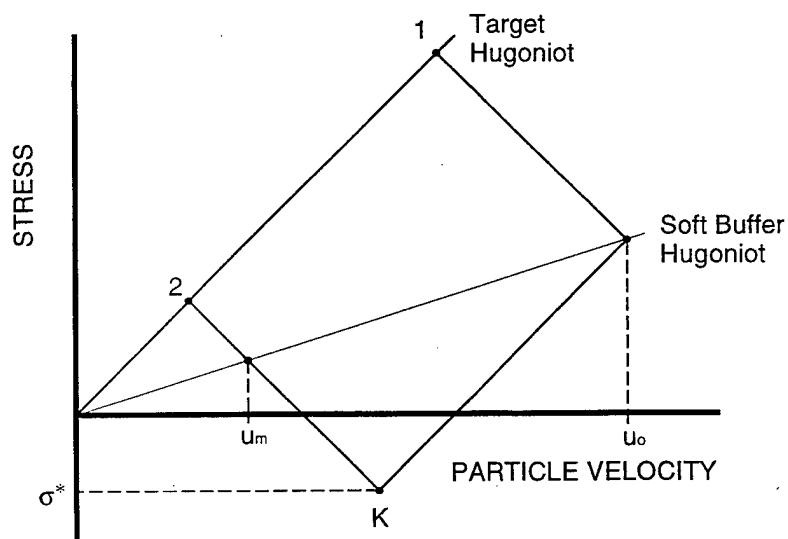
(b) Stress-particle velocity diagram for the reflection of a compression stress pulse from the interface with a softer material.

Figure 5-5. Configuration and stress-particle velocity diagram for a spall experiment with a soft buffer behind the target.

Figure 5-6. Distance-time diagram showing wave interactions during liquid cavitation caused by the reflection of a triangular compression pulse from the interface with a softer material.

131
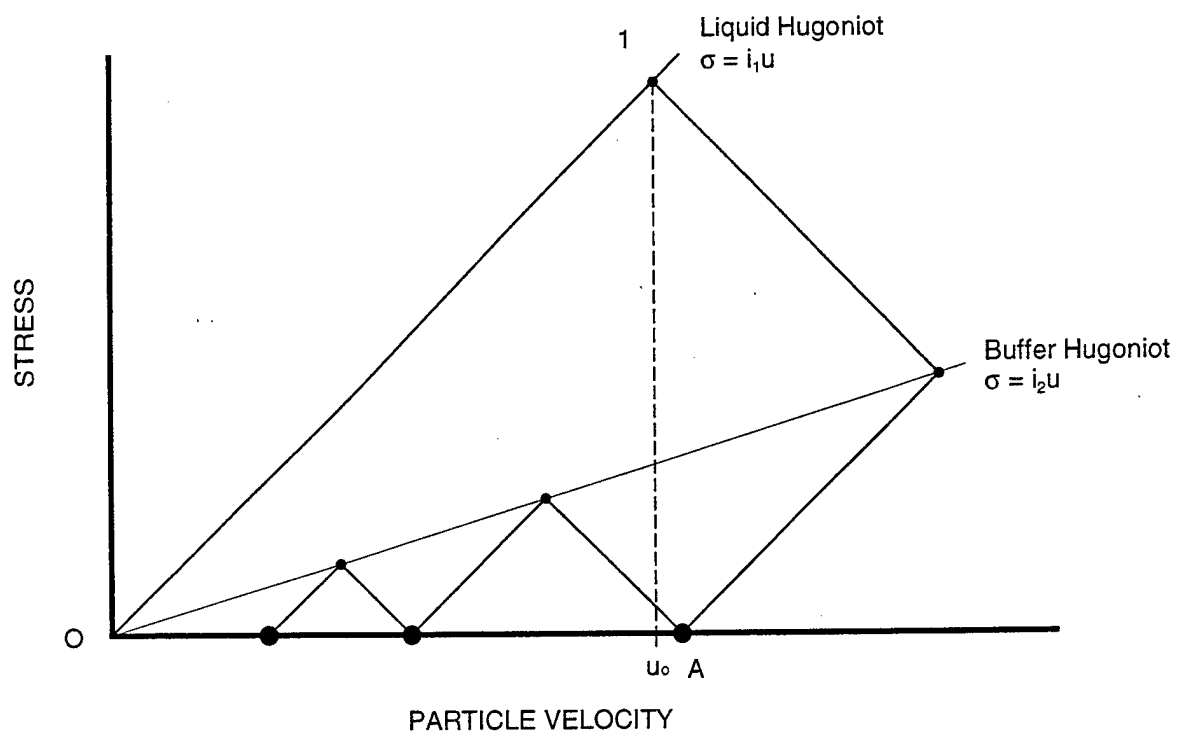
Figure 5-7.   Stress (or pressure)-particle velocity diagram for cavitation of a liquid with no strength.

132

inviscid liquid undergo a jump from u^- and V^- on the left side of the boundary to u^+ and $V^+ = V_o$ on the right side of the boundary. Mass conservation across the boundary of the cavitation zone can be expressed by using an equation similar to the mass jump condition across a shock front as follows:

$$\frac{D-u^-}{V^-} = \frac{D-u^+}{V^+} \tag{5.6}$$

where D is the boundary velocity. Thus, the trajectory AR of the cavitation zone boundary can now be described by the differential equation

$$\frac{dh_R}{dt} = D-u^+ = \frac{V^+}{V^- - V^+}\left(u^+ - u^-\right) \tag{5.7}$$

To calculate this trajectory we make use of the condition that pressure along AR is zero, and the particle velocity u^+ on the right side of AR is connected with the stress and particle velocity state $(\bar{\sigma}, \bar{u})$ along the liquid-buffer interface through the Riemann invariant along C_- characteristics. Parameters on the left side of the boundary are determined by using the condition that the particle velocity in a liquid with no strength during cavitation is constant. This velocity is given by

$$u^-(t) = 2[u_o - 2k(H-h)] \qquad at \qquad t \geq \tau - h/c_1 \tag{5.8}$$

The time rate of change of the specific volume in the cavitation zone is then given by

$$\frac{dV^-}{dt} = V_o\frac{du^-}{dh} = 4kV_o \tag{5.9}$$

Using the parameters u^-, V^-, u^+, and V^+ calculated as described above, we finally obtain the following linear equation for the trajectory AR of the right boundary of the cavitation zone:

$$h_R = Ac_1(t-\tau) \qquad for \qquad \tau \leq t \leq \tau_1 \tag{5.10}$$

where

$$A = -1 - \frac{\delta}{4} + \sqrt{1 + \frac{\delta^2}{16}} \tag{5.11}$$

$$\delta = \frac{i_1 - i_2}{i_1 + i_2} \tag{5.12}$$

and

$$\tau_1 = \tau\left(\frac{3+A}{1+A}\right) \tag{5.13}$$

133

Thus, the cavitation zone is continuously reduced with time. Its right boundary shifts to the left with a velocity Ac_1 that does not depend on the incident pulse steepness. The boundary velocity decreases with the arrival of each successive recompression wave (at time τ_1, τ_2, etc, in Figure 5-6). This motion of the cavitation boundary indicates that voids created by tensile stresses at early times could be recompacted by counterpressure from the soft buffer side at later times. This possibility must be taken into account when microscopic examinations are performed on spalled samples recovered from experiments with soft barriers.

In contrast to the case of free-surface velocity measurement, the velocity at the interface between the spall sample and a lower impedance buffer continues to decrease with time after the arrival of the spall signal at the interface. Figure 5-8 shows the interface velocity profiles calculated for $\delta = 0.5$ (i_1 / i_2 =3) with and without accounting for the shifting boundary of the cavitation zone.

5.4 OTHER METHODS OF DETERMINING THE SPALL STRENGTH.

Several methods other than the two described above in Sections 5.2 and 5.3 have been used in various studies to determine the spall threshold and the state of the material just before spall. The most straightforward of these methods relies on posttest inspection of impacted samples to determine the critical velocity that corresponds to the spall threshold. With this method, a sample of the material under investigation is impacted with a flyer plate, and the impact velocity is measured. The specimen is recovered, sectioned, and examined under a microscope for spall damage. By repeating this procedure at several impact velocities, we can determine the impact velocity that corresponds to the inception of spall damage in the impacted sample. With the critical velocity so determined, the spall threshold stress under the conditions investigated in the experiment can be determined based on the known compressibility of the material.

This method has been used to determine the spall threshold in several materials including copper (Smith, 1962) and aluminum (Blinkov and Keller, 1962). Among the advantages of this method are that it requires minimal instrumentation and the experiments are relatively easy to perform. One of its disadvantages is that it is subjective. Determining the onset of damage depends on the magnification of the microscope used to inspect the sample and the adopted criteria, which in turn introduce an uncertainty into the fracture stress at the onset of spall calculated using this method.

Another method of determining the fracture stress during spall under uniaxial strain conditions is one that relies on measuring the spalled layer thickness, then performing hydrodynamic calculations to determine the maximum tensile stress experienced by the material at the spall plane (using the experimental results to constrain the calculations). This approach of determining the fracture stress was used, among others, by McQueen and Marsh (1962) to study spall in copper and by Breed et al. (1967) to study spall in aluminum, copper, nickel, and lead. Bushman et al. (1983), who surveyed several spall strength
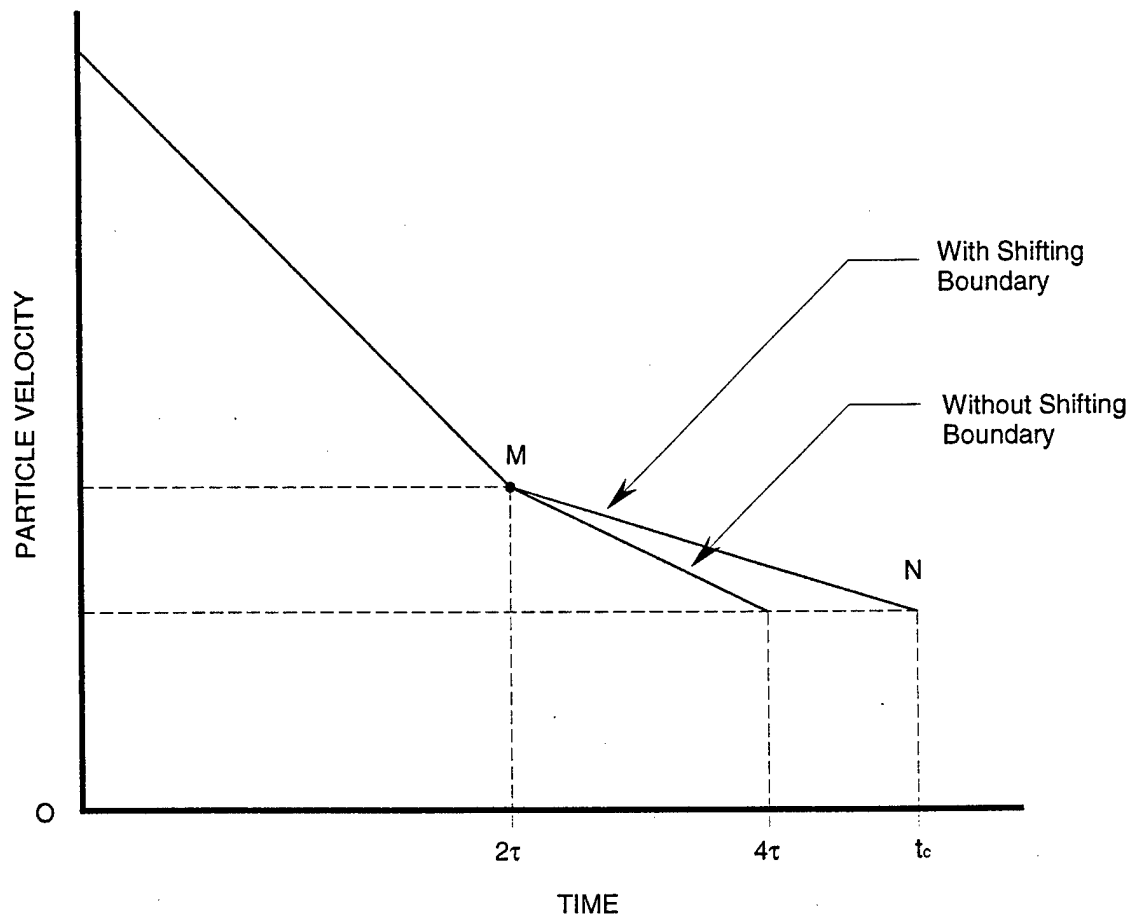
Figure 5-8.   Velocity at the liquid-soft barrier interface with and without accounting for the shifting boundary of the cavitation zone.

135

measurement studies in aluminum and copper, noted that the highest spall strength was usually obtained from experiments with relatively strong shock waves, where the strength was determined by measuring the thickness of the spalled plate, followed by hydrodynamic calculations. The spall strength in these studies is systematically overestimated because the models used in the hydrodynamic calculations neglect the effect of damage on the evolving stress waves. In general, the accuracy of this method of determining the spall strength depends, to a large extent, on the degree of sophistication built into the model used in the hydrodynamic calculations.

Yet another method of determining the spall strength involves measuring the initial velocity and average surface velocity of the spalled layer by a discrete method. The essence of this approach, which was used by Al'tshuler et al. (1966) to investigate spall in copper and by Novikov et al. (1966) to study dynamic fracture in steel, aluminum, and copper, can be explained by referring to Figure 5-1. For instantaneous (i.e., brittle) fracture by a triangular load pulse, the final velocity of the spalled plate is close to the average value

$$u_f \cong \frac{1}{2}(u_o + u_m)$$
(5.14)

and the maximum tensile stress in the spall plane can be determined using the simple expression,

$$\sigma^* = \rho_o c_o u_f$$
(5.15)

In essence, this method of estimating the spall strength is based on momentum conservation, but it does not account for dissipation due to spall damage. For this reason, Eq. (5.15) generally overestimates the spall strength and gives better estimates when the applied stress is larger than the spall strength (i.e., the material is overdriven) and when the spall process is brittle. As shown later (i.e., see Figure 7-2), if spall occurs by ductile damage growth, the velocity of the spalled plate continually decreases as damage continues to accumulate during the reverberation of the stress pulse within the spalled layer. In this case, Eq. (5.14) is a poor estimate of the average velocity. Consequently, Eq. (5.15) does not provide a reliable estimate of the spall strength. This condition also exists if complete separation at the spall plane is not achieved during the first wave reverberation (i.e., if the load duration is short). In this latter case, damage continues to accumulate during stress reverberations and the velocity continues to decrease due to energy dissipation in fracture.

The methods of spall strength determination described in this section were used primarily in early spall investigations performed during the 1960s when instrumentation and computational tools were not as developed and as sophisticated as they are today. The experimental means of continuous particle velocity and stress measurements available today were not readily available then, neither were the tools for

136

performing detailed microscopic characterizations of impacted samples. Similarly, the computational resources and advanced damage-dependent spall models at our disposal today were not available then to aid in the interpretation of experimental data. Today, these sophisticated experimental and analytical tools are all brought to bear to provide a better understanding of spall fracture and the parameters that affect it. These tools and the manner in which they are applied to investigate spall problems are described in later sections.

SECTION 6

THE INFLUENCE OF DAMAGE KINETICS ON WAVE DYNAMICS

Unlike quasi-static loading where fracture, for practical purposes, can be considered instantaneous, the duration of spall fracture under shock wave loading conditions is comparable to the duration of the applied dynamic load. As a result, stress relaxation during fracture plays an important role in the wave process. For this reason, the damage kinetics must be taken into account during the analysis and computation of the dynamic load. The measured stress and particle velocity profiles contain some information about the damage kinetics during spall. This section is devoted to providing a better understanding of these mechanical aspects of rate-dependent fracture during spalling.

6.1 EVOLUTION OF THE TENSILE WAVE.

Let us begin by considering qualitatively the evolution of a tensile wave after fracture initiation in the acoustic approach (Kanel and Chernyich, 1980). (A more detailed analysis is presented in Section 6.3.) The total specific volume of matter, $V(p,V_v)$, is considered to be the sum of the volume of intact solid material, V_s and the volume of voids, V_v:

$$V(p,V_v) = V_s(p) + V_v(t) \tag{6.1}$$

The damage rate $\dot{V_v} = \partial V_v/\partial t$ is taken to be a function of damage itself and of the pressure, p. Using Eq. (6.1), the conservation equations for one-dimensional flow in Lagrangian coordinates take the form

$$\rho_o \frac{\partial u}{\partial t} + \frac{\partial p}{\partial h} = 0 \tag{6.2a}$$

and

$$\frac{\partial p}{\partial t} + \rho_o^2 c^2 \frac{\partial u}{\partial h} - \rho_o^2 c^2 \dot{V_v} = 0 \tag{6.2b}$$

where, the constitutive relation $dp = -c^2 dV$ is used to derive Eq. (6.2b), and as before, ρ_o is the initial density, u is the particle velocity, t is time, h is the Lagrangian position, and c is the sound speed in the medium, and where plastic strains are neglected.

In this case, as in the case of nonrelaxing media, characteristics are lines with slope $dh/dt = \pm c$ in the time-distance plane. Here, we assume that the sound speed c remains constant, thus neglecting the effect of void growth on the stiffness of the distended material. Derivatives of pressure and particle velocity along the characteristics are given by

138

$$\frac{dp}{dt}\bigg|_{C_+} = \frac{\partial p}{\partial t} - \rho_o c \frac{\partial u}{\partial t} = \rho_o c \frac{du}{dt}\bigg|_{C_+} + \rho_o^2 c^2 \dot{V}_v \qquad (6.3a)$$

$$\frac{dp}{dt}\bigg|_{C_-} = \frac{\partial p}{\partial t} + \rho_o c \frac{\partial u}{\partial t} = \rho_o c \frac{du}{dt}\bigg|_{C_-} + \rho_o^2 c^2 \dot{V}_v \qquad (6.3b)$$

Since void growth under tension means that $\dot{V}_v > 0$, trajectories of changing (p,u) states along the characteristics deviate from the Riemann's invariants given by

$$p = \pm\rho_o cu + \text{constant} \qquad (6.4)$$

toward higher pressures.

Qualitative analysis of states along the characteristics allowa some preliminary conclusions about the conditions that lead to the appearance of the minimum on the free-surface velocity profile. This minimum corresponds to confluence of trajectories of changing state along C_+ characteristics. The trajectories of changing state along C_+ and C_- characteristics have a common tangent in the confluence point, because otherwise, the conditions that

$$\frac{dp}{dt}\bigg|_{C_-} = 0 \qquad (6.5a)$$

and

$$\frac{du}{dt}\bigg|_{C_-} = 0 \qquad (6.5b)$$

must be satisfied when the C_- characteristic crosses the confluence point. Since, according to Eq. (6.3), this is possible only if $\dot{V}_v = 0$, we conclude that either the confluence of trajectories of changing state along C_+ characteristics occurs on the boundary of the fracture zone, or the trajectories of changing state along C_+ and C_- characteristics have a common tangent in the confluence point. Taking into account that

$$\frac{du}{dt}\bigg|_{C_+} + \frac{du}{dt}\bigg|_{C_-} = 2\frac{\partial u}{\partial t} \qquad (6.6a)$$

and

$$\frac{dp}{dt}\bigg|_{C_+} + \frac{dp}{dt}\bigg|_{C_-} = 2\frac{\partial p}{\partial t} \qquad (6.6b)$$

we may also conclude that the trajectories of changing state along these C_+ and C_- characteristics have a common tangent with that of the particle path.

Figure 6-1 shows the $p-u$ diagram of the process calculated numerically using the acoustic approximation. The fracture process influences not only the magnitude but also the sign of the slope of the trajectories of changing state along the characteristics. It would be natural to expect that the spall signal originates at the point where the particle velocity is constant, which corresponds to a symmetric velocity distribution in the vicinity of this point. However, Figure 6-1 shows that the slope of the trajectories at the confluence point is close to the slope of the Riemann C_+ invariant. This situation and its consequences are discussed in more detail in Section 6-3.

Let us now examine the evolution of the tension wave after the reflection of a triangular compression pulse from the free surface. Superscript "+" will denote states immediately ahead of the tension jump, and "-" will denote states immediately behind the jump. The tension wave propagates in the negative direction (along C_- characteristics), and the relationship between pressure and particle velocity across the jump is

$$p^- - p^+ = -\rho_o c\left(u^- - u^+\right) \qquad (6.7)$$

Taking into account that the reflected wave is superimposed on the incident simple compression wave, where $\dot{V}_v = 0$ and $dp = \rho_o c \, du$, we obtain from Eqs. (6.3) and (6.7)

$$\left.\frac{dp}{dt}\right|_{C_-} = 2\left.\frac{dp}{dt}\right|_{C_-^+} - \left.\frac{dp}{dt}\right|_{C_-} + \rho_o^2 c^2 \dot{V}_v = 2\dot{p}_0 + \frac{1}{2}\rho_o^2 c^2 \dot{V}_{vo} \qquad (6.8)$$

where

$$\dot{p}_o = \left(\frac{\partial p}{\partial t}\right)_o = \frac{1}{2}\left.\frac{dp}{dt}\right|_{C_-^+} \qquad (6.9)$$

is the time rate of change of pressure in the incident compression pulse, and $\dot{V}_{vo}$ is the initial fracture rate immediately behind the tension jump. Within the framework of the acoustic approach, the damage does not influence the evolution of the tensile wave front when the initial damage rate is equal to zero. In the case of nonzero initial damage rate, the peak stress of the tension wave, according to Eq. (6.8), increases at a slower rate than in the case of no fracture. As an example, consider the linear dependence of the fracture rate on the pressure:

$$\dot{V}_v(p) = -\frac{2Fp}{\rho_o^2 c^2} \qquad (6.10)$$

Integrating Eq. (6.8) for the case of a triangular compression pulse ($\dot{p}_o = \text{constant}$) yields the following relationship for the peak tensile stress behind the tension jump:
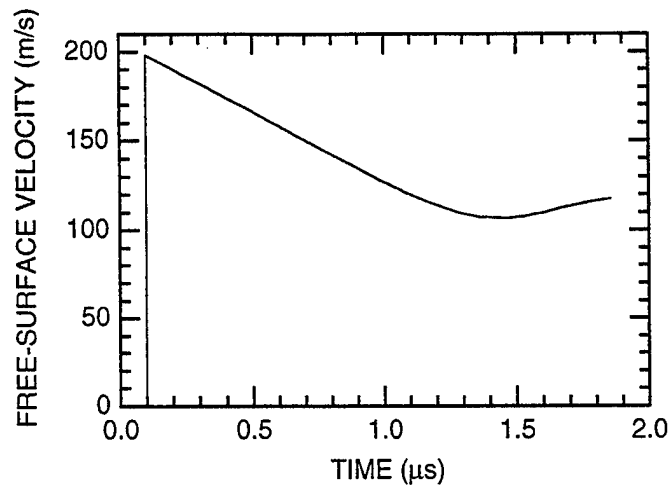
(a)   Free-surface velocity profile.
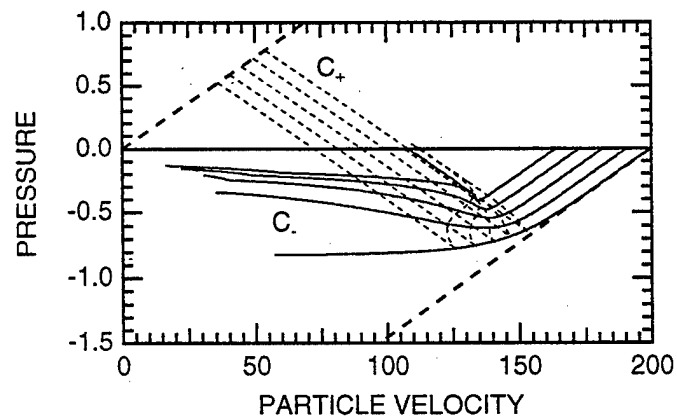
(b)   Trajectories of changing states along
        characteristics.
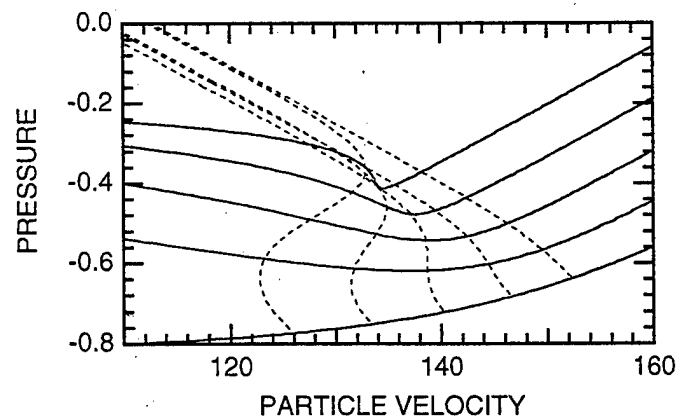
(c)   Same as (b) above, magnified in the region
        of spall pulse formation.

Figure 6-1.   Numerical simulation of the evolution of spall fracture.

141

$$p^- = \frac{2\dot{p}_o}{F}\left(1 - e^{-Ft}\right) = \frac{2\dot{p}_o}{F}\left(1 - e^{F\left(\frac{h-h_o}{c}\right)}\right) \qquad (6.11)$$

where h_o is the coordinate at the free surface of the body. The pressure in Eq. (6.11) asymptotically approaches the ultimate value $p^- = 2\dot{p}_o/F$ corresponding to the condition

$$\dot{V}_v(p^-) = -\frac{4\dot{p}_o}{\rho_o^2 c^2} \qquad (6.12)$$

which also follows directly from Eq. (6.8).

6.2 MEASUREMENTS ASSOCIATED WITH THE PEAK TENSILE STRESS AT THE SPALL PLANE.

Direct measurements of the tensile wave evolution are obviously impossible, but indirect measurements can be performed (Kanel and Glusman, 1983). The idea is as follows. When compression or rarefaction waves are reflected from an interface with a lower impedance material, the sign of the reflected wave is opposite that of the incident wave. It is possible to select a pair of materials of different compressibility such that, after shock compression, the pressure at the interface between them remains positive (compressive) during the passage of the unloading wave from the "rigid" into the "soft" material, even if the pressure reaches large negative (tensile) magnitude inside the "rigid" material. In this case a pressure profile at the interface can be measured. Then, based on an analysis of wave interactions, we can indirectly recover the peak tensile stress in the interior of the "rigid" plate.

Stress measurements were performed in copper and stainless steel samples by Kanel and Glusman (1983). Plane shock waves with approximately triangular pressure profiles were introduced into the samples through a thick paraffin layer [Figure 6-2(a)]. Pressure profiles $p(t)$ were measured at the interface between the paraffin layer and the sample using manganin gauges. The experimental oscillograms presented in Figures 6-2(b) and (c) indicate arrival time of the shock front at the gage location on the interface, the relatively slow pressure decay in the incident pulse, and the fast pressure drop (from 1 to 2) associated with the rarefaction wave reflected from the rear free surface of the specimen.

The x-t and p-u diagrams in Figure 6-3 illustrate the methodology used to determine the pressure in the tail of the reflected rarefaction wave [i.e., the pressure corresponding to point 2 in Figure 6-2(b)]. Points 1 and 2 in Figure 6-3 correspond to points 1 and 2 in Figure 6-2(b). On the x-t diagram, the line 012 is a trajectory of the paraffin-sample interface, and the line 0A is the shock front trajectory. The maximum tensile pressure in the sample occurs near the paraffin-sample interface at point K in Figure 6-3. The state of the material at this point corresponds to the intersection of trajectories of changing state along

142
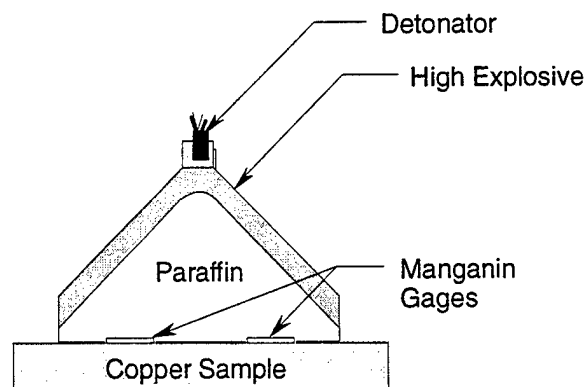
(a) Experimental configuration.
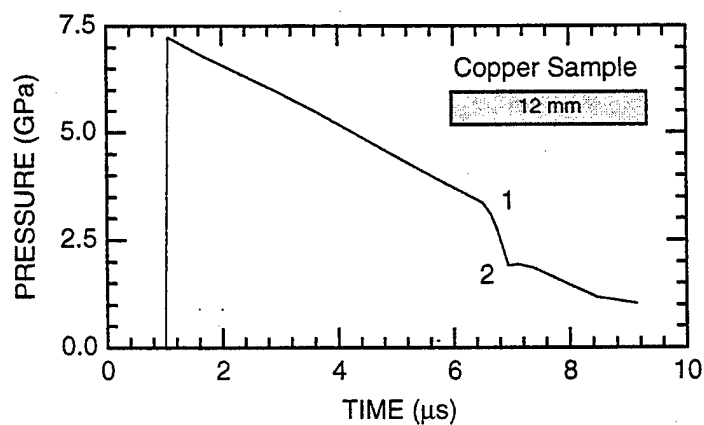
(b) 12-mm-thick copper sample made of a single plate.
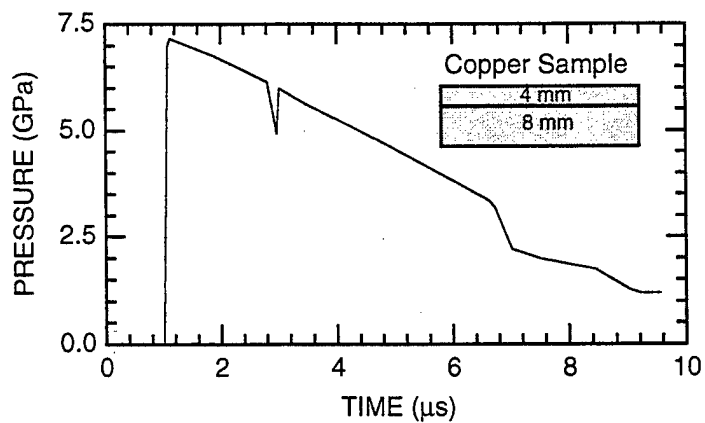
(c) 12-mm-thick copper specimen made of one 4-mm-thick plate and one 8-mm-thick plate.

Figure 6-2.   Measurements of the peak tensile stress behind the spall plane.

143
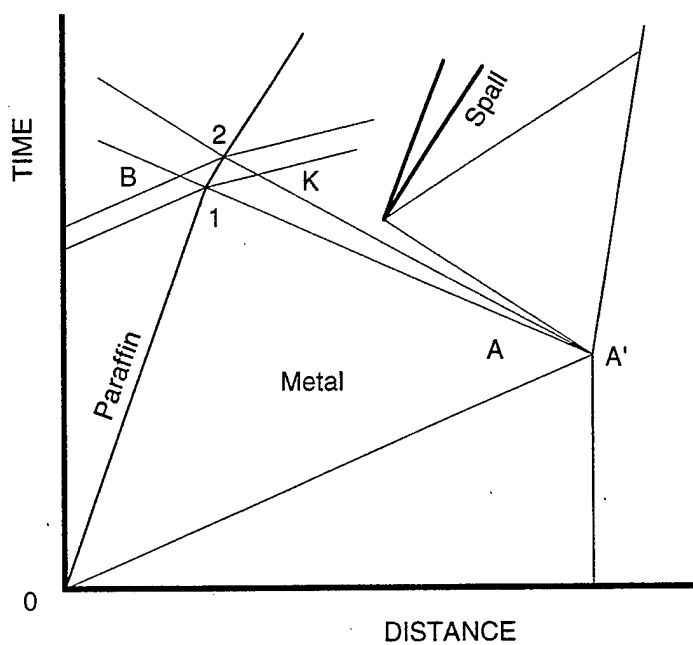
(a) Distance-time diagram.
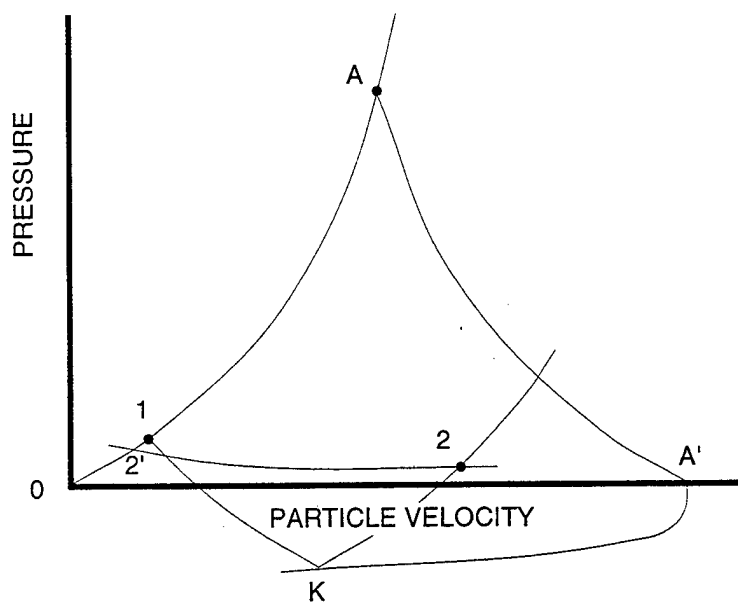
(b) Pressure-particle velocity diagram.

Figure 6-3.   Distance-time and pressure-particle velocity diagrams corresponding to the configuration and conditions shown in Figure 6-2.

144

characteristics 1K and K2. The location of the isentrope 1K on the p-u diagram is determined by using the measured pressure, p_1, at point 1 of the experimental pressure profile. The location of isentrope K2 is also determined from the measured pressure value, p_2. This pressure corresponds to point 2 on the isentrope of paraffin 2'2, which describes states along the characteristic B2. The location of this isentrope is determined from the measured pressure profile by extrapolating its incident part to time t_2.

Additional experiments with split targets were performed to verify the accuracy of this interpretation. Copper and steel samples in this case were composed of two plates, the combined thickness of which is the same as the total thickness of the corresponding solid sample. The ratio of the thickness of the front plate (nearest to the explosive) to that of the back plate in these experiments was designed to reduce the peak tensile stress in the front plate below the spall strength. Then the peak tensile stress near the interface between the sample and paraffin was determined from the measured pressure profile such as the one shown in Figure 6-2(c).

Table 6-1 give the results of measurements of peak tensile stresses, p_k, behind the spall plane in stainless steel and copper samples. Also included in Table 6-1 are the spall strength, σ^*, measured for these loading conditions and estimations of the negative pressure magnitudes, p_k', assuming no influence of fracture on the tensile wave evolution.

Taking into account possible errors, the peak tensile stresses at a distance of 4-5 mm behind the spall plane are 1.0-1.4 GPa for copper and 1.3-1.9 GPa for stainless steel. Without fracture, the estimated peak stresses near the interface are 3.5 GPa for copper and 5.5 GPa for stainless steel. In other words, the tensile stresses in stainless steel are practically limited to the spall strength (i.e., $\sigma^* = 1.85$ GPa for stainless steel). In the copper samples, a small increase of intensity of the tensile wave was observed during its propagation behind the spall plane. This small increase can be explained in terms of the dependence of spall strength on strain rate.

The main observation based on these experimental results, however, remains that the stress relaxation at fracture makes it impossible for the material to support tensile stresses in excess of some limit determined by the spall conditions. The evolution of the tensile wave is determined by the initial fracture rate.

6.3 CORRELATION BETWEEN THE SPALL FRACTURE RATE AND THE FREE-SURFACE VELOCITY PROFILE.

For fracture resulting from shock-wave loading, the fracture time can be comparable to the load duration. This means that, for many applications, dynamic fracture must be considered as a continuous process with characteristic kinetics of damage development. In general, the events that take place inside the material affect the wave profile structure; therefore; the results of dynamic wave profile measurements contain information about the kinetics of damage evolution. For instantaneous fracture, the spall pulse

145

Table 6-1. Results of measurements of tensile wave behind the spall plane.

Material	Sample thickness (mm)	Peak pressure (GPa)	p_1 (GPa)	p_2 (GPa)	p_2' (GPa)	p_k (GPa)	p_k' (GPa)
Copper	12	7.04	3.36	2.04	3.1	-1.22 ± 0.2	-3.5 ± 0.2
$\sigma^* = 0.8 \pm 0.1$ GPa	4 + 8	7.04	3.36	2.17	3.1	-0.66 ± 0.2	-1.0 ± 0.15
Spall thickness = 6 mm							
Stainless steel	12	10.1	4.46	2.53	3.98	-1.55 ± 0.3	-5.5 ± 0.2
$\sigma^* = 1.85$ GPa	6 + 6	10.1	4.46	2.54	3.98	-1.51 ± 0.1	-3.0 ± 0.15
Spall thickness = 6.9 mm	3 + 9	10.1	4.46	2.79	3.98	-0.49 ± 0.2	-1.0 ± 0.1

should have a very sharp front. Increase of damage evolution time should cause a decrease in the slope of the spall pulse front. This section attempts to establish a general quantitative relationship between the damage rate and the structure of the wave profiles. Analysis of the flow associated with stress relaxation during spalling should provide information about the kinetics of fracture in the sense of the dependence of damage rate on stress and the degree of damage.

Let us consider the evolution of a triangular compression pulse after its reflection from the free surface of a solid in the context of the acoustic approximation. The damage is assumed to be initiated by tensile stresses exceeding the critical value, $\sigma^* = -p_k$ and is described by evolution of the specific volume of voids, V_v. The total volume is equal, as before, to the sum of the damaged volume, V_v, and the volume of undamaged (solid) material, V_s. Let the damage kinetics depend only on the specific volume of pores and be a power function of V_v. The form of the kinetic relation is chosen to be convenient for the analysis. In general, of course, the damage rate depends on the acting stress, temperature and degree to which the damage has evolved. Because we are interested in the initial stage of spallation, the collapse of voids under compression will not be considered. In the context of this model, the behavior of the material is described by the following set of equations in Lagrangian coordinates:

$$\frac{\partial V}{\partial t} - \frac{1}{\rho}\frac{\partial u}{\partial h} = 0 \tag{6.13a}$$

$$\frac{\partial u}{\partial t} + \frac{1}{\rho}\frac{\partial p}{\partial h} = 0 \tag{6.13b}$$

$$\frac{\partial V_v}{\partial t} = \frac{(\rho V_v)^\alpha}{\rho \tau_\mu} \tag{6.13c}$$

$$p = \rho^2 c^2 \left(\frac{1}{\rho} - V - V_v \right) \tag{6.13d}$$

where the characteristic damage time, τ_μ, and $\alpha < 1$ are constants, and ρ is the initial density. The pressure is defined by the equation of state through the specific volume of solid material.

Figure 6-4 diagrams the flow field in the h-t plane. The free surface has a coordinate $h = 0$. Rgion 1 is free from the interaction of the incident load pulse with the reflected rarefaction wave. No tensile damage occurs in this region, and the dependencies of the particle velocity and pressure on time and position correspond to a triangular compression pulse described by the relations

$$u(h,t) = u_o - k(ct - h) \tag{6.14}$$

$$p(h,t) = \rho c u(h,t) \tag{6.15}$$

147
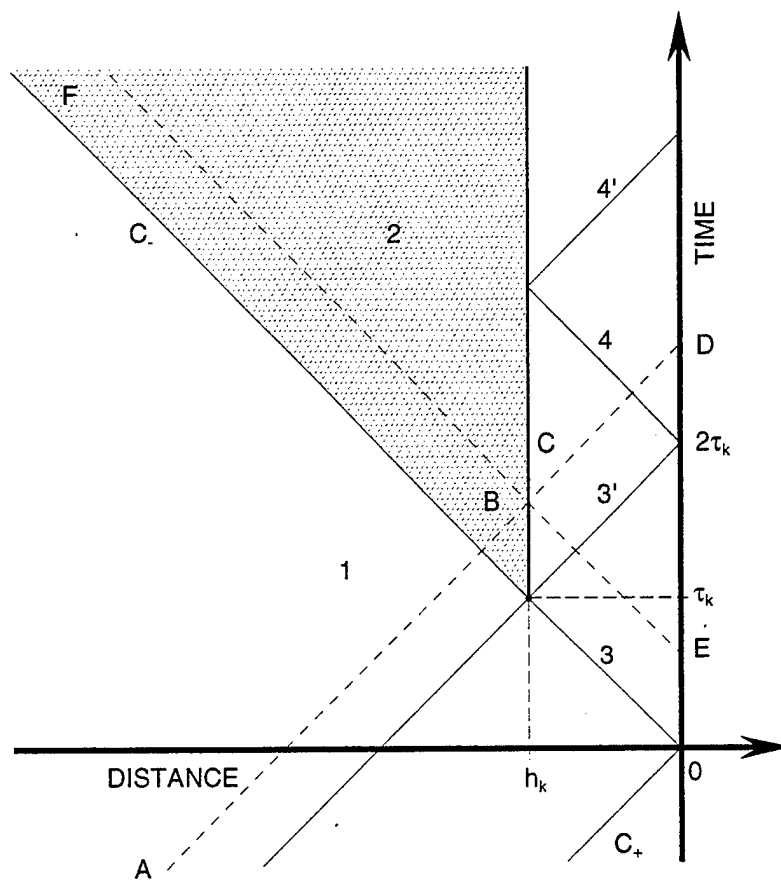
Figure 6-4. Distance-time diagram of the flow field during spalling.

where u_o is the peak particle velocity, k is a constant, and $\tau_o = -h_o/c$ defines the length, $2h_o$, of the pressure pulse through the relation $u_o = -2kh_o = 2kc\tau_o$.

Tensile stresses arise in region 3, and at the point $h = h_k = p_k/2\rho kc, t = \tau_k = -h_k/c$, the pressure reaches the critical magnitude, $p_k = -\sigma*$. The damage occurs in region 2 and the flow is determined here by solving the system of Eq. (6.2) with boundary conditions at $h = h_k$ and as $h \to -\infty$ and initial conditions along the C_- characteristic through the J_+ Riemann invariant.

To obtain a solution of Eq. (6.13), let us eliminate the terms V_ν and V and substitute $T = t + h/c$ for t. Then, applying the Laplace transformation, we obtain a system of ordinary differential equations. The solution that satisfies the initial conditions and remains stable as $h \to -\infty$ is

$$\bar{p}(h,s) = \frac{2k\rho c}{s}\left\{h - h_0 - \frac{c}{2s}\left(1 - e^{-2s\left(\frac{h-h_o}{c}\right)}\right)\right\}\theta(h - h_o) - \frac{\rho c}{2}F(s)\left(h - \frac{c}{2s}\right) + a \qquad (6.16)$$

$$\bar{u} = \frac{2k}{s}\left\{h - h_0 - \frac{c}{2s}\left(1 - e^{-2s\left(\frac{h-h_o}{c}\right)}\right)\right\}\theta(h - h_o) + \frac{1}{2}F(s)\left(h + \frac{c}{2s}\right) - \frac{a}{\rho c} \qquad (6.17)$$

Here, $\bar{p}$ and $\bar{u}$ are the Laplace conjugates of pressure and particle velocity, s is the Laplace variable, $F(s)$ is the Laplace conjugate of damage rate $\rho\dot{V}_\nu$, and $\theta(h)$ is the Heaviside unit function. The constant a is defined in such a manner as to keep the J_- Riemann invariant at $h = h_k$. For example, within the time interval $0 \leq T \leq 2\tau_k$, the constant a is given by

$$a = \frac{k\rho c}{s}\left(2h_o + \frac{c}{s}\right) + \frac{\rho c}{2}F(s)h_k \qquad (6.18)$$

Equations (6.16), (6.17), and (6.18) provide the solution of Eqs. (6.14) and (6.15) in terms of the Laplace variables in region 2 of the flow field (see Figure 6-4) for $0 \leq T \leq 2\tau_k$. Some results can be obtained immediately from Eqs. (6.16) and (6.17) without performing the inverse transformation. The pressure history along the right side of the C_- characteristic for $h > h_o$ can be determined using the known property of Laplace transformation: $\lim\limits_{s\to\infty} sG(s) = G(0+)$,

$$p = 2k\rho ch - \frac{\rho c}{2}(h - h_k)L \qquad (6.19)$$

where $L = 0$ when $0 < \alpha < 1$ and $L = 1/\tau_\mu$ for $\alpha = 0$. It follows from this equation that the pressure corresponds to the case of undamaged material if the initial damage rate is equal to zero. When $\alpha = 0$, a

149

different situation arises. After the beginning of damage evolution at point (h_k, τ_k), the pressure continues to decrease if $\tau_\mu > 1/(4k)$. It remains constant if $\tau_\mu = 1/(4k)$, or it begins to increase if $\tau_\mu < 1/(4k)$.

The free-surface velocity can be determined from Eqs. (6.16) and (6.17). Taking into account the conservation of J_- Riemann invariant along the C_+ characteristic in regions 3' and 4 (see Figure 6-4) and using the known formulas of inverse Laplace transformation, we obtain the following expression for the free-surface velocity within the time interval $2\tau_k \leq t < 4\tau_k$:

$$\frac{u(0,t)}{2u_o} = 1 - \frac{t}{2\tau_o} + \frac{c}{4u_o}\left[(1-\alpha)\frac{t-2\tau_k}{\tau_\mu}\right]^{\left(\frac{1}{1-\alpha}\right)} \tag{6.20}$$

We now analyze this solution for various values of α, the exponent in the void volume growth rate.

6.3.1 The Case $\alpha = 0$ (Constant Void Volume Growth Rate).

Figure 6-5 shows the free-surface velocity profiles plotted by means of Eq. (6.20) for three values of τ_μ. As can be seen, there is a critical value of relaxation time equal to $1/(4k)$. In this case the free surface velocity is constant after time $t = 2\tau_k$ when information about the beginning of damage reaches the free surface. For $\tau_\mu < 1/(4k)$, the damage is manifested as a spall pulse in the free-surface velocity profile. For $\tau_\mu > 1/(4k)$, the velocity continues to decrease during fracture beyond $t = 2\tau_k$. Introducing the damage rate $\dot{V}_v = 1/\rho\tau_\mu$ and the expansion rate in the unloading wave of the incident pulse, the result obtained can be stated as follows: a spall pulse on the free-surface velocity profile forms only if the initial damage rate is more than four times as great as the expansion rate in the unloading wave of the incident pulse. The slope of spall pulse front is equal to

$$\frac{d}{dt}\left(\frac{u(0,t)}{2u_o}\right) = \frac{1}{8\tau_o}\left(\frac{\dot{V}_v}{\dot{V}} - 4\right), \quad t > 2\tau_k \tag{6.21}$$

It follows from Eq. (6.21) that the initial magnitude of the damage rate, $\dot{V}_v$, can be estimated from experimental free-surface velocity profiles.

Let us now consider the changing p-u state along characteristics. The solution for the fracture zone, which follows from Eqs. (6.16) and (6.17) after inverse Laplace transformation, is

$$p(h,t) = 2\rho ckh + \frac{\rho c^2}{4\tau_\mu}\left(t - \frac{h}{c} - 2\tau_k\right) \tag{6.22a}$$
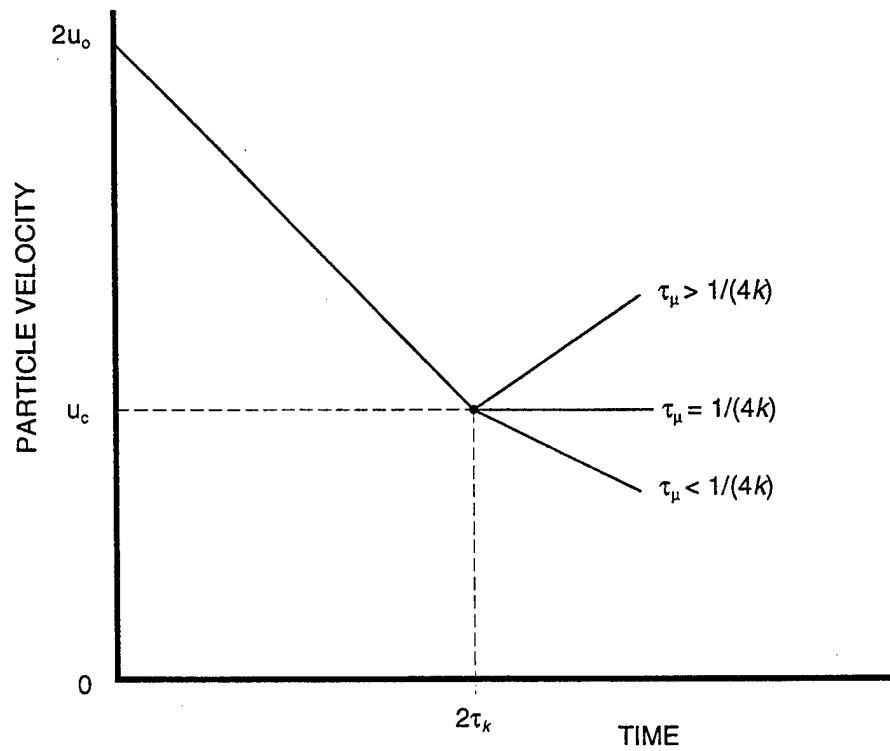
Figure 6-5. Free-surface velocity profiles for the case of constant damage rate after the spall threshold.

$$u(h,t) = 2(u_o - kct) + \frac{c}{4\tau_\mu}\left(t + \frac{3h}{c} + 2\tau_k\right) \qquad (6.22b)$$

These relationships provide a constraint on the pressure and particle velocity along the C_+ characteristic on the segment BC in Figure 6-4:

$$p - p_+ = \frac{\rho c}{\left(1/2k\tau_\mu\right) - 1}(u - u_+) \qquad (6.23)$$

where p_+ and u_+ are the pressure and the particle velocity at the point of intersection of the C_+ characteristic with the straight line $h = h_k$ (the point C in Figure 6-4). In the regions $3'$ and 4 along the same characteristic C_+

$$p - p_+ = -\rho c(u - u_+) \qquad (6.24)$$

The relationship (6.23) shows that the trajectory of changing state along the characteristic becomes vertical when $\tau_\mu = 1/2k$. The vertical slope of the trajectory does not correspond to any spall threshold, and the damage rate value in this case is half of that corresponding the appearance of the spall signal on the free-surface velocity profile. Figure 6-6 shows trajectories of changing state along C_+ characteristic ABCD shown in Figure 6-4 for the threshold situation when $\tau_\mu = 1/4k$. The arrows indicate the direction of changing of the state. After intersection with the tensile wave front, the pressure and the particle velocity along this characteristic are changed by a jump from point A to point B. The change from point B to point C occurs continuously, and thereafter the characteristic becomes trapped in the fracture zone.

Along the segment CD the relationship between the pressure and the particle velocity corresponds to Eq. (6.24). The geometry of the trajectories of changing state shows that the pressure at the spall plane $h = h_k$ increases from the threshold value p_k to zero during the time $2\tau_k$. In other words, under threshold conditions the pressure on the spall plane increases at a rate equal to the unloading rate in the incident load pulse. Figure 6-6 shows also the trajectory of changing state along C_- characteristic ECF (Figure 6-4) for this threshold case.

6.3.2 The Case $\alpha > 0$ (Variable Void Volume Growth Rate).

When $\alpha > 0$, the damage evolves at an accelerating rate, beginning at an initial rate of zero. Figure 6-7 shows the profiles of free-surface velocity for this case. Curves 1, 2, and 3 correspond to increasing
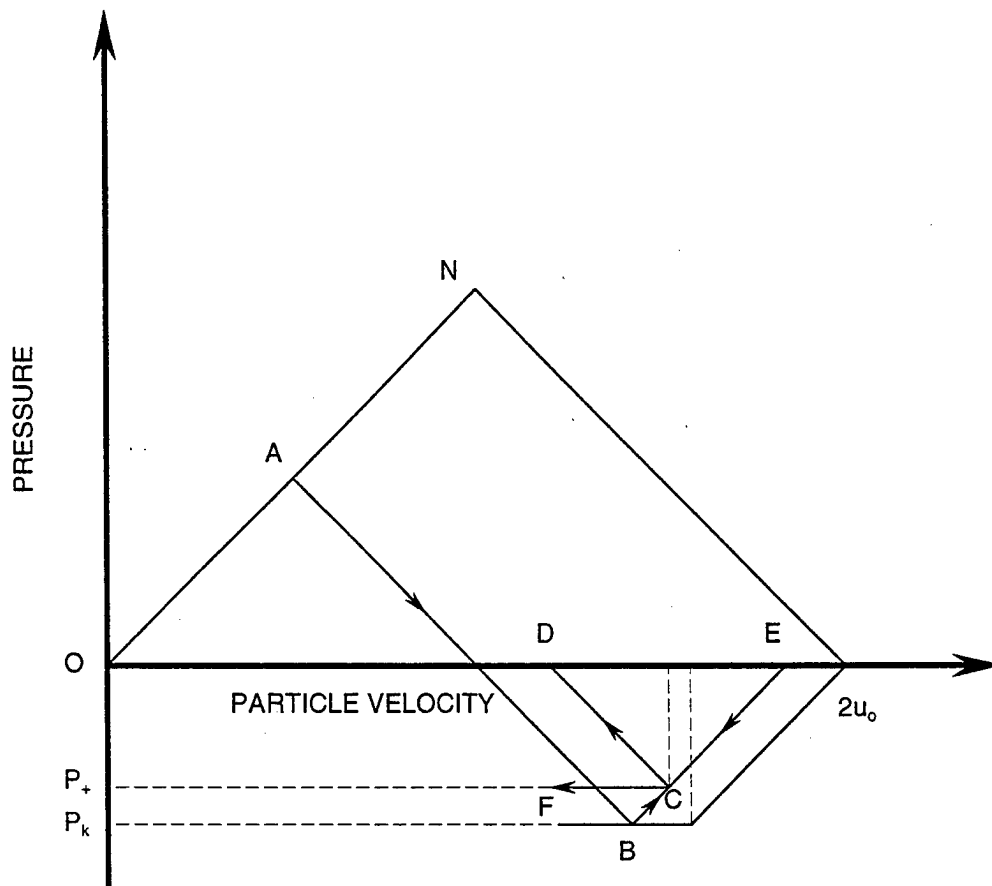
Figure 6-6.   Trajectories of changing states along characteristics at a constant damage rate.
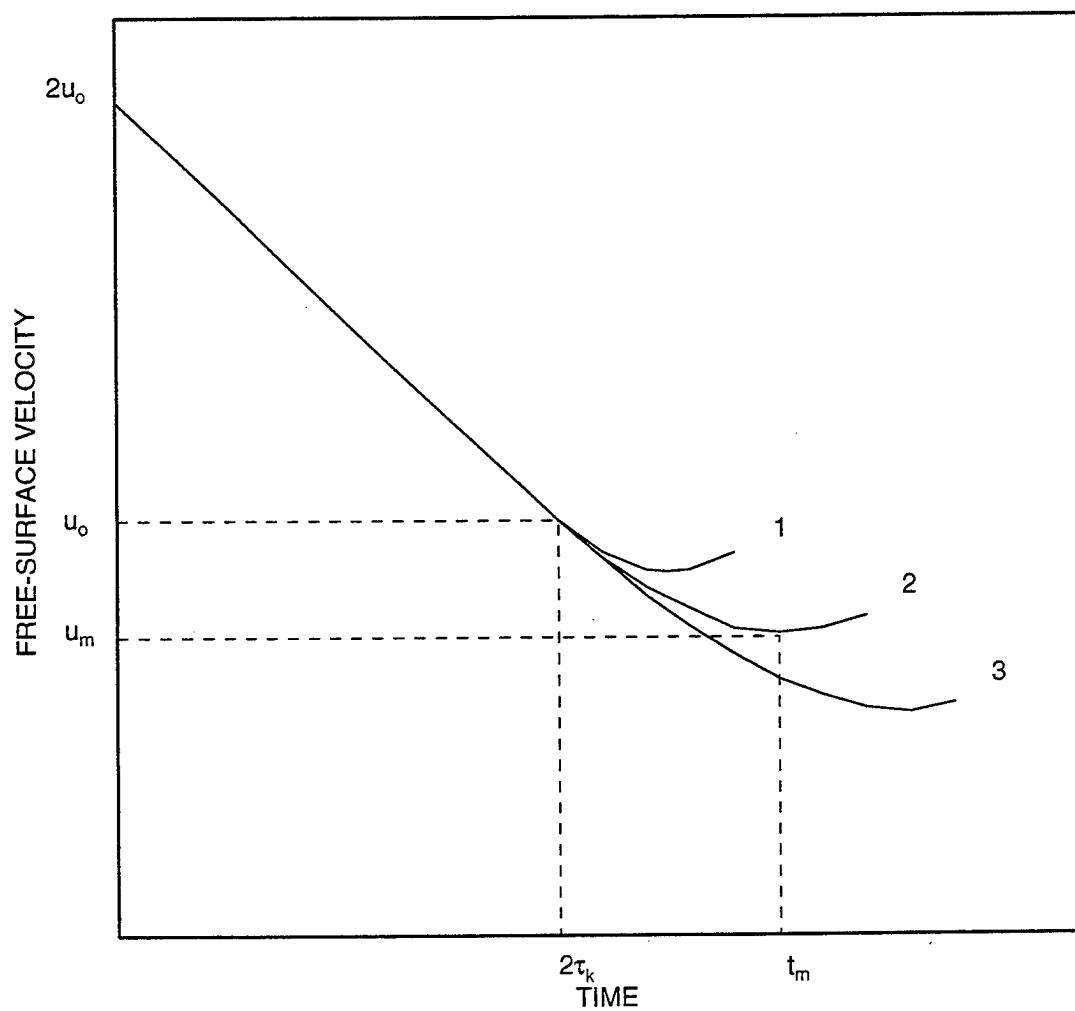
Figure 6-7.   Free-surface velocity profiles for the case of accelerating damage ($\alpha > 0$).

154

α or τ_μ. Unlike the case of constant damage rate, the derivative of free-surface velocity in this case is continuous at the point $t = 2\tau_k$, and a minimum is reached at $t = t_m > 2\tau_k$, where

$$t_m = 2\tau_k + \frac{\tau_\mu}{1-\alpha}\left(4k\tau_\mu\right)^{(1/\alpha)} \tag{6.25}$$

The corresponding velocity magnitude, u_m, is derived from Eq. (6.20). In practice, the spall strength is determined through the velocity pullback $\Delta u_{fs} = 2u_o - u_m$. For $\alpha = 0$, we have $\Delta u_{fs} = -2p_k/\rho c$. In the general case, the velocity pullback also depends on the damage kinetics and the expansion rate in the incident pulse through the relation

$$\Delta u_{fs} = -\frac{2p_k}{\rho c} + \frac{\rho c^2 \alpha}{2\rho c(1-\alpha)}\left(4\tau_\mu \rho \dot{V}\right)^{(1/\alpha)} \tag{6.26}$$

Initially, the negative pressure reaches the value $p^* = -\rho c \Delta u_{fs}/2$ in the plane with coordinate $h^* = -\sigma^*/(2k\rho c) < h_k$. Let us estimate the damage rate value that corresponds to the minimum in the free-surface velocity profile. In terms of the model of kinetics of damage that has been used, the damage rate is largest on the plane with coordinate h_k where fracture first began. Going back from the free surface to this plane and from time t_m, when the minimum velocity occurs, to time $t = t_m - \tau_k$, we find the damage rate to be equal to $\dot{V}_v = 4k/\rho = 4\dot{V}$. This result coincides with that for constant damage rate. The minimum in the free-surface velocity profile and, consequently, the beginning of spall pulse formation, is observed when the damage rate on the spall plane is equal to four times the expansion rate in the unloading part of incident pulse.

The wave dynamics for the case where the damage rate is assumed to be a function of pressure was analyzed by Utkin (1992, 1993) using an approach similar to the one discussed above. In this case, a segment with horizontal slope appears on the free-surface velocity profile when the damage rate is equal to four times the expansion rate in the unloading part of the incident compression pulse.

In reality, the damage rate is a function of both tensile stress and degree of damage. As a result, the threshold damage rate that corresponds to the appearance of a minimum in the free-surface velocity profile can be reached at many times during the development of fracture. This time interval decreases with increasing tensile stress while the reflected rarefaction wave propagates from the free surface into the body. Figure 6-8 shows the threshold line in the time-distance diagram, along which the condition $\dot{V}_v = 4\dot{V}$ is satisfied. The spall signal arrives at the sample surface from the point on the this line where the slope is

$$\frac{dt}{dx} = -\frac{1}{c} \tag{6.27}$$
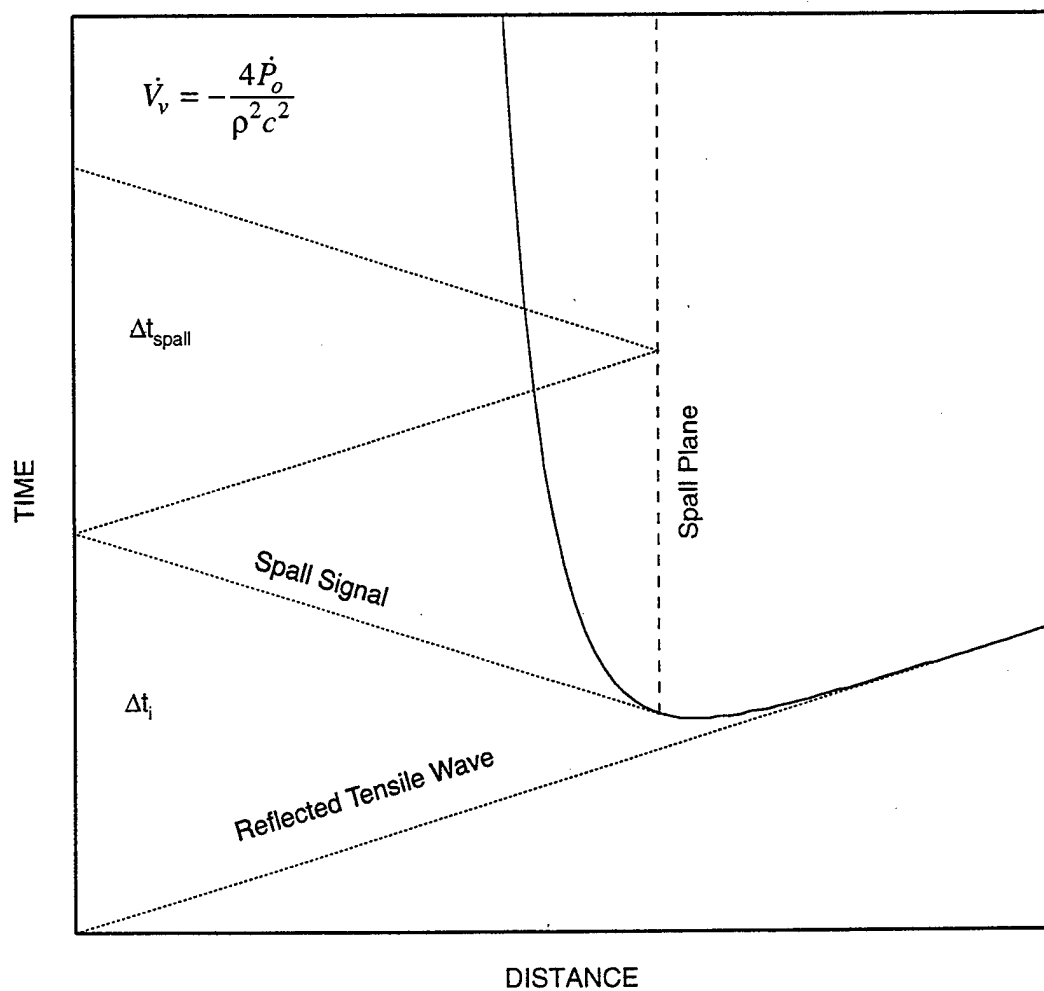
Figure 6-8. Time-distance diagram for the spall process caused by the reflection of a triangular compression pulse from the free-surface (represented by the time axis) for the case where the damage rate is a function of tensile stress and damage.

156

As a result, the duration, Δt_i, of the first velocity pulse on the free-surface velocity profile exceeds the periods, Δt_{spall}, of later (after beginning of fracture) velocity oscillations. The difference between these time intervals is interpreted as an apparent delay time of the spall fracture. Obviously, development of the fracture to the left of the spall plane is suppressed by the compression wave created as a result of the relaxation of the tensile stress in the spall plane.

SECTION 7

SPALLATION IN MATERIALS OF DIFFERENT CLASSES

This section summarizes the results of instrumented measurements of the resistance of materials of different classes to dynamic fracture. The results discussed here were obtained from wave propagation experiments under uniaxial strain conditions and consist primarily of free-surface velocity measurements. The recorded motion of the body free surface does not provide any information about cracks, voids, or other physical characteristics of spall damage, but it does provide the most direct and most reliable information about the fracturing stress magnitude and the stress relaxation at fracture. The experiments discussed here investigated the influence of the peak shock pressure, temperature, load duration and orientation, and the structure of the materials on the resistance to spall fracture for materials of different classes including commercial metals and alloys, ductile and brittle single crystals, glasses, ceramics, polymers, and elastomers.

These experiments were performed by Genady Kanel and his co-workers at the Russian Academy of Sciences. Thus, the materials investigated are those readily available in the Former Soviet Union, and in some cases, those materials are somewhat different from those available in the United States. For this reason, Appendix A of Volume 2 gives the composition of each of the tested alloys. Whenever appropriate, Appendix A also provides the U.S. equivalent of the FSU alloys.

This section includes only a fraction of the results—that fraction needed to show trends and discuss specific aspects of the behavior of the various materials investigated. A more comprehensive compilation of all the data is provided in Appendix B (Volume 2). IThis comprehensive, self-contained summary of each of 148 experiments include: (1) a description of the material investigated including its density and elastic properties, (2) a schematic diagram of the experiment, (3) the dimensions and conditions of the material investigated, (4) the technique used to perform the measurement and the associated experimental error, and (5) the experimental results which in all cases take the form of a particle velocity history recorded at the free surface of the sample or at the interface between the sample and a softer material.

7.1 METALS AND METALLIC ALLOYS.

Metals are the materials most thoroughly investigated in research on spall phenomena. Figure 7-1 shows results of experiments with strong Fe-Cr-Ni-Mo steel 35X3HM (Glusman et al., 1985). The samples were cut from a bar workpiece in two orientations. Some of the tests were performed under shock loading

158
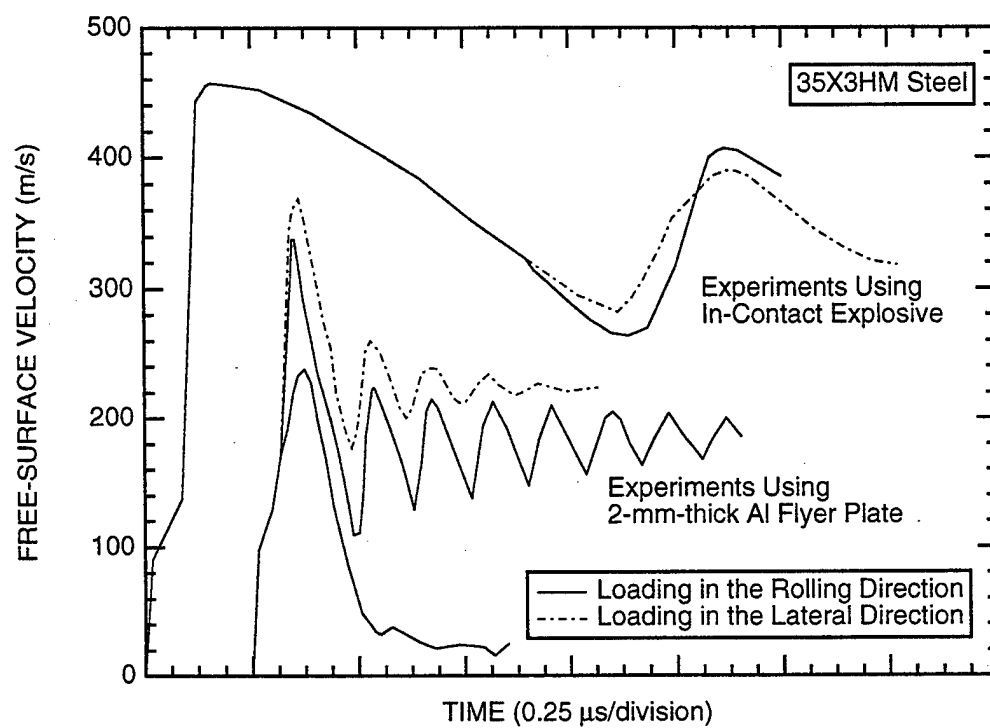
Figure 7-1. Free-surface velocity histories at spalling in 35X3HM steel (Fe-Cr-Ni-Mo).

in the rolling direction, while others were performed under shock loading in the lateral direction. In both cases, the free-surface velocity profiles were recorded.

Those profiles, shown in Figure 7-1, display the influence of load directions on the dynamic strength. The resistance to dynamic fracture is 4 to 4.4 GPa for loading in the rolling direction and 10% to 15% less for loading in the lateral direction. The faster decay of the velocity oscillations in the latter case is due to a more highly developed fracture surface. For samples loaded in the rolling direction, rather uniform, fine-grained, and light fracture surfaces were observed. In the samples loaded in the transverse direction, fracture occurred mainly along intergranular boundaries, and consequently, fracture surfaces demonstrated well-pronounced texture. The fracture surfaces were dark and much less uniform. The nonuniformity of the fracture surface accelerates the dispersion and decay of the wave reflected from the spall plane.

From the free-surface velocity profiles shown in Figure 7-1, we can estimate the average velocity of the spall plate simply by calculating the shift of the surface during one velocity oscillation and then dividing this shift by the duration of this oscillation. Such estimations indicate that the average spall plate velocity is practically constant. We may then conclude that the fracture time for this steel is less than half a period of the free-surface velocity oscillations, which is less than 10^{-7} s. Therefore, fracture of this steel is relatively brittle in nature and is completed by the end of the first half-period of velocity oscillations.

A protracted, slowly evolving spall fracture was observed for more viscous materials such as stainless steel (Kanel, 1982a and 1982b) (Figure 7-2). In this case, the spall plate continued to decelerate for a long time after the initial appearance of the spall pulse, indicating the continuous evolution of fracture. Similar behavior was also observed for other materials when the incident pulse duration was shorter than the time required for complete fracture.

Table 7-1 gives the results of measurements of spall strength for several metals and alloys at various load durations. These measurements showed that the resistance to fracture under these impact conditions increases with increasing characteristic rate of expansion. No correlation is apparent between the total time of fracture and the fracture stress dependence on the characteristic load duration. This can be verified, for example, by comparing the experimental data for stainless steel with similar data for other materials. The dependence of fracture stress on characteristic load duration appears to be determined rather by the intrinsic properties of existing damage nucleation sites and their initial growth velocity. The total time of the fracture process depends on the rate of later development and coalescence of voids.

To evaluate the effect of load duration on the measured strength, we next compare the spall strength measured under impact loading conditions with the corresponding strength determined under quasi-static conditions. Standard quasi-static tensile tests may be interpreted in terms of engineering stress (peak load divided by original cross section area), σ_b, which characterizes the maximum load withstood by the

160
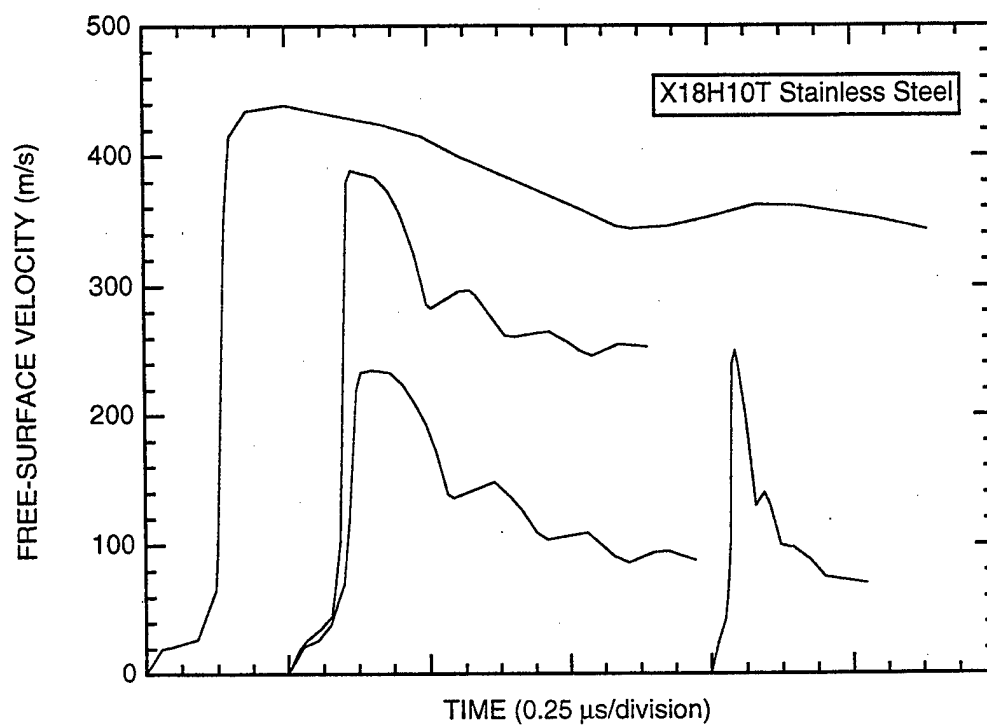
Figure 7-2.   Free-surface velocity profiles at spalling in stainless steel..

(Note the continued deceleration after the arrival of the
spall signal at the free surface.)

Table 7-1. Spall strength of metals and alloys determined based on measurements of the free-surface velocity histories.

Material	S_k (GPa)	Strain Rate (s^{-1})	Spall Strength (GPa)	Spall Thickness (mm)	Reference
Aluminum alloy AMG6m (Al-6%Mg), sheet		6.2×10^3	0.57 ± 0.1	4.7	Kanel, Razorenov, and Fortov (1984a).
		8.9×10^4	0.83 ± 0.08	0.61	
		2×10^5	1.15 ± 0.05	0.34	
		5.1×10^5	1.2 ± 0.12	0.18	
Aluminum P1C		10^5 to 10^6	0.9 to 1.2	0.25 - 0.9	Speight, Taylor, and Wallace (1973)
Aluminum alloy 2024	0.4-0.6	3×10^4	1.15 ± 0.1	2.75	Taylor (1968)
Aluminum alloy V95			1.6 to 1.8	4 to 10	Romanchenko and Stepanov (1980)
Copper M2		2.8×10^3	0.8 ± 0.1		Kanel, Razorenov, and Fortov (1984b)
		3.4×10^4	1.1 ± 0.1	0.5	
		2.5×10^5	1.64 ± 0.1	0.2	
Copper OFHC			1.2	0.8 to 3	Cochran and Banner (1977)
Magnesium Ma1		3×10^4	0.8	0.62	Kanel, Razorenov ,and Fortov (1984b)
		1.1×10^5	0.88	0.29	
Magnesium AZ31B			0.8	3 ·	McQueen et al. (1970)
Titanium alloy VT6	1.6	7.3×10^4	3.7 ± 0.2	1.7	Kanel and Petrova (1981)
		5.7×10^4	3.5 ± 0.2	1.8	
		8.3×10^3	3.4 ± 0.2	9.8	
Titanium alloy Ti 6Al 4V			4.1 to 5		Me-Bar et al. (1987)
Titanium alloy VT8		7.5×10^4	4.65 ± 0.3	1.65	Kanel, Razorenov, and Fortov (1987)
Uranium			2.4 ± 0.1	0.8 to 3	Cochran and Banner (1977)
Tantalum		8×10^4	4.6 ± 0.2	1.15	McQueen et al. (1970)
Tantalum			4.4	0.8 to 3	Cochran and Banner (1977)
Tungsten W-2			0.74		Rozenberg (1987)
Tungsten			0.42 to 0.66		Asay, Chhabildas, and Dandecar (1980)
Armco iron	1.2	2.9×10^4	1.65 ± 0.1	1.1	Kanel and Shcherban (1980)
		6×10^3	1.4 ± 0.1	4.2	
Austenit stainless steel Kh18N10T	1.6 to 1.8	1.05×10^5	2.3 ± 0.1	0.5	Kanel (1982a)
		4.5×10^4	2.0 ± 0.1	1.6	
		2×10^4	1.9 ± 0.1	3.75	
		5.3×10^3	1.85 ± 0.1	6.9	
Stainless steel 304		2.5×10^4	2.1	3.4	McQueen et al. (1970)
			3	0.8 to 3	
Austenit steel		3.2×10^4	2.9	4	McQueen et al. (1970)
Steel 4330V			4.8	0.8 to 3	Cochran and Banner (1977)

[1]S_k is the true breaking strength under static conditions.

sample, or in terms of the true stress $S_k > \sigma_b$ found with due regard for the change in the cross-sectional area of the sample in the "neck" region.

For ductile materials, the discrepancy between S_k and σ_b may be very large. Because σ_b is a measure of the loss of stability of the sample (but not of the material), it cannot be used as a basis for comparing the strength properties determined under different loading conditions (i.e., uniaxial stress for the quasi-static test and uniaxial strain for the dynamic spall test). The true tensile breaking stress S_k provides a more objective basis for comparison. Comparison of the spall strength, obtained at load durations on the order of 1 μs, with the quasi-static true breaking stress shows that the spall strength usually exceeds the static strength by a factor of 1.5 to 2.0.

Since the fracture time under shock wave loading conditions is comparable to the duration of the load, it is important to determine the stage of fracture that corresponds to the fracture stress determined by a given method. The damage rate is approximately equal to the product of the concentration of damage nucleation sites times their average growth rate. This damage growth rate cannot be arbitrarily large. Consequently, significant overstressing of the material is possible if the load is applied at a high rate. However, several thresholds of spalling (incipient fracture, intermediate stage, and the main crack formation) can be observed in samples after testing with load pulses of various durations (Smith, 1962). The existence of several thresholds is a consequence of evolution of the fracture process in time. The question arises: Which stage of fracture is related to the spall strength determined from the free-surface velocity profile?

The rate of damage that can be observed in the wave profiles depends on the decompression rate in the incident load pulse. Actually, the spall pulse can be seen on the free-surface velocity profile if the fracture kinetics are fast enough. A slower fracture process leads to an increased rise time of the spall-pulse front. At some damage rate, we can obtain the spall pulse with zero gradient in its front. In this regime the compression wave produced by stress relaxation during the relatively slow fracture process compensates for the rarefaction in the incident release wave. Obviously, the damage rate that leads to this condition will be different for different load parameters.

The situation with wave compensation is realized at the minimum point of the $u_{fs}(t)$ profile ahead of the spall pulse. The acoustic analysis presented in Section 6 shows that a minimum in the free surface velocity profile appears when the rate of damage is equal to four times the decompression rate in the incident load pulse. In other words, each spall stress value corresponds to some specific damage rate:

$$\dot{V}_v^* \approx 4\left(\frac{\dot{u}_1}{2\rho c_b}\right)$$

(7.1)

163

where $\dot{u}_1$ is the surface-velocity gradient in the decompression part of the incident load pulse. Comparison of the duration of the first velocity pulse and the periods of the following velocity oscillations (after fracture initiation) on the $u_{fs}(t)$ profile can give the delay time for achieving this damage rate. The period of oscillations must be shorter than the first velocity pulse if any delay exists. Correcting for elastic-plastic properties of the material must be taken into account. Similar analysis for metals shows that the damage rate discussed usually corresponds (practically without any delay) to the time at which the tensile stress on the spall plane reaches σ^*. Thus, an empirical dependence $\sigma^*(\dot{u}_1)$ or $\sigma^*(\dot{\varepsilon})$, where $\dot{\varepsilon} = \dot{V} = -\dot{u}_1 / 2c_b$, reflects the initial damage rate dependence on the applied tensile stress, i.e., $\dot{V}_V(\sigma)$.

Thus, the measured fracture stress determines the conditions of spall initiation. Note that irregularities of the fracture surface become finer with decreasing load pulse duration, and this is accompanied by an increase in the overstress in the sample. Smaller and more numerous damage nucleation sites are activated as the peak stress increases during propagation of the tensile wave into the sample, leading to an increase of the initial damage rate. Near the surface of the sample, the tensile stresses are not so high and fracture is initiated at coarser defects. Because the number of coarse defects is relatively small, the resulting fracture is not fast enough to provide substantial relaxation of tensile stresses. Development of fracture near the surface of the specimen is arrested by unloading because the fast fracture in deeper layers of the sample.

Comparing the spall strength deduced from free-surface velocity measurements with thresholds of spallation determined through metallographic examination of recovered samples shows that the spall strength values agree with the incipient fracture threshold or, in some cases, are even less than this threshold. Two other thresholds, corresponding to intermediate and complete fracture, occur at higher shock intensities. This does not necessarily mean that fracture occurs under higher tensile stresses. Indeed, stress relaxation just after fracture initiation limits the growth of tensile stresses as the shock wave intensity is increased. Full separation of the sample at the spall plane occurs much later than the time instant when maximum tensile stress is reached. The development and completion of the fracture process occur at lower stress and require additional consumption of energy.

Figure 7-3 shows the results of experimental data for five metals plotted in terms of σ^* as a function of $(\dot{V}/V_o)$. The decompression rate in the load pulse, $(\dot{V}/V_o)$, has been chosen as a parameter characterizing the time dependence of the spall strength because such a dependency can be used to construct kinetic relationships according to the analysis presented in Section 6. The resistance to spall fracture can be represented as a power function of the decompression rate of the form

$$\sigma^* = A(\dot{V}/V_o)^m \qquad (7.2)$$

164
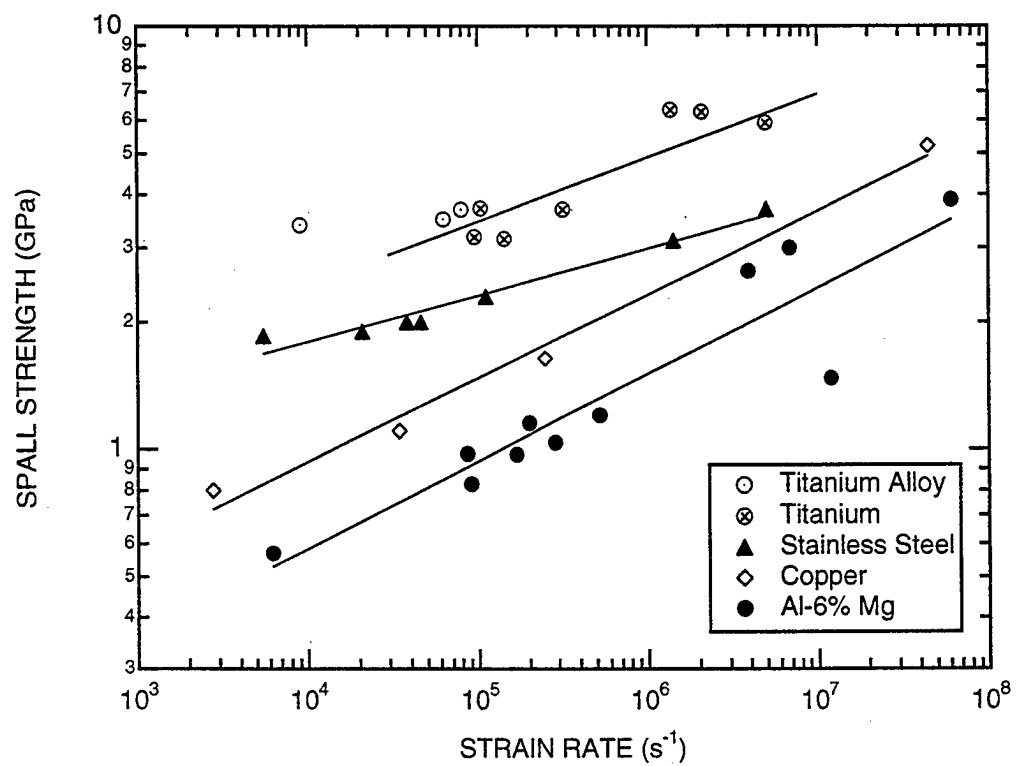
Figure 7-3. Spall strength as a function of unloading strain rate in the incident load pulse.

The constants A and m in this equation are presented in Table 7-2 for stainless steel, titanium, copper, aluminum, and magnesium.

Under conditions of shock-wave testing, materials undergo fast compression and heating before the beginning of tension and fracture. Thus, the effect of temperature on the resistance to spall must be evaluated to properly interpret experimental results. Kanel et al. (1987) studied the effect of temperature on the spall strength of titanium alloys in the peak shock pressure range of 2 to 90 GPa. Samples of VT8 titanium alloy were impacted by 2-mm-thick aluminum flyer plates at velocities of 660 m/s, 1900 m/s, and 5300 m/s. This range of impact velocities led to peak shock pressures ranging from 6.5 to 77 GPa, a variation of more than an order of magnitude.

The results, in the form of free surface velocity profiles, are shown in Figure 7-4. These measurements show that the spall strength of the alloy is 4.16 ± 0.06 GPa under the conditions investigated, it remains practically constant, and it does not depend on the peak shock pressure before the fracture. Note that the residual temperature of samples before spall fracture occurred reached as high as 1100∞K as a result of irreversible heating in the shock front, and the total deformation in the complete loading-unloading cycle was as high as 60%. Furthermore, these experiments, as well as experiments involving variation of the load direction, show that, because deformation in the shock front and shock-induced changes in the material microstructure do not influence the resistance to spalling, damage nucleation sites are relatively coarse preexisting defects, such as inclusions, micropores, and grain boundaries. It is natural to assume that higher stresses are necessary for damage nucleation on a dislocation level.

Figure 7-5 shows experimental data on the spall strength of aluminum AD1 (Al 1100) over a wide range of peak pressures and load durations (Kanel et al., 1996a). The spall strength, in fact, does not depend on the peak shock pressure in a range up to 35 GPa. Two experiments were performed at a peak pressure of 50 GPa. Measurements at this pressure were not very accurate, but in general the results show approximately a 20% decrease in the spall strength. According to the equation of state of aluminum (McQueen and Marsh, 1960), the residual temperature of the sample after unloading from a peak shock pressure of 50 GPa is about 450∞C, or about 70% of the 660.2∞C melting temperature of aluminum.

These results suggest that the spall strength of metals decreases with increasing temperature near the melting point. Further evidence of this trend is illustrated in Figures 7-6 and 7-7, which show the dependence of spall strength on temperature for tin and lead, respectively (Kanel et al., 1996b). These measurements show a substantial drop in the spall strength when the peak shock pressures approach values high enough to achieve melting after the shock-wave compression and unloading process.

Relatively few spall studies have been conducted on moderately preheated materials (Bless and Paisley, 1984; Dremin and Molodets, 1990); Duffy and Ahrens, 1994), and in contrast to results obtained

Table 7-2. Spall strength as a function of the strain rate for selected materials.

Material	A (GPa)	m
Stainless steel 35Kh3NM	0.65	0.11
Titanium	0.39	0.19
Copper	0.15	0.2
Aluminum - 6%Mg alloy, sheets	0.088	0.21
Aluminum AD1 (1100), rod	0.635	0.059
Magnesium Mg95, casting	0.39	0.072
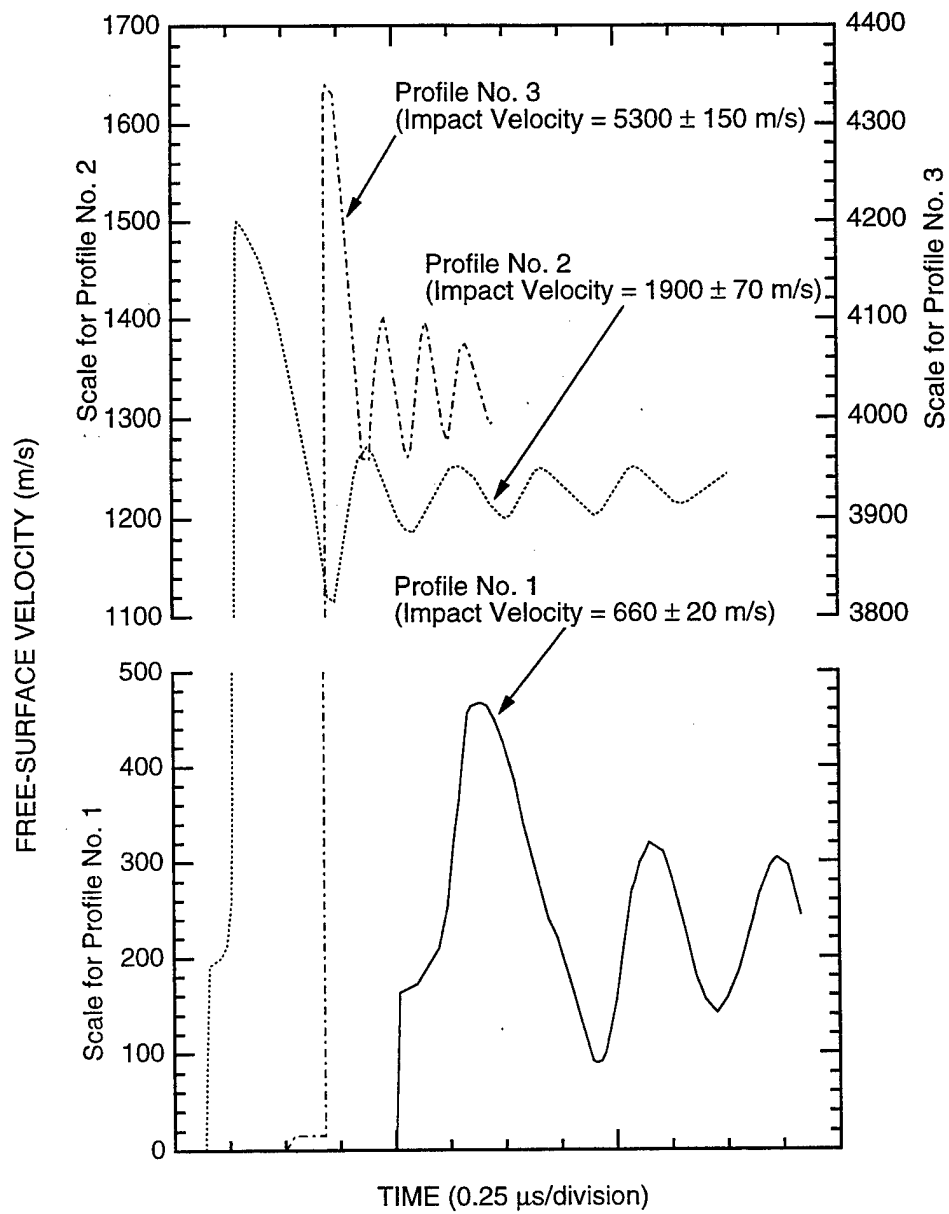
Figure 7-4. Free-surface velocity profiles for the VT8 titanium alloy obtained using the plate impact experimental configuration.
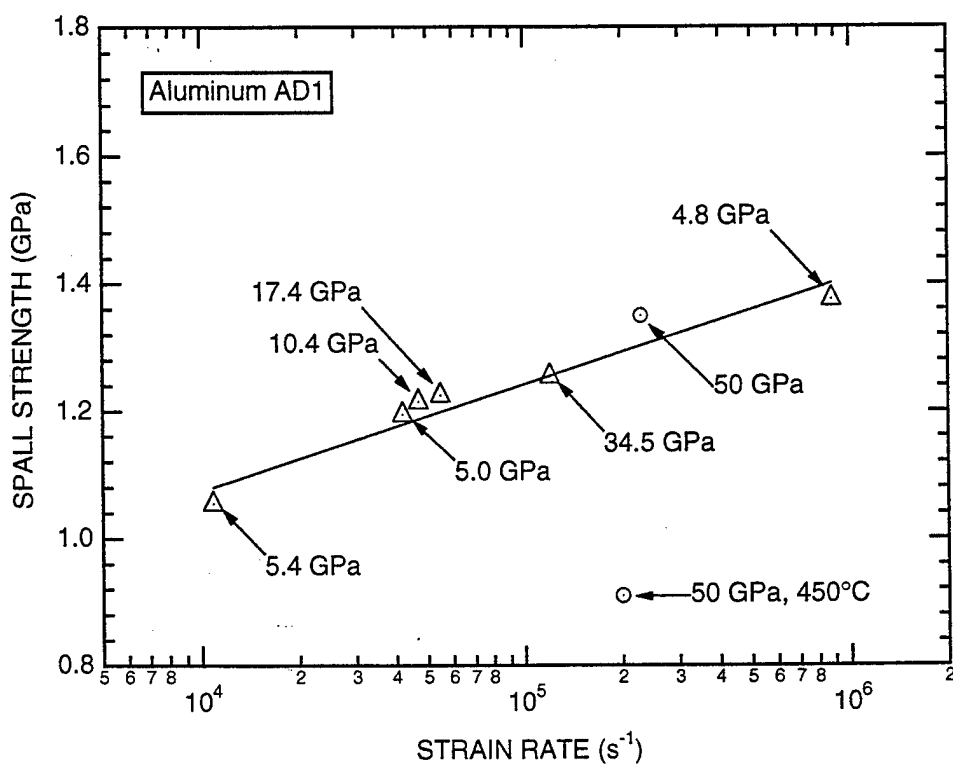
Figure 7-5.   Spall strength of aluminum AD1 (Al 1100) as a function
of strain rate and peak applied pressure.
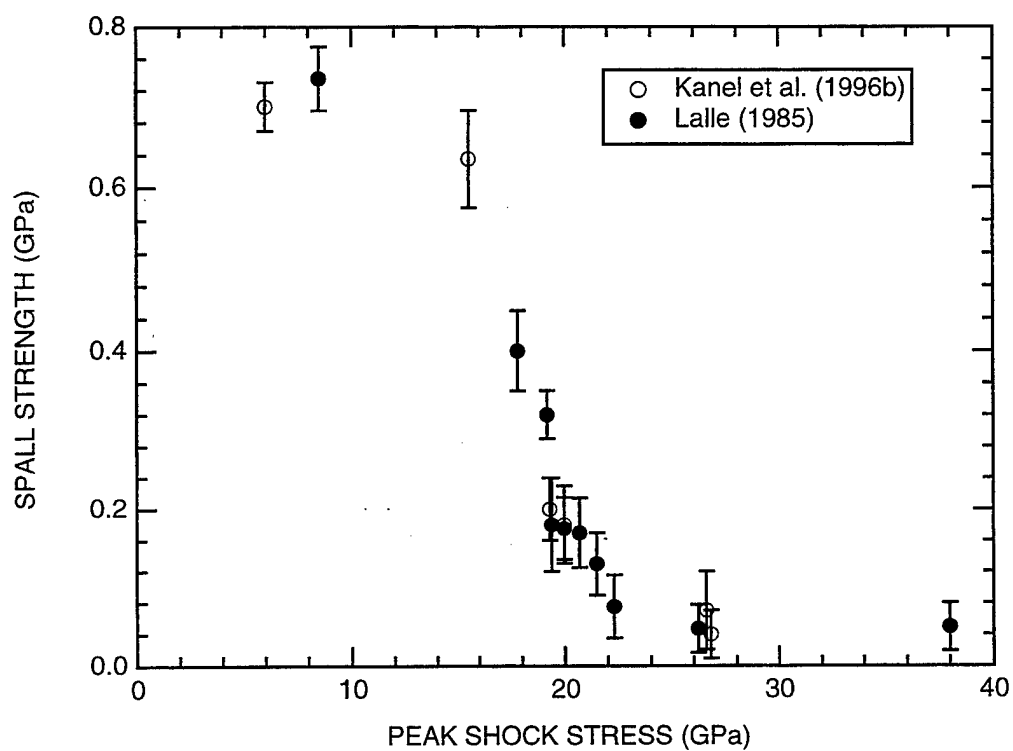
Figure 7-6.   Spall strength of tin as a function of peak shock stress.
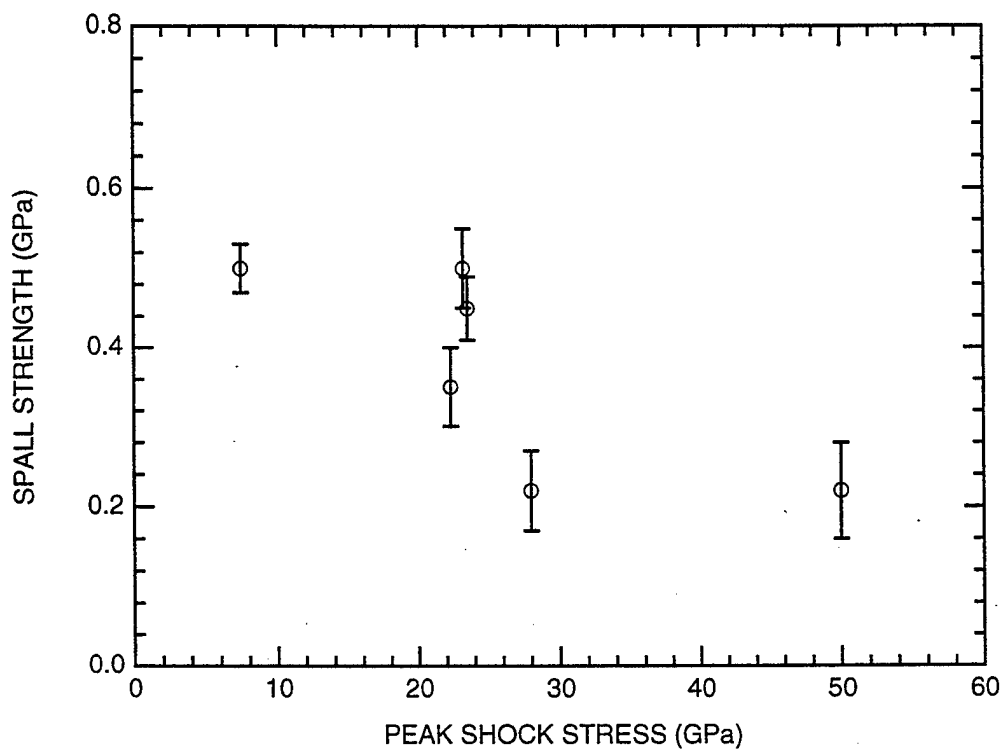
Figure 7-7. Spall strength of lead as a function of peak shock stress.

under quasi-static loading conditions, these results show that the dynamic strength of metals is usually not affected significantly by moderate increases in temperature. Free-surface velocity profiles obtained in experiments with copper at 300 K and 700 K initial temperatures (Bless and Paisley, 1984) did not display any essential variations of the spall strength. Experiments with pure molybdenum preheated to 1700 K (Duffy and Ahrens, 1994) resulted in a spall strength of 2.4 GPa, only slightly different from the value of 2.31 GPa reported for room temperature molybdenum by Chhabildas et al. (1990) at the same peak pressure and from values ranging of 1.3 to 2.4 GPa measured for commercial grade molybdenum at room temperature (Kanel et al., 1993). Similar experiments with Armco-iron (Dremin and Molodets, 1990) over an initial temperature range from 77 K to 540 K showed an insignificant decrease of spall strength with increasing temperatures that did not exceed the experimental error.

Metallographic examination of recovered samples tested by impact at various impact velocities and different temperatures provide additional insight into the effect of temperature on spall. Experiments with OFHC copper at room temperature and at 425°C (Bless and Paisley, 1984) indicate that increasing the temperature causes a slight increase in the stress required to initiate damage. The voids are more spherical in room temperature copper, and more small voids are present at elevated temperature. The observed void distributions are consistent with the hypothesis that voids grow slower at elevated temperature. According to Golubev et al. (1985), the incipient fracture threshold for copper decreases from ~1.8 GPa at an initial temperature of -196°C to ~1.2 GPa at 800°C. The room temperature spall strength of copper deduced by Cochran and Banner (1977) and by Kanel (1982a) from free-surface velocity profiles at the same load conditions is also 1.2 GPa. For nickel the incipient fracture threshold decreases from ~3.5 to ~1.5 GPa over this same temperature range (Golubev et al., 1985); the spall strength value measured instrumentally at room temperature is 1.5 GPa. For aluminum alloys from -196°C to 600°C, the damage nucleates at approximately the same stress between 1 and 1.2 GPa (Golubev et al., 1983). According to Golubev et al. (1988), the incipient fracture threshold of Al - 6% Mg alloy decreases from 1 GPa at 0°C to 0.7 GPa at 500°C for rod samples and is approximately constant at ~0.7 GPa over this temperature range for sheet samples.

Spall measurements on samples preheated over the full temperature range from ambient to near melting were performed by Kanel et al. (1996a). Figure 7-8 shows the dependence of the spall strength on the initial temperature for aluminum AD1. All but one of these measurements were done at a 5.8 GPa peak shock pressure. In general, the spall strength decreases with increasing initial temperature. A sharp drop in the spall strength is associated with heating above 550°-600°C. One experiment in this series was done with peak shock pressure of 10.4 GPa and an initial temperature of 610°C. Comparisons of spall strength data at different shock intensities and similar initial temperatures shows that, as a result of the additional heating of the material by the shock wave, the spall strength is a strong function of the peak shock pressure when the initial temperature is near the melting point.
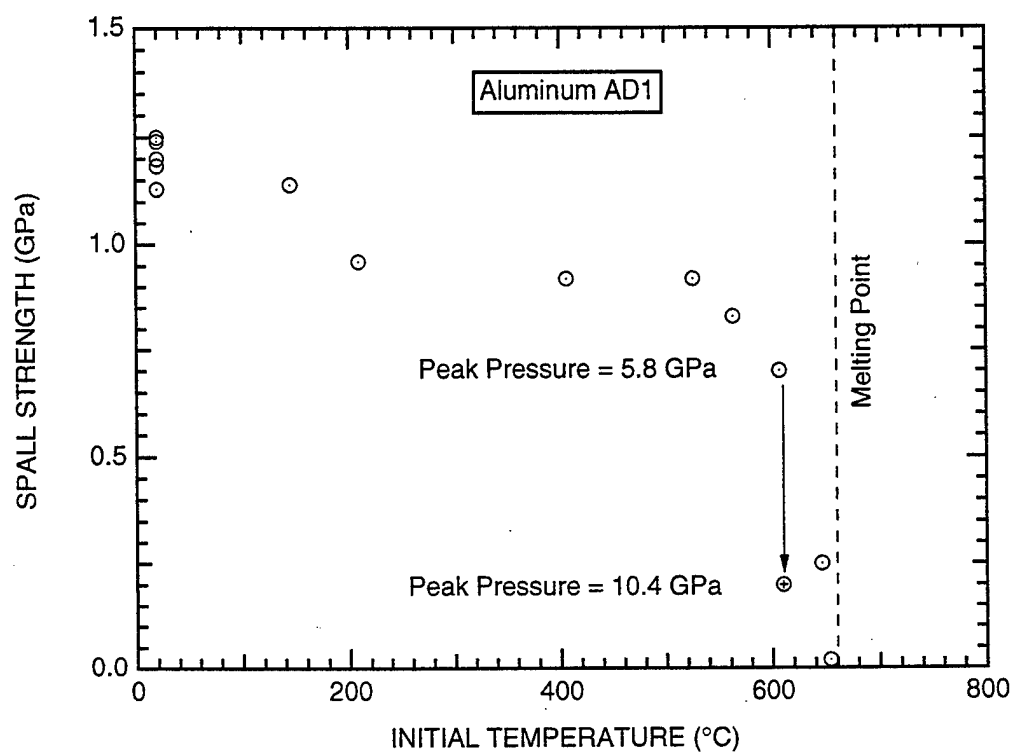
Figure 7-8. Spall strength of aluminum AD1 as a function of initial temperature at peak shock pressures of 5.8 and 10.4 GPa.

Figure 7-9 shows spall strength measurements for magnesium Mg95 as a function of initial temperature. As for aluminum, a precipitous reduction in spall strength was observed for magnesium as temperatures neared the melting temperature. The sharp drop initiates at temperatures exceeding approximately 500°C.

An additional complication in the dynamic response of iron and steels is the reversible phase transformation that occurs at approximately 13 GPa. This phenomenon, as well as the incident state of the material, can influence the resistance of the material to dynamic fracture.

Low-pressure experiments with 4340 steel after various heat treatments (Butcher, 1967) exhibited an increase in the incipient spall threshold from 2.55 GPa to 4.4 GPa with increasing hardness of the samples from 15 HRC to 54 HRC. This behavior correlated with the low-strain-rate true strength values of 1.33 and 2.66 GPa for the 15 HRC steel and the 45 HRC steel, respectively. The influence of heat treatment on the spall strength of Russian 40Kh (40X in Russian letters) steel was studied by Golubev and Novikov (1984). Microscopic examination of samples impacted at different velocities showed that the spall threshold increases from ~3 GPa at 20 HRC initial hardness to ~5 GPa at 55 HRC. The damage nucleated on the sulfide inclusions or on the boundaries of martensite blocks. Work hardening as a result of shock loading was observed for all initial states of the samples.

The effects of microstructure on spall fracture were studied for 1008 carbon steel (Zurek and Follansbee, 1990; Zurek et al., 1990) in more detail. The measurements indicated that there is no essential grain size dependence in the range of 25 to 45 μm. However, there is a substantial dependence of the spall strength on the number of carbides per unit volume. The spall strength of 1008 steel increases from 1.2 to 1.8 GPa at decreasing carbide size distribution from 1.5×10^{3} carbides/μm^{3} to 3.7×10^{-4} carbides/μm^{3}. In other words, because the carbides serve as nucleation sites for the brittle fracture, the material with the larger spacing between the damage nucleation sites exhibited the higher spall strength. However, 1007 carbon steel of 5-μm grain size and submicron carbides (Zurek et al., 1990) exhibited the higher spall strength (2.4 GPa) and transition to ductile fracture.

The influence of shock prestrain and peak pressure on the spall strength of pearlitic 4340 steel was studied by Zurek et al. (1992). They found that increasing the shock wave amplitude from 5 to 10 GPa led to a decrease in the spall strength from 3.1 to 2.6 GPa. At 15 GPa peak pressure, which is above the 13-GPa transition pressure, an increase in the spall strength up to 4.8 GPa was observed for annealed samples. Prestrain decreased the spall strength down to 2.9-3.9 GPa at above the 13 GPa transition pressure and had a small effect at 10 GPa peak pressure.

Figure 7-10 shows the free-surface velocity profiles for 40Kh steel samples in two initial states. The 40Kh is a chromium-doped structural steel with the following chemical composition (wt %): C - 0.4, Si - 0.3, Mn - 0.6, Cr - 1. The material was tested in two conditions: "as-received" with a hardness of
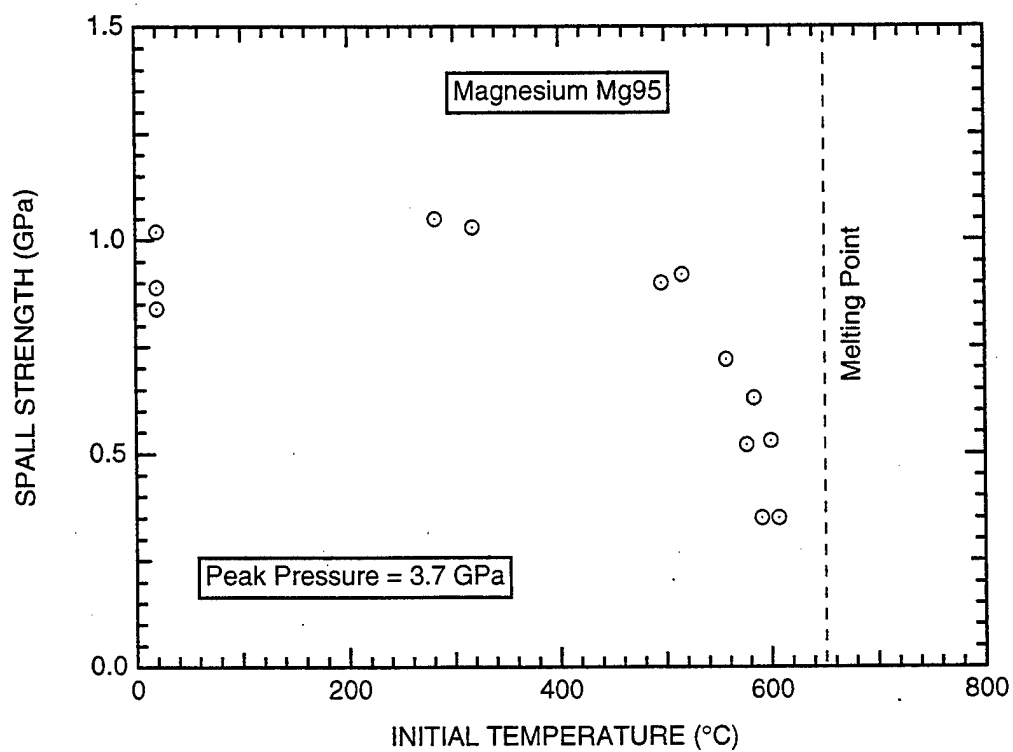
Figure 7-9. Spall strength of magnesium Mg95 as a function of initial temperature at a peak shock pressure of 3.7 GPa.
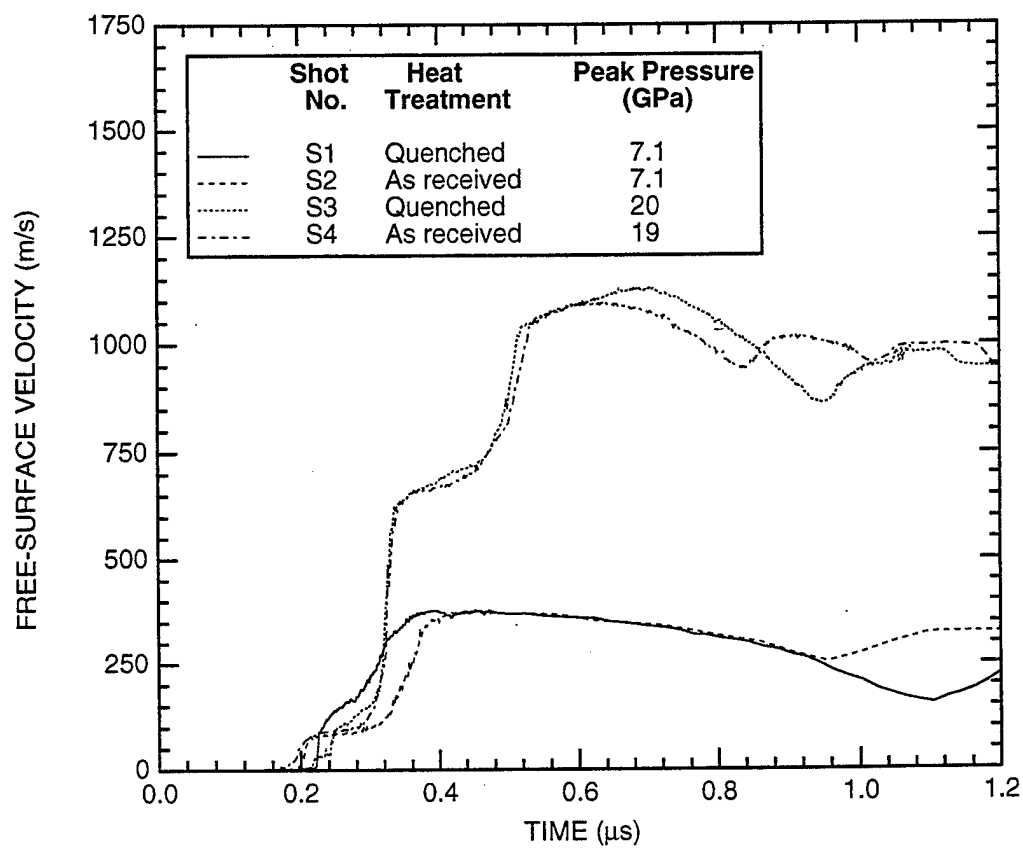
Figure 7-10. Free-surface velocity profiles for chromium-doped structural
steel 40Kh subjected to different heat treatments and shock
pressures.

17 to 19 HRC and quenched with a hardness of 45 to 54 HRC. In the "as received" state, the steel had a ferrite-pearlitic structure with a ferrite grain size of ~20 to 30 μm and pearlitic wafers of about 0.5 to 1.5 μm. The carbide content was about 10%. Quenched steel samples had a martensite structure with isolated grains of the residual austenite (about 2%) and chromium carbide (about 1%). The martensite needles were ~0.5 μm in diameter and ~15 μm long; the austenite grain size was ~1.5 to 2.5 μm. The heat treatment did not result in a large HEL increase, but had a much larger effect on the spall strength values.

Results of the spall strength measurements are summarized in the Table 7-3. The periods, Δt_{sp}, of velocity oscillations after spall fracture and the time interval between the first and the second plastic waves in shot S4 are both equal to ~0.18 μs, which means that the spall fracture occurred near the boundary between the material in the pretransition state and the transformed matter. At low peak stresses, the spall strength values are in a good agreement with the incipient spall threshold that was determined by microscopic examination (Golubev and Novikov, 1984). Measurements show the strength increases as a result of reversible phase transformation for both states of the steel. It is known that the reversible phase transformation causes reduction in the grain size, produces numerous defects, and, as a result, provides a sharp increase in the hardness. These effects hinder the growth of microcracks, which can be the reason for the increase in spall strength. Quenched samples initially have a fine grain martensite structure; therefore, the strengthening effect of the reversible phase transformation is lower in these samples.

7.2 METAL SINGLE CRYSTALS.

The study of spall phenomena in single crystals yields information about favorable conditions of damage nucleation at a structure level close to that of the ideal crystal structure. Single crystalline materials of high purity are free from such relatively coarse defects as grain boundaries and inclusions. The largest nonuniformities of the structure of single crystals, which can serve as stress concentrators for damage nucleation, are formed as a result of interactions of dislocations during plastic deformation.

To shed light on the behavior of single crystals under shock wave loading conditions, Kanel et al. (1992a, 1994a) measured the spall strength of copper and molybdenum single crystals. These two metals differ from each other in many ways including crystal structures (copper has a face-centered cubic structure and molybdenum has a body-centered cubic structure), ductility, elastic limits, and other characteristics of strength. The small lateral dimensions of available single-crystalline samples required the use of shock-wave generators with short load duration. Foil impactors or radiation from a high intensity ion beam were used to produce shock loadings of submicrosecond and nanosecond durations. The influence of crystal orientation, as well as the intensity and duration of the applied load, on the resistance to the spall fracture was investigated.

Figures 7-11 and 7-12 show the free-surface velocity profiles of copper single crystals and commercial-grade copper. Differences between the response of single crystals and polycrystalline material are

Table 7-3. Results of the spall strength measurements for the chromium-doped structural steel 40 Kh at different heat treatment and peak shock pressure.

Shot No.	Sample		Loading Conditions	Peak Stress (GPa)	Strain Rate (10^5 s^{-1})	Spall Thickness (mm)	Spall Strength (GPa)
	Condition	Thickness					
S1	Quenched	3.17 mm	2-mm-thick Al impactor 6-mm-thick Al base plate 0.7 km/s impact velocity	7.1	0.73	1.85	4.2
S2	As received	3.95 mm	2-mm-thick Al impactor 6-mm-thick Al base plate 0.7 km/s impact velocity	7.1	0.54	1.50	2.3
S3	Quenched	3.17 mm	2-mm-thick Al impactor 1.9 km/s impact velocity	20	1.7	0.53	4.7
S4	As received	3.95 mm	2-mm-thick Al impactor 1.9 km/s impact velocity	19[1]	1.6	0.50	2.9
S7	Quenched	3.17 mm	2-mm-thick Al impactor 6-mm-thick Al base plate 5.3 km/s impact velocity	~80[2]	2.4	0.38	4.75
S8	As received	3.95 mm	2-mm-thick Al impactor 6-mm-thick Al base plate 5.3 km/s impact velocity	~75[2]	2.1	0.37	4.0

[1] Spall fracture occurred at the boundary between the material in incident phase and transformed matter.

[2] A decay of the shock wave occurred. The peak stress was estimated using computer simulation of the experiment.
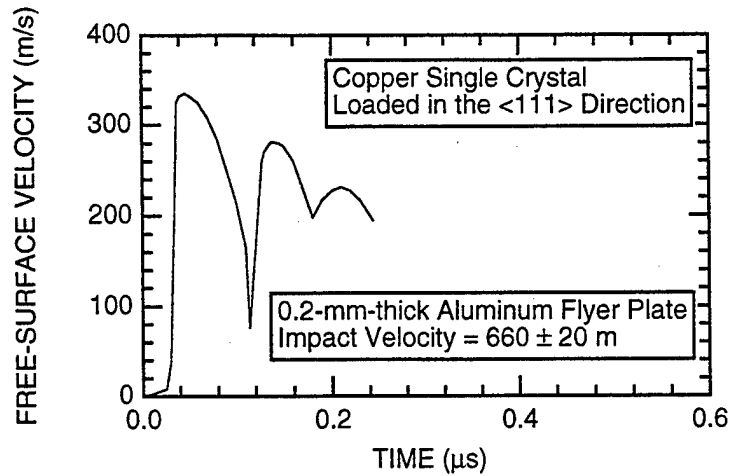
(a) Single crystal (0.2-mm-thick aluminum flyer plate).
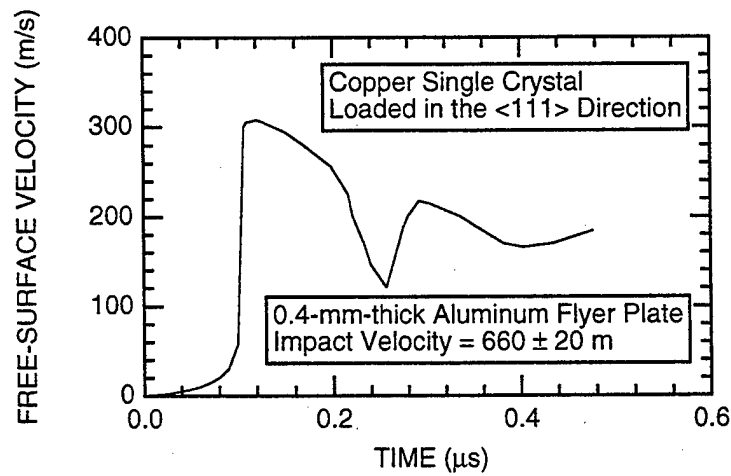
(b) Single crystal (0.4-mm-thick aluminum flyer plate).
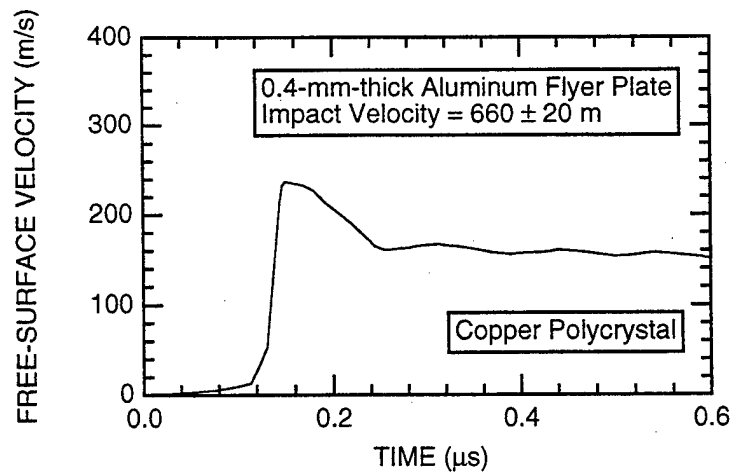
(c) Polycrystal (0.4-mm-thick aluminum flyer plate).

Figure 7-11. Free-surface velocity profiles for copper samples.

179
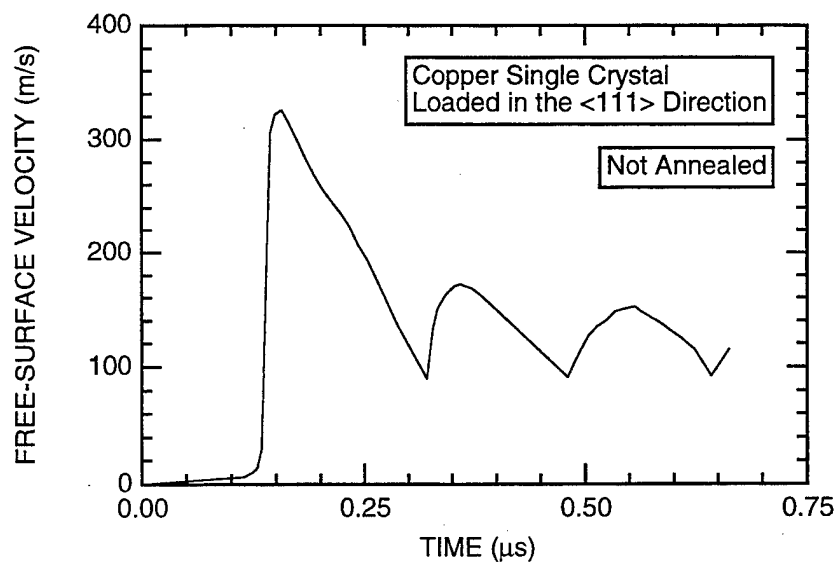
(a) Untreated single crystal loaded ion the <111> direction.
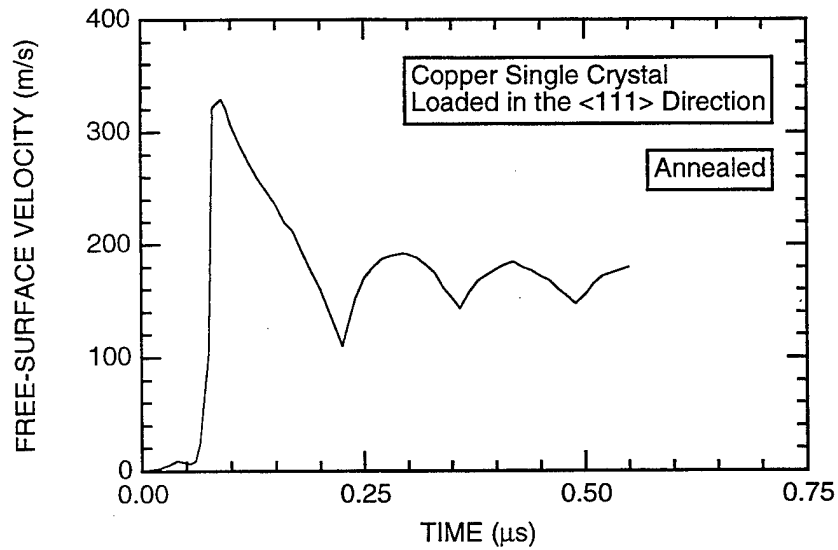
(b) Annealed single crystal loaded ion the <111> direction.

Figure 7-12.   Effect of heat treatment on the free-surface velocity
profiles for copper single crystals.

immediately apparent from comparison of these profiles. The spall strength of single crystals is approximately three times larger than the strength of polycrystalline copper (see also Figure 7-13). For single crystals, the spall pulse is more clearly pronounced. It has a steeper front and higher amplitude than for polycrystalline copper. It is possible to conclude that fracture of single crystals is more brittle in the sense that there is a more pronounced threshold and more rapid evolution of the damage.

Another essential difference between the behaviors of single crystals and polycrystalline material is the rate of decay of the velocity oscillations in the $u_{fs}(t)$ profiles. The slowest decay was observed in single crystals loaded in the <100> direction. Visual observations of shock loaded specimens showed that single crystal specimens loaded in this direction had a smoother fracture surface than the other samples. Comparison of the duration of the incident load pulse with that of the velocity oscillations after spall suggests a delayed fracture. Annealing of single crystals at 900°C for two hours had a small effect on the Hugoniot elastic limit and no effect on spall strength, as shown in Figure 7-12.

The strain-rate dependencies of the spall strength of copper presented in Figure 7-13 show that the strength of polycrystalline copper becomes equal to the measured strength of single crystals when the strain rate reaches 3-7 x 10^7 s^{-1}. This strain rate corresponds to a load duration of ~0.5 ns or to a load pulse length of several micrometers. This result suggests that several micrometers is the characteristic distance between damage nucleation sites that have the same nature in a polycrystalline body and in single crystals. The same size determines the diameter of copper whiskers, where tensile strength values close to those measured in our experiments are realized.

Figures 7-14 and 7-15 show typical free-surface velocity profiles for undeformed and deformed molybdenum and niobium single crystals and for polycrystalline molybdenum. Results of measurements of the spall strength as a function of strain rate are summarized in Figure 7-16. As for copper, the dynamic strength of the molybdenum single crystals is much higher than that of polycrystalline samples. Some small but remarkable delay of fracture was observed in shots with single crystals of all orientations.

The spall strength of molybdenum single crystals is approximately twice the strength of polycrystalline material. As mentioned above, for copper this difference amounted to a factor of 3. The difference between deformed and undeformed single crystals is not so large. However, the amount of dislocations generated by high-speed plastic deformation at the shock front is comparable to the initial dislocation density (~10^{10} cm^{-2}) in the deformed single crystals. The measured spall strength was not reproducible for the copper and molybdenum single crystals in the experiments performed. Because the scatter of experimental data is large, it is difficult to reveal unambiguously the influence of the orientation on the resistance to spall fracture. However, cubic crystals are highly isotropic, and under our load conditions the stress tensor is nearly spherical. Probably, due to these reasons, anisotropy of strength does not exceed the experimental scatter. The reason for the scatter in the strength of single crystals is not clear, but it could reflect a scatter in the initial state of the material. Experiments with more thoroughly characterized

181
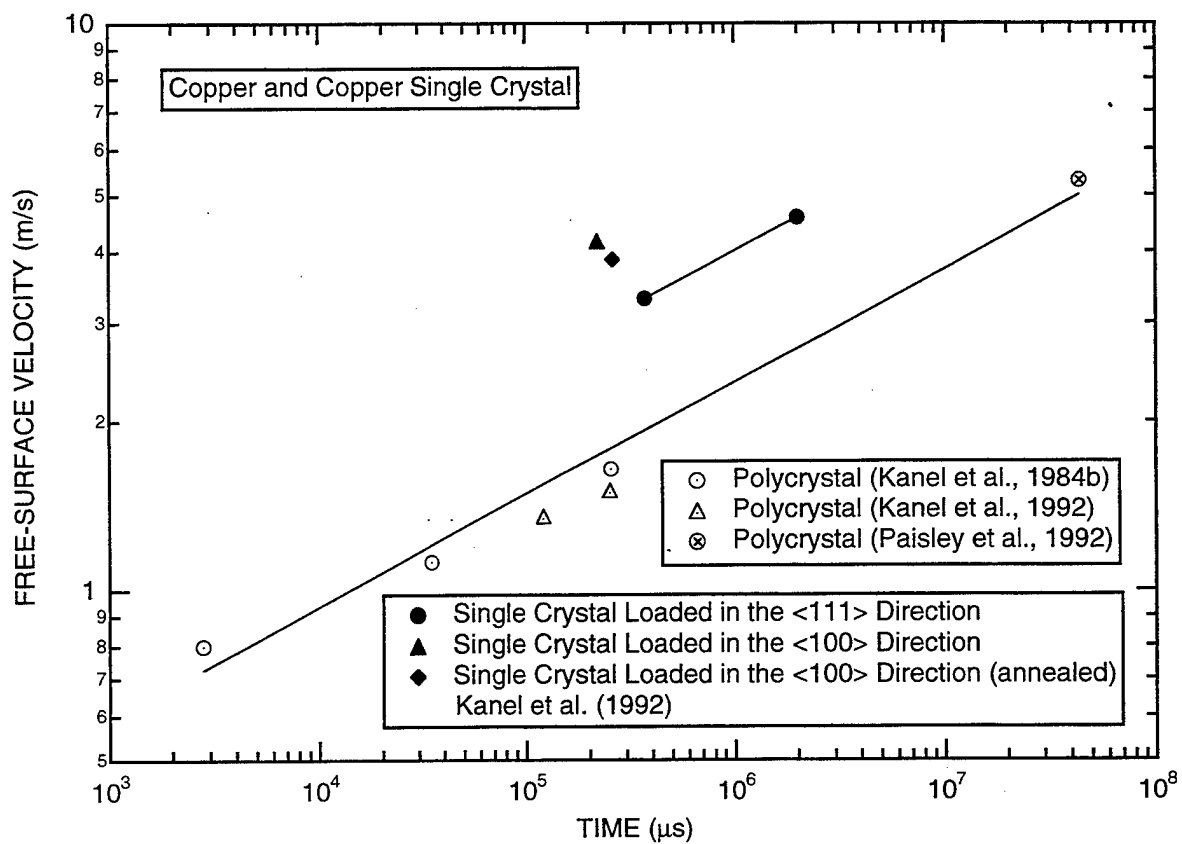
Figure 7-13. Spall strength of commercial grade copper and copper single crystals as a function of strain rate.
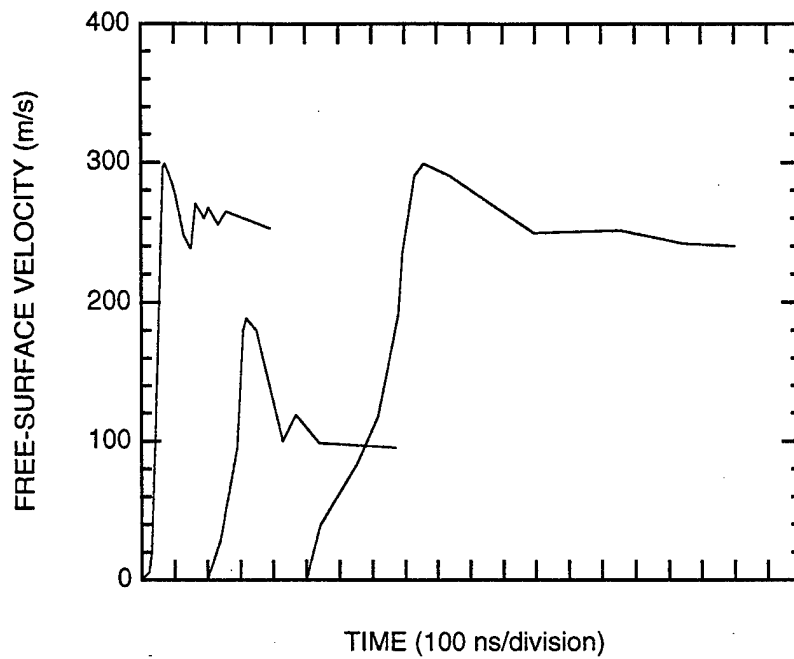
(a) Free-surface velocity profiles in molybdenum.
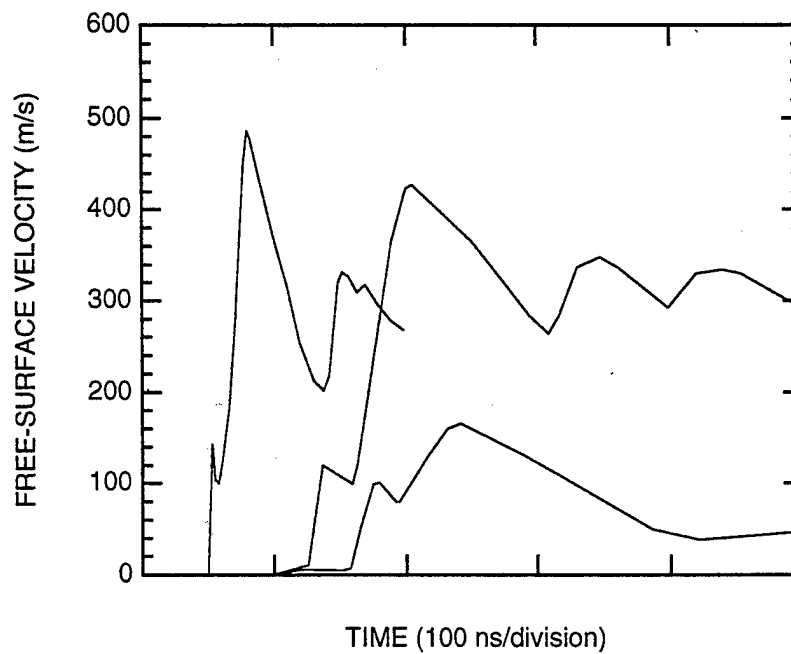
(b) Free-surface velocity profiles in molybdenum single crystal.

Figure 7-14. Spallation in molybdenum and molybdenum single crystals.
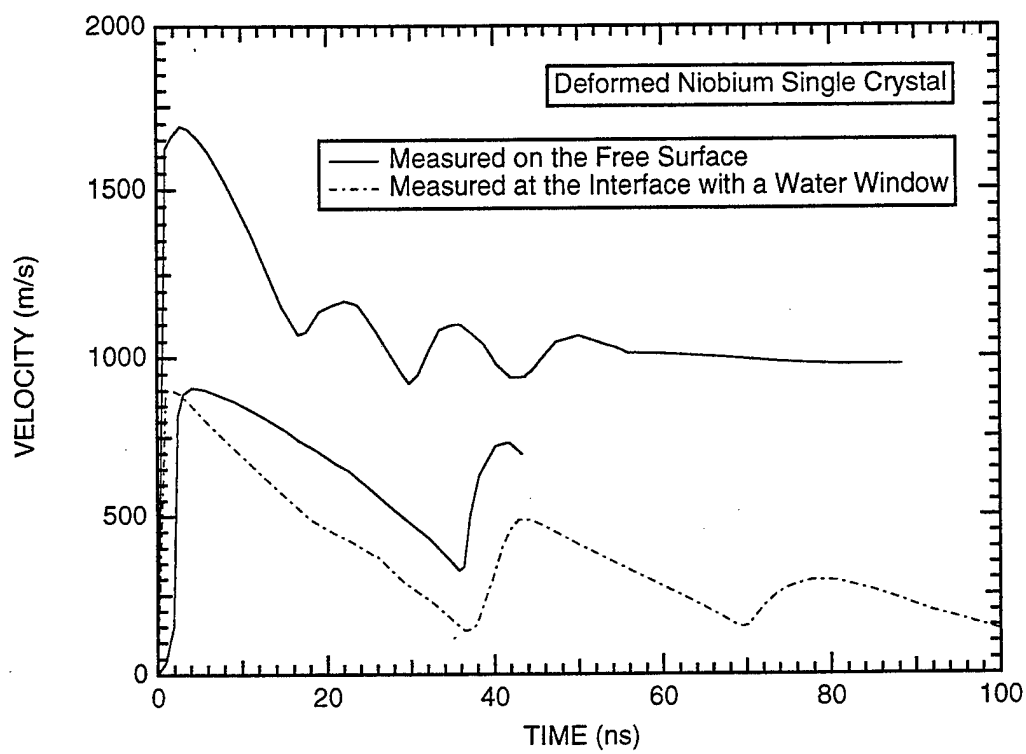
Figure 7-15. Results of spall measurements for deformed niobium single crystals.
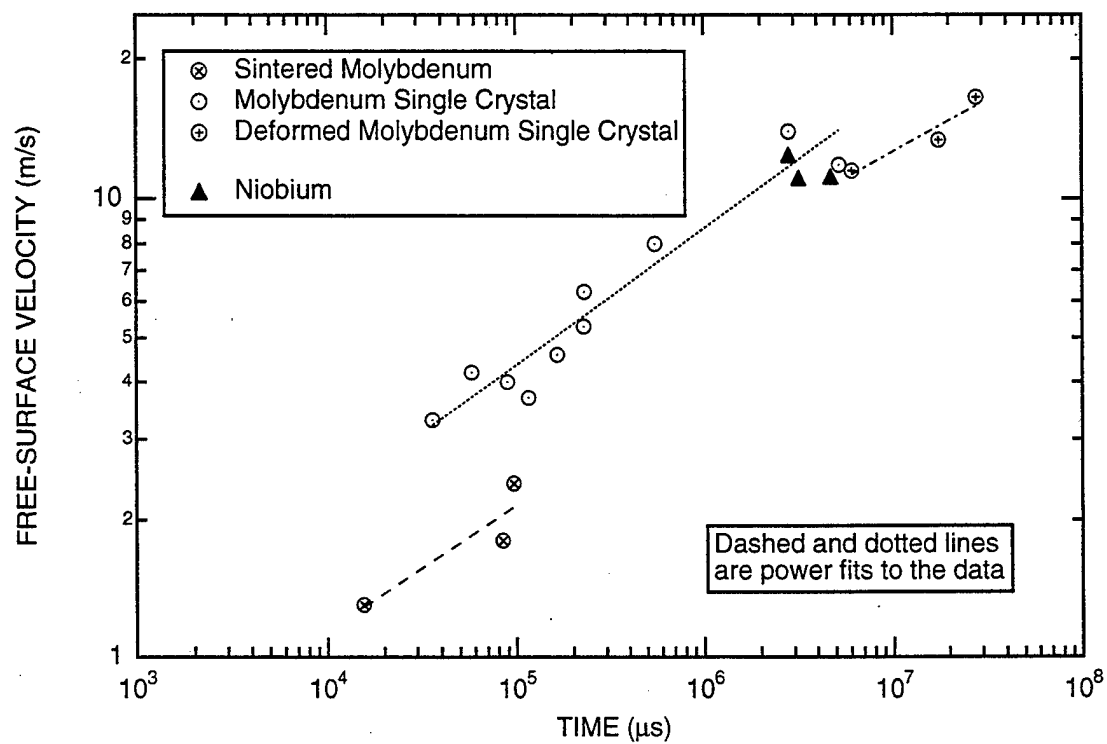
Figure 7-16. Spall strength as a function of strain rate for molybdenum and niobium.

samples should lead to a better understanding of the nature of damage nucleation on the microstructural level.

In pure single crystals, damage nucleation may result from dislocation interactions during plastic deformation. In this case the concentration of damage nucleation sites must increase with plastic deformation, i.e., with increasing shock load intensity. Therefore, the absence of a significant influence of shock wave amplitude on the spall strength of single crystals is unexpected. Nevertheless, we can conclude that damage nucleation at the dislocation level requires relatively high tensile stresses and will occur in single crystals only. In polycrystalline materials, the fracture can be initiated on coarser defects, and as a result of stress relaxation, tensile stresses do not have time to reach the necessary magnitude to activate finer defects.

It is interesting to compare the measured spall strength values with the ultimate theoretical strength. Estimates of the ultimate tensile strength are on the order of $K/10$ to $K/6$, where K is the bulk elastic modulus. The ultimate tensile strength can also be estimated through the minimum of the $p(V)$ Hugoniot curve as

$$S_{th} = \frac{\rho_0 c_0^2}{4_s}$$

(7.3)

where c_0 and s are coefficients of the linear relation between the shock front velocity and the particle velocity. Such estimations give $S_{th} = 55$ GPa for molybdenum, 36 GPa for niobium, and 24 GPa for copper. The corresponding experimentally measured values are 16.5, 12.4, and 4.6 GPa. In other words, up to 35% of the theoretical strength is reached in single crystals subjected to loading pulses on the order of a nanosecond. Extrapolation of the measured spall strength data shows that the ultimate strength of molybdenum single crystals can be reached at a strain rate of about 5×10^8 s^{-1}, which corresponds to a load duration of 0.5-1 ns. This value is only one order of magnitude smaller than the shortest shock compression pulses realized in the performed experiments, and exceeds the period of atomic oscillations in solids by three to four orders of magnitude.

7.3 CONSTITUTIVE FACTORS AND CRITERIA OF SPALL FRACTURE IN METALS.

Experiments with steel specimens of various orientation as well as experiments with single crystals show that spall strength is a structure-sensitive parameter. Owing to the finiteness of the fracture rate, the dynamic strength of metals increases appreciably with increasing strain rate. The resultant excess stresses initiate fracture at increasingly smaller and more numerous damage nucleation sites. From the ratio between the fracture stresses for single crystals and polycrystalline metals, it follows that fracture initiation

at a dislocation level occurs only in single crystals. Here, the tensile strength is two to three times larger than the fracture stress for the polycrystalline material.

Shock-wave loading is accompanied by supplementary factors that can influence the fracturing process. Extremely high strain rates develop in shock waves. The shock-wave loading is adiabatic, and it is associated with material heating. It is important to understand the factors that govern the fracture of metals under these conditions. Experiments show that the fracturing stresses are much less sensitive to the shock-induced temperature rise and plastic deformation. That the effect of shock heating on the resistance to high-rate fracture is small may be explained in terms of a change of plastic deformation mechanisms in the vicinity of flaws. Transfer from thermally activated to the thermal overbarrier dislocation slip may occur under large overstressing in the material (Merzhievsky and Titov, 1986). The fast drop in dynamic strength near the melting point is probably explained by spontaneous nucleation of large amount of vacancies in the premelting state. Coalescence of these vacancies to micropores forms new damage nucleation sites.

As for the effect of plastic deformation on fracture, we note the results of studies in large plastic flow and fracture performed by Bridgman (1964) under quasi-static conditions. The strain was varied by an order of magnitude or more in these experiments, but in fact, rupture occurred when stresses reached the ultimate strength value independent of prestraining. Thus, the total deformation itself is not a critical influence on a material's resistance to fracture.

However, experiments by Chhabildas and Asay (1992) on tantalum indicate a 27% increase in spall strength for samples precompressed to 60 GPa quasi-isentropically compared with samples precompressed to only 19 GPa. Thus, we cannot exclude the possibility of simultaneous but opposite effects of the plastic strain and temperature on the spall strength. These contributions can be separated by measurements on preheated samples.

The "spall strength" obtained in a given experiment defines only the conditions for damage nucleation; it does not exhaustively characterize the material response. Development and completion of the spall process occur at lower stress, but require consumption of additional energy for the growth of flaws and the associated plastic deformation of material around them. When the initial load pulse is short, fracture, once started, may not proceed to complete separation of the body into distinct parts.

An energy criterion (Grady, 1988; Ivanov, 1975; Kanel, 1982a,b) defines the possibility of complete rupture through comparison of the work of fracture and the amount of energy stored in the body. The work of fracture is the energy expended per unit cross-section area of the body during fragmentation. In reality, the dissipation of energy due to fracture takes place in some layer of finite thickness; therefore, the work of fracture, generally speaking, increases with increasing thickness of the failed zone.

Estimation of the energy dissipated in a fracture process can be based on either of two kinds of experiments. The first kind of experiments determines the critical impact velocity that produces spall for given thicknesses of impactor and sample. Using the critical impact velocity thus determined and parameters of the experiment, the energy dissipated is determined through consideration of the balance of energy and momentum as

$$E_d = \rho h_i v^2 (1 - h_i / h_t) / 2 \tag{7.4}$$

where v is the impact velocity, and h_i and h_t are thicknesses of the impactor and target, respectively. The dissipated energy thus calculated is an upper bound for the magnitude of the work of fracture. The second kind of experiment involves measurements of a free-surface velocity profile. The loss of kinetic energy of the spall plate as it decelerates during the spall process can be inferred from this profile and can be used for estimating the work of dynamic fracture.

The fracture stress and work of fracture describe the strength properties of the materials when subjected to one-dimensional dynamic tension. However, these two parameters are not enough to predict the occurrence of complete separation of scab or to estimate its velocity after the separation.

Figure 7-17 shows the evolution of spalling in a limited area of a plane body (Razorenov and Kanel, 1991). The incident shock is attenuated not only by the axial unloading waves but also by the lateral release. Upon reflection of this attenuated load pulse from the free surface, the tensile stresses and energy stored, which are sufficient for the complete fracture, are realized only near the axis. Thus, the fracture of the body by the plane wave is limited to some inner region. The later evolution of the process is determined by the kinetic energy stored in the spalled layer.

The inertial motion of the spalled layer is decelerated by bonding forces in the periphery of the scab. The scab motion can be decelerated, and even arrested, by the edge effects. Additional work is necessary for plastic deformation and fracture to take place along the edge of the scab. The work of edge deformation and fracture is proportional to the length of the spall element perimeter, whereas the value of energy stored in the element is proportional to its area. The ratio of these two values increases with decreasing spalled layer radius. For a small radius, development of spalling can be stopped at some intermediate stage and the spalled layer remains connected to the main body. Investigation of spalling with spall layers of different radii allows us to determine the critical stored energy value required for complete separation to take place. This variation of the spall layer radius can be arranged by varying the radius of the impact area or by placing a limiting ring on the rear surface of the sample.
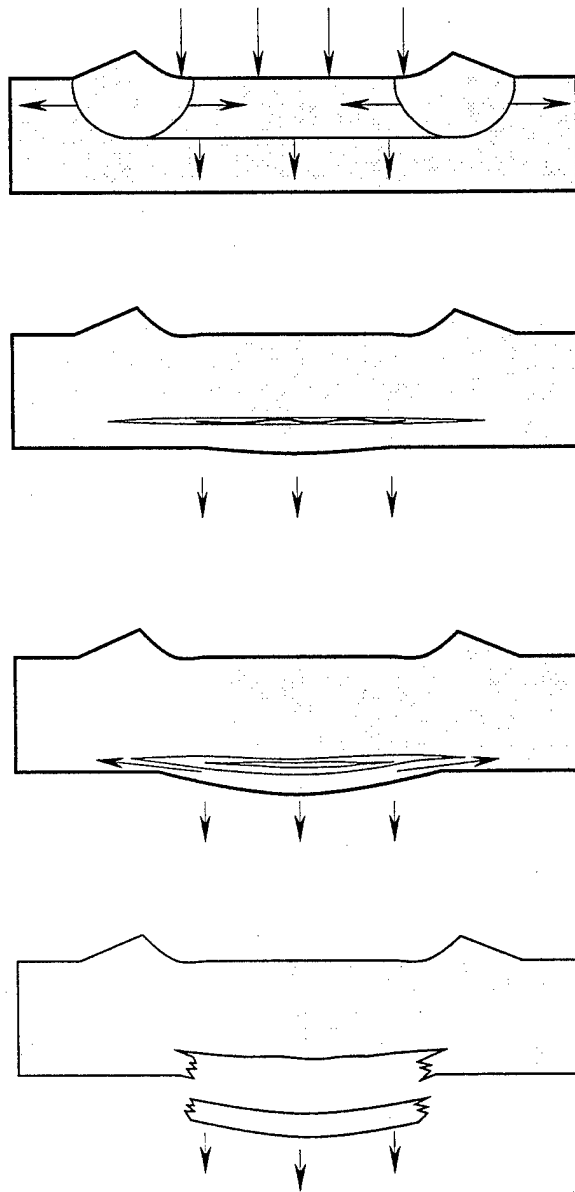
Figure 7-17.   Edge effects at spallation.

7.4   BRITTLE MATERIALS: CERAMICS, SINGLE CRYSTALS, AND GLASSES.

Hard ceramics contain many stress concentrators including pores, microcracks, and grain boundaries. A localized fracture can nucleate at the sites of these inhomogeneities even in the region of elastic deformation of the material as a whole. Microfracture in such brittle materials can appear during the compression phase. The degree of fracture increases with increasing load intensity, and the damage that occurs under compression decreases the capacity of the brittle material to resist the tensile stresses that follow the initial compression phase.

This behavior can be seen in Figure 7-18, which presents results of spall strength measurements as a function of normalized peak stress for alumina (Rozenberg, 1992; Dandekar and Bartkowski, 1994) [Figure 7-18(a)], titanium diboride (Grady, 1992; Winkler and Stilp, 1992; Dandekar, 1994) [Figure 7-18(b)], silicon carbide (Grady, 1992; Kipp and Grady, 1992; Winkler and Stilp, 1992) [Figure 7-18(c)], and boron carbide [Figure 7-18(d)]. Figure 7-18(c) indicates that the spall strength of silicon carbide in the elastic region increases with increasing peak pressure. This propably occurs because silicon carbide is the most "ductile" of these brittle ceramics. However, even for silicon carbide, a sharp drop is observed in the tensile strength when the peak stress becomes larger than the HEL. The data for boron carbide in Figure 7-18(d) do not exhibit any loss of strength because the peak stress reached is lower than the HEL.

Staehler et al. (1994) tested vacuum-hot-pressed alumina samples to shock pressures ranging from 1.3 to about three times the HEL. They found that the spall strength undergoes a transition, first decreasing near the HEL, then increasing with increasing pressure above the HEL. This transition was attributed to a change in the dominant inelastic deformation mechanism from microcracking near the HEL to dislocation activities at higher peak stresses.

The spall strength of ceramic materials has been shown to increase with decreasing initial porosity and grain size of the ceramic material (e.g., Nahme et al., 1994; Bourne et al., 1994).

Figure 7-19 shows free-surface velocity profiles of samples of a ceramic consisting of titanium carbide particles bonded with nickel (Kanel and Pityulin, 1984). The mass fraction of titanium carbide in the composite is 80%. The free-surface velocity records do not show a well-pronounced elastic precursor in the wave profile of this ceramic. This is due to wave dispersion caused by multiple reflections of the stress waves between constituents with different dynamic impedances. The spall strength is 0.4 to 0.55 GPa and it decreases with increasing peak stress. Because the spall strength of nickel is three to four times higher than the values measured for the titanium carbide-nickel ceramic, the results confirm that fracture nucleates in the brittle titanium carbide phase.

Realization of the ultimate tensile strength in the practically undistorted initial structure is possible for single crystals with high Hugoniot elastic limits, because, for such materials, generation of large tensile
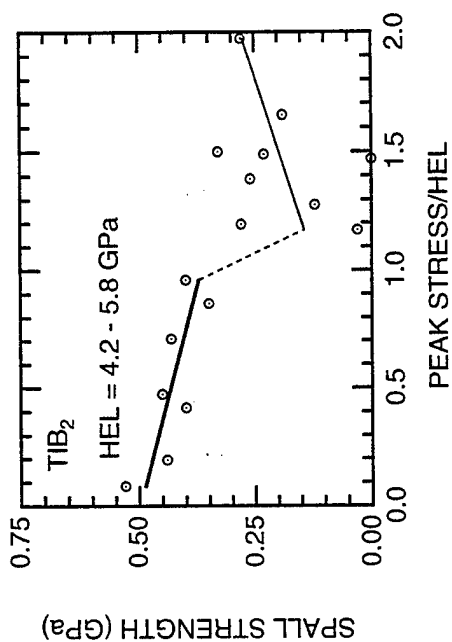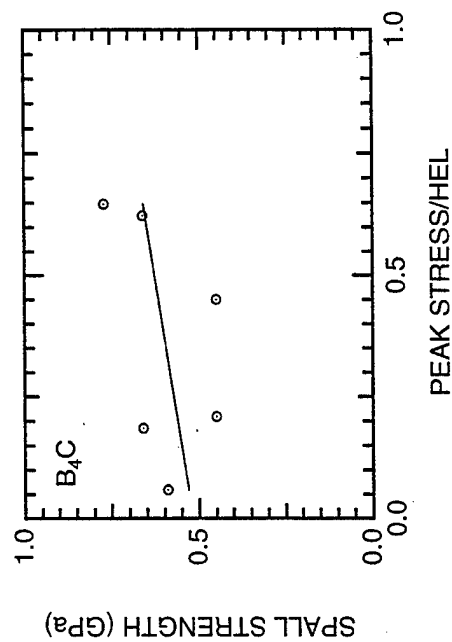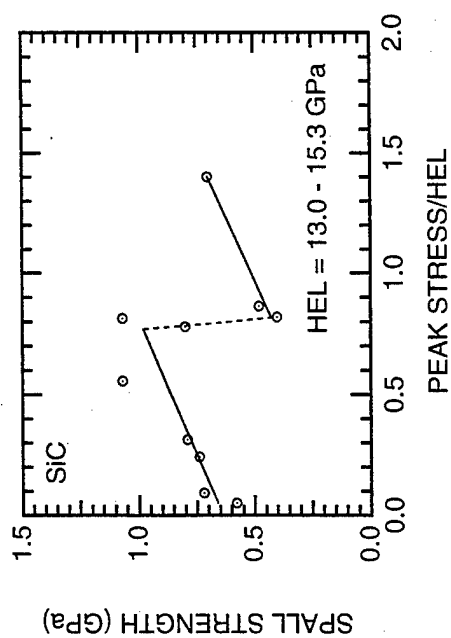
Figure 7-18. Spall strength of various ceramic materials as a function of the peak shock stress.

191
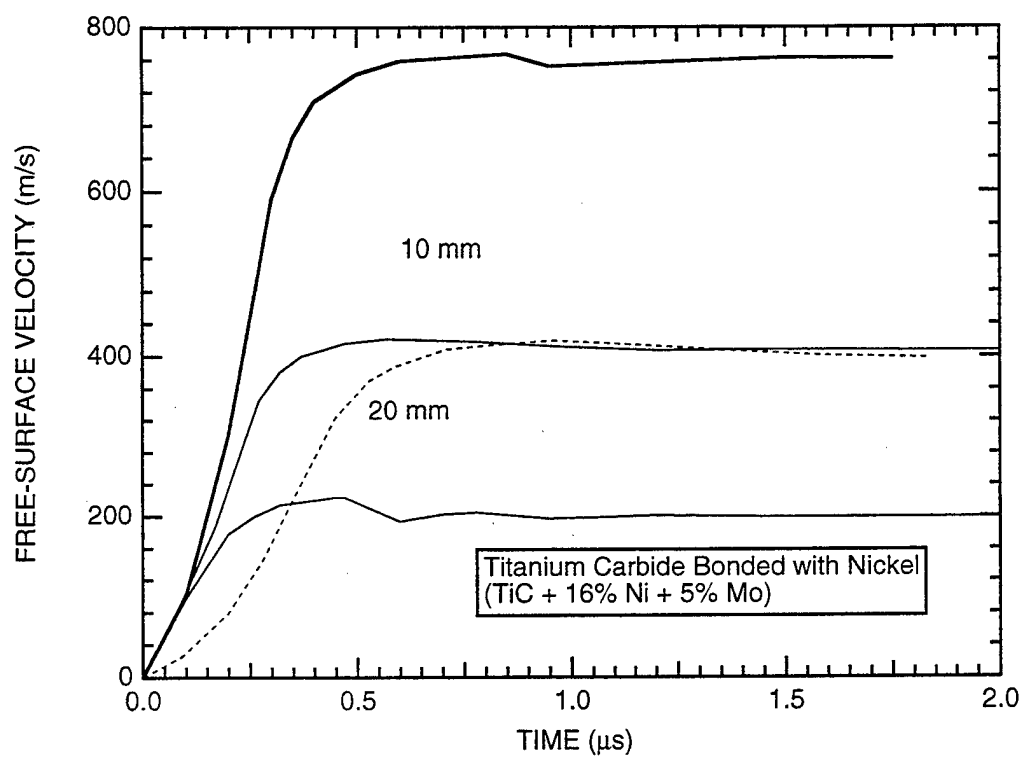
Figure 7-19. Free-surface velocity profiles for titanium carbide bonded
with nickel.

stresses without any plastic deformation is possible below the HEL. In this case fracture initiates at a structural level near that of the ideal crystal lattice.

Figure 7-20 shows free-surface velocity profiles measured for x-cut quartz samples (Kanel et al., 1992b). Shock pulse amplitudes near the rear surface were 2.8, 4.6, and 5 GPa. According to Graham (1974), the HEL of x-cut quartz is 6 GPa.

The free-surface velocity profile corresponding to a shock pulse amplitude of 2.8 GPa in Figure 7-20 replicates the form of the compression pulse inside the sample and does not display any symptoms of spallation. Increasing the pulse amplitude to 4.6 GPa causes spall damage, as evident from the spall pulse in the free-surface velocity profile. A further increase in pulse amplitude to 5 GPa modifies the free-surface velocity profile dramatically. The unloading part of the pulse does not pass to the surface, which means that the tensile strength is practically zero in this case.

These measurements show that the dynamic tensile strength of x-cut quartz reaches 4 GPa for shock loading below the HEL and falls to zero for loading close to the HEL. Cracking in the brittle single crystals under compression is a plausible explanation for the diminishing tensile strength near the HEL.

Experiments analogous to those just described were conducted with ruby (Razorenov et al, 1993) and sapphire (Kanel et al., 1994a). Measurements were made at shock wave intensities below the HEL, which is 14 to 20 GPa for alumina single crystals (Graham and Brooks, 1971). Figure 7-21 shows experimental profiles for z-cut sapphire and ruby crystals. The spall pulse in this case has a drastically steep front—a strong indication of a damage evolution process with fast kinetics. The spall strength of ruby was found equal to 8.6 GPa at 15.1 GPa peak shock stress and 10 GPa at 13.5 GPa peak stress. No spallation was observed in one of two shots with sapphire, where the shock intensity was 23 GPa and the peak tensile stress reached 20 GPa. In the other shot, the peak shock intensity was 24 GPa and spallation was observed at a tensile stress of 10.4 GPa. Thus, the high homogeneity of sapphire allows it to sustain higher tensile stresses than those measured in any other alumina.

In contrast to the behavior of hard single crystals, the spall strength of glasses is not sensitive to shock intensity at levels near the HEL. Figure 7-22 shows free-surface velocity profiles for K19 glass (Razorenov et al., 1991). Spall was not observed in these shots, which means that the spall strength of the glass exceeds 4.2 GPa both below and above the HEL. An irreversible densification occurs in glasses compressed beyond the elastic limit, both under static and dynamic conditions (Sugiure et al., 1981). Densification can play the role of a plastic deformation mechanism for glasses (Ernsberger, 1968), which could suppress cracking under compression.

Shock wave loading of glass can be accompanied by the formation of failure waves. The possibility of fracture wave formation imposes certain constraints on the design of experiments with homogeneous brittle materials. The failure wave was observed in the following experimental configuration
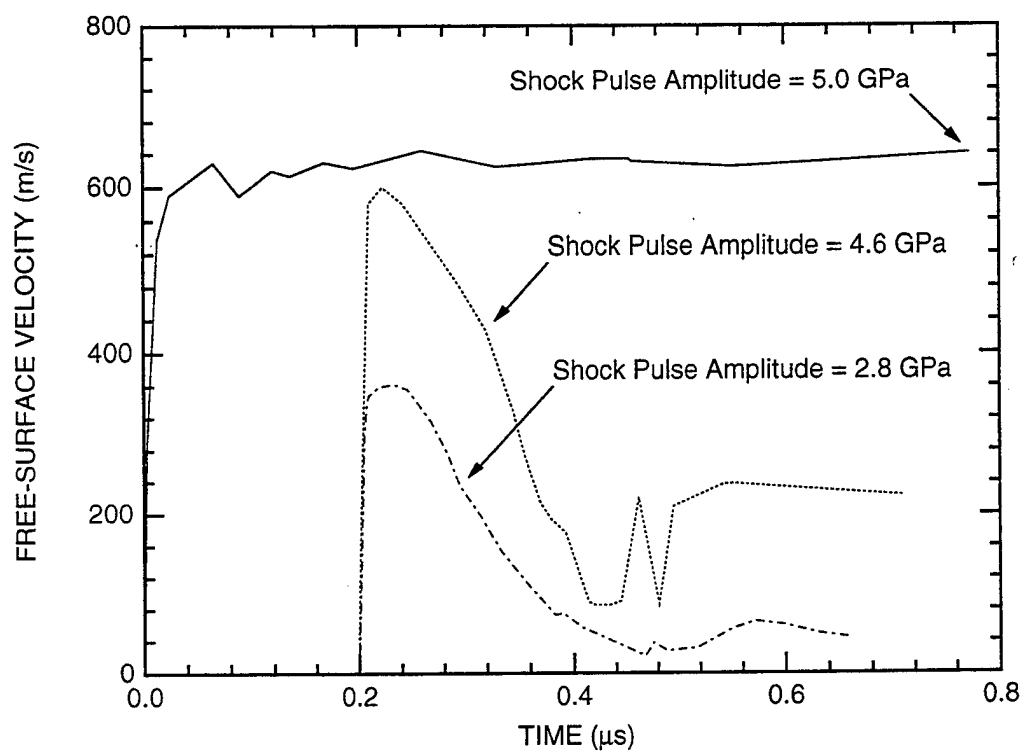
Figure 7-20. Free-surface velocity profiles for x-cut quartz at different peak shock amplitudes.
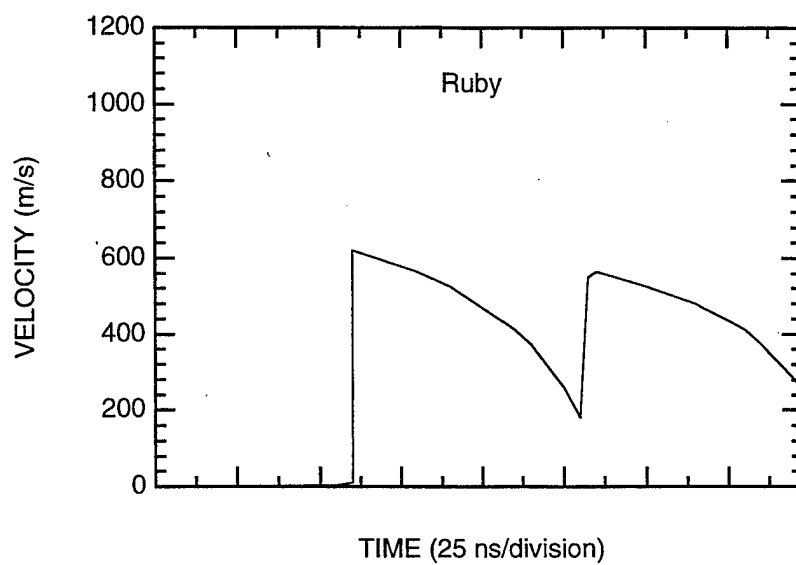
(a) Free-surface velocity profile in ruby.
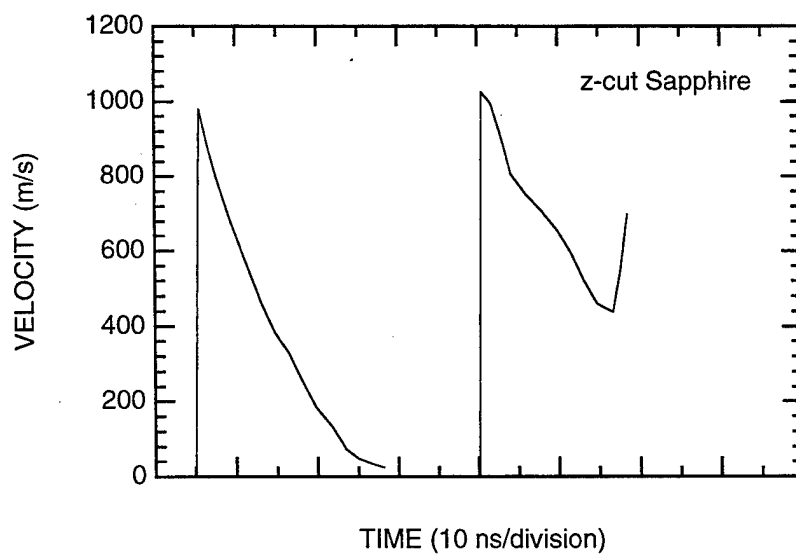
(b) Free-surface velocity profile in z-cut sapphire.

Figure 7-21. Spallation in alumina single crystals.
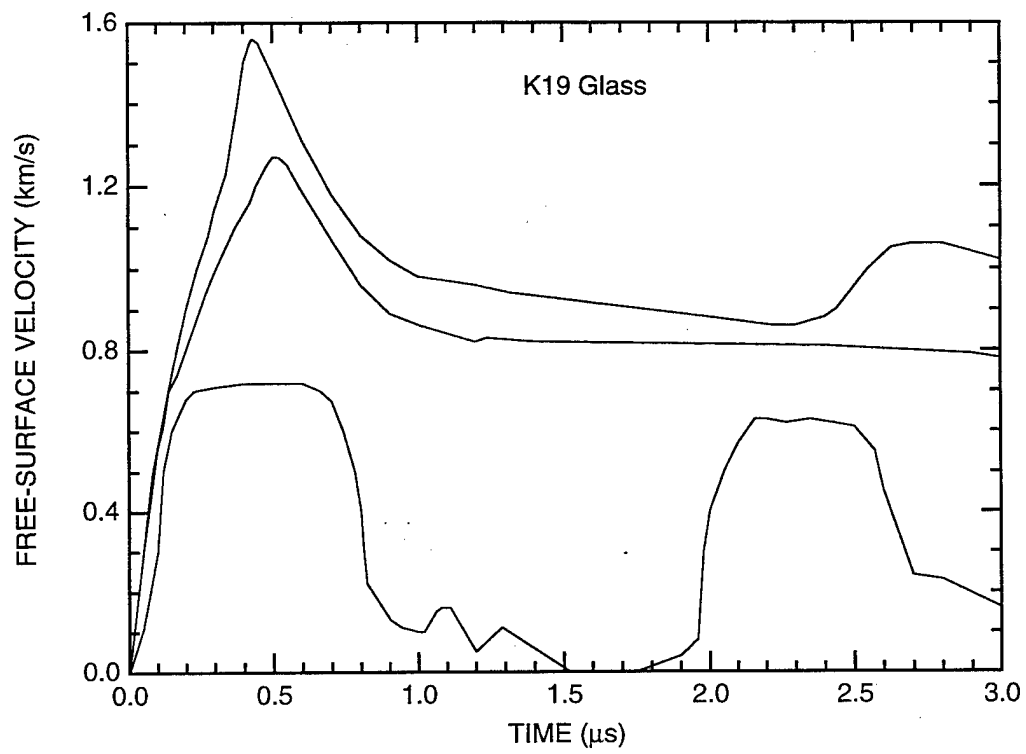
Figure 7-22.   Free-surface velocity profiles for K19 glass impacted by aluminum
flyer plates at different impact velocities.

(Razorenov et al., 1991). A triangular, long duration, 4.5-GPa shock pulse was introduced into a plane sample through a thick copper base plate, and the free-surface velocity profiles were measured. In experiments with fused quartz samples, $u_{fs}(t)$ profiles contained short negative velocity pullbacks as shown in Figure 7-23(b). This pullback was a result of rereflection of the rarefaction wave at the sample-base plate interface [Figure 7-23(a)]. The base plate had a higher shock impedance than the sample, which caused the rarefaction wave to be reflected back into the sample as a rarefaction wave. This rereflection produced a short tensile pulse in the unloaded sample, which propagated through the sample and produced a negative velocity pullback when it reached the rear surface.

No rereflected tensile pulses were observed in experiments with K19 glass [Figure 7-23(c)]. Instead, a small velocity rise was noted on the free surface, and the arrival time of the second velocity jump at the free surface was less than the elastic wave reverberation time for the sample. This modification of the wave process can be explained in terms of a failed layer formation near the sample-base plate interface. This layer has a lowered impedance and zero tensile strength. Probably, this layer is a network of cracks initiated by uniaxial compression. Experiments with samples of different thicknesses have shown the thickness of this failed layer to increase with time. This process can be interpreted as a failure wave propagation, and the velocity of the failure wave decreases with propagation distance. Experiments with short load pulses have shown that unloading will arrest the failure wave propagation.

Failure waves in glass were observed at stress levels near, as well as below, the HEL. Compression above the HEL causes irreversible densification of glasses, which plays the role of a plastic deformation mechanism. Brar et al. (1991) in their spall experiment showed that, behind the failure wave, the tensile strength drops and the transverse stress increases, indicating a decrease in shear strength. Raiser and Clifton (1994) confirmed this observation. They also found that surface roughness does not appear to play a significant role in the formation of a failure wave.

7.5   POLYMERS AND ELASTOMERS.

Figure 7-24 shows the free-surface velocity profiles of polymethylmethacrilate (PMMA) samples at various peak pressures and durations of the shock load. In the low-pressure range, PMMA behaves as a brittle material and is fractured through the growth of penny-shaped cracks nucleated at preexisting solid and gas inclusions in the intact material. The form of the wave profiles at low intensities of shock load is typical for solids. A peculiarity of this material is the appearance of small-scale oscillations on the spall pulse.

The character of spalling changes with increasing peak pressure. The fracture becomes more viscous, manifested as a protracted deceleration of the spall plate as observed in the free-surface velocity profiles. The most plausible reason for this trend is the heating and plastification of the material in the shock wave.
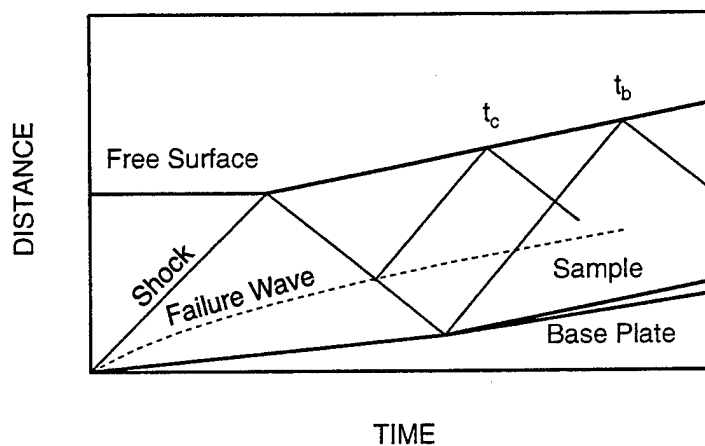
(a) Distance-time diagram.
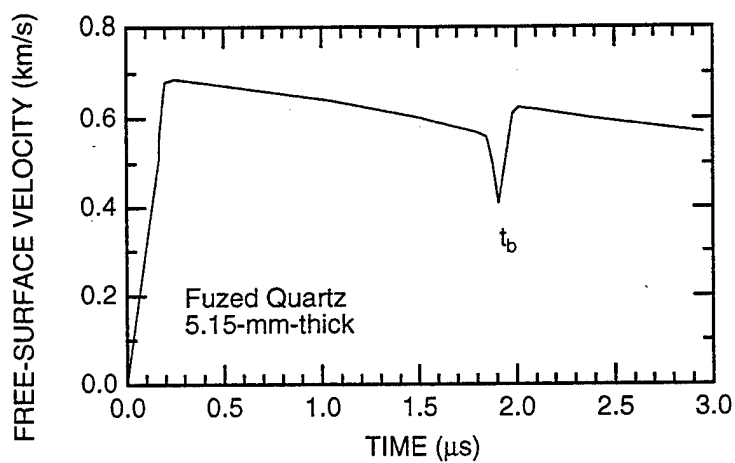
(b) Free-surface velocity profile in fuzed quartz.
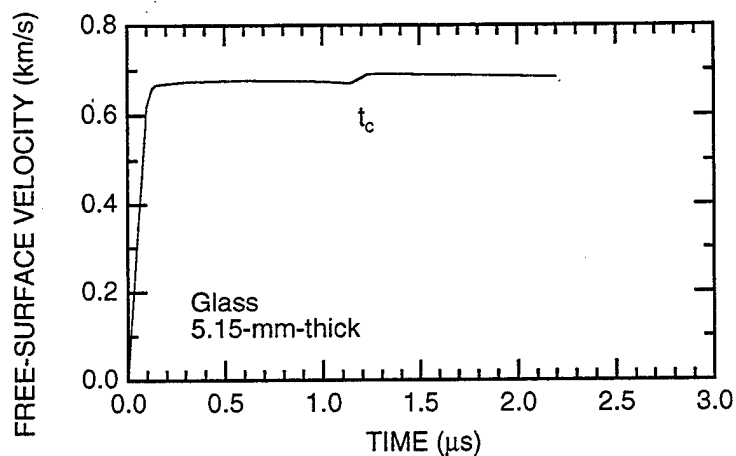
(c) Free-surface velocity profile in glass.

Figure 7-23. Failure wave in glass.

198
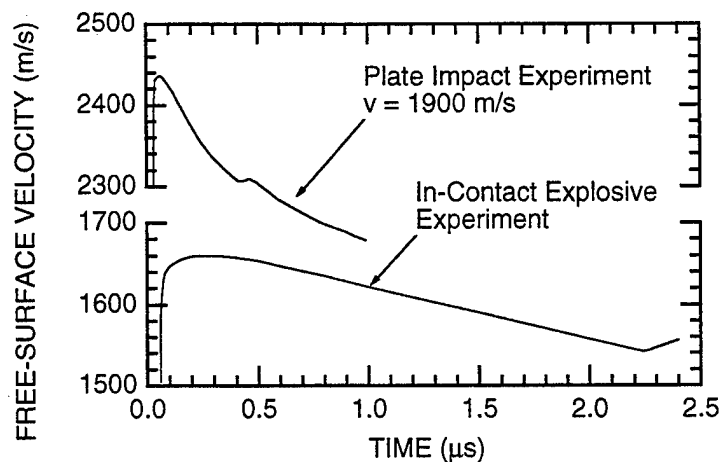
(a) Experiments at high peak pressure.
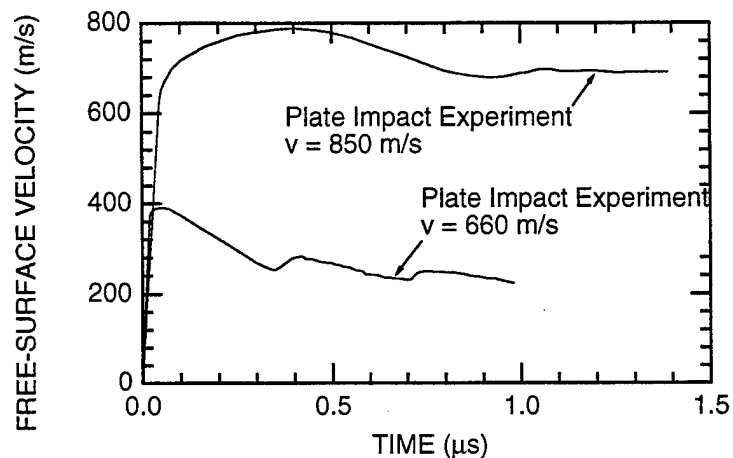
(b) Experiments at relatively low peak pressure.
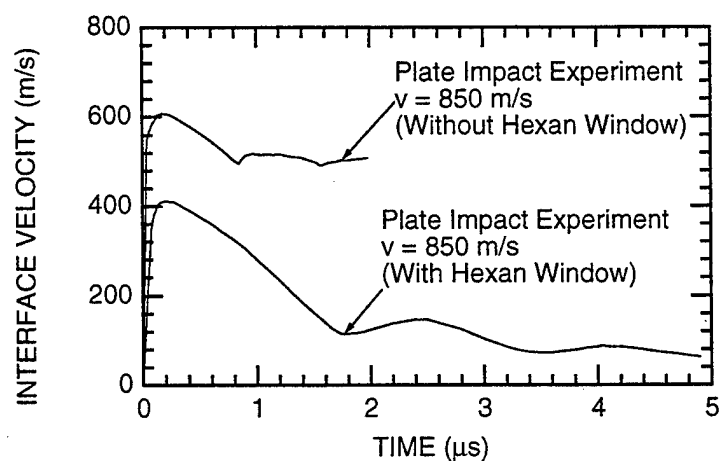
(c) Experiments with and without a Hexan window.

Figure 7-24. Free-surface velocity profiles for PMMA at
different peak pressures.

199

Examination of samples recovered after tests at different temperatures (Golubev et al., 1982a) showed an increasing zone of local plasticity near the crack tips, accompanied by a reduced crack propagation velocity. We cannot exclude the possibility of collapse of the incident microvoids in the material by shock pressure, which reduces the number density of the fracture nucleation sites, thereby reducing the rate of the fracture. Measurements have showed that, in spite of the varying fracture characteristics, the spall strength of PMMA is practically independent of peak shock pressure over the range of 0.6 to 6 GPa and depends only mildly on strain rate, increasing from 0.17 GPa at $\sim 10^4$ s^{-1} to 0.21 GPa at 10^5 s^{-1}. The spall strength of epoxy under the same conditions is about 0.3 GPa. It seems that spall strength values of 0.1 to 0.3 GPa are typical for homogeneous polymers (Golubev et al., 1982b).

Elastomers, like rubber, are characterized by an ability to undergo large reversible deformations and for this reason, they constitute a unique class of polymer materials that deserves special attention. The behavior of these materials at spall fracture is different from that of other solids, including polymers.

Experimental results for rubber (Kalmykov et al., 1990) are presented in Figure 7-25. The dashed lines in the figure represent the free-surface velocity profiles calculated from results of window tests with the assumption that rubber is not damaged in the negative pressure region. If the material does not have any appreciable resistance to tension, its surface velocity behind a shock front would be constant. The measured free-surface velocity profile (curve 3) takes some intermediate position between these two extreme cases. A small initial part of the measured free-surface velocity profile corresponds to the incident loading pulse, followed by a weak spall pulse registered at point s. Then, a slow protracted deceleration of the surface velocity is observed. Visual examination of the recovered samples did not reveal any remarkable damage. The measured value of the spall strength of rubber is 27 ± 3 MPa. The true breaking stress S_k under quasi-static tension has been found equal to 88 MPa.

Figure 7-26 presents the free-surface velocity histories for a butadienenitrile caoutchouc-based filled elastomer propellant simulant (Kanel et al., 1994b). The filler content was 75% by mass, including 61.6% KCl. Two compositions with different filler particle sizes were tested: a coarse-dispersed composition with 160- to 200-μm KCl particles and a fine-dispersed composition with 20- to 50-μm particles. The initial density of the material was 1.6 g/cm^3, and its sound velocity at ambient conditions was 1.85 km/s. The measured free-surface velocity profiles for these propellant simulants are similar to those for rubber. Measured values of the spall strength are 24 to 30 MPa for fine-dispersed samples and ~15 MPa for coarse-dispersed samples. The samples from shots 1 and 2 were recovered for posttest inspection. Like rubber, these propellant simulant samples did not show evidence of a distinct spall plane even though the peak shock pressure in shots 1 and 2 was equal to ~150 MPa, which exceeds the measured spall strength value by a significant amount.
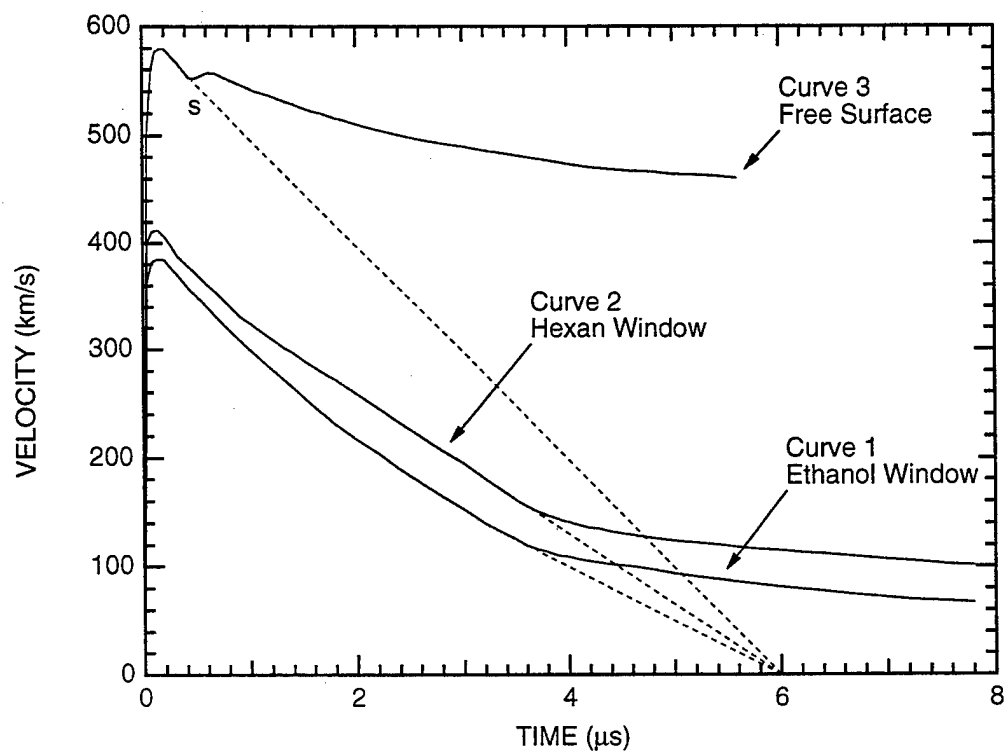
Figure 7-25. Wave profiles under spall conditions in rubber.
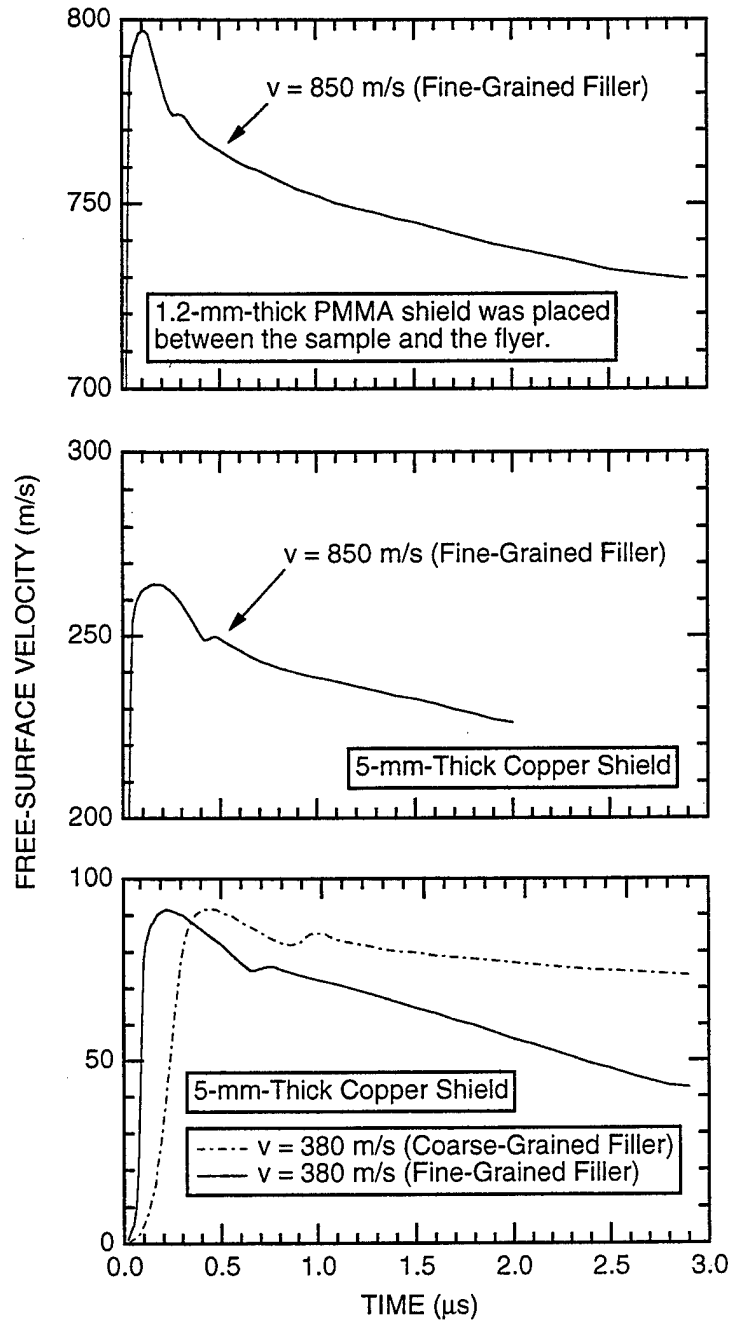
Figure 7-26. Free-surface velocity profiles for rocket propellant simulants impacted by PMMA flyer plates at impact velocities of 380 and 850 m/s.

202

It is known that void formation precedes the rupture of elastomers. These voids nucleate under much lower stresses than is required to break the sample. Origination of microdiscontinuities is not yet a destruction event itself. Thus, in tests of natural vulcanizates under triaxial tension (Gent and Lindley, 1959), voids formed at stresses of 1 to 3 MPa and insignificant deformation occurred. Then, after this stage, samples underwent further deformation, reaching several hundred percent. According to these findings, it seems reasonable to assume that the measured spall strength values of 15 to 30 MPa characterize the nucleation of microdiscontinuities in elastomer, but do not characterize its failure.

The velocity deceleration behind the spall pulse is determined by the resistance of the material to tension. Among the elastomers tested, the resistance to tension is highest for rubber (curve 3 in Figure 7-25), lower for the elastomer with a fine-dispersed filler (curves 1, 3, and 4 in Figure 7-26), and lowest for the coarse-dispersed elastomer (curve 2 in Figure 7-26). The observed free-surface deceleration is inversely proportional to the size of the filler particles. For the fine-dispersed filler, the velocity deceleration is 3.5 times as high as that of coarse-dispersed sample. Filler particle size also influences the shock front rise time. The rise time for coarse-dispersed composition is twice as long as for the fine-dispersed sample.

7.6 DYNAMIC STRENGTH OF LIQUIDS.

Liquids, like solids, have some resistance to multidimensional tension, which can be treated as a bulk strength property of the liquid material. The ultimate bulk strength value for liquids can be estimated from intermolecular bonding forces (which, for example, for water gives a value on the order of 1 GPa) or by extrapolation through the minimum of the isotherm in the negative pressure region (which for water gives a value on the order of ~300 MPa).

The strength of liquids can be measured experimentally if the experiment is arranged to prevent the lateral narrowing of the sample under tension (Kornfeld, 1951; Trevena, 1967). Static measurements have shown that the bulk tensile strength of liquids is one to two orders of magnitude lower than the ultimate theoretical estimations. In part, this may be explained in terms of the small bubbles of gas or vapor that are always present in liquids. The resistance to growth of a bubble of finite dimensions is determined by the surface tension forces, which are much lower than intermolecular forces. Even thermal fluctuation in liquids can create sites of nucleation of voids under tension.

Application of plane shock waves provides the necessary conditions for measuring the bulk strength of liquids, because the motion is one-dimensional under these conditions and because the tension is realized inside the body where surface effects do not influence the rupture process. Typical values of the spall strength of liquids have been obtained for several liquids including water and glycerol. According to Erlich et al. (1971), the spall strength of glycerol is ~25 MPa, which corresponds to the initial embryonic bubble size of ~0.01 μm. The dynamic strength of water at load duration of ~10^{-4} s was estimated by

Couzens and Trevena (1969) to be 0.85 MPa. Deionization of water increases its bulk strength up to 1.5 MPa. In the microsecond load duration range, Marston and Unger (1986) measured the spall strength of water to be 3.9 to 11.5 MPa.

SECTION 8

ESTIMATING SPALL FRACTURE KINETICS FROM THE FREE-SURFACE VELOCITY PROFILES

Fracture needs to be predicted in many applications ranging from micrometeorite impact and pulsed laser attacks to large-scale impacts and explosions. The fracture model should be efficient over a wide range of load durations. Many fracture models based on approaches ranging from microstatistical to empirical have been developed to describe damage and fracture kinetics under dynamic loading conditions. The nucleation and growth (NAG) modeling approach, described in detail in Section 9, is a well known example of the microstatistical approach. NAG models are usually validated by comparing the measured damage distributions and the wave profiles predicted by the model with those measured in spall experiments. This comparison requires many laborious tests accompanied by careful posttest examinations of the impacted samples.

For some applications, however, this approach may not be necessary. Constitutive models simpler than those developed using the NAG approach can be constructed and verified based only on information derived from experimentally measured free-surface velocity profiles. The development of such simple empirical models can be facilitated if the model formulation is guided by an analysis of a series of free-surface velocity profiles. The analysis can provide preliminary information about the damage kinetics and may permit the estimation of some parameters of the chosen constitutive relationship.

Section 6 describes an acoustic analysis of the spall process in an attempt to correlate the free-surface velocity profiles with the rate of fracture at the spall plane. This section describes a method for formulating empirical constitutive relationships for fracture damage under spall conditions based on the results presented earlier in Section 6.

The analysis of the spall process presented in Section 6 permits us to make the following observations about the initial stages of spall fracture in a specimen loaded by a triangular stress pulse. The fracture process sets a limit on the growth of the peak tensile stress behind the spall plane when the reflected tensile wave propagates into the body. Assuming the damage rate, $\dot{V}_v$, depends linearly on the pressure, p (see Eq. 6.10), the ultimate tensile stress is reached at the damage rate

$$\dot{V}_v = -\frac{4\dot{p}_o}{\rho^2 c^2} \tag{8.1}$$

where $\dot{p}_o$ is the unloading rate in the incident compression pulse. Thus, the ultimate magnitude of the reflected tensile pulse corresponds to a void growth rate equals to four times the unloading rate in the incident compression pulse. This same damage rate leads to the appearance of the minimum (i.e., spall signal) on the free-surface velocity profile. The spall signal is formed only if the damage rate is more than four times as great as the expansion rate during unloading in the incident compression pulse.

Under the threshold conditions represented by Eq. (8.1), the pressure at the spall plane increases at a rate exactly equal in magnitude to the unloading rate in the incident load pulse. In other words, the appearance of the spall signal on the free-surface velocity profile means that the damage rate is increasing so rapidly with the development of fracture, that this increase compensates for the relaxation of the tensile stress. Therefore,

$$\frac{\partial \dot{V}_v}{\partial V_v} \geq -\frac{\rho^2 c^2}{4} \frac{\partial \dot{V}_v}{\partial p} \qquad (8.2)$$

The pressure and void volume vary continuously during fracture; as a result, the damage rate also varies. The damage rate after damage initiation is related to the rise time of the spall pulse front. The slope of the spall pulse front is

$$\frac{du_{fs}}{dt} = \frac{\dot{p}_o}{8\rho c}\left(\frac{\dot{V}_v}{\dot{V}_o} - 4\right) \qquad (8.3)$$

where $\dot{V}_o$ is the expansion rate in the incident pulse.

It is reasonable to assume that the damage rate is a function of both tensile stress and degree of damage. As a result, the threshold damage rate that corresponds to the appearance of a minimum in the free-surface velocity profile can be reached at many times during the development of fracture. This time interval decreases with increasing tensile stress, while the reflected rarefaction wave propagates from the free surface into the body. Figure 6-8 showed the threshold line in the time-distance diagram, along which the condition $\dot{V}_v = 4\dot{V}$ is satisfied. The spall signal arrives at the sample surface from the point on this line where the slope is

$$\frac{dt}{dx} = -\frac{1}{c}. \qquad (8.4)$$

As a result, the duration, Δt_i, of the first velocity pulse on the free-surface velocity profile exceeds the periods, Δt_{spall}, of later (after beginning of fracture) velocity oscillations. The difference between these time intervals is interpreted as an apparent delay time of the spall fracture. Obviously, development of the

206

fracture to the left of the spall plane is suppressed by the compression wave created as a result of the relaxation of the tensile stress in the spall plane.

As an example, let us consider the spall fracture rate for the Al - 6% Mg alloy. Figure 8-1 shows results of measurements of the spall strength σ^* as a function of the unloading expansion rate in the incident shock pulse. The dashed line in Figure 8-1 is a fit to the power function

$$\sigma^* = 0.12\left(\frac{\dot{V}}{V_o}\right)^{0.18} \text{ GPa} \tag{8.5}$$

where V_o is the initial specific volume of the material. This empirical relationship reflects the dependence of the damage rate on the applied tensile stress. Using the results of the analysis discussed above, we may conclude that the damage rate depends on the tensile stress as

$$\dot{V}_v = 4V_o\left(\frac{\sigma}{0.12}\right)^{\frac{1}{0.18}} \tag{8.6}$$

Experimental profiles for this alloy do not indicate any notable delay of the fracture; within the experimental error of the measurement, the period of the velocity oscillations after the beginning of spall fracture corresponds to the duration of the first velocity pulse with allowance for the difference between the propagation velocities of the spall pulse front (longitudinal sound velocity c_l) and the incident unloading wave ahead of it (bulk sound velocity c_b). Additionally, free surface velocity profiles for this alloy do not show any notable stress relaxation ahead of the spall signal. Thus, the expression for $\dot{V}_v(\sigma)$ obtained above describes the initial, or near initial, damage rate. Experimental profiles show also that the steepness of the spall pulse front is always proportional to the velocity gradient in the incident unloading wave.

In other words, a faster initial damage rate is accompanied by a proportionally faster damage rate on the following phases of the fracture process. The initial damage rate and the damage rate at later times seem to be controlled by the same parameter that appears as a multiplier in the constitutive relationship. This multiplier can represent, for example, the number of damage sites. We cannot determine the concentration of the damage sites from the free-surface velocity profiles, but it is reasonable to assume that this concentration is determined, for example, by the ultimate tensile stress at which damage is activated.

A simple constitutive relationship consistent with our observations can be expressed in the following form:

$$\frac{\dot{V}_v}{V_o} = \frac{\sigma}{\tau\sigma_n}\left(\frac{\sigma_{max}}{\sigma_n}\right)^{\alpha-1}\left(\frac{V_v}{V_o}\right)^{\beta} \tag{8.7}$$
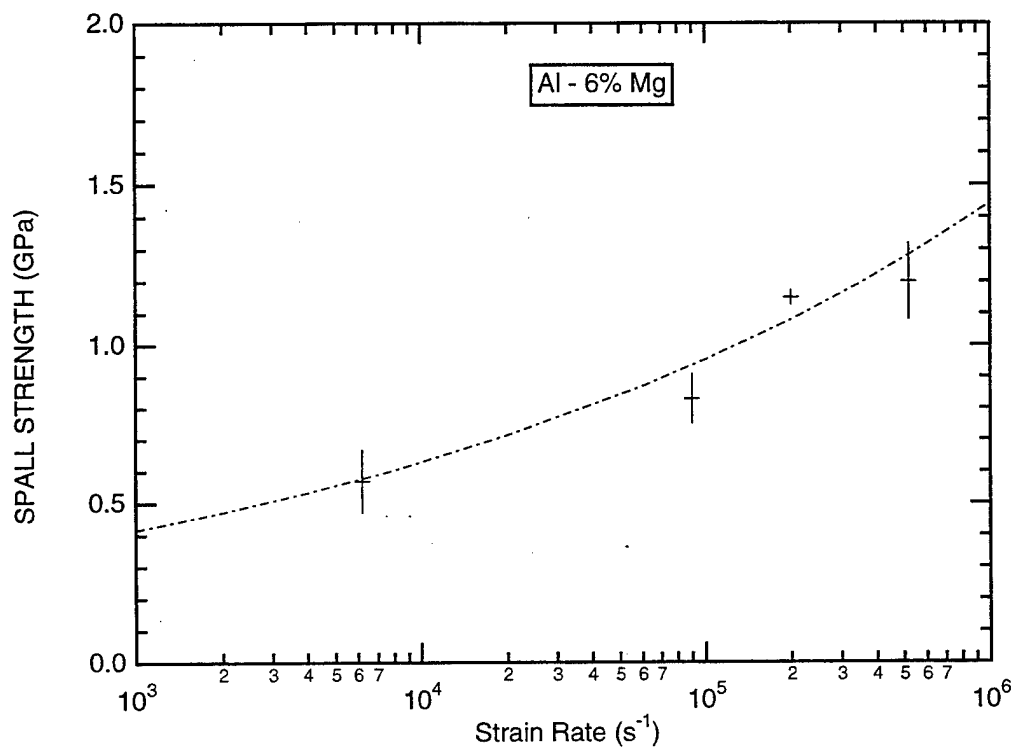
Figure 8-1. Dependence of the spall strength of the Al-6%Mg alloy on strain rate.

where σ_{max} is a point function representing the peak tensile stress experienced by the material during the passage of the rarefaction wave, constants σ_n and α are taken from the empirical relationship (8.6), and the time factor τ and the parameter β are yet to be determined. The relation (8.7) carries the implication that all damage nucleation sites are activated simultaneously when the peak tensile stress is reached.

For preliminary estimations, let us begin by finding the threshold line for the spall process after reflection of a triangular compression pulse from the free surface. Let the pressure gradient at unloading in the incident pulse be $\dot{p}_o = -(1/2)kc$, which corresponds to the expansion rate of

$$\dot{\bar{V}} = \frac{-\dot{p}_o}{\rho c^2} = \frac{k}{2\rho c}$$

(8.8)

The ultimate tensile stress increases as a linear function of the distance of propagation of the reflected rarefaction wave into the body:

$$\sigma = kx$$

(8.9)

As a first approximation, we consider only the initial stage of the fracture development, assuming that small initial increments of voids do not lead to substantial relaxation of stress. In this case, the condition (8.1) gives

$$\dot{\bar{V}}_v = A\sigma^\alpha \bar{V}_v^{*\beta} = \frac{2k}{\rho c}$$

(8.10)

where $\bar{V}_v = V_v / V_o$ and $A = 1/\tau\sigma_n^\alpha$. Solving for the volume of voids we obtain

$$\bar{V}_v^* = \left(\frac{2k}{\rho c} \frac{1}{A\sigma^\alpha}\right)^{\frac{1}{\beta}}$$

(8.11)

Another expression for the void volume can be obtained by integrating the kinetic relationship (8.7):

$$\bar{V}_v^* = \left[(1-\beta)A\sigma^\alpha \Delta t\right]^{\frac{1}{1-\beta}}$$

(8.12)

where Δt is the time interval needed to reach V_v^*.

The last two relationships can be combined to obtain the following expression for Δt:

$$\Delta t = \frac{1}{A(1-\beta)}\left(\frac{2k}{A\rho c}\right)^{\frac{1-\beta}{\beta}} \sigma^{-\frac{\alpha}{\beta}}$$

(8.13)

and the threshold line in the time-distance diagram is obtained as $t = \dfrac{x}{c} + \Delta t$, or

$$t = \frac{x}{c} + \frac{1}{A(1-\beta)} \left(\frac{2k}{A\rho c} \right)^{\frac{1-\beta}{\beta}} (kx)^{-\frac{\alpha}{\beta}} \tag{8.14}$$

The spall signal is formed at the point where the slope of this curve is $-1/c$. This condition is satisfied at the distance

$$x^* = \frac{1}{k} \left[\frac{c}{2} \frac{k\alpha}{A\beta(1-\beta)} \left(\frac{2k}{A\rho c} \right)^{\frac{1-\beta}{\beta}} \right]^{\frac{\beta}{\alpha+\beta}} \tag{8.15}$$

Figure 8-2 shows threshold lines for the damage kinetics (8-7) calculated with different values of β for the same x^*. In these calculations the time factor τ was increased with decreasing β. The apparent delay of the spall is almost linearly proportional to the value of β. Let us now check the condition (8.2). For the fracture kinetics (8.7), this condition is

$$\frac{\sigma}{\overline{V_v}} \geq \frac{\rho c^2}{4\beta} \tag{8.16}$$

In the case of smaller β, the condition (8.2) ceases to be satisfied at smaller porosity, which means decreasing amplitude of the spall signal. At some small β, the condition (8.2) is satisfied only at $\overline{V_v} \leq \overline{V_v}^*$ and a spall signal cannot form. The apparent delay of the fracture seems inevitable with the assumed fracture kinetics in the form of Eq. (8.7).

Calculations of the threshold line are much simpler than complete computer simulation of the spall process and are an effective tool for obtaining preliminary estimates of the constitutive model parameters.

Figure 8-3 compares experimental free-surface velocity histories with the results of computer simulations of the spall experiments, using the constitutive relationship (8.7). The model parameters used in the simulations are $\sigma_n = 0.12$ GPa and $\alpha = 5.65$, as it follows from Eq. (8.6), and $\beta = 0.5$ and $\tau = 4.2 \times 10^{-2}$ s. In the calculations, complete fracture was assumed to correspond to a void volume equal to 25% of the initial volume, or $0.25 V_o$. The computer simulations were done with the one-dimensional Lagrangian code EPIF. The elastic-plastic properties were described by the structural Marzing model, which represents each elementary volume of the body as a set of parallel elements with different yield strengths.

210
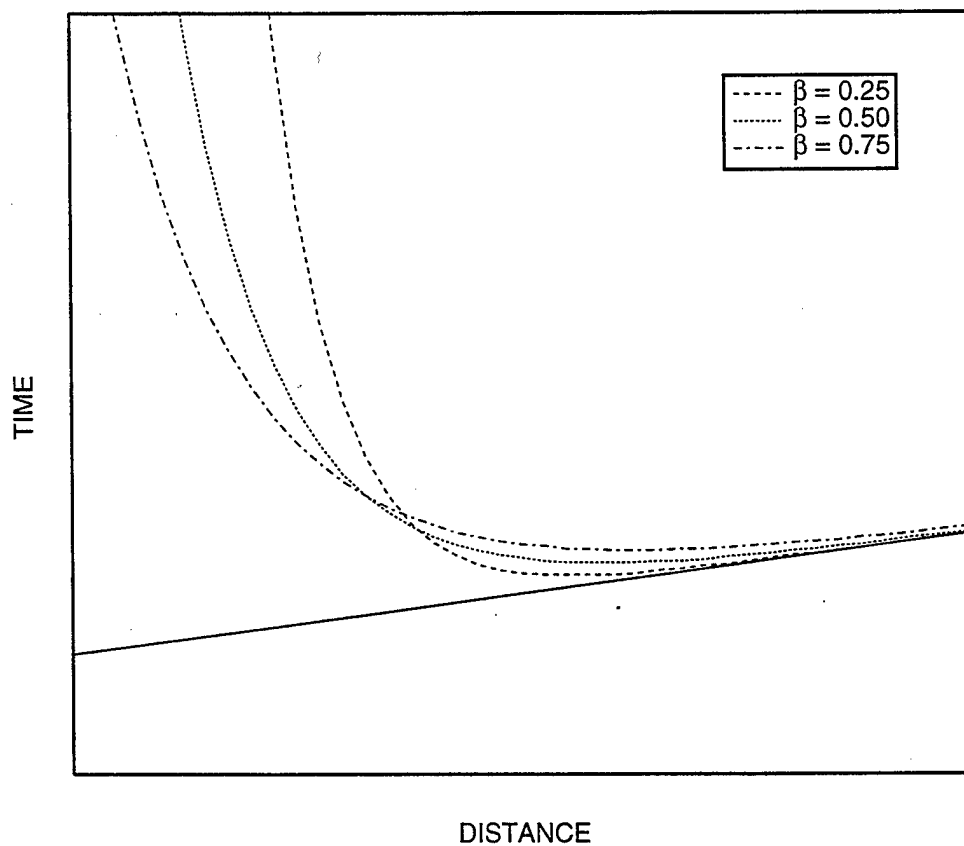
Figure 8-2. Threshold lines calculated with the constitutive relationship (8-7).
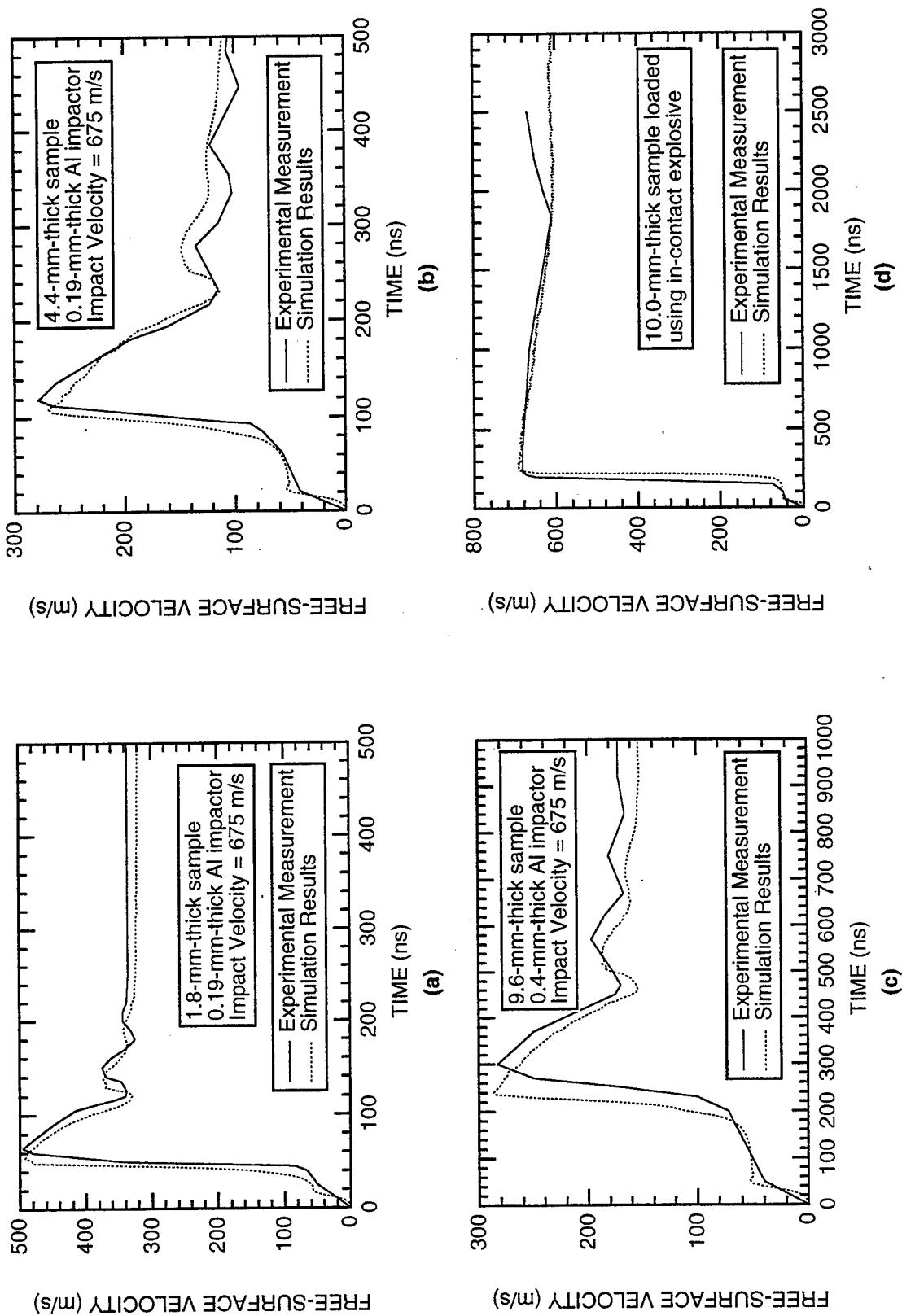
Figure 8-3. Comparison of measured free-surface velocity profiles with those calculated using the constitutive relationship (8-7) for the Al-6%Mg alloy.

212

In this section, we have demonstrated how a simple constitutive model for describing spall damage can be established based only on free-surface velocity profiles. The model is empirical, and it does not attempt to relate damage in the material to underlying micromechanisms. This model can be improved, but that will require additional experimental and theoretical information and will lead to a more complicated and less computationally efficient set of equations, which is beyond the scope set forth at the beginning of the section. Section 9 provides a detailed description of the theoretical, experimental, and numerical aspects of the nucleation-and-growth (NAG) modeling approach, an approach used to develop microstructurally based constitutive models for describing the dynamic behavior of ductile and brittle materials.

SECTION 9

CONSTITUTIVE MODELS OF THE FRACTURE PROCESS

9.1 OVERVIEW OF FRACTURE MODELING APPROACHES.

Several approaches have been used in past studies to model dynamic fracture. The simplest of these approaches is the threshold stress criterion in which dynamic fracture is assumed to take place when the stress reaches some critical value. This approach is consistent with the Griffith criterion (Griffith, 1925) for brittle fracture under quasi-static conditions, but it is not consistent with experimental observations of dynamic fracture where failure is caused by the propagation of many microcracks, not a single macrocrack. Experimental observations in many materials, both ductile and brittle, indicate that dynamic fracture is a time-dependent process. Thus, a time-dependent criterion is required to provide a realistic description of the time-dependent fracture under dynamic loading conditions.

Early attempts at correlating fracture stress under dynamic loadings with applied stress pulse parameters included a criterion based on the applied stress gradient (Breed et al., 1967) and another criterion based on the stress rate at fracture (Skidmore, 1965). A well known general criterion for time-dependent dynamic fracture, which includes the stress rate at fracture criterion and the stress gradient criterion as special cases, was developed by Tuler and Butcher (1968). This criterion is

$$(\sigma_o - \sigma)^\lambda \Delta t = K \tag{9.1}$$

where σ_o is the stress below which fracture does not occur, σ is the stress (taken to be negative under tension), t is time, and K and λ are material parameters. As noted by Barbee et al. (1970), when $\lambda = 1$, Eq. (9.1) is a simple impulse criterion, and when $\lambda = 2$, Eq. (9.1) can be shown to be equivalent to an energy criterion.

A more advanced energy-based set of criteria for spall fracture was proposed by Grady (1988). In that treatment, Grady developed criteria for the spall strength, P_s, time to fracture, t_s, and average fragment size, s, for brittle and ductile materials and for liquids. In each case, it is assumed that spall occurs when the sum of the strain energy and kinetic energy is at least as large as the fracture energy. For brittle solids, the fracture energy dissipated in the creation of new fracture surfaces is derived by using a fracture mechanics approach and is characterized in terms of the fracture toughness of the solid, K_c. In this case, the expressions for spall strength, time to fracture, and fragment size are

$$P_s = \left(3\rho c_o K_c^2 \dot{\varepsilon}\right)^{1/3}$$

$$(9.2a)$$

$$t_s = \frac{1}{c_o}\left(\frac{\sqrt{3}K_c}{\rho c_o \dot{\varepsilon}}\right)^{2/3}$$

$$(9.2b)$$

$$s = 2\left(\frac{\sqrt{3}K_c}{\rho c_o \dot{\varepsilon}}\right)^{2/3}$$

$$(9.2c)$$

where ρ is the density, c_o is the bulk sound speed, and $\dot{\varepsilon}$ is the strain rate.

For ductile solids, spall is assumed to occur by the ductile growth of spherical voids. Accordingly, the fracture energy is derived from the plastic work expanded in growing the void. In this case, the expressions for spall strength, time to fracture, and fragment size are

$$P_s = \sqrt{2\rho c_o Y \varepsilon_c}$$

$$(9.3a)$$

$$t_s = \sqrt{\frac{2Y\varepsilon_c}{\rho c_o \dot{\varepsilon}^2}}$$

$$(9.3b)$$

$$s = \sqrt{\frac{8Y\varepsilon_c}{\rho \dot{\varepsilon}^2}}$$

$$(9.3c)$$

where Y is the yield strength and ε_c is the critical strain (or void volume fraction) for stable void growth.

In both the brittle and ductile cases, the inherent flaw structure is assumed to be "favorably disposed" such that spall occurs as soon as the energy criterion is satisfied. Single crystal structure is an example where the inherent flaw structure might not be "favorably disposed," and spall fracture occurs at considerably higher stresses than those predicted by the energy balance criteria above.

For liquids, Grady (1988) considered two cases, one based on the fracture energy being dominated by the surface energy (similar to brittle spall) and another based on the fracture energy being dominated by viscous dissipation (similar to ductile spall). In the former case, when the surface tension, γ, dominates the fracture energy term, the expressions for spall strength, time to fracture, and fragment size are

$$P_s = \left(6\rho^2 c_o^3 \gamma \dot{\varepsilon}\right)^{1/3}$$

$$(9.4a)$$

$$t_s = \frac{1}{c_o}\left(\frac{6\gamma}{\rho \dot{\varepsilon}^2}\right)^{1/3}$$

$$(9.4b)$$

$$s = \left(\frac{48\gamma}{\rho\dot{\varepsilon}^2}\right)^{1/3}$$ (9.4c)

When viscous dissipation dominates the fracture energy term, the expressions for spall strength, time to fracture, and fragment size are

$$P_s = \sqrt{2\rho c_o^2 \eta \dot{\varepsilon}}$$ (9.5a)

$$t_s = \sqrt{\frac{2\eta}{\rho c_o^2 \dot{\varepsilon}}}$$ (9.5b)

$$s = \sqrt{\frac{8\eta}{\rho\dot{\varepsilon}}}$$ (9.5c)

where η is the viscosity of the liquid.

The dynamic fracture criteria developed by Tuler and Butcher (1968) and Grady (1988) consider spall to be an instantaneous event. For this reason, the usefulness of these criteria is limited to applications where damage evolution is not important. Experimental observations have fairly well established that spall is an evolution process that involves nucleation, growth and coalescence of microscopic flaws. The development of damage during spall modifies the stresses, and the changing stresses, in turn, modify the growth of damage. When the details of this damage evolution process are important, a different kind of fracture model is needed—a fracture model that accounts for the nucleation, growth, and coalescence of damage at every step of the deformation history. Several approaches for developing this kind of model are available, and in the remainder of this section, we focus on one of these approaches: the nucleation-and-growth approach, or NAG.

9.2 FRACTURE STUDIES BY THE NUCLEATION-AND-GROWTH APPROACH.

The SRI nucleation-and-growth (NAG) approach to fracture arose naturally from our observations of the damage in cross sections of metal targets impacted in SRI's gas gun experiments. We saw increasing numbers of voids or cracks as a function of the stress level and of the load duration. From these observations, we were led to postulate the existence of nucleation processes for the initiation of the voids or cracks and growth processes for their gradual development under continued loading. We postulated that the damage occurred in response to the tensile stresses felt in the material and that the damage was indifferent to the external loading conditions (explosive, impact, thermal radiation) that had caused the tensile stresses. Therefore, we intended to develop an understanding of the fracture processes at a level that would allow us to treat directly the actual processes in the material. With such an understanding,

216

we expected that fracture under all types of loading would be identical and therefore could be treated in the same way.

Our model can predict many aspects of the fracture phenomena: modifications of the stress or particle velocity histories by the developing damage and location, number, and size of cracks or voids throughout the specimen. In this way, the model (and the whole approach) is strongly constrained by the available data, although the model is also based on mechanics and especially on available solutions from micromechanics. The processes and parameters in the model should be uniquely defined by the data. We expect that the processes and parameters thus identified by the fracture experiments are basic to the material and not merely fitting functions that describe certain kinds of fracture under a narrow range of loading types and rates. Rather we expect that the processes we study in fracture are the same processes that also control the shock front thickness, creep, fatigue fracture, and other material phenomena.

For our micromechanical approach, we chose to work at a particular level of detail, and this level is a characteristic of the NAG approach:

- The damage is examined microscopically (nominally at about 100X) and each microvoid or crack is measured. Thus we are normally seeing damage that has characteristic dimensions of 1 μm up to about 100 μm or somewhat larger.

- The microdamage is considered statistically. That is, we count microvoids or cracks, but we mainly work with crack or void size distributions, not individual cracks or voids.

Because we always start with observations of the damage, NAG has a strong experimental basis. The theoretical models are always developed from observed types of damage and measured processes. Yet the models are also firmly based on established mechanics principles and known constitutive properties and processes for intact material. Hence, the models represent a unique combination of observed processes for the development of damage and standard mechanics principles for the behavior of intact material.

This section explores the development of both the ductile and brittle fracture NAG models. In each case, we describe first the experiments on which the model is based and then the development of the model.

9.2.1 Experimental Aspects of Ductile Fracture.

"Ductile" fracture here means damage processes that occur by the development of voids in the material; hence, large amounts of plastic flow accompany the fracture (the plastic flow fits with the usual meaning of "ductile," which refers to large plastic deformation). As described in Section 4, plate impacts are used for the fracture tests: full damage occurs with tensile stress pulse durations on the order of a microsecond. In addition to the usual measurements in these tests, detailed metallographic studies are made of cross sections through the specimens. The observed voids are counted and organized into size distributions. These observations of damage are the basis for a proposed fracture model that accounts for the nucleation (initiation) and growth (enlargement) of voids in ductile fracture.

217

Here, we consider in more detail the damage seen in cross sections of impacted plate specimens such as those shown earlier in Figure 2-5. The voids tend to be circular in plane and are therefore in fact spherical. They appear in a range of sizes and are distributed through the plate thickness: they are not of a single size, nor do they occur in a single plane. These plate specimens were impacted by a flyer plate in a gas gun and were, therefore, subjected to planar, one-dimensional loading. Therefore, the tensile stress history and hence the damage per unit volume should vary only with distance through the specimen in the direction of shock wave propagation. We shall see that tensile stresses occurred in the locations where we now see the voids and that longer durations of tensile stress loading coincided with the locations of the highest void density and of the largest voids. Hence, we have concluded that void presence and sizes are closely related to the transient tensile stresses in the specimens. Our approach is to count the damage and organize these counts so that they can be quantitatively related to the stress histories. Then we derive nucleation and growth rates for the voids from these data.

For the data analysis, we assume that the sample is isotropic and homogeneous and that spherical voids are nucleated at random with a concentration and total growth that depend only on the tensile stress history. The voids may actually be nucleated at inclusions or at grain boundaries, but not along bands or planes of inclusions. Under our assumptions the preceding compressive stresses do not cause damage directly, although they may precondition the material through work hardening or heating.

Quantitative analysis of the observed void damage in the specimen consists of the following steps:

(1) Sectioning, polishing, and photographing the fracture specimen so that the damage region can be studied.

(2) Determining from the photographs the areal density $n(r,x)$ of voids, which intersect the surface with a radius r at position x.

(3) Using a statistical transformation of $n(r,x)$ to determine the volume density $\rho(R,x)$ of voids of radius R at position x. Then the volume density is summed to provide the cumulative density function

$$N(R,x) = \int_R^\infty \rho(R',x)dR' \tag{9.6}$$

(4) Determining the nucleation and growth rates by correlating the function $N(R,x)$ with the computed stress history $\sigma(x,t)$.

The following subsections deal with these steps in more detail.

9.2.1.1 Determination of the Void Size Distribution. The photomicrographs of the damaged specimens show a range of void sizes, with larger ones concentrated near the expected spall plane and many small voids throughout the region near this plane. We determine quantitatively the density of voids (number per unit volume) and the size of voids as a function of location in the specimen.

For the metallographic examination, the specimens are sectioned perpendicular to the spall plane (several sections can be made to increase the number of observations and therefore improve the statistics of the damage counts). After sectioning, the surfaces are polished. This polishing must be performed carefully because, with soft materials, the removed material may be moved into the voids and thus change the observable dimensions of the voids. In some cases, it may be necessary to etch the surfaces to make identification of the voids easier. Following these preparations, the fracture surfaces are photographed through a microscope for the quantitative study.

With the photomicrographs available, we then count the voids present. A cross section of a target in aluminum is shown in Figure 2.5 of Section 2 in a form ready for counting. We use two methods for counting the voids and organizing the information from the counts.

(1)   Our initial method is appropriate for large numbers of voids. We divide the specimen cross section into 5 to 10 thickness intervals and perform separate counts within each interval. We note the maximum radius of voids (say, 100 µm) and the minimum radius observable (often around 1 µm). Then we divide the range of radii into radius intervals, starting at say 2 µm and expanding geometrically such that we have 10 to 20 radius intervals. Then for each interval, we count the number of voids that lie within each radius interval.

(2)   The second method is more flexible and especially appropriate for small numbers of voids. For each void, we determine and record the position and radius. Then, we can organize the voids into position and radius intervals later.

In either case, the result is a discretized void size distribution that can be represented by $n(r,x)$. The distribution $n(r,x)$ is the areal density of voids at position x (or, in the vicinity of x), which intersect the surface with a radius r (or in an interval from r_i to r_{i+1}). A sample count from such a study is shown in Table 9-1 for a laser radiation in an 1100 grade aluminum. Each void was recorded by radius and location in the sample.

The next step in processing this data is to divide by the area counted (50 µm wide and 2000 µm long) to determine the number per unit area. Next, we form cumulative numbers $\sum n(r,x)$ by summing the number densities from the largest radii to the smallest. The division by the area over which the count has been made makes the result independent of the x-interval size. The cumulative operation makes the result independent of the size of the radius interval. The cumulative void counts for the values in this table were shown earlier in Figure 2-13 (these are cumulative counts, not void densities per unit area).

219

Table 9-1. Void counts on a cross section of 1100 grade aluminum.

Range of Radii (μm)	Distance from the Rear Surface (μm)				
	0 – 50	50–100	100-150	150–200	200–250
0.0 to 2.4	2	7	2	1	0
2.4 to 2.95	6	12	6	2	2
2.95 to 3.57	4	18	17	1	1
3.57 to 4.3	7	11	7	8	0
4.3 to 5.17	3	5	7	3	0
5.17 to 6.2	2	11	9	5	1
6.2 to 7.64	3	10	2	0	0
7.64 to 9.45	0	7	2	1	0
9.45 to 11.9	0	4	3	0	0
11.9 to 15.3	0	3	1	0	0
15.3 to 20.2	0	3	0	0	0
20.2 to 27.5	0	1	0	0	0

By use of the standard technique of Scheil (1931, 1935), the volume density $\rho(R,x)$ of voids of radius R are computed from $n(r,x)\Delta r\Delta x$. For our purposes, it is convenient to work with the cumulative density function:

$$N(R,x) = \int_R^\infty \rho(R',x)dR' \tag{9.7}$$

which is the density of cracks at position xx with a radius greater than R.

Figure 9-1 shows an example of the void distributions resulting from the volume transformations of surface data for an impact that caused a tensile stress of 920 MPa for about 0.5 µs in a plate of 1145 aluminum. Shown are the cumulative numbers of voids per unit volume as a function of the void radius. Each curve is from a different 80-µm-wide zone through the thickness of the specimen, numbering from the region of high damage toward the free surface (counts from zones on the side of the high damage region toward the impact plane are not shown). The ordinate is the volume-related void density. The intercept at $R = 0$ is the total number of voids per cubic centimeter. Note that more and larger voids were present in zones labeled F01 and F03 than in the adjacent zones.

By comparing void distributions such as those of Figure 9-1 with computed stress histories, we observed that larger voids and larger numbers of voids were associated with longer durations of the peak stress. Therefore, a combination of nucleation and growth mechanisms would explain the presence of the voids.

For deriving the growth and nucleation functions, the void distribution function $N(R,x)$ is related to the stress history at location x calculated using a one-dimensional wave propagation computer code. The relationships between stress histories at various locations in the sample can be shown as follows. For the simple case of a square stress pulse, an x-t plot of an impact experiment can be constructed as shown in Figure 9-2. A projectile F moving from left to right impacts a sample S at time t = 0, inducing compressive shock waves (1 and 2), which move into the sample and projectile, respectively. When these impinge on the free surfaces, they are reflected as compression-release waves. These waves interact in region A_1, producing a tensile stress. The tensile waves (3 and 4) then propagate to the free surface of the sample and are reflected as recompression waves. Tensile waves labeled 4 are reflected at the interface between the projectile and the sample because this interface does not sustain a tensile wave. The time t at stress (for this first tensile pulse) at any position x is then given by a vertical section of the tensile region T [Figure 9-2(a)]. This time-at-stress was plotted as shown in Figure 9-2(b). This simple analysis defines the time at peak tensile stress for any plane x parallel to the impact surface for a simple square wave.

Now the function $N(R,x)$, the size distribution of voids in the zone at position x, can be related to a time t at tensile stress through the time-at-stress versus position plot shown in Figure 9-2(b).
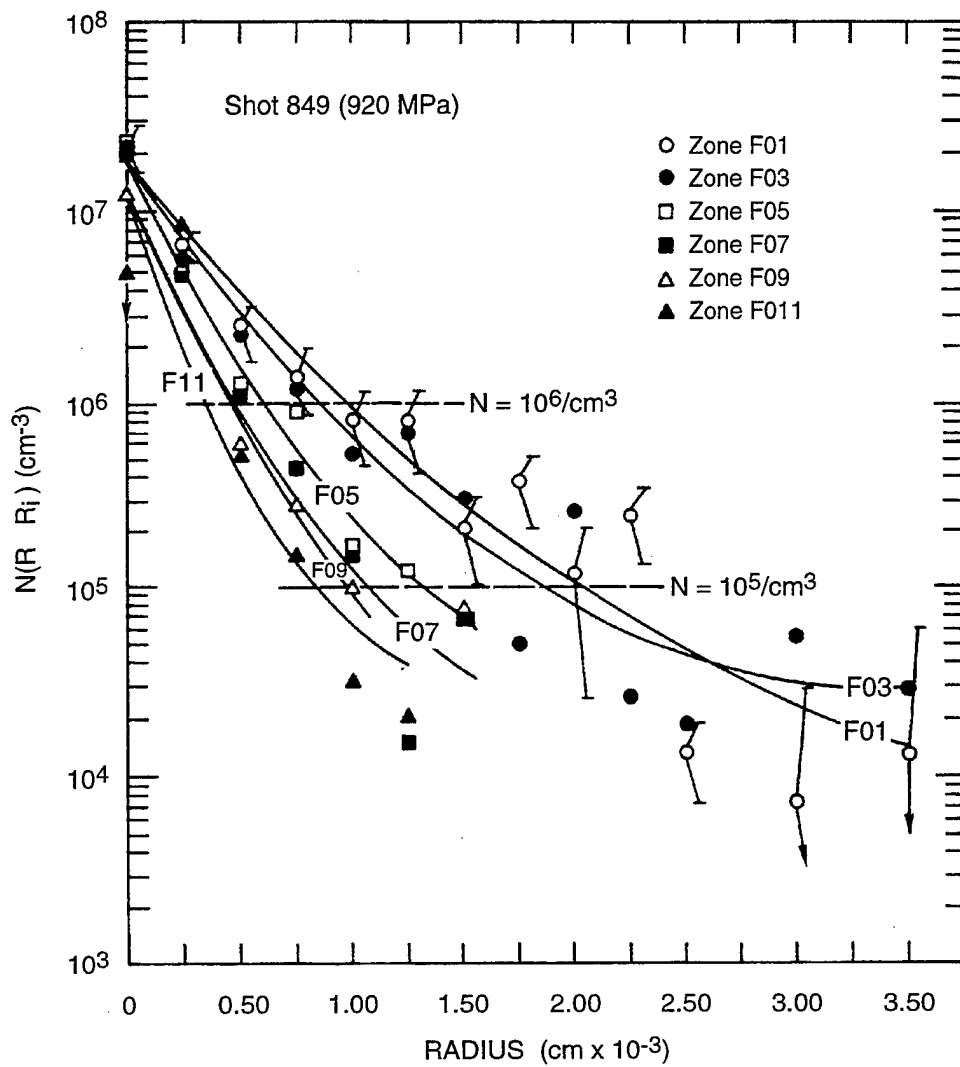
Figure 9-1. Distribution of voids (error lines are slanted to avoid overlap).
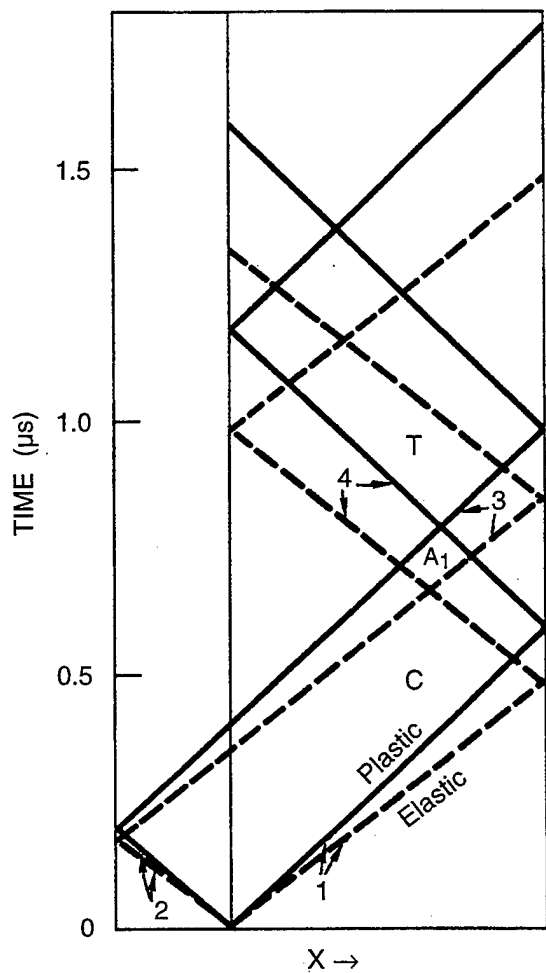
(a) Simple x-t plot of impact experiment
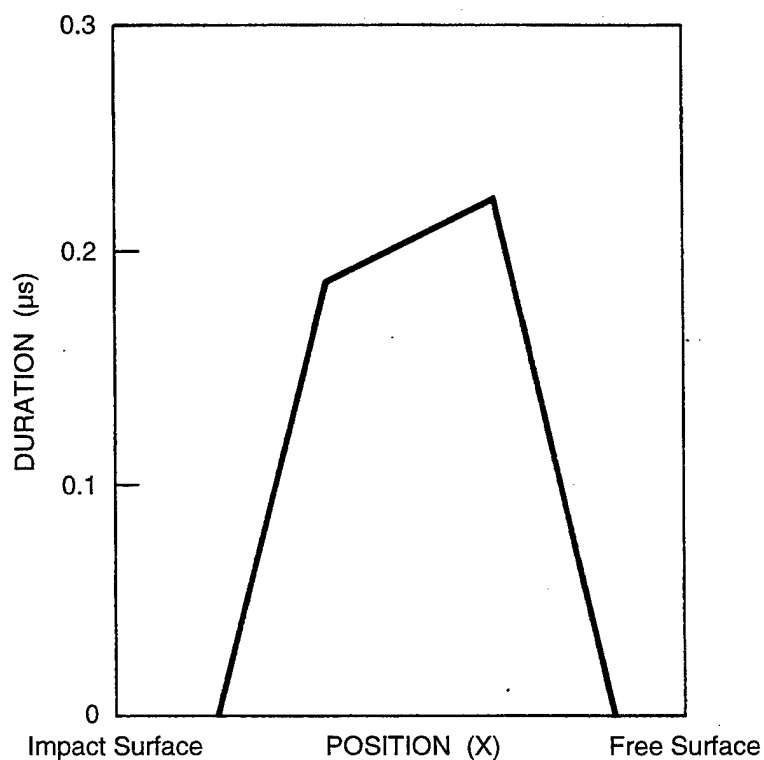
(b) Time at stress versus position derived from simple x-t plot

Figure 9-2.   Computed stress waves in an impact specimen and the derived duration of peak tensile stress for a simple square wave with a precursor.

9.2.1.2 Void Nucleation Rate. The void nucleation rate is determined from plots of the void density as a function of stress level and stress duration. The void density data available from two experiments on 1145 aluminum are shown in Figure 9-3 with a time-at-stress plot as in Figure 9-2(b). The apparent correspondence between stress duration and the void density encouraged us to plot void density against time as in Figure 9-4. Except for Shot 873, the shots indicate an approximately linear relationship between the number of nuclei and time. Therefore, we presumed that the basic nucleation relation is

$$N(\sigma_m, t) = \int_o^\infty \dot{N}(\sigma_m) dt = \dot{N}(\sigma_m)\Delta t \tag{9.8}$$

for a square wave and that $\dot{N}$ is independent of time during the duration Δt of the peak tension. σ_m is the mean stress.

From the observed patterns of the void densities, we fit the void count data to the following form:

$$N_g = N_o e^{-\left(\frac{R}{R_1}\right)} \tag{9.9}$$

where N_g is the number of voids per unit volume with radii greater than R, N_o is the total number of voids per unit volume, and R_1 is a size parameter. Then N_o is used to determine a unique nucleation rate.

To determine the stress dependence of $\dot{N}(\sigma_m)$, we plotted the nucleation rate versus mean stress, as in Figure 9-5. This nucleation rate is

$$\dot{N} = \dot{N}_o \left\{ e^{\left(\frac{\sigma_m - \sigma_{no}}{\sigma_1}\right)} - 1 \right\} \tag{9.10}$$

where $\dot{N}_o$ is the nucleation rate constant, σ_{no} is the threshold stress for nucleation, and σ_1 is the stress sensitivity factor. All three of these parameters are new material properties that are obtained from the fracture experiments.

9.2.1.3 Void Growth Rate. The void growth rate $\dot{R} = (\partial R/\partial t)_N$ is calculated by comparing the function $N(R,x)$ from several tests with computed stress histories at the same x-locations as the data were taken. The approach to this calculation is indicated with the aid of Figure 9-1. These distributions are taken from different zones in the material, and for each zone there is a different duration. Because there is increasing damage with stress duration, the distributions can be visualized as a historical sequence of the damage at one location. Considered in this way, the curves provide a velocity when we divide the change in radius of a particular void by the difference in the stress duration. Note that this
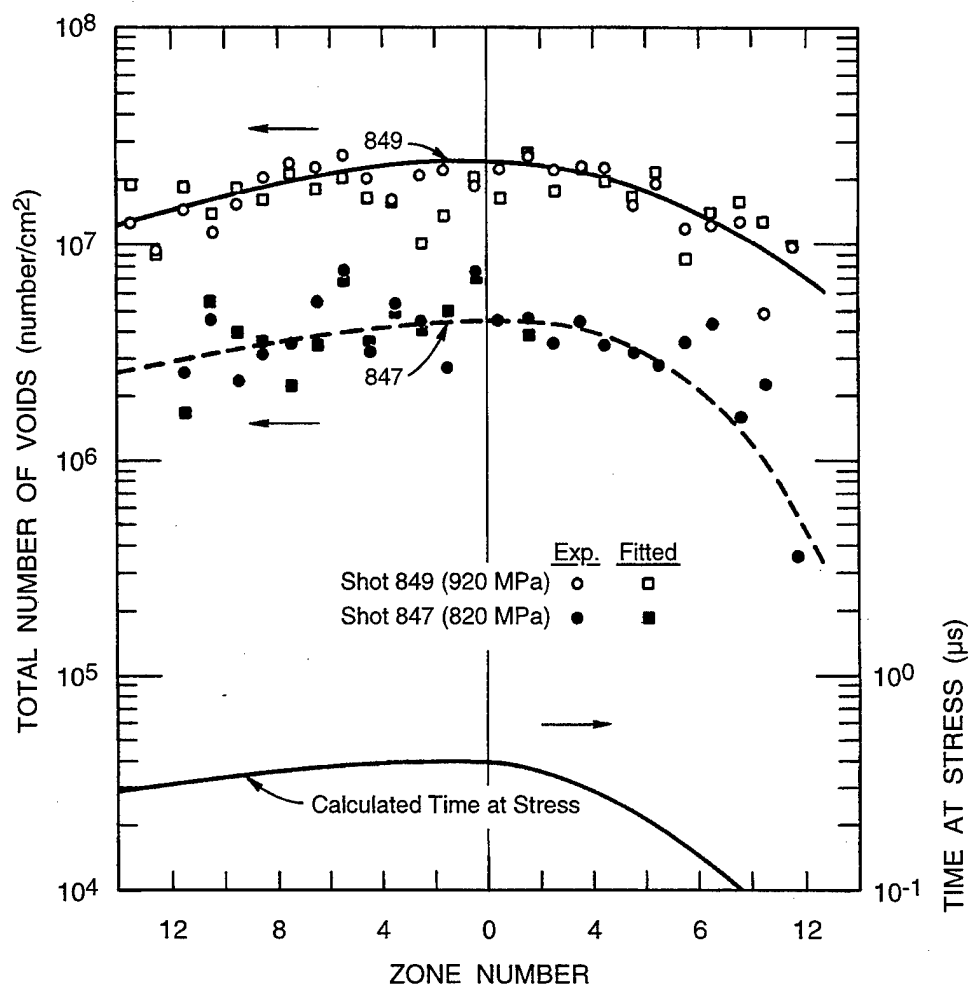
Figure 9-3.   Comparison of the spatial variation of the number of voids and the time-at-stress.
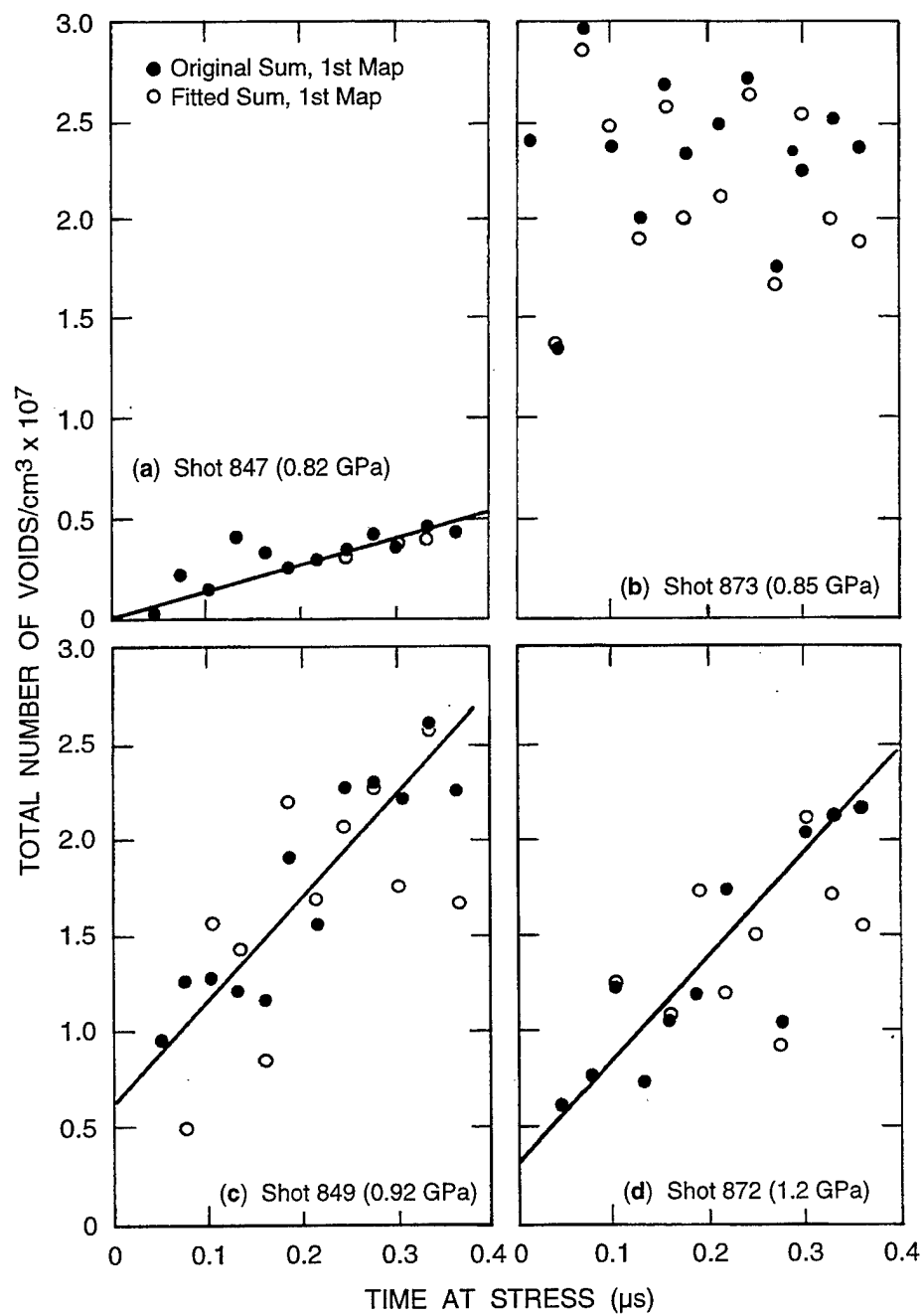
Figure 9-4.   Dependence of the void density on the time at stress
               for shots 847, 873, 849, and 872.
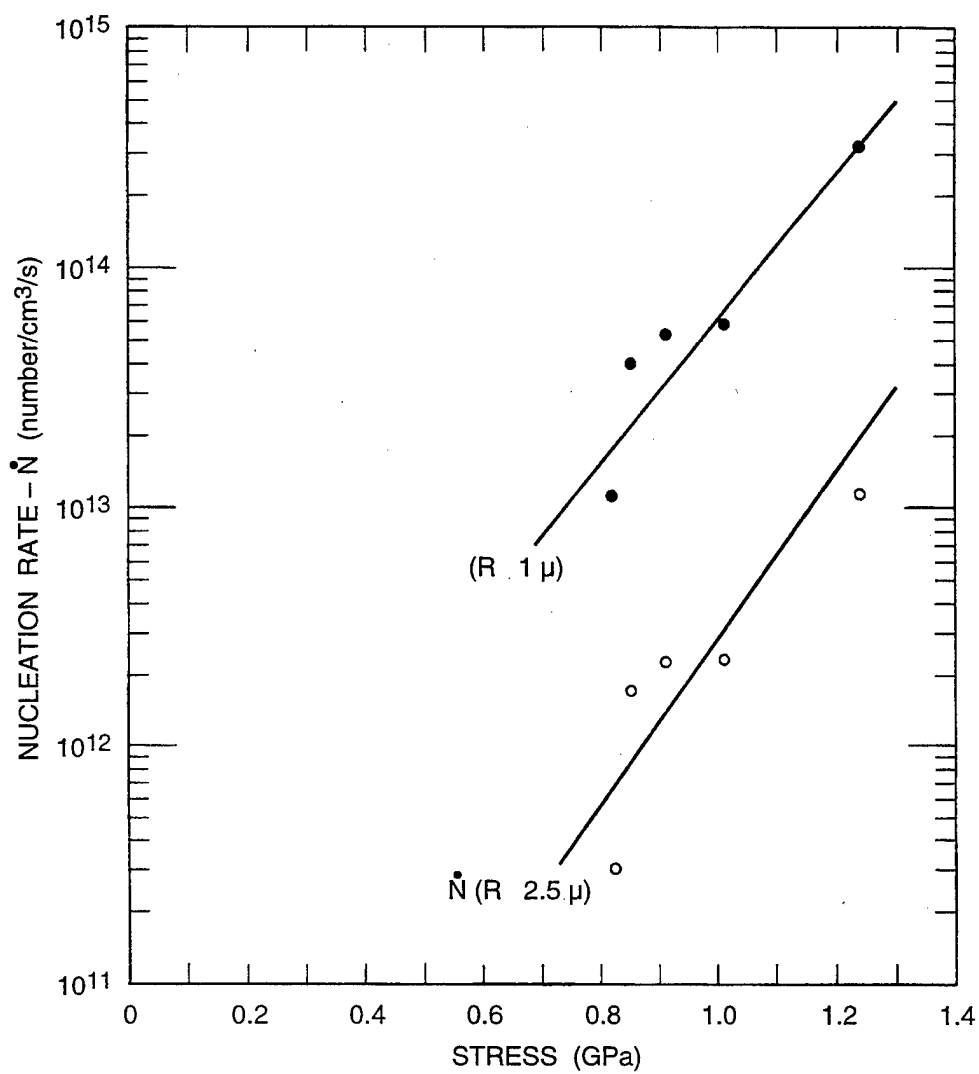
Figure 9-5.   Dependence of nucleation rate on stress for shots 847, 873, 849, and 872.

examination of growth neglects that we have nucleation occurring at the same time, so what we are interpreting as $(\partial R/\partial t)_N$ is partially associated with nucleation. Nevertheless, the simpler interpretation is useful for discussion of the underlying physics and gives a good approximation to the growth rate coefficient.

For example, take the void that is number 1 million/cm^3 when ranked by size, that is, at $N_g = 10^6$/cm^3. Under our assumptions (and neglecting the continuing nucleation), this void will remain number 1 million throughout the growth because all voids are governed by the same growth laws. When we plot the log of the radius of the 1 millionth void versus duration, we obtain an essentially straight line as in Figure 9-6, suggesting a relation of the form

$$\dot{R} = AR \tag{9.11}$$

where A, the slope of the lines, is independent of N_g but a function of the nominal mean stress in the test. By multiplying Eq. (9.11) by $4\pi R^2$, we can express the growth law in terms of void volume V_v as follows:

$$4\pi R^2 \dot{R} = \frac{4}{3}\pi R^3 (3A) \qquad \text{or} \qquad \frac{dV_v}{dt} = 3AV_v \tag{9.12}$$

This volume expression is useful because we may consider V_v to be the relative volume of the entire void size distribution instead of the volume of a single void.

Values of the growth factor A from four experiments are plotted in Figure 9-7 to determine the stress dependence of A. The growth factor appears to be a linear function of mean stress σ_m above a threshold stress. This result is consistent with the following equation for growth derived by Poritsky (1952) for expansion of a void under tension in a viscous fluid.

$$\dot{R} = \frac{\sigma_m - \sigma_{go}}{4\eta} R \tag{9.13}$$

where η is the material viscosity and σ_{go} is a mean threshold stress. In Poritsky's equation, σ_{go} is the internal tensile pressure in the void, but here we assume it corresponds to a strength of the solid material. The derivation of Carroll and Holt (1972a) indicates that σ_{go} is several times the yield strength of the material.

Thus, we have a void growth rate that has been derived directly from the experimental observations of voids, yet it is also consistent with theoretical derivations. This is one of the processes to be inserted into any model for describing ductile fracture.

228
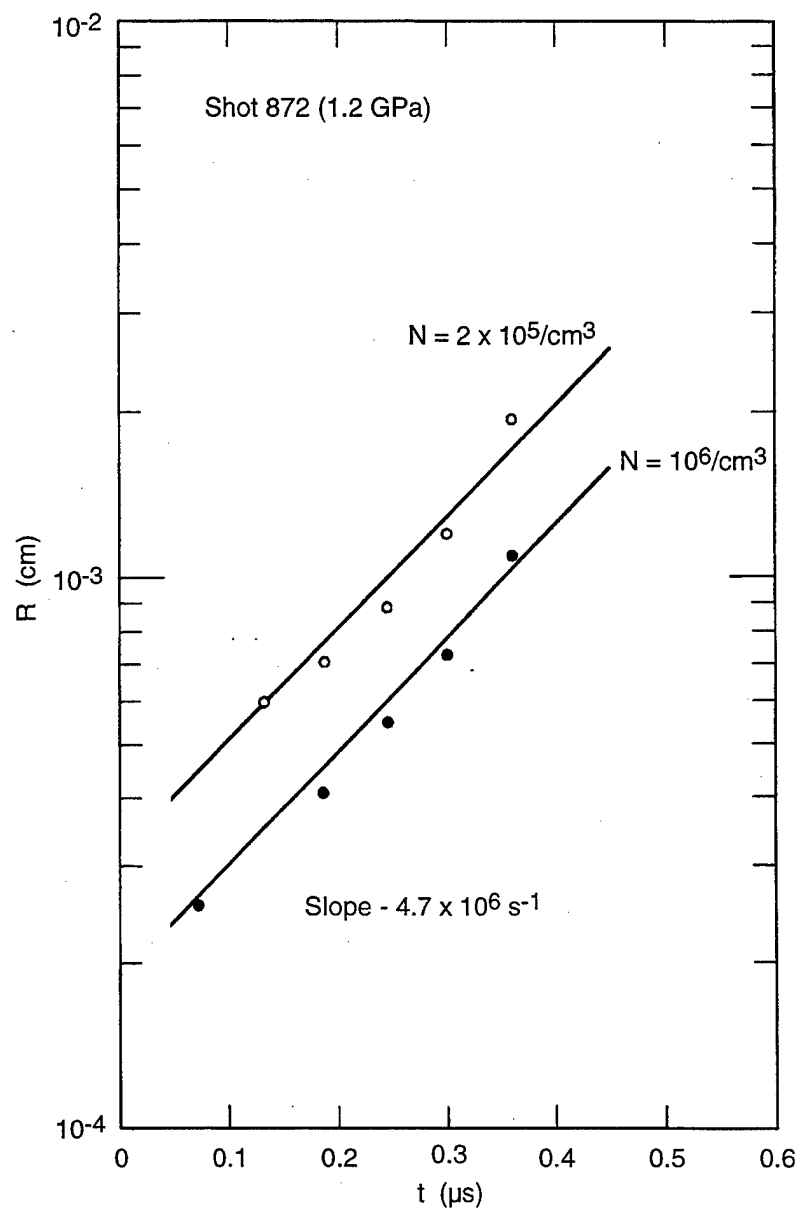
Figure 9-6.   Void growth rate for two values of N for Shot 872.
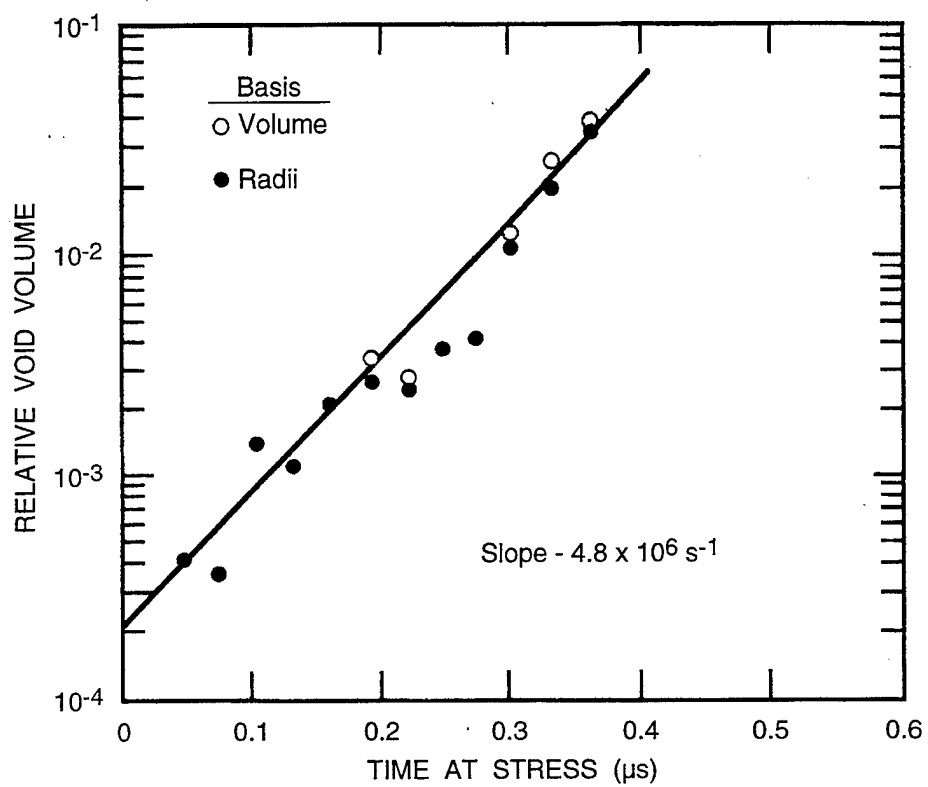
Figure 9-7. Time dependence of void volume.

9.2.1.4 Nucleation Void Size. Nucleation may occur physically through the debonding of the matrix material from an inclusion or through a vacancy development at a triple point between metal crystals. We can determine the size distribution at nucleation either by counting the inclusions or other defects that lead to void development or by extrapolating from the counted void size distribution. It is desirable to follow both procedures, if possible, to verify the physical appropriateness of the modeling approach to the material under study.

The extrapolation to determine the nucleation void size from the void counts is undertaken in two steps:

(1) The volumetric void size distributions (number per unit volume) are fitted to the exponential form in Eq. (9.9), thereby determining the parameters N_o and R_1 for several tests and several x-locations in each test.

(2) The logarithms of R_1 are plotted versus the tensile impulse $(\sigma_m - \sigma_{go})\Delta t$, where Δt is the nominal duration of the tensile stress.

The slope of the line through the R_1 values gives material viscosity η in Eq. (9.13). The intercept of the line on the vertical axis at zero impulse gives the value of $R_1 = R_n$ at nucleation.

9.2.1.5 Damage Characterizing Parameters. Thus far we have characterized the damage with the parameters N_o and R_1 (or R_n at nucleation). However, the void volume is more important in determining both the strength degradation and the effect on the stress waves. The relative void volume at any time is

$$V_v = \frac{4\pi}{3}\int_o^{N_o} R^3 dN = \frac{4\pi}{3}\int_o^\infty R^3 dN\left(-\frac{dN}{dR}\right)dR = 8\pi N_o R_1^3 \tag{9.14}$$

Thus, in addition to the total number of voids per unit volume N_o, either the characteristic radius R_1 or volume V_v may be specified.

9.2.1.6 Interaction of Stress and Damage. Even fairly small levels of damage significantly modify the stress history in the sample from that without damage. When damage occurs (void volume increases), recompression waves emanate from the damaged spot and alter stress histories in adjacent material. Figure 9-8 shows a sample of a computed stress history that was altered by a relative void volume of about 0.5% at the spall plane. These recompression waves appear to overtake the tensile waves and attenuate them. Therefore, usually the peak tension is not reached throughout the tensile region of the target, and stress histories at points adjacent to the spall plane are modified even more than those at the spall plane.

From these computed results, we can conclude that for high damage, the peak stress and the stress duration from no-damage calculations are only rough approximations to the actual values. Hence, it is

231
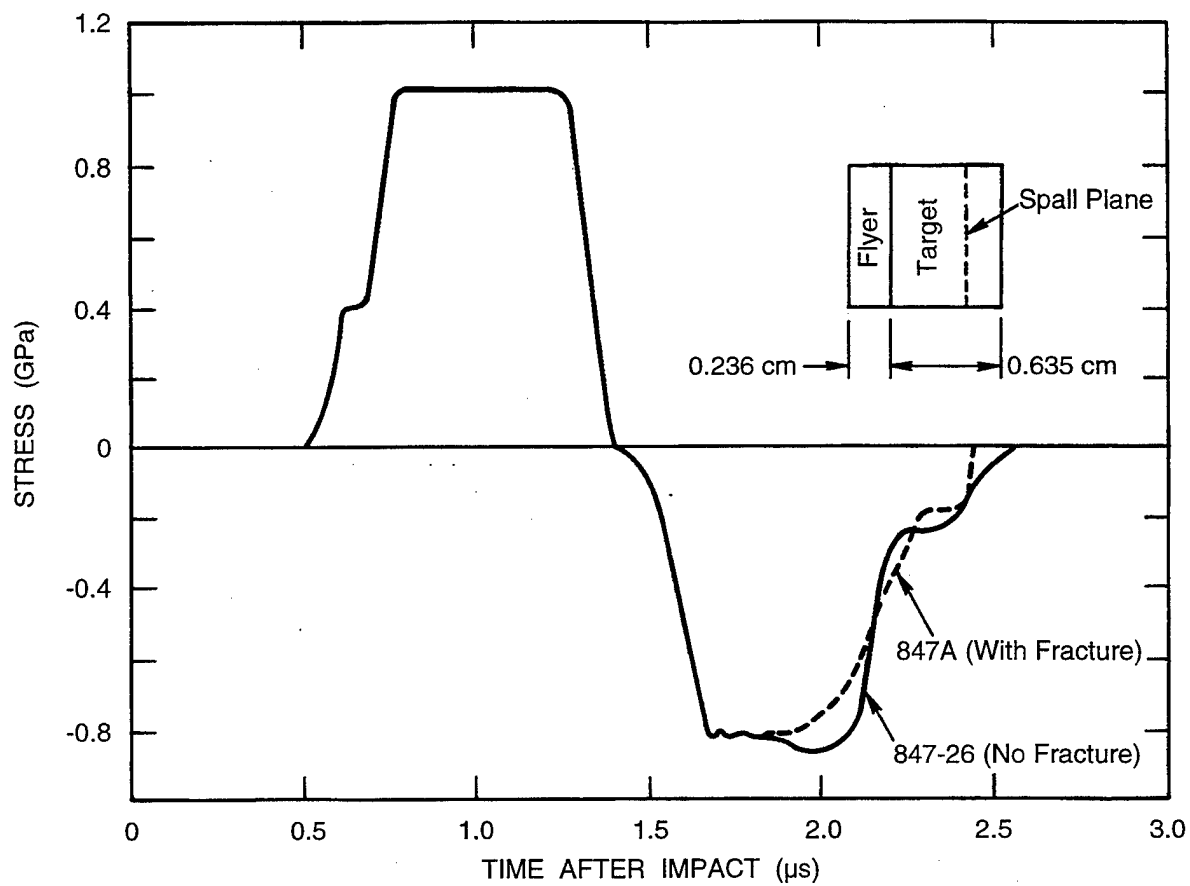
Figure 9-8.   Effect of damage on stress history at spall plane of shot 847 (0.82 GPa).

necessary to use a fairly accurate damage model for the wave propagation simulations to obtain reliable estimates of the stress histories.

9.2.1.7 Summary. Experimental techniques have been developed for conducting impact tests to determine ductile fracture processes. The damage appears as distributions of microvoids that appear to be nucleated at inclusions and to grow until they may coalesce and sever the sample. Quantitative posttest examinations of the partially fractured samples provide the nucleation and growth rates for the development of these voids. The data obtained are a basis for models describing the tensile fracture of ductile materials.

9.2.2 Ductile Fracture Model Development.

A model termed DFRACT was developed at SRI (Barbee et al., 1970, 1972; Seaman et al., 1971; and Curran et al., 1987) to describe the fracture processes that occur by the nucleation and growth of voids in very ductile materials. The model represents fracture under conditions of projectile impact, air shock loading, deposition of intense thermal radiation (from x-ray, electron beam, or laser sources), or explosion. This model is appropriate for loadings with tensile durations of a few microseconds or less. The model has been written into a computer subroutine for use with wave propagation or structural analysis programs.

The model has a micromechanical basis: it contains algorithms for nucleating and growing distributions of voids and stress-strain relations that account for the developing damage. Thus, the DFRACT model is a nucleation-and-growth (NAG) model. It is based both on metallographical observations of damaged specimens and on the customary continuum mechanics treatment of constitutive laws. The model derivation given here includes the nucleation and growth processes, the damage-affected stress-strain relations, and the solution procedure to determine the current stress and damage state under imposed strains.

9.2.2.1 Damage Processes in the Model. Damage in the model is represented by the total number of voids per unit volume and the relative void volume (V_v). The void density quantity N_o is actually the total number of all voids per unit of initial volume. With this definition, the number does not change with expansion of the material, but only through nucleation of new voids. The relative void volume, however, is the amount of void volume relative to the current total volume; hence, it changes because of nucleation, and growth and from changes in the overall volume of the material. We assume that the void size distributions retain the form of Eq. (9.9) throughout their history. Here, we consider separately the change in void volume caused by nucleation and growth and then sum these two contributions to find the total change in void volume.

Nucleation in the model occurs as the addition of new voids to the existing set. These new voids are presumed to occur in a range of sizes with a size distribution given by Eq. (9.9). At nucleation, the parameter R_1 equals R_n, the nucleation size parameter (a material constant). The number of voids nucleated is governed by the nucleation rate function in Eq. (9.10). The number nucleated in a time interval Δt is simply

$$\Delta N = \dot{N}_o \left\{ e^{\left(\frac{\sigma_m - \sigma_{no}}{\sigma_1} \right)} - 1 \right\} \Delta t \qquad (9.15)$$

for mean stresses above the threshold stress σ_{no}. The mean stress is generally taken as the stress at the center of the time interval. The void volume nucleated in a time interval Δt is found by combining Eqs. (9.14) and (9.15):

$$\Delta V_{vn} = 8\pi \Delta N R_n^3 \qquad (9.16)$$

Growth in the model is represented by Eq. (9.13), altered as in Eq. (9.12) to represent the increase in void volume due to growth:

$$\left(\frac{\partial V}{\partial t} \right)_N = \frac{3}{4} \frac{\sigma_m - \sigma_{go}}{\eta} V_v \qquad (9.17)$$

Because this expression is independent of the size and number of voids, we can also use it for the growth of the volume of the entire void size distribution. The growth of the void volume during a time interval Δt is obtained by integrating Eq. (9.17) to obtain the change in volume V_v caused by void growth. Thus,

$$\Delta V_{vg} = V_{vo} e^{\left(\frac{3}{4} \frac{\sigma_m - \sigma_{go}}{\eta} \right) \Delta t} - V_{vo} \qquad (9.18)$$

where V_{vo} is the void volume at the beginning of the time interval. Because every void in the distribution grows by the same exponential factor, even the size parameter R_1 grows according to Eq. (9.13).

$$R_1 = R_{10} e^{\left(\frac{\sigma_m - \sigma_{go}}{4\eta} \Delta t \right)} \qquad (9.19)$$

where R_{10} is the size parameter at the beginning of the time interval. Then the new void volume can also be found from Eqs. (9.16) and (9.18):

$$V_v = V_{vo} + \Delta V_{vn} + \Delta V_{vg} \qquad (9.20)$$

234

where $V_{vo} = 8\pi N_o R_{10}^3$, the void volume at the beginning of the time internal.

9.2.2.2 Stress-Strain Relations with Damage. In our model, the stress-strain relations for material undergoing fracture account for the presence of the voids. We construct these stress-strain relations by requiring that the sum of the volumetric strains taken in the solid material and in the void must equal the imposed volumetric strain. Thus, we conserve volume at all times:

$$V = V_s + V_v = 1 \tag{9.21}$$

where V_s and V_v are the relative volumes in solid and void. The gross stresses σ_{ij} on the mixture of void and solid are reduced by the void volume from the stresses σ_{ij}^s that exist in the solid component:

$$\sigma_{ij} = \sigma_{ij}^s (1 - V_v) \tag{9.22}$$

This consistency in the model is essential to allow the damage to have an appropriate effect on the stress-strain relations and thus on the moduli and effective wave velocities. This damage effect is important in defining the breadth of damage near a spall plane and in providing for multiple spalls.

For the derivation of the stress-strain relations, the stress in the solid material is separated into mean stress and deviatoric components. The mean stress is related to the specific volume and internal energy through the Mie-Grüneisen equation of state:

$$-\sigma_m = K_1 \left(\frac{\rho_s}{\rho_{so}} - 1 \right) + K_2 \left(\frac{\rho_s}{\rho_{so}} - 1 \right)^2 + K_3 \left(\frac{\rho_s}{\rho_{so}} - 1 \right)^3 + \Gamma \rho_s E \tag{9.23}$$

where K_1 is the bulk modulus, K_2 and K_3 are higher order terms in the series for bulk modulus, Γ is the Grüneisen ratio, E is internal energy, ρ_s is the solid density, and ρ_{so} is the initial density of the solid. The mean stress has a negative sign here because we are treating stress as positive in tension, but the usual sign convention of Eq. (9.23) is for pressure, which is positive in compression. The mean stress computed from Eq. (9.23) is necessarily an average, because the actual stress states will vary greatly through partially fractured material.

The mean stress on the gross section of the fractured material can now be related to the mean stress in the solid components according to a relation derived by Carroll and Holt (1972b) for porous material:

$$\sigma_{mg} = \frac{\rho}{\rho_s} \sigma_m \tag{9.24}$$

where σ_{mg} is the mean stress on a section and ρ is the average density of the porous material. A combination of Eqs. (9.23) and (9.24) relates the average pressure P to the energy E and density ρ.

The deviator stresses are computed by the usual elastic and plastic relations. However, the damage that occurs is presumed to affect both the yield strength and the effective shear modulus of the material. The modulus is reduced as a function of the developing porosity according to the elastic relations of MacKenzie (1950). His formulation, in the present nomenclature, is

$$G = G_o(1 - V_v \rho F) \tag{9.25}$$

where G is the effective shear modulus of the solid and void combination, G_o is the shear modulus of the solid, V_v is the specific volume of voids, and

$$F = 5\frac{3K_1 + 4G_o}{9K_1 + 8G_o} = 15\frac{1-v}{7-5v} \tag{9.26}$$

where v is Poisson's ratio of the solid.

The yield strength degrades more rapidly than the modulus as the porosity increases. Our dynamic calculations of void growth (Seaman et al., 1971) indicated that the yield strength, Y, should degrade from its initial value Y_o, according to the relation

$$Y = Y_o(1 - 4V_v) \tag{9.27}$$

This expression is used in the fracture subroutine.

9.2.2.3 Solution Procedure. During its use in a wave propagation code, the ductile fracture model is provided with a strain increment tensor and the model must provide the new stress tensor, in addition to updating the number and size of voids. The determination of the stresses requires the simultaneous solution of the nucleation rate Eq. (9.15), growth rate Eq. (9.17), pressure-volume relation (9.23), and the consistency Eqs. (9.21) and (9.22). We have successfully used two solution procedures:

(1) First-order predictor-corrector technique, treating the growth equation as primary, and all other equations as secondary. The predictions are made by a Newton-Raphson method, followed by *regula falsi* for the iterations.

(2) Fourth-order Runge-Kutta method, treating the differential equations for growth and nucleation equally.

The results are equivalent, although the first is faster at later times when the damage is large and the second is better for small void volumes and very rapidly changing stresses. Simulations that have been made with the DFRACT model in a wave propagation computer program are shown later in Section 9.2.5.

9.2.3 Experimental Aspects of Brittle Fracture.

The experimental portion of a study of fracture is outlined here in which the goal was to develop a micromechanical model (Seaman et al., 1976). Here we are considering brittle fracture only: we define "brittle" to mean fracture in which the damage appears as cracks at a magnification of about 100 times.

The experiments were all conducted by impacting one plate against a thicker target plate of the same material such that fracture or spall occurred within the target plate. Following impact, the targets were sectioned and polished, and the cross sections were examined for damage. The cracks were counted. These counts were correlated with the stress durations to develop nucleation and growth rates for the damage. The materials tested include polymers, rocks, concrete, ceramics, propellant, steels, iron, and other metals.

We describe some of the fracture observations, the method for transforming from the crack counts to a volume basis, and indicate the method for deducing nucleation and growth rates.

9.2.3.1 Fracture Observations.

The experimental methods used here are essentially the same as those described in Section 4 and in Section 9.2.1. The target plate may be backed by a plate of epoxy (or other low impedance material), and a stress gage placed at the interface of the epoxy and target to record the stress history there.

Following the impacts, the targets are sectioned and polished, and the damage is observed. Such cross sections are shown in Figure 9-9 for Armco iron. We see that the cracks vary in number, in size, and in orientation with respect to the direction of propagation (vertical in the figure). As the cracks are counted, they are grouped according to length and orientation. For example, length groups of 0 to 5 μm, 5 to 10 μm, 10 to 15 μm, 15 to 25 μm might be used. Similarly, 10 angle groups of 9 degrees each may be used to represent the orientations. In this way a large matrix of counts is obtained for each region of the specimen. These cracks observed on a cross section must then be transformed to a volume basis (number per unit volume) to be considered material properties. The required transformation is outlined in the next section.

We have chosen here to illustrate brittle fracture processes by a series of observations in Armco iron. In Section 9.2.5, we show observed fractures in other brittle materials. Some representative sections from Armco iron targets originally examined by Seaman et al. (1976) and Barbee et al. (1970) are shown in Figures 9-9, 9-10, and 9-11. In Figure 9-9, the direction of propagation is vertical; in the others it is horizontal. All these sections show many small cracks at many angles. In Figure 9-9, the number and lengths of the cracks appear to increase with the tensile stress duration. This observation leads us to postulate a nucleation and growth process for the cracks, that is, processes in which the numbers and sizes increase with time.
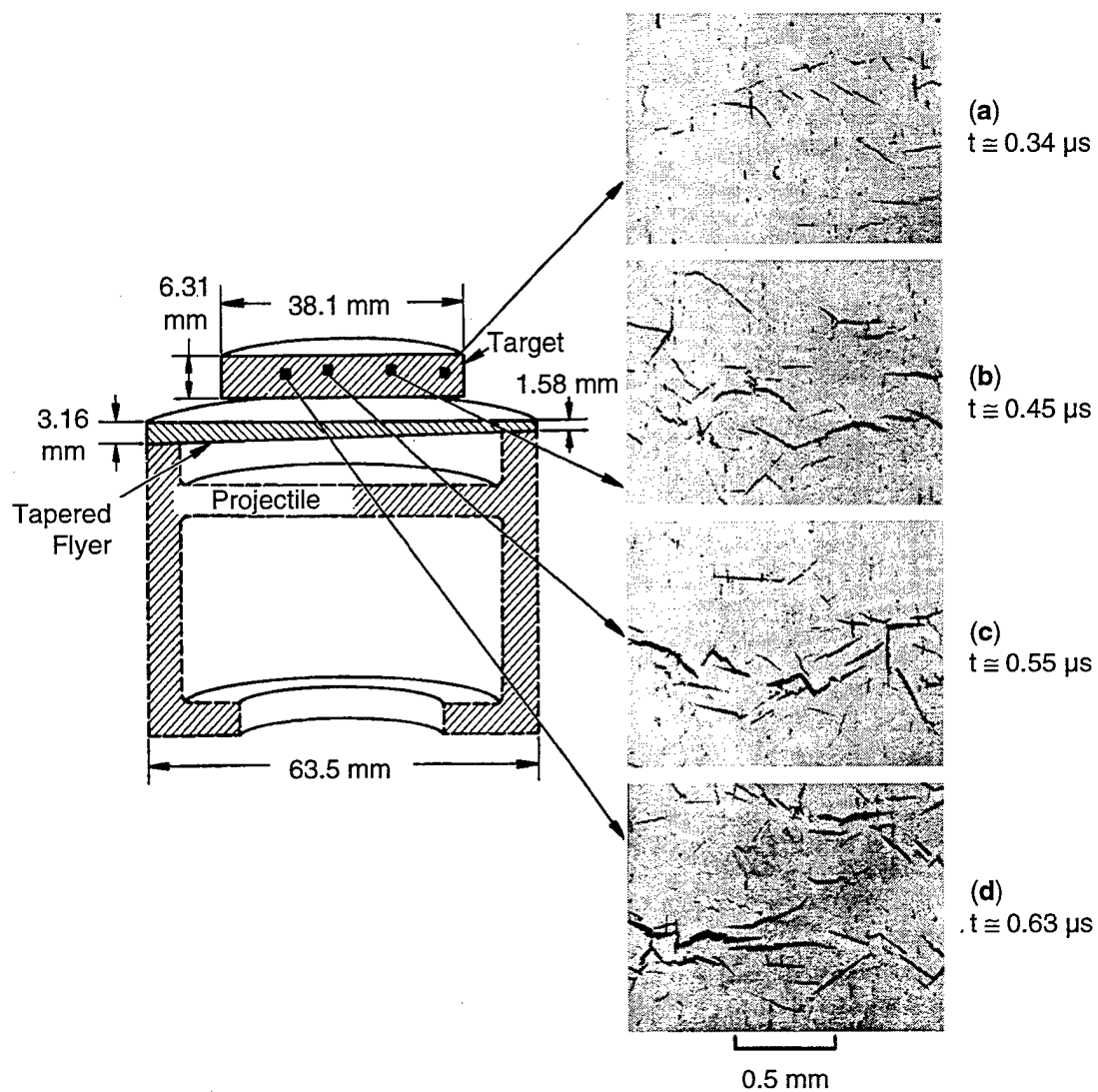
Figure 9-9. Configuration of a tapered flyer impact experiment in Armco iron (shot S1) and observed damage on a cross section of the target.

238
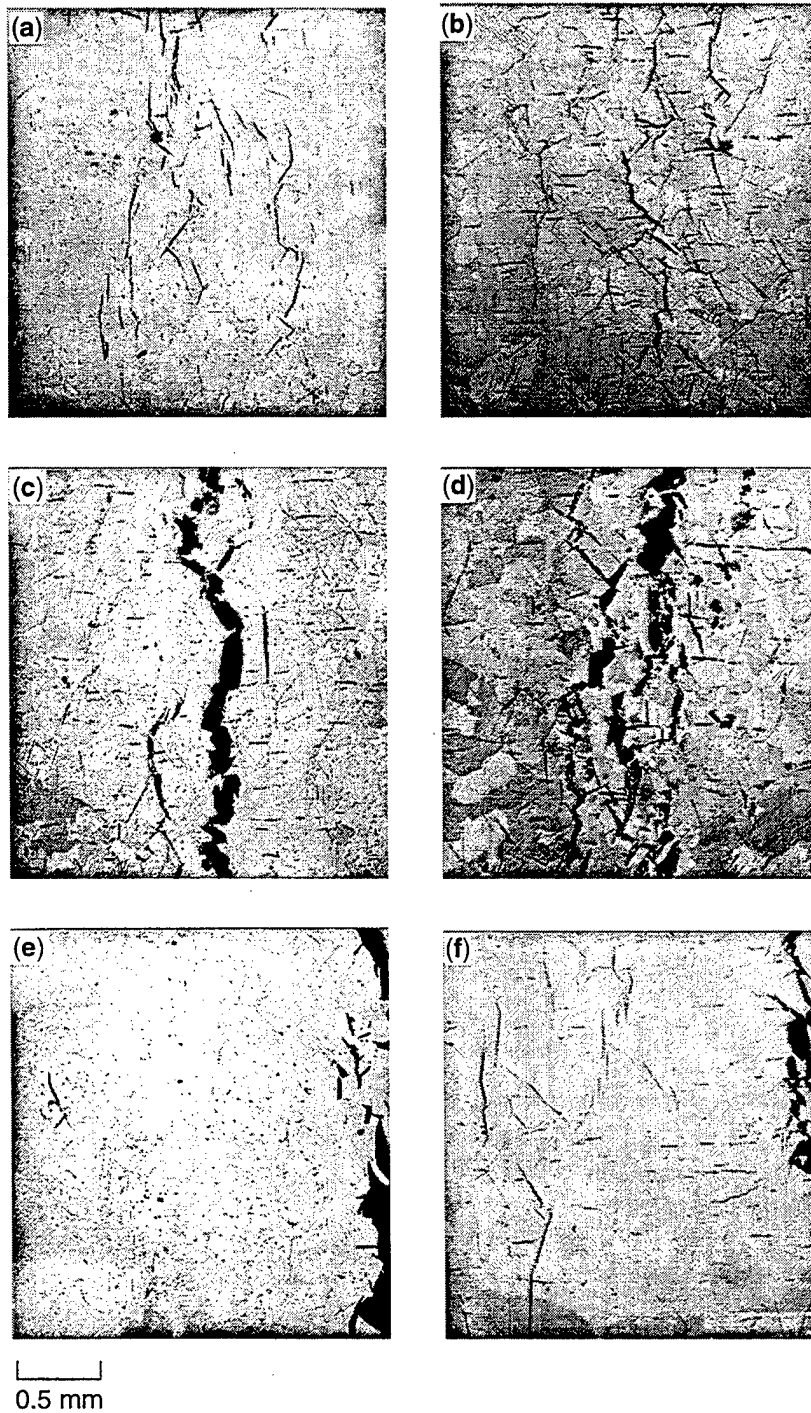
Figure 9-10. Photomicrographs of damage in Armco iron.

0.5 mm

239

100 μm

Figure 9-11. Twins in the area of high crack density in Armco iron.

240

In some of these figures, the small cracks have intersected to form longer cracks. These longer cracks correspond with the macrocracks usually referred to in fracture mechanics. We can see from these figures that the rough surfaces often seen on macrocracks really arise because the large crack is formed by the coalescence of many small cracks and not by an irregular growth of a single large crack.

The grain structure of the Armco iron can be compared with the crack patterns in Figures 9-10(d) and 9-11. It appears that the microcracks are essentially straight cuts across a grain or along a grain boundary. Thus, the basic length of the microcracks is like the distance across a grain.

The counts made on the cross section of an Armco iron target impacted at about 4 GPa are shown in Figure 9-12 from Seaman et al. (1971 and 1978b). (For the plot, the counts for all orientations have been summed.) Here, each curve refers to a different position through the target and hence to a different tensile stress duration. The duration is maximum near the center of the specimen and smaller above and below. By comparing the damage curves in the figure with the stress duration, we see that the number and size of cracks increase with duration in a regular manner. Hence, the data may be uniform enough to be a basis for a model of microcracking.

Following the procedure developed for ductile fracture, we plotted the number of cracks or crack size versus stress duration to determine the nucleation and growth rates. The counting process is illustrated schematically in Figure 9-13. The cross section is divided into several strips such that all the material in each strip has about the same stress duration. Then the cracks are counted by size and assembled into size distributions for each orientation (not illustrated) and strip. These surface distributions (number per unit area) are transformed as outlined later into number per unit volume.

The nucleation rate is then obtained from a plot like that in Figure 9-14, in which we have plotted points from the planes of maximum damage from several impacts. The ordinate is the number density divided by the nominal stress duration; the abscissa is the peak tensile stress from a no-damage calculation. The trend line through the data gives the nucleation function.

The growth function is obtained from the plot in Figure 9-15. To produce this plot, the size distributions on the planes of maximum damage from several impacts were fitted to the exponential form

$$N_g = N_o e^{-\left(\frac{R}{R_1}\right)} \tag{9.28}$$

Then the R_1 values were plotted versus the tensile impulse: the peak tensile stress σ_{max} times the stress duration Δt. The trend line here gives the growth relation for the cracks.

The forms of the data shown in Figures 9-14 and 9-15 are idealized: the actual data from brittle fracture experiments are generally much more complex. Therefore, the results have not been so easy to
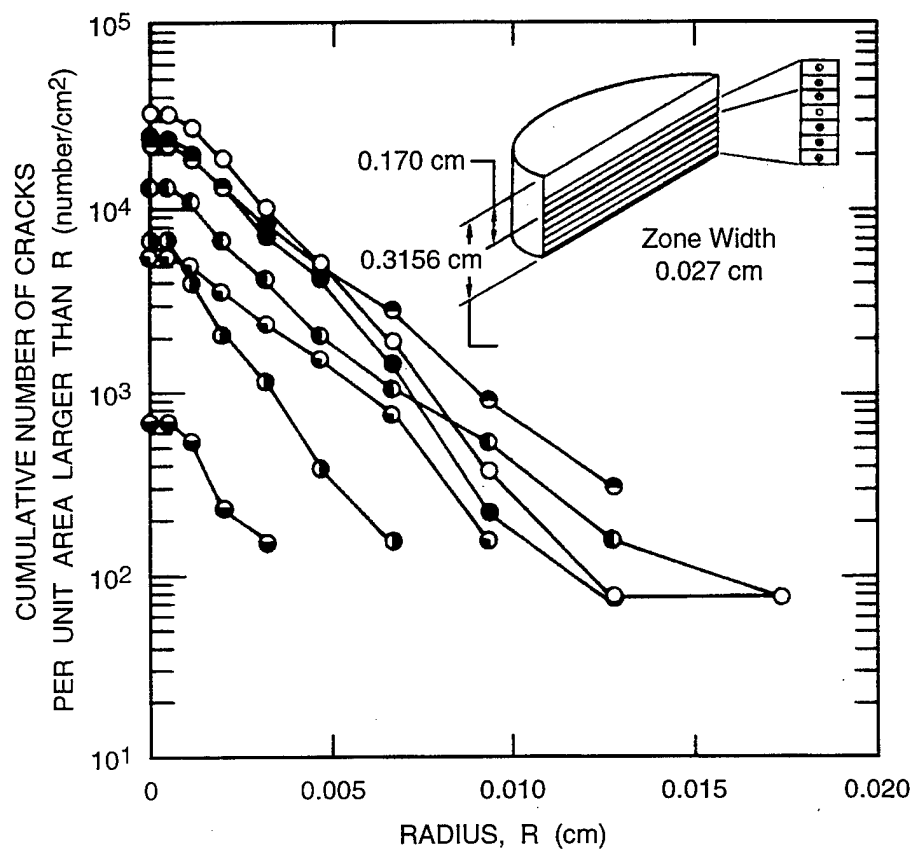
Figure 9-12. Observed cumulative crack concentrations on a cross section of a cylindrical target of Armco iron impacted at a nominal stress of 4 GPa.
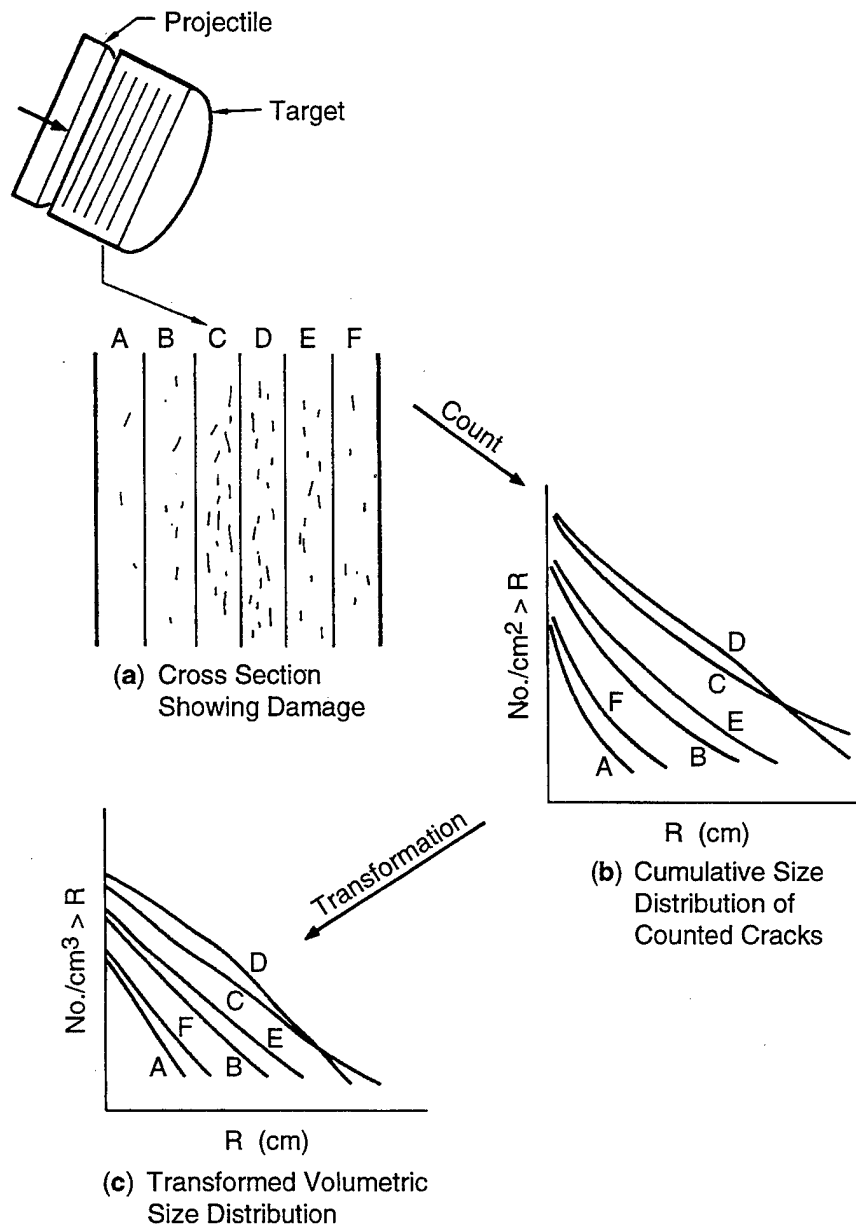
Figure 9-13. Acquisition and transformation of crack count data from cross sections of impacted cylindrical targets.
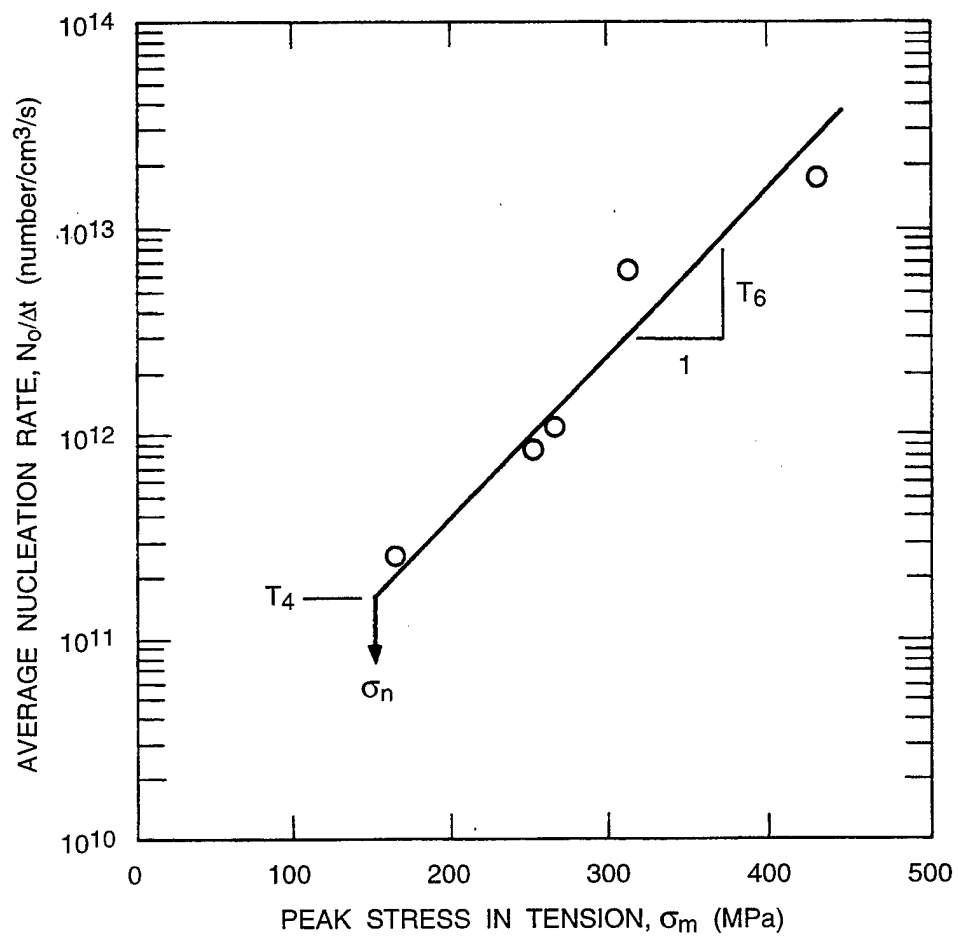
Figure 9-14. Plot of observed number of cracks with computed stress σ_m and duration Δt for obtaining nucleation rate parameters T_4 and T_6.
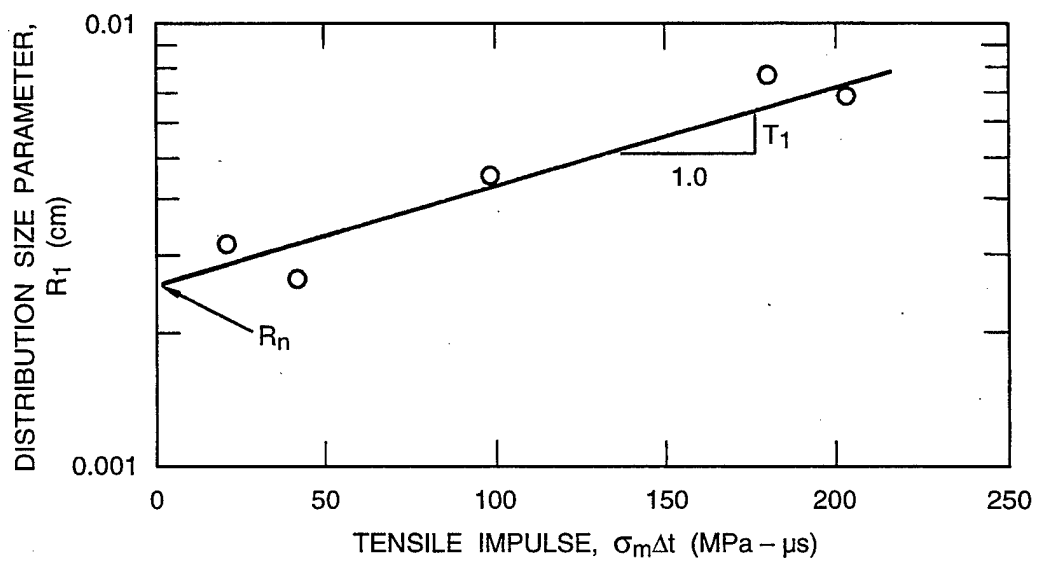
Figure 9-15.   Plot of observed crack sizes with computed stress σ_m and duration Δt for obtaining growth rate parameters R_n and T_1.

understand as they were in the ductile fracture case. There are several possible explanations for the complexity. First, there is more scatter in the data so that major trends in the data are not readily observed. Second, the damage strongly affects the stress; hence, the nominal stress and stress duration obtained from a no-damage calculation are not closely related to the actual stress and duration that occurred in the specimen.

9.2.3.2 Transformations from Surface Counts to Volumetric Distributions. The study of brittle fracture is greatly aided if the number, size, and orientations of microcracks can be measured in test specimens. When such quantitative information is related to stress level and stress duration, nucleation and growth rates for the cracks may be obtained. For transparent materials, this quantitative information may be obtained directly by counting. However, for nontransparent materials, the counting can be conducted only on a cross section. The counting does not give true lengths, true orientations, or true numbers of cracks, but if many cracks are present, a statistical analysis can be made to calculate the true lengths, orientations, and number of cracks that would lead to the count observed on a cross section.

This section outlines a statistical analysis developed to transform surface (observed) crack size and orientation distributions to volumetric (true) distributions. The crack orientation distribution is assumed to be symmetric about one direction in the sample, and each crack is assumed to have a circular cross section. Thus, the analysis applies to spherical voids as well as to penny-shaped cracks. Furthermore, the analysis applies not only to cracks, but also to inclusions, grains, twins, new phase platelets, and other metallographic features that obey the stated assumptions. No assumption is made about the form of the volumetric distributions, but the transformation works best when the number of cracks decreases exponentially with increasing crack size.

The present transformation is an extension of the work of Scheil (1931, 1935) and Saltykov (1958), who calculated true grain size distributions from apparent grain sizes on a section. Our approach is the same as Scheil's; however, our transformation is more complex because both size and orientation are considered, whereas Scheil considered only size.

For the crack counting operation, the shock-loaded specimen is sectioned on a plane that contains the direction of propagation of the initial compressive wave (Z direction in Figure 9-16). Each crack is measured to determine its apparent length $2c$, orientation angle α, width w, and position z through the thickness of the sample (see Figure 9-16). The ranges of length, orientation, width, and position are discretized into small intervals Δc, $\Delta \alpha$, Δw, and Δz for the calculations. We have chosen to consider either length or width separately to simplify the analysis. Also, the transformations for different Δz intervals are independent. Thus, for the transformation analysis all cracks are assigned to elements of a two-dimensional matrix of the form

$$n(\alpha, c) \qquad \text{or} \qquad n(\alpha, w) \qquad (9.29)$$

$\overline{N}$ is normal to the crack plane
Points N, A, B, O, and Y lie in one plane
XZ is the plane of polish
Points A, D, B, and E lie on the plane of polish
2c is the apparent crack length
α is the apparent crack orientation

Figure 9-16.   Circular crack intersecting the plane of polish.

247

where n is the number of cracks per unit area in the plane of polish in the intervals between α and $\alpha + \Delta\alpha$, c and $c + \Delta c$, and w and $w + \Delta w$. A sample crack size distribution observed in Armco iron is shown in Figure 9-17 for a 3.8-GPa impact; here, the orientation is suppressed. Each curve represents $n(c)$ for a particular Z.

The crack distribution of interest is the volume distribution of cracks, specifically, $N(\phi, \theta, R, W)$, where ϕ is the angle that the normal to the actual crack surface makes with the Z axis, θ is the angle by which the normal to the crack plane is rotated around the Z axis, R is the true radius of the circular crack, and W is the true crack opening displacement (see Figure 9-16). Then N is the number of cracks per unit volume in the appropriate intervals of ϕ, θ, R, and W. The following analysis shows the development of a procedure for transforming from n (per unit area on the cross section) to N (per unit volume).

The analysis is based on the following simplifying assumptions:

- The cracks are assumed to be penny-shaped.

- The crack distributions are independent of θ, the angle of rotation about the direction of wave propagation. Thus, it is assumed that there is an axis of symmetry for the orientation distribution.

- The distributions do not vary in directions normal to the Z axis; that is, the wave propagation is one-dimensional and planar. Thus, a dominant direction of propagation and a reasonably homogeneous and isotropic material are assumed.

- The crack length and width distributions may be handled separately.

In the analysis, we consider only the length distributions. The same transformation may be applied separately for the widths. We follow Scheil's method in proposing to divide the continuous functions n and N into discrete ranges and relate the values in those ranges by a matrix A_{ij}^{km}.

$$n(c_j, \alpha_i) = \sum A_{ij}^{km} N(R_m, \phi_k) \qquad (9.30)$$

where $n(c_j, \alpha_i)$ is the number of cracks observed on the cross section with apparent radii between c_j and c_{j+1} and with apparent inclinations between α_i and α_{i+1}; $N(R_m, \phi_k)$ is the number of cracks per unit volume with radii between R_m and R_m and with true inclinations between ϕ_k and ϕ_{k+1}; and A_{ij}^{km} is a fourth rank tensor. The derivation for A_{ij}^{km} was given by Seaman et al. (1978b).

The expression for A_{ij}^{km} can be separated into the product of two matrices F_j^m and G_i^k:

$$A_{ij}^{km} = F_j^m G_i^k \qquad (9.31)$$

where F_j^m contains only length quantities and G_i^k contains only angular quantities. Now F_j^m is identical with the transformation matrix used for spherical inclusions (see Scheil, 1931, 1935). The observed

surface distributions shown in Figure 9-12 for Armco iron were smoothed and then transformed with the BABS2 computer code. The resulting distributions were summed over all orientations to reduce the numbers to functions only of crack radius and position in the specimen. These distributions, which are shown in Figure 9-17, indicate an exponential relation between cumulative number and crack radius.

The transformation described here calculates true size and inclination of cracks or similarly shaped inclusions from counts of the cracks seen on a cross section. The transformation requires the calculation of two matrices: one contains size terms only and is identical to Scheil's matrix for transforming spherical void counts; the other matrix contains only inclination terms. Comparisons were made for an exact analytical case to demonstrate the accuracy of the method.

9.2.3.3 Discussion. Brittle fracture under high-rate loading conditions leads to a range of fracture types. In Armco iron the microfractures occur across grains, and growth is actually a coalescence of many microcracks to form a longer crack. Quite different behavior has been observed in the other materials described in Section 9.2.5. For the most ductile materials, there is an exponential cumulative crack size distribution (like that seen with ductile void growth). This shape for the crack size distribution suggests that the crack growth rate is not strongly size-dependent (the void growth threshold is independent of the void size). For more brittle materials, such as the ceramic ZnS (shown in Section 9.2.5.5), the size distribution has two exponential portions connected by a nearly horizontal section: this shape for the crack size distribution is expected from linear elastic fracture mechanics.

In brittle materials, it is difficult to obtain incipient damage by plate impacts. This difficulty indicates a narrow range in tensile stress between no damage and a fairly high level of damage. For this reason, the brittle fracture experiments are much harder to perform and to control than similar ductile fracture experiments.

9.2.4 Brittle Fracture Model Development.

A continuum model, BFRACT3, for dynamic tensile fracture and fragmentation was developed for the detailed simulation and study of brittle fracture processes in elastoplastic materials (see Barbee et al., 1970; Seaman et al., 1976; Seaman et al., 1985; Curran et al., 1987). "Brittle" fracture is defined here as fracture occurring on the microlevel with a cleavage morphology rather than with a ductile void morphology. Included in the model are a threshold for the initiation of damage, a nucleation process for forming microcracks under tension, growth processes that depend on the tensile stress, a coalescence and fragmentation process with the resulting fragment size distribution, and stress relaxation associated with the developing damage. Cracks occur in a range of sizes at nucleation and throughout the calculation.

Many researchers have developed similar microfracture models for special applications. Davison et al. (1977) derived a general approach to such models. Margolin (1983) developed a model for an elastic

249
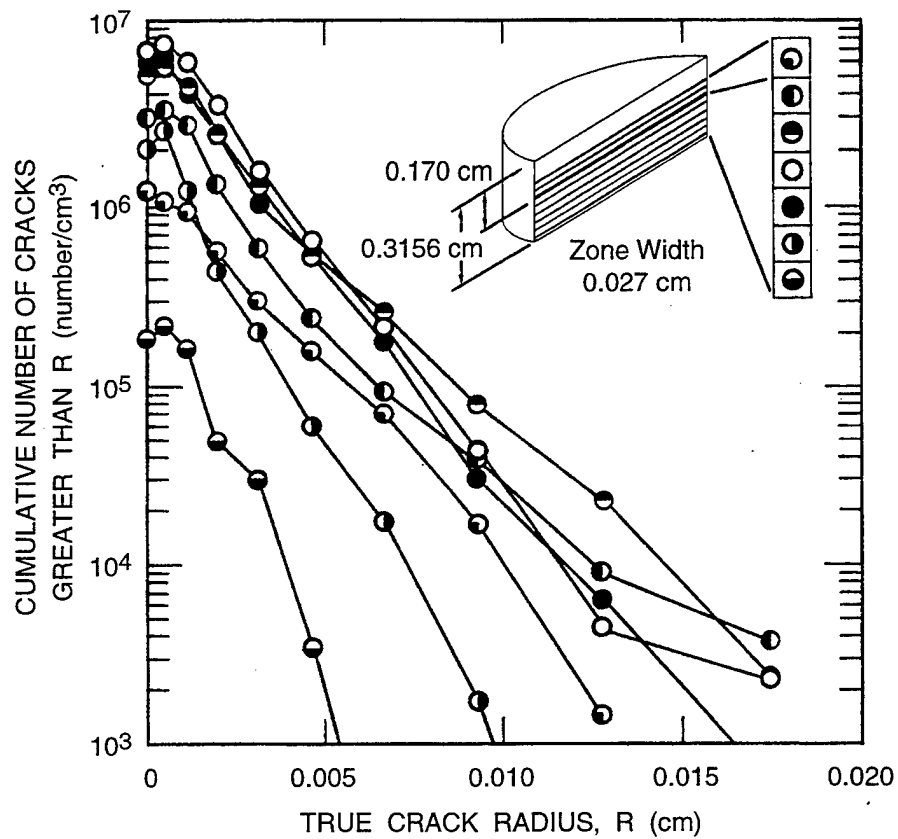
Figure 9-17. Crack size distribution in zones near the spall plane in an
Armco iron target after a one-dimensional impact: Shot S25.

material with distributions of cracks in arbitrary orientations. He provides for both tensile opening and shear slip on the circular cracks. For his case, in which there is no nucleation and growth occurs at a constant velocity, the stress state can be computed explicitly at any time. A similar elastic-brittle model was derived by Krajcinovic and Fonseka (1981) for application to concrete fracture. Kipp et al. (1980) and Grady (1982) developed a brittle fracture model that has some micromechanical features. With their model, they were able to show that the fracture strength is proportional to the one-third power of strain rate (as observed experimentally) and to reproduce the measured change of fragment size with strain rate.

Evans et al. (1980) gave an example of a detailed study of crack formation in ceramic under impact, using a combination of analytical and experimental efforts. A similar study was undertaken by Kumano and Goldsmith (1982), who also derived a model to represent their findings. Several Russian investigators (see, for example, Dremin and Molodets, 1980) are developing microfracture models, but they do not treat the cracks in detail.

Meyers and Aimone (1983) reviewed fracture models for spalling in metals. Johnson (1981) and coworkers have been developing models for fracture in brittle materials (as well as ductile materials) and have a model with many features similar to SRI's BFRACT. John Dienes has been continuing the modeling effort begun with Margolin and extended it from layered rock fracture to the fracture of other materials, including rocket propellant. This model is like BFRACT but has somewhat different nucleation and growth processes and has many crack orientations instead of the single orientation of BFRACT.

Espinosa and Brar (1995) presented a model for brittle fracture of ceramics that allows for nucleation and growth of cracks in many orientations simultaneously. This model appears to explain many of the characteristics of ceramic fracture under shock loading.

The processes in the present BFRACT model have represented, with reasonable fidelity, high-rate fracture processes in beryllium (Barbee et al., 1972; Seaman et al., 1976; Shockey et al., 1973b), Armco iron (Shockey et al., 1973a), polycarbonate (Curran et al., 1973; Seaman et al., 1982), oil shale (Murri et al., 1977), novaculite quartz (Shockey et al., 1974), and rocket propellant (Seaman et al., 1985). By "represent" we mean that computations with the model are able to satisfactorily match measured stress or velocity histories obtained during impacts and to match the measured numbers and sizes of cracks observed throughout the specimen after the impact.

The analytical basis and some experimental bases for the major equations of BFRACT are presented below. These equations are used in a subroutine BFRACT3, which has been used with several wave propagation computer programs to simulate fracture processes. BFRACT3 acts as a stress-strain relation in such programs.

251

9.2.4.1 **Microcrack Kinetics in the Model.** The model for tensile microfracture is designed to represent observations from dynamic experiments in which fracture damage occurred. The fracture observations were used to distinguish and quantify the following series of processes in the model:

- Initiation of fracture—When the tensile stress normal to the crack plane exceeds a critical level, fracture begins.

- Nucleation of cracks—Cracks are nucleated with a range of sizes and as a function of the tensile stress level.

- Growth of cracks—Two types of growth laws are provided, depending on the ductility of the material.

- Coalescence and fragmentation—As the number and sizes of cracks increase, fragments form until the entire material disintegrates into fragments.

Each of these processes is explored in the following paragraphs. The effects of the growing damage on the stress-strain relations are then examined.

Cracks and Crack Size Distributions. The microcracks in the model are penny-shaped: circular and flat. This shape was actually observed in polycarbonate (Curran et al., 1973), which is transparent. Because a great number of cracks occur (usually 10^4 to $10^8/cm^3$), they are treated statistically, rather than individually. An indication of the form of a representative crack size distribution is shown in Figure 9-17 for a disk-shaped sample of Armco iron impacted by a flat plate to a shock stress of 3.8 GPa. The cracks observed in this sample varied in orientation as well as length, but the angular variation is suppressed in this plot. The several distributions shown represent different stages of growth (those further to the right have grown longer). To represent the observed crack sizes, the size distribution is usually given in the analytical form:

$$N_g = N_o e^{-\left(\frac{R}{R_1}\right)}$$
(9.32)

where N_o and N_g are the total number of cracks per unit volume and the number per unit volume with a radius greater than R, and R_1 is the shape parameter for the distribution. For computer simulations, the distributions are represented by a series of line segments in the $N - R$ plane so they need not remain exponential during calculations.

The statistical nature of the crack distribution is indicated by the fact that N is a crack density (number per unit volume). Thus, the model assigns a crack density at each point in the material. The model is a continuum model, and the crack distribution acts as an internal state variable (i.e., it is an additional property of the continuum). This statistical approach is especially appropriate for finite-difference or finite-element calculations in which the material is represented by a number of small cells or elements.

The crack density is independent of cell size, whereas the common treatment of individual cracks is highly dependent on cell size.

In the model, the cracks are presumed to open elastically under a stress σ_n normal to the crack plane (see Sneddon and Lowengrub, 1969):

$$\delta = \frac{4(1-v^2)}{\pi E} R \sigma_n \qquad (9.33)$$

where δ is one-half the maximum separation of the crack faces and E and v are Young's modulus and Poisson's ratio. This elastic opening process only roughly approximates real material behavior in which cracks in fact open with a finite velocity and may remain open when the load is removed. The crack faces form an ellipsoid with three semiaxes, δ, R, and R. Thus, the volume of a crack is

$$V_{1c} = \frac{4\pi R^2 \delta}{3} = \frac{16(1-v^2)}{3E} R^3 \sigma_n \qquad (9.34)$$

The volume of the entire crack size distribution can be obtained by combining Eqs. (9.32) and (9.34) into the following integral:

$$V_c = \int_{R_a}^{R_b} V_{1c} dN = \frac{16(1-v^2)}{3E} \sigma_n \int_{R_a}^{R_b} R^3 dN = \frac{16(1-v^2)}{3E} \sigma_n \tau_z = \varepsilon_n^c \qquad (9.35)$$

where R_a and R_b are minimum and maximum radii in the distribution. The quantity τ_z is introduced to represent the effect of the total crack distribution. The strain ε_n^c represents an average elongation strain normal to the crack plane.

In the current model, all cracks in the distribution in a given computational cell lie in a single orientation, although they may be considered to represent some range of orientation angles (in spherical coordinates) in the actual material. For each material element, the crack orientation is fixed normal to the maximum tensile stress at the time that any stress first exceeds the initiation stress criterion for nucleation.

Nucleation and Growth Processes. Two alternative types of nucleation and growth processes are provided in the model:

(1) A constant threshold stress σ_{go} for growth. All sizes of cracks are nucleated and all grow when this tensile stress is exceeded. This process is appropriate for crack growth in ductile materials, in which considerable plastic flow accompanies cracking.

253

(2) A fracture mechanics threshold for growth. Only cracks above a stress-determined size can nucleate and grow. This threshold seems to fit the more brittle materials, such as oil shale, ceramic, and novaculite (a quartzite rock).

In our model, therefore, somewhat different nucleation and crack growth relations are provided for these two types of growth threshold.

Nucleation in the model occurs as the new cracks are added to the existing set. These new cracks occur in a range of sizes with the size distribution given by Eq. (9.32). At nucleation, the parameter R_1 equals R_n, a material constant indicating the inherent flaw size. The rate at which cracks are nucleated is governed by the following function:

$$\frac{dN}{dt} = \dot{N}_o \left\{ e^{\left(\frac{\sigma_n - \sigma_{no}}{\sigma_1}\right)} - 1 \right\}$$

(9.36)

where dN/dt refers to the rate of increase of N_o, the total number of cracks per unit volume; $\dot{N}_o$ and σ_1 are material quantities with the dimensions of number/m^3/s and Pa; and σ_n is the average stress normal to the crack plane during the time interval Δt. For the constant threshold stress, the size distribution nucleated at any time extends from $R = 0$ to R_n^{max}, which is the maximum nucleated crack size (a material input parameter). For the fracture mechanics threshold, the size distribution nucleated in a time increment extends only from $R = R_c$, which is a critical size defined below, to $R = R_n^{max}$.

The crack growth law derived from our experimental data on cleavage crack growth in Armco iron and beryllium is

$$\frac{dR}{dt} = \left(\frac{\sigma_n - \sigma_{go}}{4\eta}\right) R$$

(9.37)

where η is a growth factor with the dimensions of viscosity, and σ_{go} is a growth threshold stress. For σ_n less tensile than σ_{go}, no growth occurs. In our model, the crack velocity is not allowed to exceed the Rayleigh wave velocity in intact material. The preceding growth law was derived theoretically by Poritsky (1952) for the expansion of spherical voids in a viscous fluid and hence may be termed a viscous growth law. Its observed occurrence for cleavage cracks in Armco iron and beryllium suggests that significant plastic flow at the microcrack tips may control growth.

When an exponential distribution of flaws, represented by Eq. (9.32), grows according to this law, the distribution remains exponential. Thus, in any material in which the crack size distribution is observed to remain exponential for a range in levels of damage, a viscous growth law is indicated. For fairly ductile

254

materials, such as Armco iron, in which considerable plastic flow accompanies growth, σ_{go} is observed to be a material constant; i.e., alternative (1) above is taken.

Growth with the constant threshold stress law is obtained by integrating Eq. (9.37) and taking σ_n as the time average of the solid stress normal to the crack plane:

$$R_{m+1} = \begin{cases} R_m e^{\left(\frac{\sigma_n - \sigma_{go}}{4\eta} \Delta t\right)} & \text{for} \quad \sigma_n \geq \sigma_{go} \\ \\ R_m & \text{for} \quad \sigma_n < \sigma_{go} \end{cases} \tag{9.38}$$

where Δt is the time increment, and R_m and R_{m+1} are radii at the beginning and end of the time increment, respectively. This expression shows that every radius in the distribution increases by the same ratio. Therefore, the new distribution obtained after growth is still an exponential, with the new value of the size parameter R_1 obtained from the old one by Eq. (9.38). The crack size distributions have been observed to remain essentially exponential throughout their growth history (see Figure 9-17).

For more brittle materials, such as rock, σ_{go} is the critical stress for crack growth according to linear elastic fracture mechanics, as in alternative (2) above:

$$\sigma_{go} = \sqrt{\frac{\pi}{4R}} K_{1c} \tag{9.39}$$

where K_{1c} is the fracture toughness, a material constant. With Eq. (9.39) in the growth law, no growth occurs for cracks with a radius smaller than R_c,

$$R_c = \frac{\pi K_{1c}^2}{4\sigma_n^2} \tag{9.40}$$

When the fracture mechanics form of the growth law (9.37) is integrated, accounting for the variation in σ_{go} according to Eq. (9.39), we obtain

$$\sqrt{R_{m+1}} = \left\{ \sqrt{R_m} - \sqrt{R_c} \right\} e^{\left(\frac{\sigma_n \Delta t}{8\eta}\right)} + \sqrt{R_c} \tag{9.41}$$

where R_{m+1} and R_m are values of R at the end and beginning of the time increment Δt. Here, the final size R_{m+1} is related in a complex way to R_m, so that the final distribution is not an exponential. To provide fidelity to the growth process in the model, we have represented the size distribution by a series of

exponential segments. Then the growth of the R values at the ends of the segments is computed by Eq.(9.41).

After nucleation and growth during a time increment, the nucleated crack size distribution is added to the growing distribution to form a single distribution representing the current state of damage in the material. This combined distribution may grow during the next time increment.

Coalescence and Fragmentation. The model coalescence processes were developed to represent observations in novaculite quartz (Shockey et al., 1974). There the resulting fragments occurred in a range of sizes from 35 μm to 5 mm, and all sizes had approximately the same aspect ratio, as shown in Section 9.2.5.4.

The physical process of coalescence occurs when the cracks become so large that they begin to intersect other cracks. They may intersect in the same plane, thus forming larger cracks, and they may intersect at right angles, forming corners of fragments. Also, cracks in the same orientation, but on different planes, may coalesce by developing crack extensions out of the plane to join nearby cracks. Thus, a family of cracks in one orientation can coalesce and form a rough, multifaceted spall plane. These three coalescence possibilities are illustrated in parts (a) through (c) of Figure 9-18. Because cracks in only one orientation are permitted in the current version of the model, only coalescence of the first and third types are possible.

At present, we are considering only the third type of coalescence. In this coalescence pattern, we obtain fragments in each cell that fully fractures. If cells above and below also fragment, as in Figure 9-18(d), we have a region of rubble. If only a horizontal line or plane of cells fragments, as in Figure 9-18(e), we have essentially a spall plane, with some loose chunks on the plane.

The physical processes of these crack intersections are not considered explicitly in the model; rather, the model provides only for a gradual transition from undamaged to fully fragmented material and an accounting of the fragment size distribution at the end. Let us consider the fully fragmented state first.

The fragments occur in a size distribution that we presume is related to the crack size distribution. Furthermore, we assume that for each size range, there is a constant ratio β between the number of cracks and the number of fragments:

$$\beta = \frac{N_o^f}{N_o} \qquad (9.42)$$

where N_o^f is the total number of fragments per unit volume. Thus, we expect small cracks to coalesce with small cracks to form small fragments, and large cracks to form large fragments. Chunky fragments are usually formed by a crack face above and below and by crack extensions on the vertical sides.
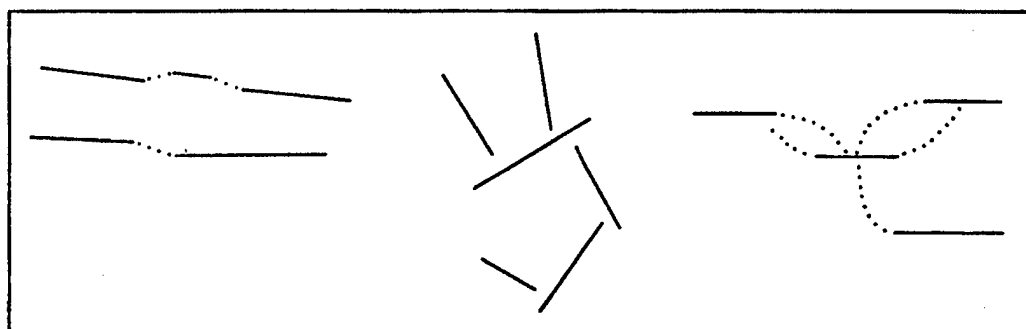
(a) Coalescence to form larger cracks

(b) Coalescence at right angles to form fragments

(c) Coalescence of crack by out-of-plane extensions to form fragments
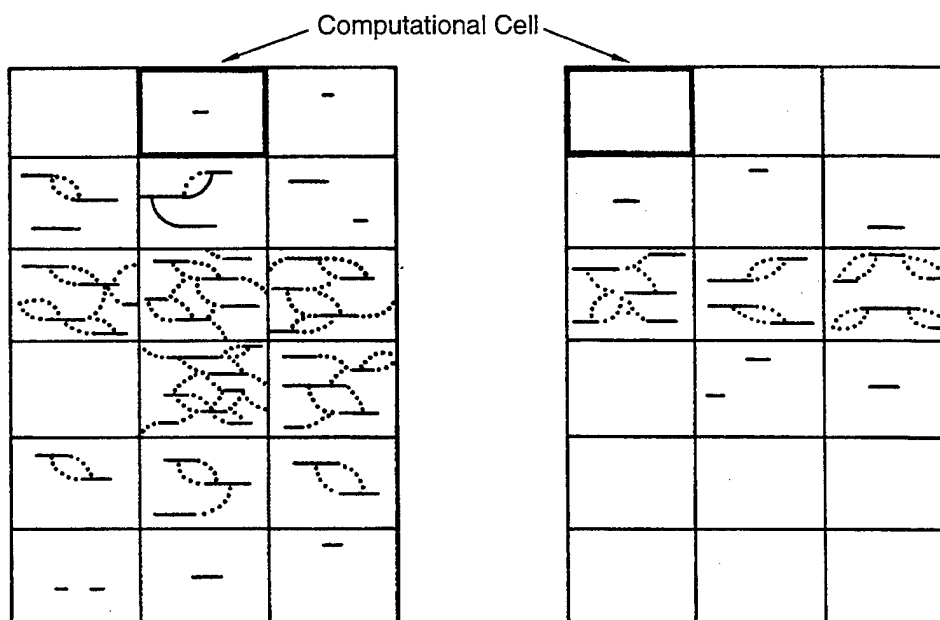
(d) Fragmented region formed by coalescence in a group of cells

(e) Spall plane formed by fragmentation of a row of cells

Figure 9-18.   Coalescence and fragmentation processes envisioned for the model.

257

Because each crack forms a side of two fragments and each fragment requires two crack faces, one crack is associated with each fragment; therefore β is approximately one. Similarly, the fragment sizes are related to the crack sizes by a factor γ:

$$\gamma = \frac{R^f}{R} \tag{9.43}$$

where R^f is the radius of the top or bottom of the fragments. The cracks forming the fragment top and bottom have about the same area as these fragment surfaces, so γ is about one.

To determine the fragment volume, we need some further information about the fragment shape. If we take the top and bottom of the fragment as roughly circular, then the area is $\pi\left(R^f\right)^2$. The thickness of the fragment is related to the radius R^f by the proportionality factor α such that the thickness is equal to αR^f. The fragment volume is then V_1^f

$$V_1^f = \alpha\pi\left(R^f\right)^3 = T_F\left(R^f\right)^3 \tag{9.44}$$

Here, the coefficients in the volume expression have been combined into a single constant T_F, which characterizes the aspect ratio of the fragments. Our experimental measurements indicate that T_F should be between 1 and 3. The relative volume of fragments, τ_f, is obtained by integration over N^f:

$$\tau_f = T_F \int_{R_a}^{R_b} \left(R^f\right)^3 dN^f = T_F\beta\gamma^3 \int_{R_a}^{R_b} R^3 dN = T_F\beta\gamma^3\tau_z \tag{9.45}$$

Thus, the fragment volume τ_z is closely related to the crack volume factors V_c and τ_z, as expressed in Eq. (9.35) and derived from the crack size distribution. When $\tau_f = 1$, the entire volume is full of fragments.

The process of gradual coalescence and fragmentation is treated in the model by requiring that τ_f always represent the portion of the material element that has fragmented.

9.2.4.2 Stress Calculations Coupled with Damage. The stress calculations for intact material are conducted until the stresses exceed a threshold level and damage is initiated. At that time the plane of fracture is determined, as discussed later. For damaged material, the following sequence of calculations is required:

- Transform the average stresses in the external X, Y coordinate system to stresses in the solid material in directions normal and tangential to the fracture plane.

- Compute the stresses in the solid intact material, accounting for the stress relaxation (material softening) due to the nucleation, growth, and opening of cracks.

- Transform the stresses back to the external coordinate system, accounting for the reduction in area of intact material.

Each of these steps is outlined in the following sections, and a special calculation is provided for the case of full fragmentation resulting in a spall plane.

Stress-Strain Relations. The stress-strain (constitutive) relations include the usual elastic-plastic relations for intact material, plus a method to account for the effect of the developing damage on the stresses. We first present the stress-strain relations for undamaged material and then proceed to those for damaged material.

The pressure P_s or average stress in the solid material is given by a Mie-Grüneisen relation that provides for linear thermoelastic behavior

$$P_s = K_1\mu + K_2\mu^2 + K_3\mu^3 + \rho_s\Gamma E \tag{9.46}$$

where

$$\mu = \frac{\rho_s}{\rho_{so}} - 1$$

is the compressive strain, K_1, K_2, and K_3 are the bulk modulus series, Γ is the Grüneisen's ratio, E is the internal energy, and ρ_s and ρ_{so} are current and initial solid density.

The deviator stress-strain relation is based on elasticity and Mises plasticity with nonlinear work hardening.

For calculating stress-strain relations modified by damage, the damaged material is taken as a composite of intact material with some separated fragments and material with reduced strength near cracks. Two sets of stresses are considered: solid and continuum. The solid stresses are the average of those stresses appearing in the intact material; continuum stresses are the average stresses on a cross section of a combination of intact and fractured material. Continuum stresses are transmitted out of the subroutine to the calling program because they represent the stresses acting between computational cells.

The stresses are computed in two steps, and each step is affected by the amount of damage. In the first step, the imposed strain is separated into a portion ε_s taken by the intact material and a portion ε_c representing the crack opening. The separation of the total strains into solid and crack opening components is very important for small amounts of damage. From ε_s the solid stresses are computed.

The gross stresses are then computed from the solid stresses, using the fraction of intact material as a reduction factor. This transformation from solid to gross stresses dominates near the point of fragmentation or complete separation.

259

For the first step of calculating the stress in the solid material, the gross strain increments normal to the crack plane are separated into three portions following a suggestion of Herrmann (1971):

$$\Delta\varepsilon_n = \Delta\varepsilon_n^s + \Delta\varepsilon_n^c + \Delta\varepsilon_n^{op} \qquad (9.47)$$

where the superscripts indicate strains taken by the solid material (superscript s), the crack opening (c), and the strain associated with the spall opening (op) that occurs in full separation. $\Delta\varepsilon_n^s$ is used in the elastic-plastic constitutive equations for the solid. The crack opening strain increment is computed as the change in crack volume from Eq. (9.35). The third term is simply the separation of the broken material, calculated on a true strain basis. Note that these are continuum strain increment averages over the material in the cell—not strains defined at a point.

As tensile loading occurs, $\Delta\varepsilon_n^s$ initially increases (in tensile magnitude). After cracks begin to nucleate and grow, $\Delta\varepsilon_n^c$ increases. With continued tensile straining, larger portions of the strain $\Delta\varepsilon_n$ are taken in crack opening $\Delta\varepsilon_n^c$. As the damage increases, the tensile solid strain $\Delta\varepsilon_n^s$ reaches a maximum and then begins to decrease. When separation occurs, the cracks close, so that $\Delta\varepsilon_n^c$ becomes zero. Simultaneously, $\Delta\varepsilon_n^{op}$ increases to fulfill Eq. (9.47).

The second step, the transformation from solid to continuum stresses, is accomplished using the damage quantity τ_f from Eq. (9.45):

$$\sigma_n^g = \sigma_n\left(1 - \tau_f\right) \qquad (9.48)$$

where σ_n^g and σ_n are continuum and solid normal stresses on the kth plane, the plane of fracture. (No other stresses are modified to account for damage.) This relationship between the solid and continuum stress is borrowed from the analysis of Carroll and Holt (1972b) for a porous material:

$$P_g = \frac{\rho}{\rho_s} P_s \qquad (9.49)$$

where P_g and P_s are continuum and solid pressures, and ρ and ρ_s are continuum and solid densities.

Spallation. When large amounts of damage occur, the fractures are assumed to coalesce and form a local spall plane within the computational cell. Specifically, the criterion is that spall occurs when $\tau_f = 1$, where τ_f is the fragmented fraction from Eq. (9.45). Then the state of stress at the spall plane is taken to be one of plane stress, with zero stress normal to the spall plane. The spalled state route in the model contains the calculations of the stresses, plus an incrementing of the spall opening strain $\Delta\varepsilon_n^{op}$. The stress state is obtained from the usual elastic relations for the case of a free boundary. If yielding occurs, the stresses are computed using Mises plasticity and a normality rule.

9.2.4.3 Solution Procedure. To provide stress-strain relations that are sensitive to the growing damage, a method is required for determining the stress tensor for an imposed strain increment while accounting for the nucleation, growth, and coalescence processes. The governing equations that must be solved to determine the stresses are

- Growth law, Eq. (9.37)

- Nucleation rate law, Eq. (9.36)

- Crack opening relation, Eq. (9.35)

- Stress-strain relation for intact material, Eq. (9.46)

- Strain decomposition, Eq. (9.47).

The solution method is essentially an integration of the nucleation and growth rate laws, combined with the auxiliary algebraic equations giving the stress-strain relations.

Because of the complexity of the stress-strain and damage relations, a direct solution for the stresses is generally not possible. Therefore, an approximate procedure combining both subcycling and iteration is used. Subcycling (dividing the imposed time and strain increments into smaller units) is used to require that the stress-strain path be followed with small enough strain steps to define the process accurately. At each strain step, a combined Newton-Raphson and *regula falsi* solution technique (multiple trials of sets of stresses) is used to obtain sufficient accuracy for the stresses.

9.2.4.4 Summary of Model Capabilities. A basic model for representing the brittle microfracturing and fragmentation processes under high-rate tensile loading has been developed. It contains nucleation, growth, fragmentation, damage-caused stress-relaxation processes, and a stress solution procedure suited to highly nonlinear behavior. The model handles multiple loadings, unloadings, and reconsolidation. The model has been used to represent brittle fracture in a wide range of materials. However, it is not expected to match all materials. The current model is an extension of earlier models into the high-damage range where full separation and fragmentation occur. It is expected that this basic model would be used initially to represent fracture in any new material. The initial attempts to match experimental data would indicate any needed modifications in the processes. These processes, which are isolated in the model, so that each can be altered independently of the others, would be changed in the computational model and the experiments would be resimulated until a satisfactory match was obtained. Thus, the model is one element in a flexible experimental-computational approach to fracture problems.

9.2.5 Applications of the Nucleation-and-Growth Fracture Method.

Here, we present a few illustrative samples of the applications of the NAG (nucleation-and-growth) fracture approach. The section spans over the range of materials that have been considered, noting the two

261

basic types of fractures: ductile and brittle. In some cases, the data are well-defined and appear to fit the general assumptions of the approach and hence are well represented by the model. In others the data are limited, of poorer quality, or only estimated and do not fit well the expectations of the model or the approach. In most cases, the tests considered are plate impacts.

As we have seen in earlier sections, the NAG is a complicated approach, requiring an extensive set of carefully controlled experiments followed by a demanding data analysis process. Under what circumstances is the NAG approach to be used, as opposed to simpler methods that indicate the level of damage?

(1) When there is a need to represent fracture over a wide range of strain rates or sizes. Then, a knowledge of the underlying physics makes the interpolation or extrapolation more reliable. For example, in current propellant research, fracture is being examined over strain rates from 0.01/s to 10^5/s and scales from grams to megagrams, so a detailed treatment of the physics aids in the formulation of the model.

(2) When the end result is desired in detail, for example, the fragment size distribution. In many situations we need to know the fragments because of later damage they may cause in other materials.

(3) When multiple stress waves are to be represented so the behavior of partially damaged material is needed, or when the later strength of the material after fracture is desired.

We begin our set of examples with 1145 aluminum to illustrate fracture in ductile materials. The experimental results here indicate the variation of damage with distance through the sample and from sample to sample as well as the reliability we may expect from our model. Then, we describe fracture in a polycarbonate, a transparent material, so that we can examine the damage directly as well as on a cross section. With the study of novaculite quartzite, we continue the fracture study to full fragmentation. The study of fracture in solid rocket propellant provides a sample of the NAG approach in a very complex composite material with significant rate effects in the undamaged material. As a sample of damage in a very brittle material we show some observations (but not modeling) in a ceramic. Some results in a structural grade of beryllium are presented to indicate that the same kind of fracture occurs under electron-beam, x-ray, and other radiation loading as under impacts. Finally, we show some results in two steels and in Armco iron.

9.2.5.1 Ductile Fracture of Commercially Pure Aluminum. Commercially pure aluminum is a good sample of a very ductile material. We use this material as a means for introducing the nucleation-and-growth approach in detail. The damage in this material appears initially as nearly spherical voids that enlarge and increase in number with advancing damage. We wish to illustrate how fracture processes actually occur, especially the likely scatter in data and to show which aspects of fracture are represented by the model assumptions and which are not.

The nucleation-and-growth (NAG) model used here is called DFRACT (for Ductile FRACTure). When the model does not fit the data well, we expect that the model assumptions are inappropriate or that additional, unaccounted for phenomena are occurring. For example, impurities may have been randomly distributed in the material or even bands of impurities, giving preferential locations for the voids and also weakening the bonding so that lower thresholds were appropriate in one sample than in the other samples.

To study fracture in commercially pure aluminum, we undertook a series of plate impact tests in 1145 aluminum. Table 9-2 summarizes the configurations and important parameters of these tests. After the tests, the samples were sectioned following the procedures outlined in Section 2.3. The numbers of voids were counted by sizes and then transformed according to the statistical procedure of Scheil as described in Section 9.2.1. These data on void volume were the basic data on which the DFRACT model is based.

Figures 9-19 and 9-20 contain plots of the variation of the relative void volume as a function of distance through the specimens. Generally, the void volume plots show a fairly sharp peak at the region of maximum damage; whereas, except for test 939, there is only a broad peak for the number density. We conclude from the variation of the numbers of voids that nucleation occurs early during the tensile pulse and that the stress amplitudes are little affected by the adjacent damage. However, growth continues throughout the period of tension and is therefore strongly affected by the adjacent damage.

From these plots, we also get an indication of the scatter in the damage quantities. For example, in Test 847 the relative void volume in the region of maximum damage (0.38 cm from the impact interface) varies from 0.003 to 0.013, or by a factor of 4. Similarly, the number density for Test 847 varies by a factor of 2. An indication of the scatter of the data from test to test was obtained by plotting the peak void volumes and number densities as a function of impact velocity as shown in Figures 9-21 and 9-22. Test 939 was conducted with the target and impactor each about half as thick as those for Tests 847, 873, 849, and 872, so the damage for 939 is expected to be about half what it would be for full-scale.

The average void volume data for the full-scale tests shown in Figure 9-21 fit together fairly well, with Test 849 being probably too high. Within tests, the void volume values vary within a factor of 2 to 3. The average number density shows more scatter: Tests 873 and 849 are probably high by a factor of 2 or 3 and 847 is 30% low. These plots give some indication of the accuracy with which we can expect to represent a suite of data with the model. The computed results for both relative void volume and number density should be within a factor of two of the experimental observations.

Figures 9-21 and 9-22 also show the damage computed on the planes of maximum damage for the selected set of fracture parameters listed in Table 9-3. An additional simulation was made for a pseudo-Test 872 with the dimensions of Test 939. From the results of this pseudo-test, we were able to plot the trend lines between the velocities for Tests 872 and 939. It is evident that the model can represent the main trends of

Table 9-2. Configurations for 1145 aluminum Impacts.

Test No.	Velocity (m/s)	Peak Stress (GPa)		Thickness (cm)		Damage		
		Compression	Tension	Impactor	Target	Void Volume Fraction	Crack Density (Number/cm³)	Comment
847	128.9	9.8	8.8	0.236	0.635	6.0×10^{-3}	4.7×10^{6}	Incipient
873	132.0	10.0	9.0	0.236	0.635	1.5×10^{-2}	2.2×10^{7}	Incipient
849	142.6	10.8	9.8	0.236	0.635	6.2×10^{-2}	2.3×10^{7}	Intermediate
872	154.2	11.7	10.7	0.236	0.635	8.4×10^{-2}	2.7×10^{7}	Intermediate
939	185.6	14.1	13.1	0.114	0.317	1.4×10^{-1}	8.1×10^{7}	Incipient
857	207.9	15.7	14.7	0.236	0.635	No count	—	Intermediate
798	250.5	19.0	18.0	0.173	0.632	No count	—	Full separation
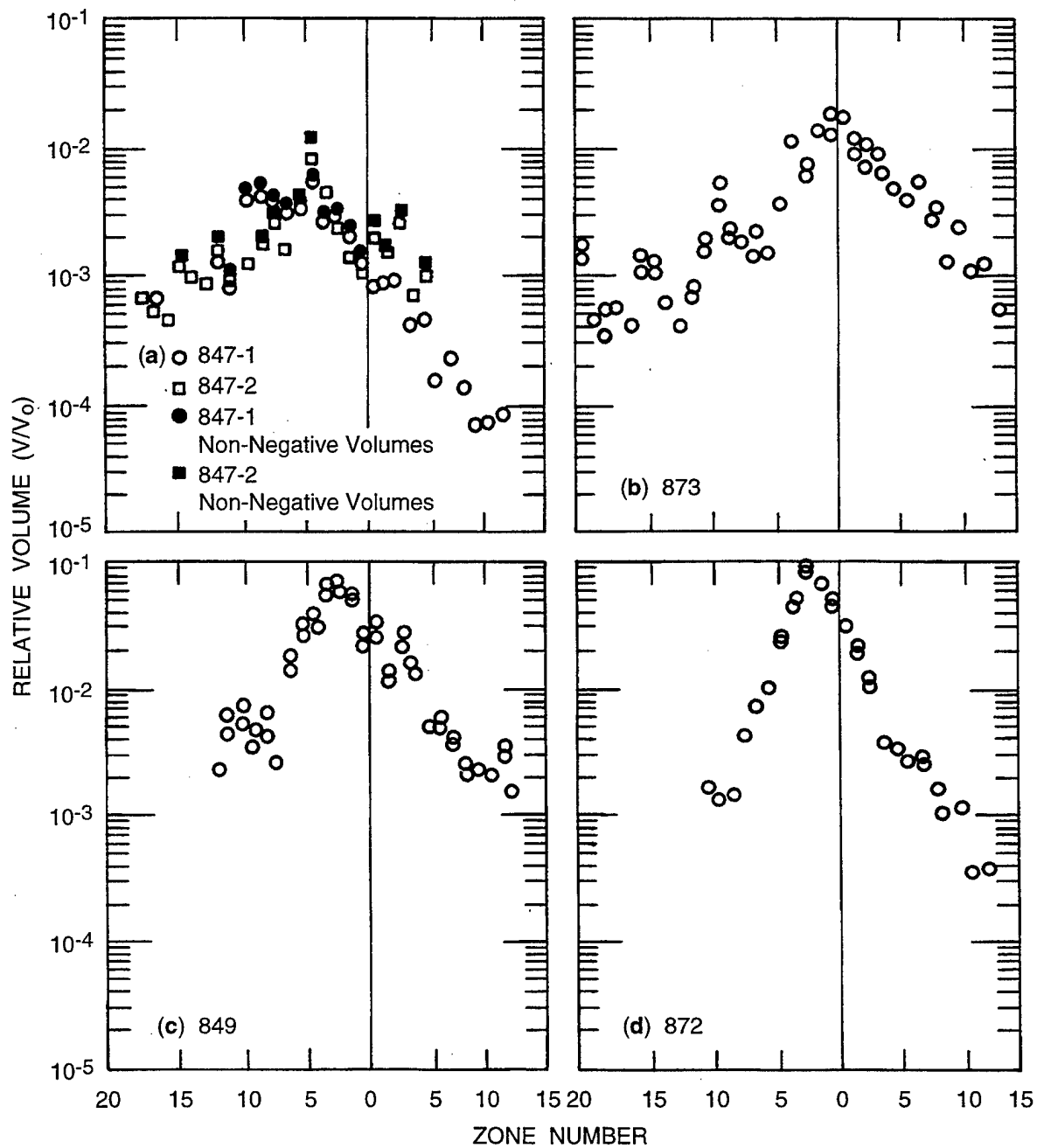
Figure 9-19. Void volume distributions as a function of position in Al 1145 targets 847, 873, 849, and 872.
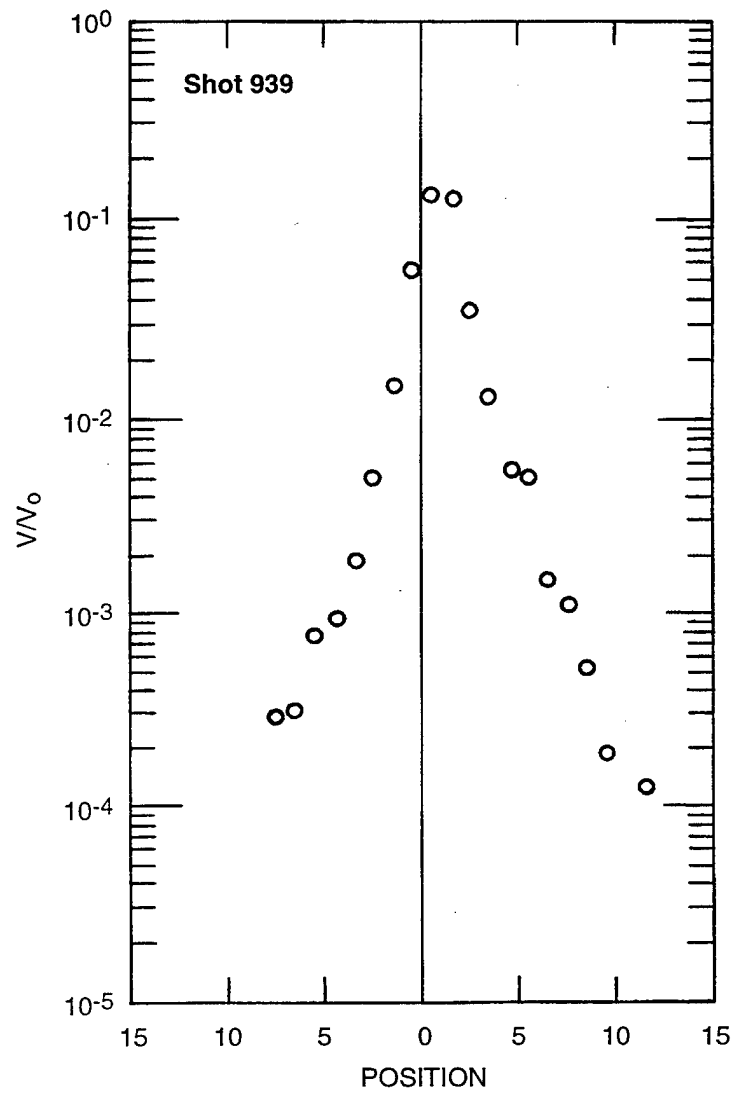
Figure 9-20. Void volume distributions as a function of position in Al 1145 target 939.
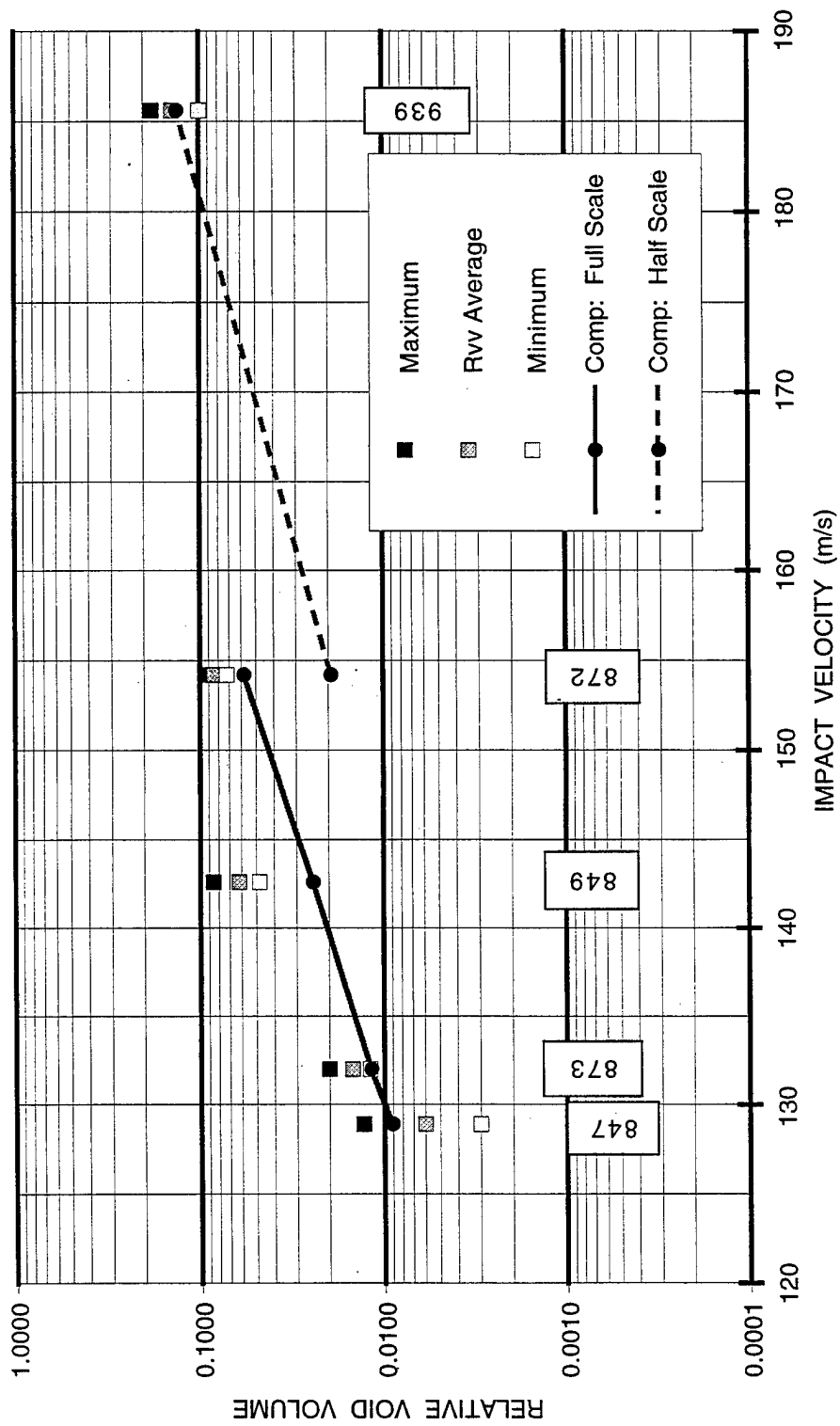
Figure 9-21. Velocity of void volume with impact velocity in Al 1145.
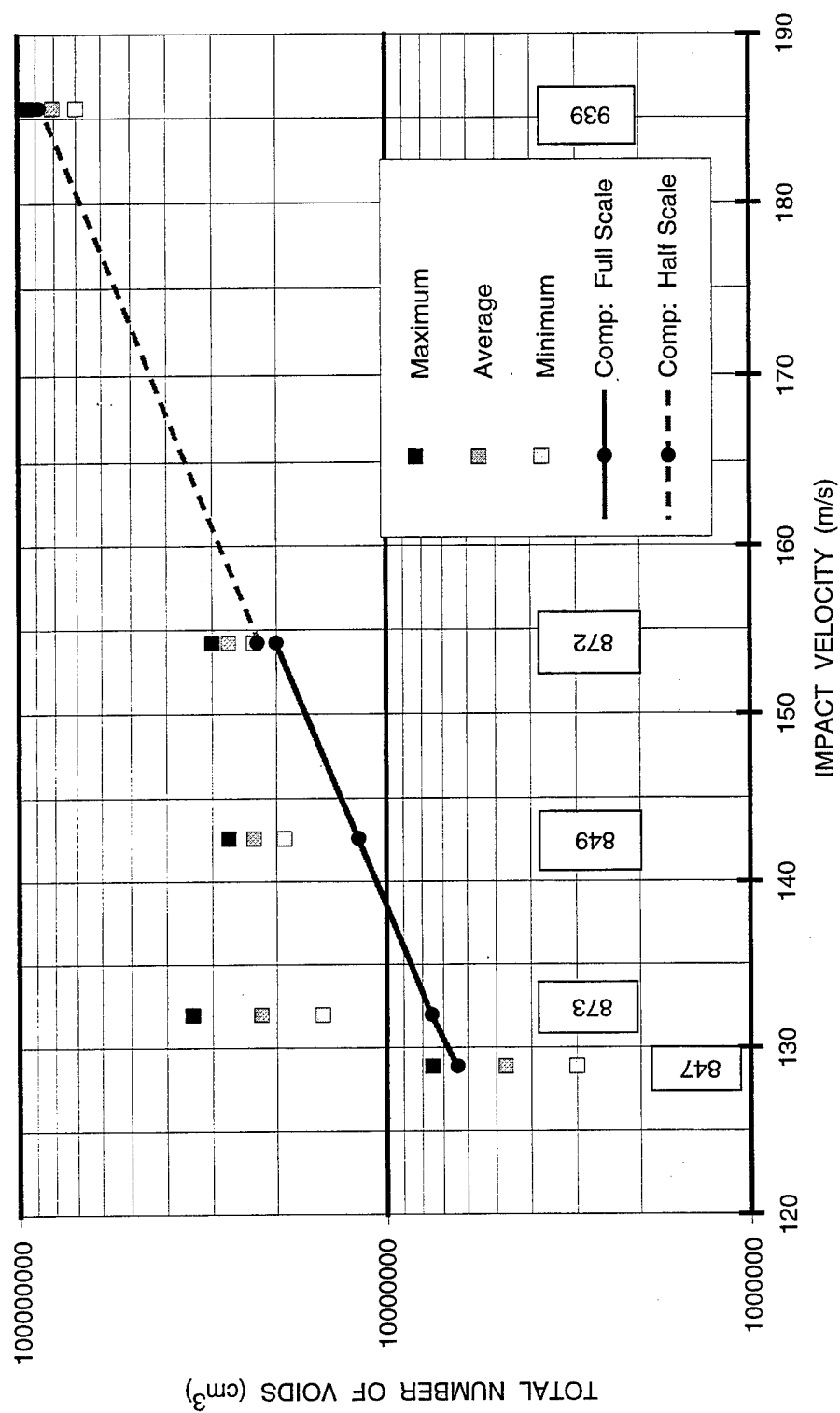
Figure 9-22. Variation of the number of voids with impact velocity in Al 1145.

Table 9-3. Fracture parameters for 1145 aluminum.

Symbol	Units	Value	Description
T_1	$(MPa{\cdot}s)^{-1}$	1.0×10^5	Growth rate coefficient
σ_{go}	MPa	450	Threshold for growth
R_n	cm	1.0×10^{-4}	Mean radius at nucleation
$\dot{N}_o$	Number/m^3/s	5.0×10^{16}	Nucleation rate coefficient
σ_{no}	MPa	300	Threshold for nucleation
σ_1	MPa	65	Stress sensitivity for nucleation

the data, but also that there is considerable variation from test to test. Matching the model to the data for the highest damage levels is especially difficult. The cross sections showing the highest damage also showed signs of significant amounts of coalescence, a phenomenon not yet represented in the model.

9.2.5.2 Brittle Fracture of Polycarbonate ("Bullet-Proof Glass"). The first illustration of the use of BFRACT, the NAG model for brittle, crack-like behavior, is with polycarbonate, a tough, transparent plastic used as bullet-proof glass. Under impacts it showed crack-like fractures that could be readily seen because the material is transparent. Several tests were made spanning a good range of damage and the results were consistent with each other (suggesting that the material behavior is repeatable from sample to sample) and with the assumptions of our model. This study of polycarbonate showed that, with a few carefully conducted experiments and posttest examinations, we can determine appropriate parameters for the NAG fracture model. Because of its transparency, this study allowed us to verify the assumptions behind our crack counting and transformation methods.

Plate impact experiments were performed on polycarbonate (Curran et al., 1973) to determine the shock compression parameters, yield strength under shock, and spall behavior. The spall tests considered here, listed in Table 9-4, show a range of impact velocities and computed stress levels that provided damage levels from just above a threshold level to almost sufficient to produce a plane of spall separation in the target.

The heavy damage observed in Test 5 is illustrated in the cross section shown in Figure 9-23 and in the crack size distributions of Figure 9-24. As we see in Figure 9-23, there is a main region of damage that could be described as a single macro crack, but it really consists of many short cracks at many distances through the specimen. These microcracks are essentially all horizontal, although they sometimes bend out of this plane to intersect with other cracks. Figure 9-24 contains the quantitative information about the damage: the location of each zone of damage that was counted and the cumulative size distribution of cracks in each zone. These size distributions have already been transformed from a surface count on the cross section to a volumetric size distribution using the method of Scheil as noted in Section 9-2-3. The variation of damage from zone to zone suggests that the sample contained a narrow band of heavy damage, with only narrow zones of collateral damage, and then was undamaged outside this band.

From these fracture data and from the other data collected during the study, we assembled a complete set of (elastic-plastic) constitutive relations and fracture parameters. With the BFRACT model in a one-dimensional wave propagation computer program, the experiments were simulated and the fracture parameters were adjusted to give a good fit to the experimental data.

Figure 9-25 compares the computed and measured crack-size distributions on the planes of maximum damage. The comparison is reasonably good, if not exceptionally so. The model comparisons for

Table 9-4. Spall tests in polycarbonate.

Test No.	Thickness (mm)		Impact Velocity (m/s)	Peak Tensile Stress (MPa)	Observed Damage
	Flyer	Target			
5	3.05	6.58	152.2	183	Near separation
6	3.17	6.45	142.8	171	Near separation
7	3.17	6.53	137.2	164	Minor, threshold

[1]Peak tensile stress was computed on the assumption of no damage.

[2]Both the flyer and target were of polycarbonate.
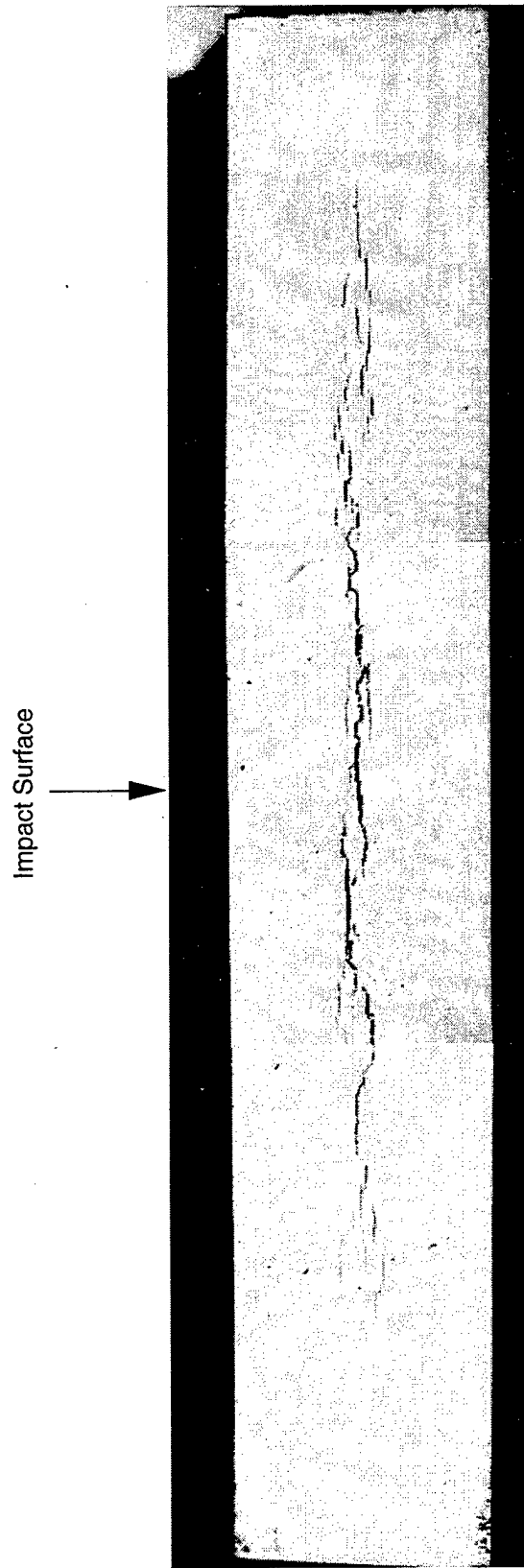
Figure 9-23. Polished section through polycarbonate specimen 5, showing the distribution of crack traces intersecting the surface.
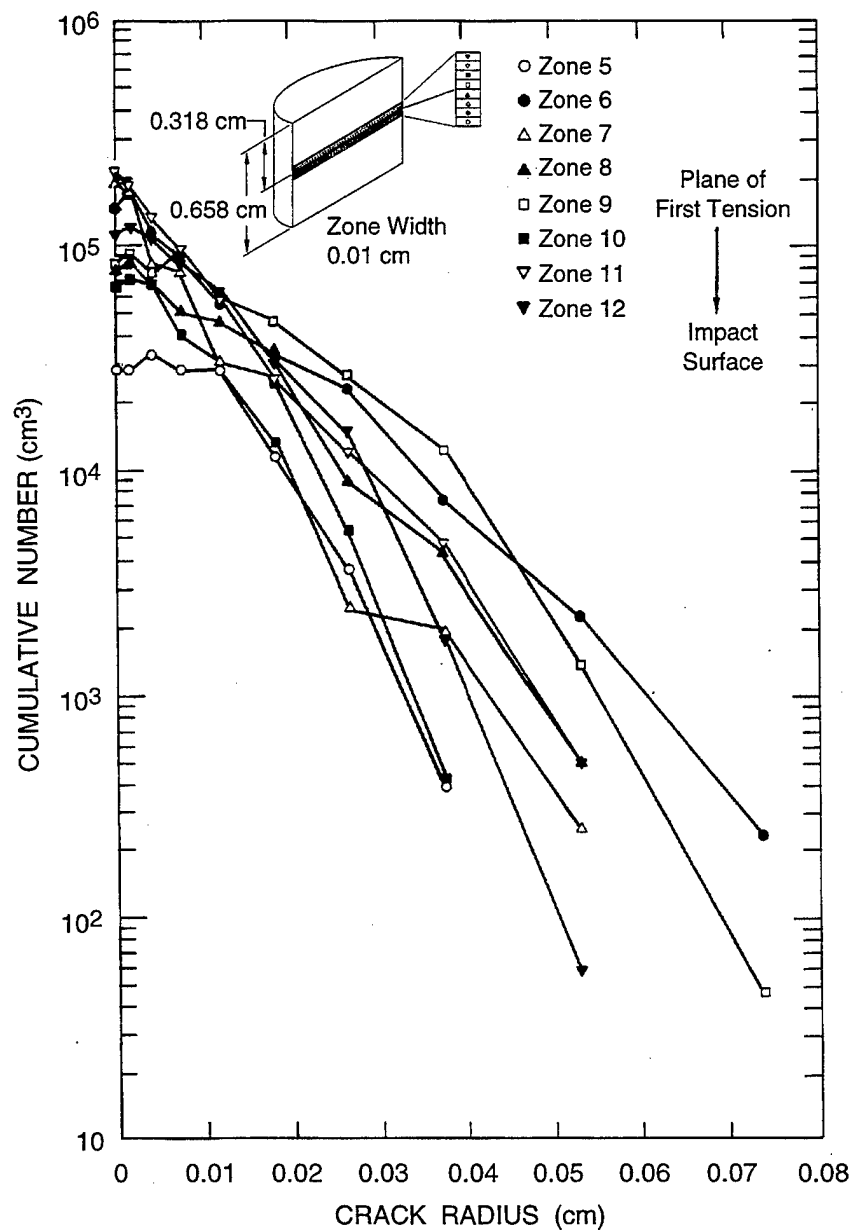
272

Figure 9-24. Volumetric crack size distributions in polycarbonate target 5 at several distances through the target.
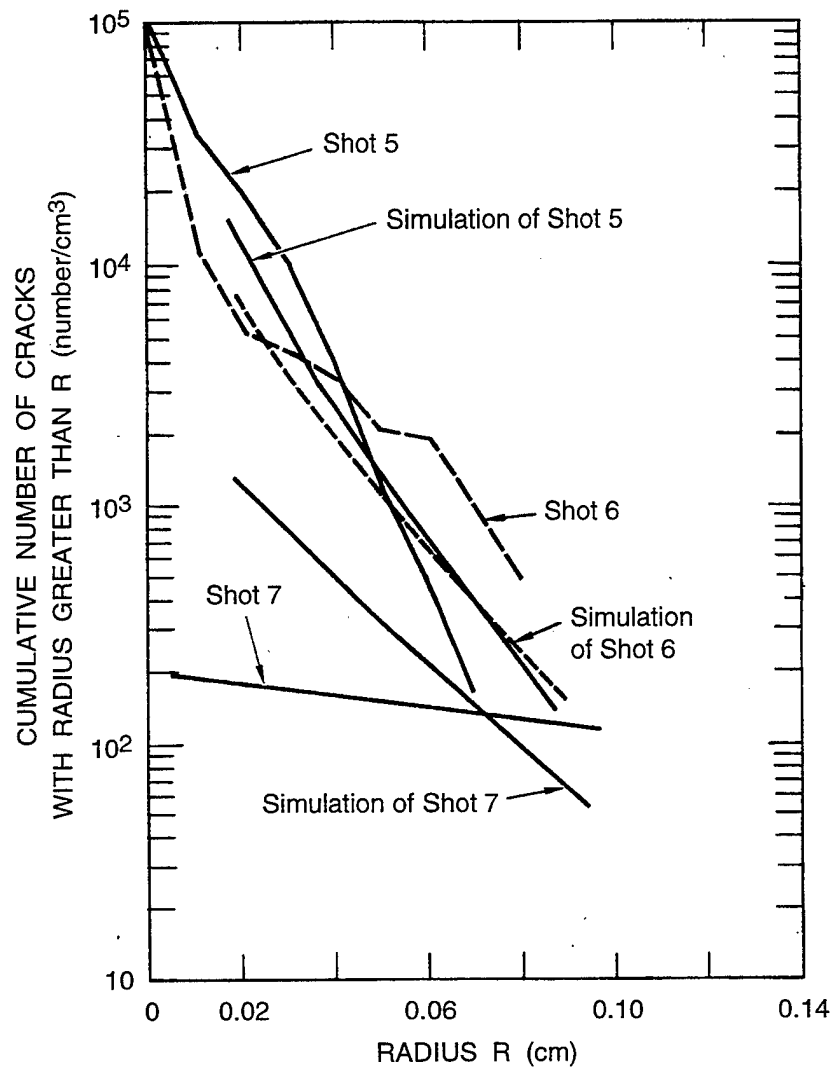
Figure 9-25. Comparison of computed and observed crack size distributions on planes of maximum damage in three polycarbonate target disks.

Test 7 suggested that this test had a stress level just above the threshold for nucleation. Very little nucleation occurred (very few cracks), but these grew a fair amount, providing the unusually shallow slope to the observed crack size distribution. The fracture parameters determined for this material are listed in Table 9-5. The range in experimental data is not sufficient to claim that we have a unique set of parameters, so special caution should be exercised in extrapolating outside the domain within which these parameters have been verified.

9.2.5.3 Fracture and Fragmentation of Rock (Quartzite).

Impact experiments were conducted by Shockey et al. (1974) in a fine-grained quartzite to determine its fracture and fragmentation behavior under high rate loading. The quartzite, called Arkansas novaculite, is a naturally occurring polycrystalline quartzite. It is pure, dense, homogeneous, and consists of equisized, equiaxed, and randomly oriented quartz grains having an average diameter of about 10 μm. A population of flat flaws preexists on planes roughly parallel to each other. For one sample, these flaws were counted on cross sections and transformed to the three-dimensional crack size distribution displayed in Figure 9-26.

Controlled impact experiments on novaculite were performed with a light gas gun, using a flat projectile impact technique, so that fracture and fragmentation occurred under one-dimensional strain conditions. The cylindrical specimens were 6.3 mm thick and 13 to 38 mm in diameter. They were fitted into constraining rings of aluminum (which has approximately the same impedance as quartzite) to permit recovery of the sample after the impact with minimal additional damage.

The 53 impact tests resulted in some samples with no damage, some with a few cracks, and others with fragments. Some samples were sectioned, as shown in Figure 9-27, to reveal the cracking. The impacts were from the top in the figure, and we see that the cracks are horizontal, that is, normal to the direction of the maximum tensile stress. The number of cracks, length of the cracks, and the general level of damage increase with impact stress.

Microscopic observations of the markings on crack surfaces in some samples indicated that the cracks were approximately circular and that their growth occurred by radial extension. The initiation sites could not be determined, but we presumed that cracks started at the small crack-like flaws that existed in the rock before the application of any external load.

Sample 53 was impacted at 48.9 m/s [essentially the same impact velocity and test conditions as sample 52 shown in Figure 9-27(d)], but this sample was separated from the constraining ring and allowed to disintegrate. The fragments were sieved into separate size groups, and samples of these fragments are shown in Figure 9-28. The individual fragments are roughly equiaxed with six to eight major facets regardless of the fragment size. From these observations, we concluded that each facet had been formed from a single crack; hence six to eight cracks had participated in forming each fragment. Because each facet seemed to be formed by a single crack, we concluded that large cracks had formed large fragments

Table 9-5. Fracture parameters for polycarbonate, novaculite, and propellant.

Symbol	Units	Polycarbonate	Novaculite	Propellant	Description
T_1	$(\text{MPa·s})^{-1}$	5.0×10^3	3×10^6	1.5×10^5	Growth rate coefficient
K_{Ic}	$\text{MPa}\sqrt{\text{cm}}$	3.6	11.0	1.28	Fracture toughness
R_n	cm	2.0×10^{-3}	5.7×10^{-3}	5.2×10^{-3}	Mean radius at nucleation
$\dot{N}_o$	Number/m³/s	7×10^{18}	3.86×10^3	6×10^{13}	Nucleation rate coefficient
σ_{no}	MPa	160	0	50	Threshold for nucleation
σ_1	MPa	14.1	4×10^{-3}	10	Stress sensitivity for nucleation
R_{max}	cm	1.0×10^{-2}	0.05	2.0×10^{-2}	Maximum radius at nucleation
$\beta\gamma T_f$	—	4.0	1.0	1.33	Crack-to-Fragment factor

[1]The nucleation rate is given by the gradual activation of the known size distribution of preexisting flaws.
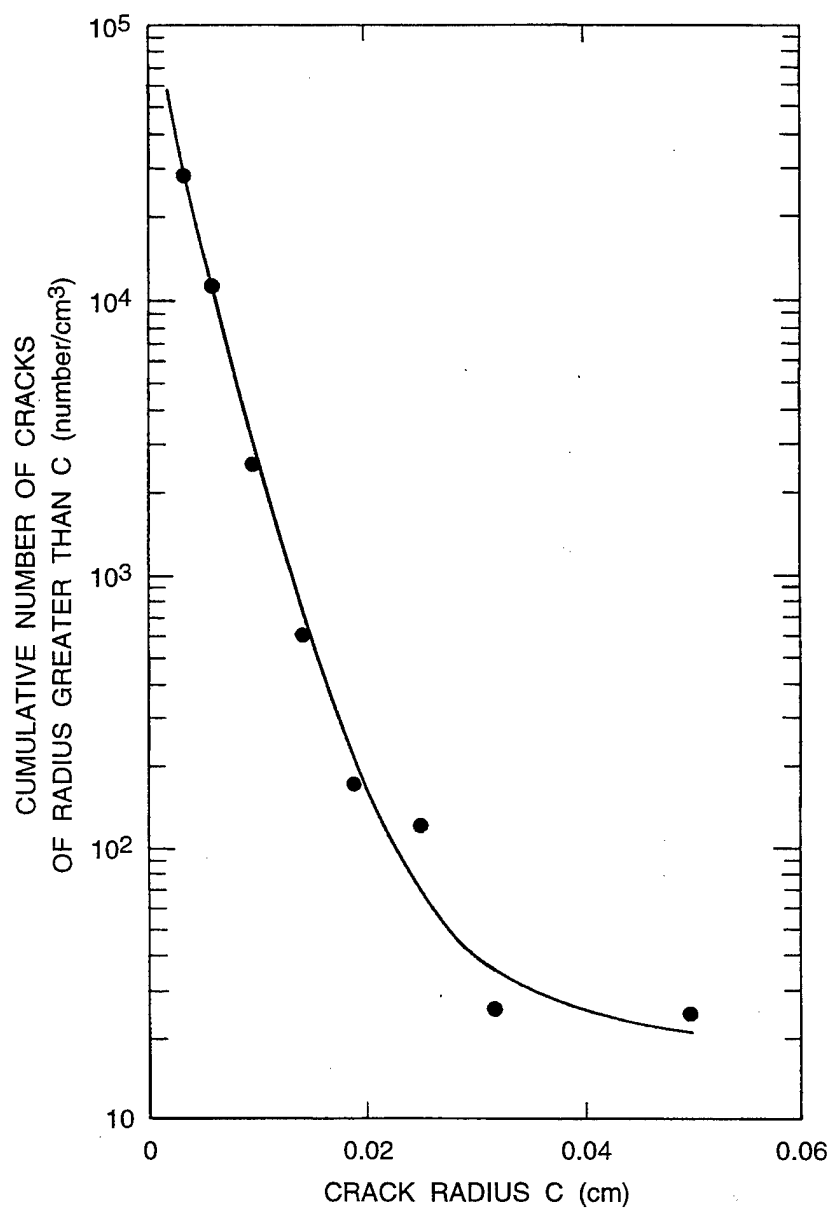
Figure 9-26. Size distribution of inherent flaws in Arkansas novaculite.
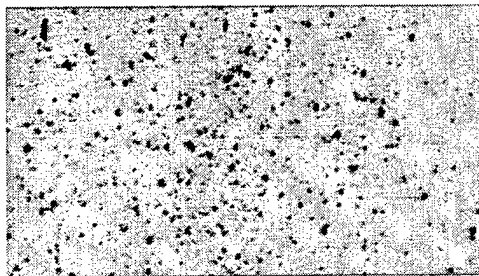
(a) Experiment 48
   41.4 x 10^6 Pascal*
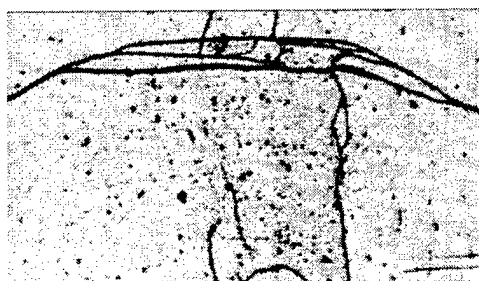
(b) Experiment 47
   45.8 x 10^6 Pascal*
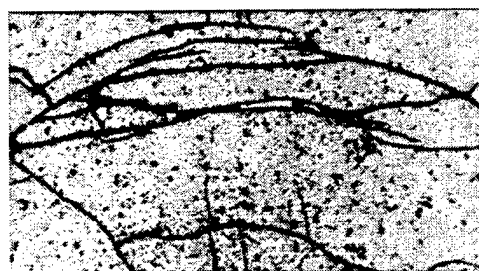
(c) Experiment 46
   53.1 x 10^6 Pascal*
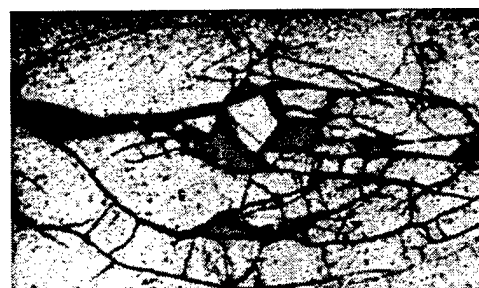
(d) Experiment 52
   138 x 10^6 Pascal*

*1 Pascal = 1 N/m^2 = 10^8 kbar

Figure 9-27. Polished cross sections of Arkansas novaculite specimens,
            showing the extent of fracture damage produced at
            increasing levels of dynamic tensile stress.

278
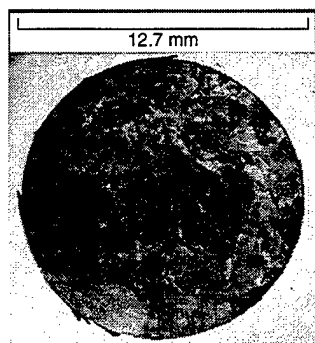
Unfragmented Portion
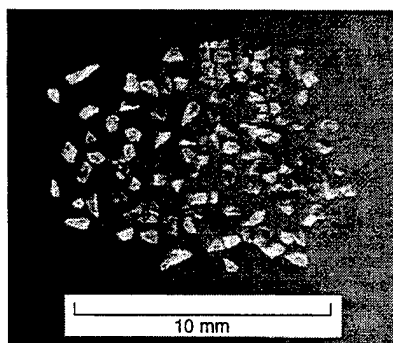
Radii 149 to 210 µm
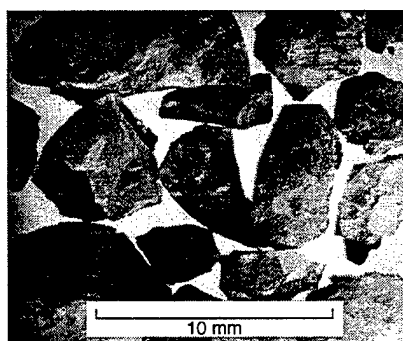
Radii Greater than 1000 µm
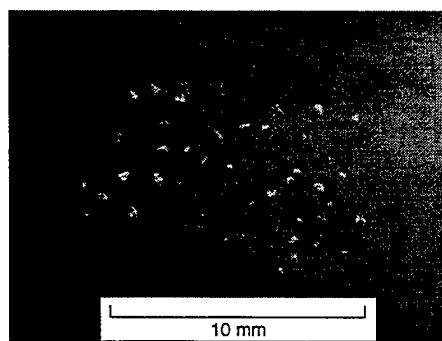
Radii 74 to 149 µm
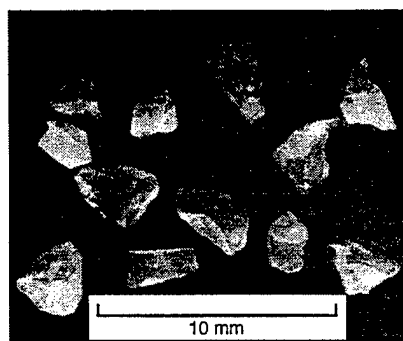
Radii 420 to 1000 µm
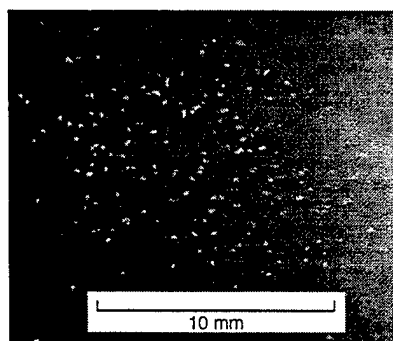
Radii 37 to 74 µm
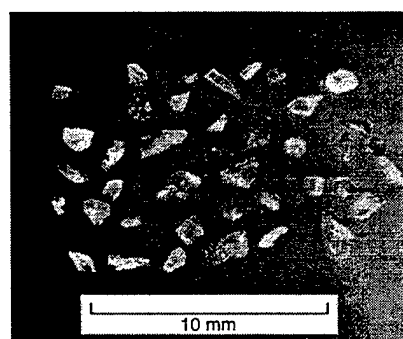
Radii 210 to 420 µm
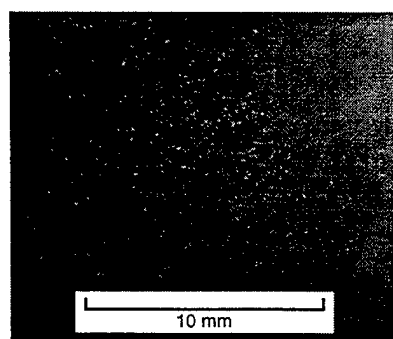
Radii 18 to 37 µm

Figure 9-28.   Photomicrographs of various sized fragments from experiment 53.

and (for mathematical convenience) we assumed that small cracks had formed small fragments. Large fragments tended to contain cracks that had not yet coalesced; therefore, not all the cracks participated in forming the fragments.

From the foregoing observations, we formulated a quantitative description of the fragmentation process; this description is the basis for the fragmentation process in the BFRACT fracture model. After a certain degree of crack growth and coalescence, fragments of various sizes form. The fragment sizes reflect the crack size distribution that led to the fragmentation. To compute the fragment size distribution, we assumed relationships between the numbers of cracks and the numbers of fragments, the crack sizes and the fragment sizes, and we assumed the shape of the fragments. The fragment radius (radius of an equivalent sphere) is given by

$$R_{if} = \gamma R_{ic} \qquad (9.50)$$

where R_{if} and R_{ic} are the ith radii in the size distribution table for the fragments and cracks respectively, and γ is a constant with a value of about 1. Similarly, the numbers of cracks and fragments are related by

$$N_{if} = \beta N_{ic} \qquad (9.51)$$

where N_{if} and N_{ic} are numbers of fragments and cracks corresponding to the ith radii in the size distribution table. β is a constant with a value of $1/3$ to $1/4$ to agree with the fact that 6 to 8 cracks form each fragment (each crack forms facets of two fragments). Here we are neglecting the fact that not all cracks may coalesce and form fragments.

The volume of the fragments at the ith radius is given by

$$\Delta V_f = T_f \left(-\frac{\partial N_f}{\partial R_f} \Delta R_f \right) R_f^3 \qquad (9.52)$$

where $\left(-\partial N_f / \partial R_f \right) \Delta R_f$ is the number of fragments in the radius interval and T_f is a material constant to account for the bulkiness of the fragments ($T_f = 4\pi/3$ for spheres).

A new variable τ was introduced to represent the progress toward fragmentation. At full fragmentation, τ is the total volume of fragments per unit volume, that is, one. Using Eq. (9.52) we can define τ as

$$\tau = T_f \int_0^{R_{max}} \left(-\frac{\partial N_f}{\partial R_f} \right) R_f^3 dR_f$$

$$= T_f \beta \gamma^3 \int_0^{R_{max}} \left(-\frac{\partial N_c}{\partial R_c} \right) R_c^3 dR_c \qquad (9.53)$$

Thus, the progress variable τ can be computed from the crack size distribution.

From the foregoing data and observations, we formulated a fracture model to represent both the cracking and the fragmentation seen in the quartzite. The nucleation aspect was treated by allowing a gradual activation of the initial flaw size distribution shown in Figure 9-26. Growth was treated with the usual relation for growth as a function of stress level above a size-related threshold stress. The material constants are shown in Table 9-5. The constants that did not come directly from the observations were determined by multiple simulations of the impact experiments illustrated in Figure 9-27. Then experiment 53 was simulated and the computed and observed fragment size distributions were compared, as shown in Figure 9-29. Evidently, the model can be used to represent many aspects of the fracture and fragmentation processes.

9.2.5.4 Fracture and Fragmentation of Solid Rocket Propellant. Solid rocket propellant is a fairly soft, rubbery composite made by adding grains of a high-energy explosive to a polymer with adhesive and viscous properties. The present review concerns a prototype propellant designated SRI-A. The equation-of-state data for the propellant in Table 9-6 were obtained from impacts, ultrasonic tests, and other measurements. Fracture may occur by decohesion of the polymer from the grains because of excessive shear or tensile stress. The material appears to be very ductile, because its elongation under tensile strain can be 50% to 200% before fracture becomes apparent. But the appearance of the damage is crack-like. During tensile, fracture voids probably open around the explosive particles and other inclusions and enlarge both viscoelastically and viscoplastically until some critical rupture strain is reached around the stretching periphery. Then tearing occurs through the rubbery matrix. When the stress is removed, the void closes and looks only like a crack.

Four planar gas-gun impacts were conducted on the prototype propellant with projectile velocities from 44 to 191 m/s (computed impact stresses from 80 to 370 MPa). No fracture occurred in the lowest velocity impact, but various levels of spall and fragmentation took place in the other three. Unfortunately, no low-damage results were obtained, although such data are needed for an accurate determination of the nucleation and growth parameters. Only the larger cracks appear to grow under dynamic loading; therefore, we selected the fracture mechanics growth threshold approach, using a fracture toughness to govern the stress threshold. The fracture parameters were obtained from iterative simulations of the four

281
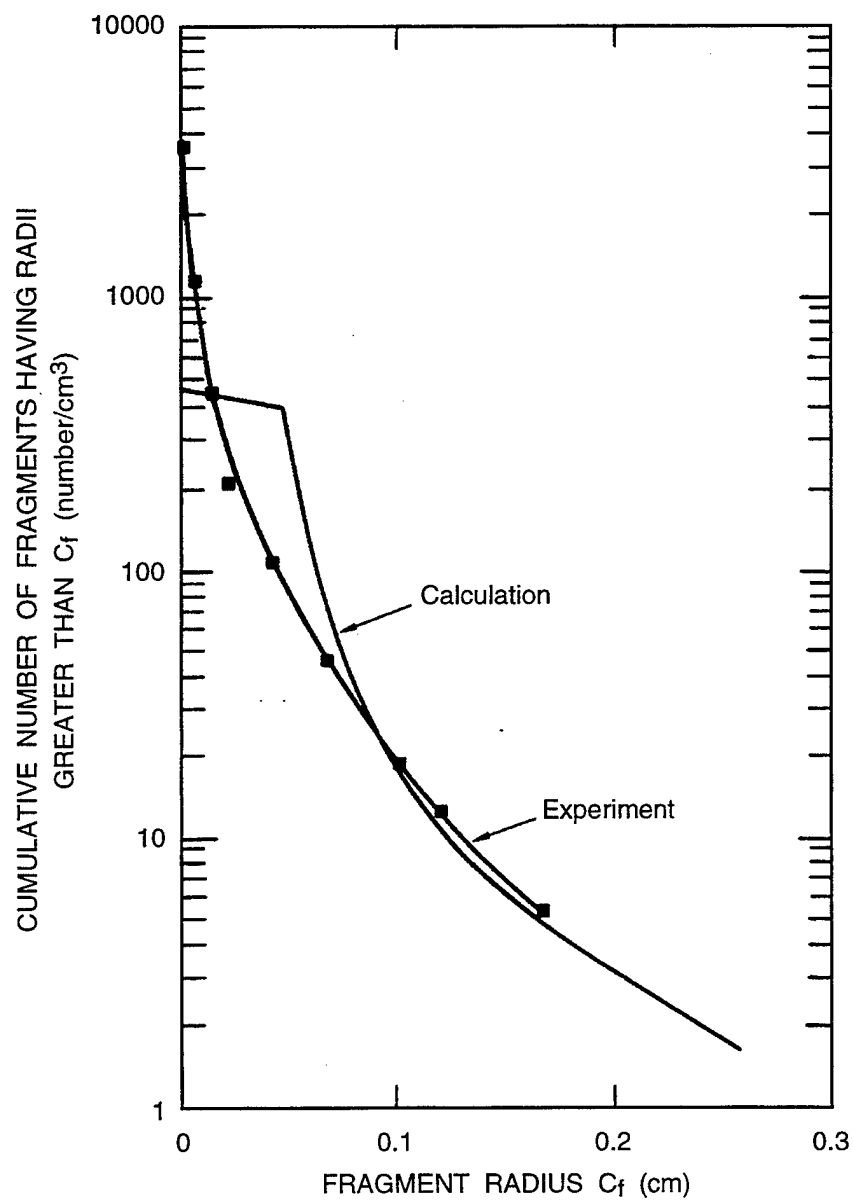
Figure 9-29. Comparison of experimental and computed fragment size distributions for experiment 53.

Table 9-6. Equation-of-state parameters for propellant SRI-A.

Description	Symbol	Value	Units
Density	ρ_{so}	1.85	Mg/m^3
Yield stress	Y	50.0	MPa
Shear modulus	G	1.24	GPa
Bulk modulus	K_1	5.67	GPa
Second bulk modulus coefficient	K_2	39.1	GPa
Third bulk modulus coefficient	K_3	182.	GPa

experiments; these parameters are given in Table 9-5. The damage computed with these parameters generally agrees well with the observed damage, as detailed below.

A cross section of a propellant specimen impacted by a tapered flyer at 73 m/s is shown in Figure 9-30 from Murri et al. (1982). The spall plane appears to be fairly well-defined in this test, although there is actually considerable damage in the form of small cracks in the material adjacent to this plane (seen in higher magnification views). The figure shows good agreement between computed and observed spall locations and widths of the spalled region. The location of the spall plane is readily predicted by most dynamic fracture models because it corresponds to the plane of first tension, which can be identified even without a fracture model. The thickness of the fractured region producing the separation, however, depends on the damage-induced stress relaxation processes in the model, and is therefore a more severe discriminator between models.

A specimen impacted at 160 m/s (Figure 9-31) showed evidence of a double spall. According to the simulation of this test, two rarefaction waves intersected to form a tensile stress and then to cause a broad region of damage, including the uppermost spall, during the first period of tensile stresses following impact. This spall caused the formation of recompression waves that propagated away from the spall region and toward the free surfaces of the specimen. These recompaction waves caused more rarefaction waves as they reflected from the free surfaces. These secondary rarefaction waves were strong enough to cause a second period of tensile damage and even a second spall closer to the impact plane.

An impact in the propellant at 191 m/s resulted in complete fragmentation of the sample. The fragment size distribution for the sample is shown in Figure 9-32. The "average radius" given on the abscissa is the radius of an equivalent sphere of the propellant with the same mass as the actual fragment. Both the computed and observed distributions show a change of slope around 0.1 to 0.2 cm; this effect is probably associated with the fracture mechanics concept that allows only cracks larger than a critical size to grow.

The observed results of the four experiments ranged from no fracture to spallation to fragmentation. All three levels of damage were well represented by the model simulations, which used a single set of fracture parameters. Unfortunately, no low-damage impacts were available; hence, the nucleation and growth parameters for the model cannot be considered unique.

Examination of these experimental data and comparison of the data with the results obtained with the model indicated two areas where further developments are needed:

- Results for low and intermediate damage are needed to determine the nucleation and growth parameters more accurately.

- A more physically descriptive model of the fragmentation process should be developed. The current treatment, although it represents the fragmentation data quite well, includes no detailed steps from the cracked state to the fragmented state.
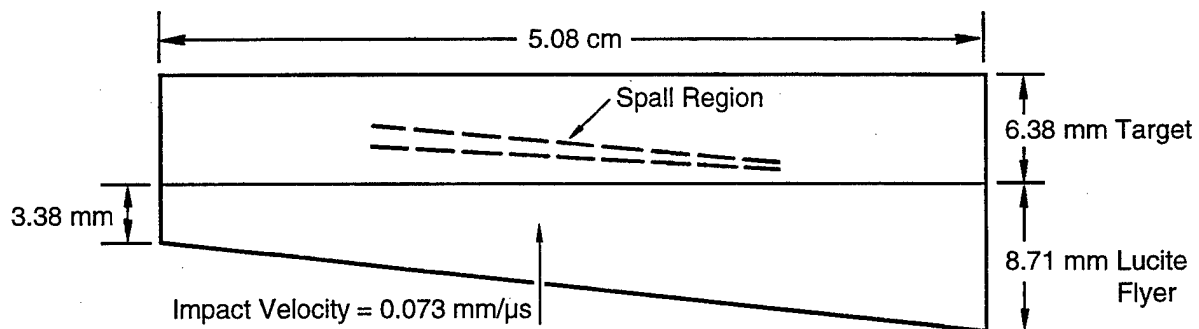
(a) Initial configuration and calculated width and location of spall plane
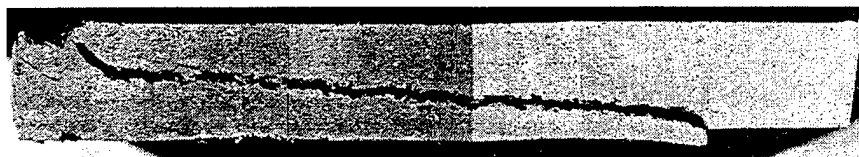
(b) Cross section of recovered target sample

Figure 9-30. Comparison of computed and observed spall plane locations in experiment 1458 in propellant A.
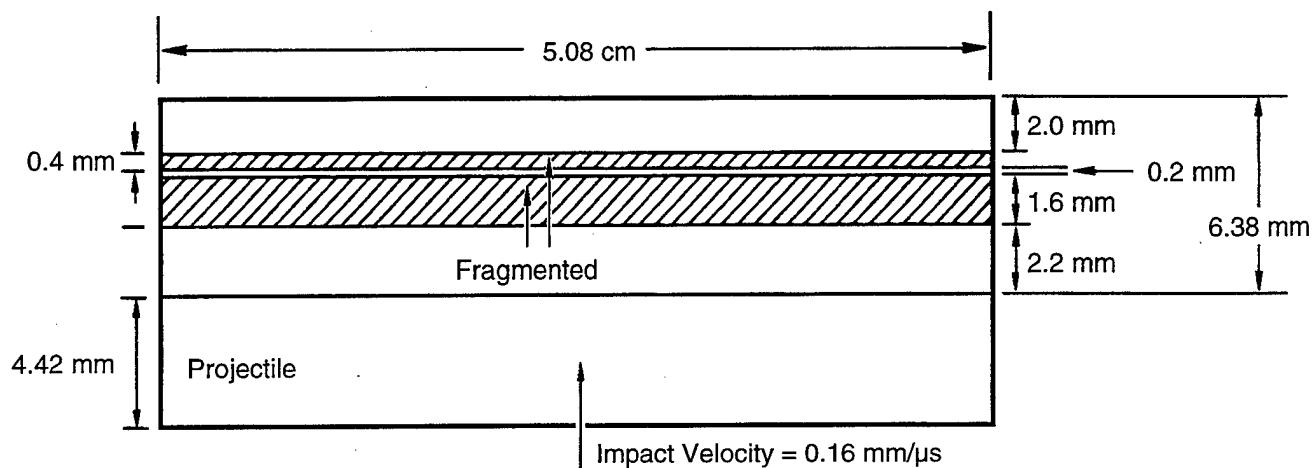
(a) Configuration and computed results showing two fragmented regions
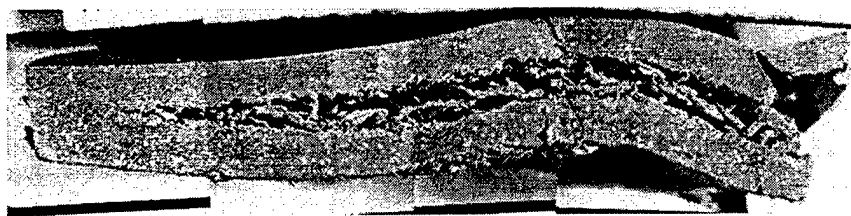
(b) Cross section of specimen recovered from experiment 1460 showing "double" spall

Figure 9-31. Comparison of computed and observed fragmented regions in experiment 1460 in propellant A.
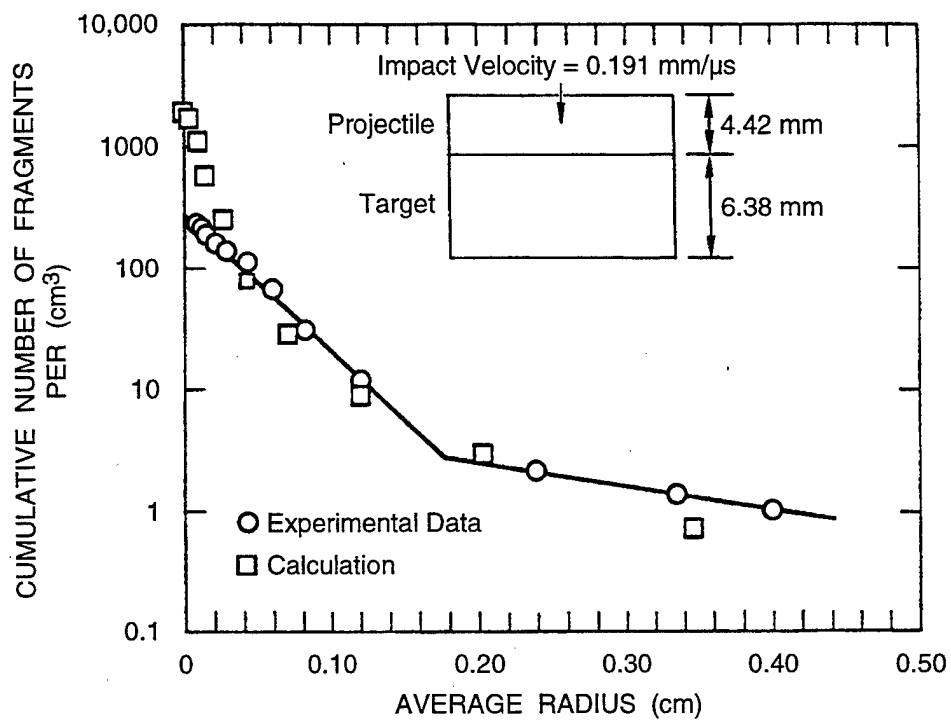
Figure 9-32. Comparison of computed and experimental fragment size distributions for experiment 1462.

9.2.5.5 Impact Fracture in Zinc Sulfide Ceramic. Shockey et al. (1981) conducted a preliminary study of impact damage in zinc sulfide (ZnS) ceramic by firing small steel and tungsten carbide spheres at plates of the ceramic. For low velocity impacts, there was only a plastic indentation and no cracking, but at higher velocities, the targets developed cracks that extended radially from the center of the impact point as well as cracks in the shape of a ring in the contact region. The cracks were counted by size for several impacts, as displayed in Figure 9-33 from Curran et al. (1987) for impacts from 6 to 80 m/s. The numerical values on the figure refer to the radius of the residual cavity in the target. In ZnS, the cracks tend to be in just two size groups: large ones of nearly a single size at each location and a distribution of small sizes. The break between the two size groups is probably related to the fracture toughness and the stress level; hence, this material may be brittle enough to follow the patterns of linear elastic fracture mechanics. We presume that the tensile stress during the impact caused the nucleation of a size distribution with an approximately exponential form. Continued tensile stress caused the growth of those cracks that were larger than the critical size according to fracture mechanics. This later growth occurred at a high velocity and independent of the original size, so all the larger cracks are of essentially the same size.

Recently, Espinosa and Brar (1995) developed a brittle fracture model of the nucleation-and-growth type to represent the fracture of ceramic. They use a detailed treatment of the microstatistical processes and include microcracks in multiple orientations.

9.2.5.6 Fracture of Beryllium under Impact and Thermal Radiation. Several grades of beryllium under impact loading and under thermal radiation. Here, we emphasize the results for S-200 beryllium, a structural grade. The impact and the initial modeling work were reported by Shockey et al. (1973b) and the radiation results were described by Shockey et al. (1979). We used plate impacts to produce a range of fracture levels and to derive from these the relevant fracture parameters. The S-200 beryllium is strongly strain-rate-dependent; therefore, we used a deviator stress model from Read and Cecil (1972) based on the concepts of dislocation dynamics. For beryllium, this model replaced the standard elastic-plastic model for the deviator stresses in the brittle fracture model. Here we examine the use of the model and parameters to represent some thermal radiation experiments.

The extent of fracture damage produced in a S-200 beryllium specimen subjected to a burst of electron beam radiation was calculated from the measured nominal fluence and from the dynamic fracture parameters determined earlier from the results of plate impact experiments. A plate specimen 3.86-mm-thick was irradiated at a fluence level of 98 ± 10 cal/cm^2 (a peak dose of 85 cal/g at the front), then sectioned and polished to reveal the internal cracks shown in Figure 9-34(b). The brittle fracture model was used to simulate this experiment, using the fracture parameters from the plate impact experiments.

The comparison between the computed and measured numbers and sizes of cracks as a function of position in the specimen (shown in Figure 9-35) shows satisfactory agreement in view of the uncertainties
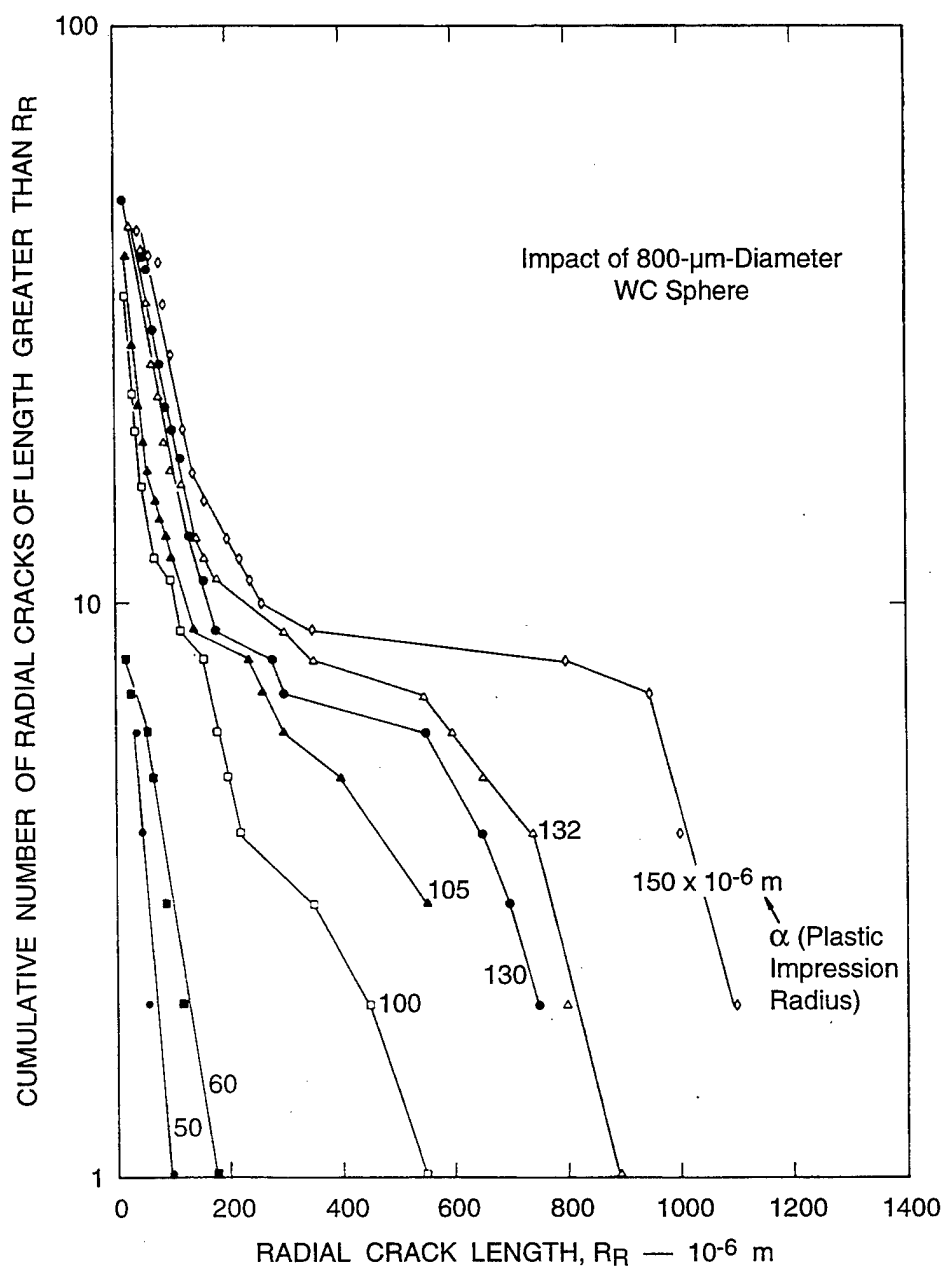
Figure 9-33.   Measured size distributions of radial cracks produced
by 800-μm-diameter WC spheres at various impact velocities.
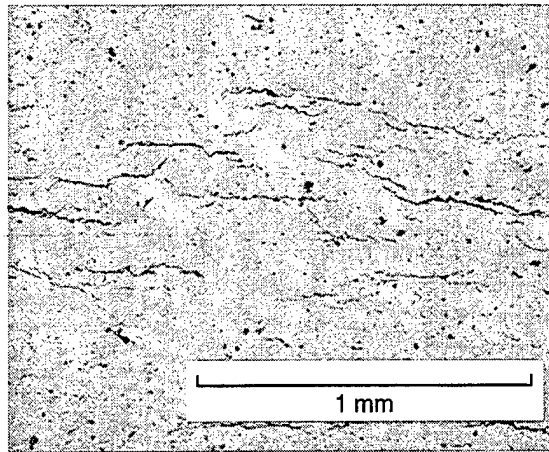
(a) 74 cal/cm^2
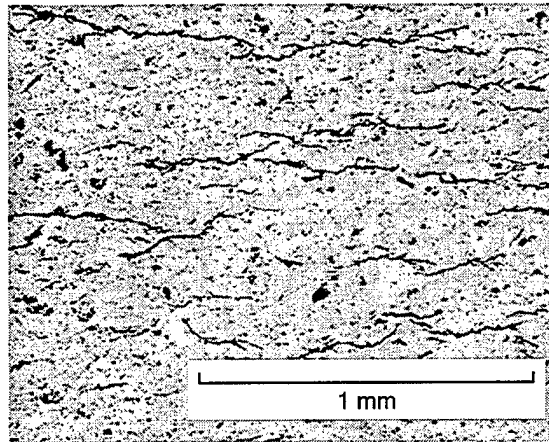
(b) 98 cal/cm^2
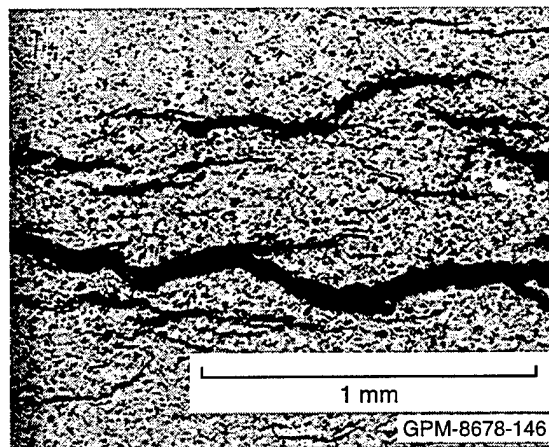
(c) 124 cal/cm^2

Figure 9-34. Polished and etched cross sections through plate specimens of S-200 beryllium, showing internal brittle cracks induced by irradiation with an electron beam at three intensities.

290
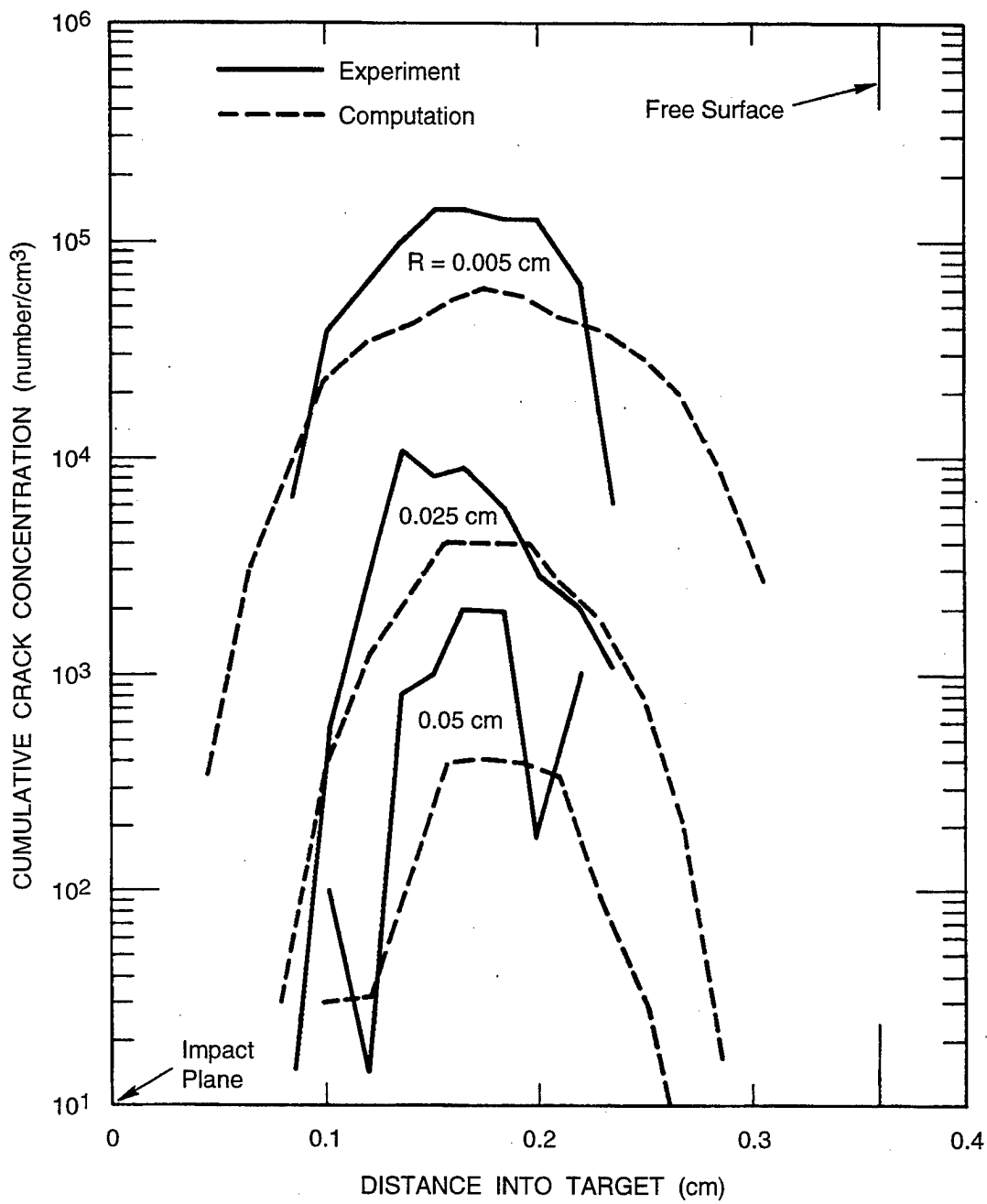
Figure 9-35. Comparison of computed and measured fracture damage in a beryllium specimen irradiated with an electron beam at a fluence of 98 cal/cm^2.

The numbers of cracks with radii larger than 0.005, 0.025, and 0.050 cm are shown.

291

in electron beam fluence. Also, there is clearly a significant amount of scatter in the observed numbers of cracks in the specimen. The disagreement is most noticeable for the largest cracks: the model tends to predict too few large cracks.

The 74- and 124-cal/cm^2 dose experiments illustrated in Figure 9-34 were also simulated, but the agreement with the observed damage was not as good. The reasons for the disagreement indicate several of the current shortcomings of the model, as listed below.

The cracks we see in Figure 9-34 are very close together, have been influenced by their neighbors, and some of them remain open after the test. Yet our counting procedure and modeling technique were developed for isolated cracks only. In the present case, the counting procedure led to essentially the same crack size distributions on the central planes for all three samples. However, we have the impression from the cross sections that a marked increase in damage occurs with increasing fluence levels. By contrast, the simulations led to distinctly different crack size distributions for the three doses: incipient, intermediate, and full fragmentation levels were predicted.

The brittle fracture model at the time of these simulations provided for elastic opening only, although the surrounding intact material can be elastic or elastic-plastic and even exhibit rate-dependent behavior. A plastic crack opening procedure should have been provided. The model also could have been provided with a limit on the number of nucleation sites for cracks. Then, we could have represented the fact that the same numbers of cracks were observed in all three tests.

The main purpose of this study of beryllium was to examine the inherent differences between fracture under thermal radiation (in this case, by electron beam) and fracture under mechanically induced stresses alone. The material undergoing fracture was not heated significantly by the beam. The observations were that the fractures that occur under thermal radiation appeared to be the same as in impact tests. Also, the simulations indicated that the cracks nucleated and grew under the same levels of tensile stress that had caused these fracture processes under impacts. Hence, the fracture modeling approach seems appropriate under thermal radiation as well as under impact loading: the cracks respond only to the stress levels they experience and there is no special response to radiation.

No fracture parameters for beryllium are listed in the tables for this section because this material required a special form of the model, including the rate-dependent deviator stress model from Read and Cecil (1972) and somewhat different nucleation and growth processes.

9.2.5.7 Fracture of Several Steels and Iron under Impact. Here, we examine how fracture occurs in practical engineering materials: steel and iron with a range of ductilities. Two of the materials are strong, tough steels, which are also termed "rolled homogeneous armor" or RHA because of their military use: Mil-S-12560B and XAR30. The third material is Armco iron. The appearance of cracks in these materials is shown, and we suggest the processes by which they were formed. In each case, we

attempt to represent the damage by the NAG brittle fracture model BFRACT. Table 9-7 summarizes the fracture parameter for all three materials.

XAR30 Armor Steel. Dynamic fracture of XAR30 (a type of rolled homogeneous armor steel) was undertaken with a series of flyer plate impacts that caused partial spall of varying levels. The yield strength is 1.45 GPa, the ultimate tensile strength is 1.6 to 1.8 GPa, the Rockwell C hardness is 52, and the elongation is 14.5%. Figure 9-36 shows cross sections of two disks that were impacted at 200 and 259 m/s. In both cases, the flyer plates were about half the thicknesses of the samples (12.1 and 2.54 mm), but tapered as indicated in Figure 9-37. The taper causes a variation in the duration of loading and in the location of the fracture plane from the impact plane. Both specimens show many cracks in a region of fracture near their centers, not a single crack or plane of fracture. In Figure 9-36(a), the cracks do not follow the taper, but lie parallel to the plate surfaces (rolling plane) indicating that the material has a lower threshold for fracture in the through-the-thickness direction. The sample in Figure 9-36(b) has an almost completely formed fracture plane, which probably occurred by coalescence of many small cracks.

The crack counts along one cross section in sample 5 are shown in Figure 9-37, the region with the longest duration of loading (because the flyer is thickest at this end). This impact was simulated using a stress-wave propagation code with the BFRACT model for brittle fracture. The resulting crack size distributions for both cross sections A-A and B-B are shown in Figure 9-38. In this case, the BFRACT version had only an exponential crack size distribution (rather than the table of number versus radius now in use), but the correspondence with the experimental data is quite good.

MIL-S-12560B Armor Steel. A similar series of plate impact spall tests was performed on MIL-S-12560B, another rolled homogeneous steel with a much lower hardness. The yield strength is 1.03 GPa, the ultimate tensile strength is 1.12 GPa, the Rockwell C hardness is 38, and the elongation is between 15% and 25%. Figure 9-39 shows a cross section of a disk impacted at 201 m/s. The larger cracks are composed of many cracks about 1 mm long that have coalescenced to form the long cracks. As shown in Figure 9-40, the section in Figure 9-39 is just one of three sections taken through a target impacted by a tapered flyer. Figure 9-40 also shows the crack concentrations on section A-A.

This impact was simulated using BFRACT, and the resulting crack size distributions for cross sections A-A, B-B, and C-C are shown in Figure 9-41. This BFRACT version had only an exponential crack size distribution, but the correspondence with the experimental data is quite good. Another comparison is made in Figure 9-42, which plots the variation of the number of cracks per unit volume as a function of position through the target. This result demonstrates that the simulations are providing approximately the correct breadth of damage.

To examine how the appearance of fracture changes between quasi-static loading and plate impact loading, we examined the fracture surfaces as indicated in Figure 9-43. The surfaces are formed by the coalescence

293

Table 9-7. Fracture parameters for steels and Armco Iron.

Symbol	Units	MIL-S-1256B	XAR30	Armco Iron	Description
T_1	$(MPa \cdot s)^{-1}$	900	550	6000	Growth rate coefficient
K_{Ic}	$MPa\sqrt{cm}$	–	–	3.4	Fracture toughness
or, σ_{go}	MPa	200	10	–	Threshold for growth
R_n	cm	3.0×10^{-3}	4.0×10^{-3}	1.0×10^{-4}	Mean radius at nucleation
$\dot{N}_o$	Number/m^3/s	2.5×10^{14}	4.0×10^{14}	1×10^{19}	Nucleation rate coefficient
σ_{no}	MPa	1120	250	300	Threshold for nucleation
σ_1	MPa	100	179	950	Stress sensitivity for nucleation
R_{max}	cm	–	–	–	Maximum radius at nucleation
$\beta\gamma T_f$	–	1.0	–	–	Crack-to-Fragment factor
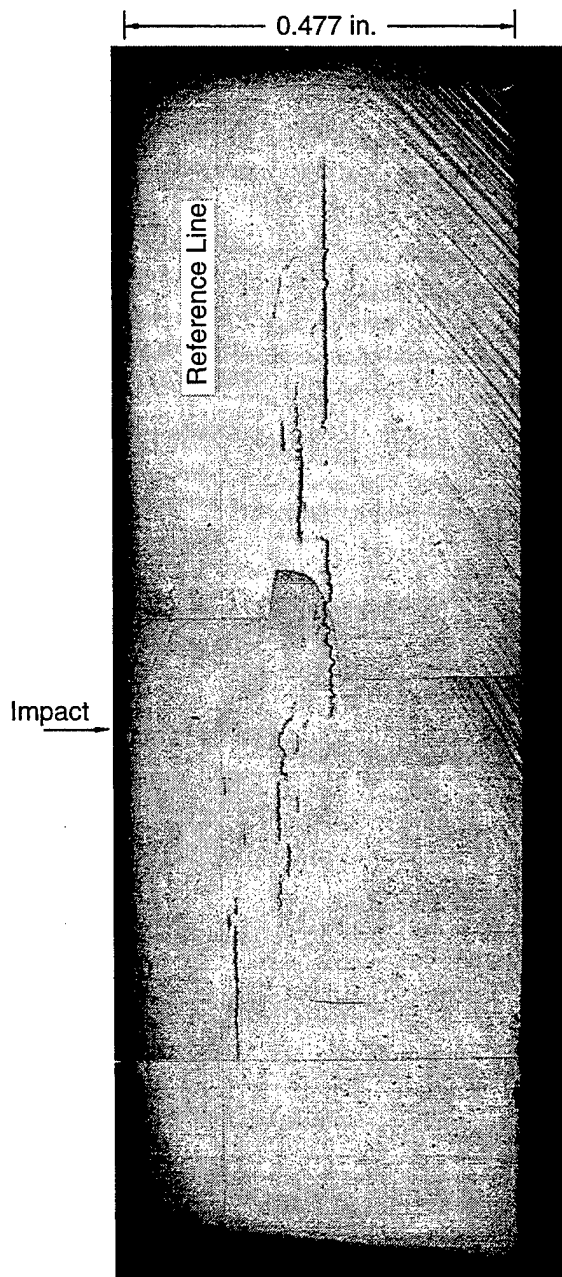
(a) Specimen 2024-4, Section A-B
(Surface is parallel to taper of flyer)
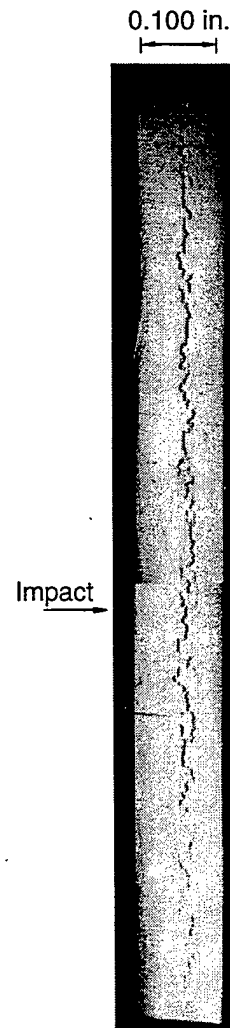
(b) Specimen 2024-5, Section A-A
(Surface is perpendicular
to taper of flyer)

Figure 9-36.   Polished cross sections of XAR30 samples, showing that cracks are parallel
to the rolling direction.
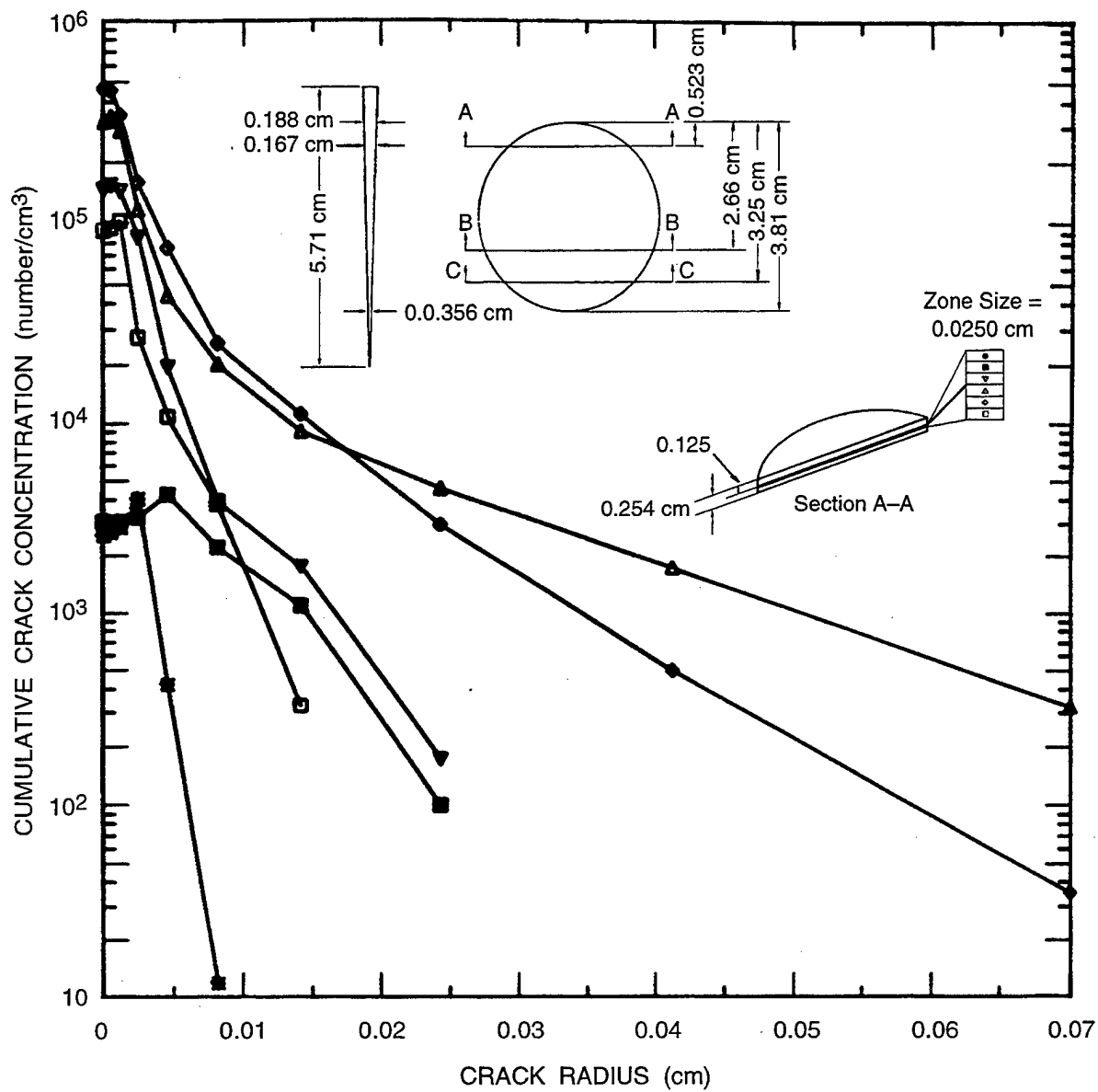
Figure 9-37. Measured crack size distribution in XAR30 steel on section A–A of test 5.
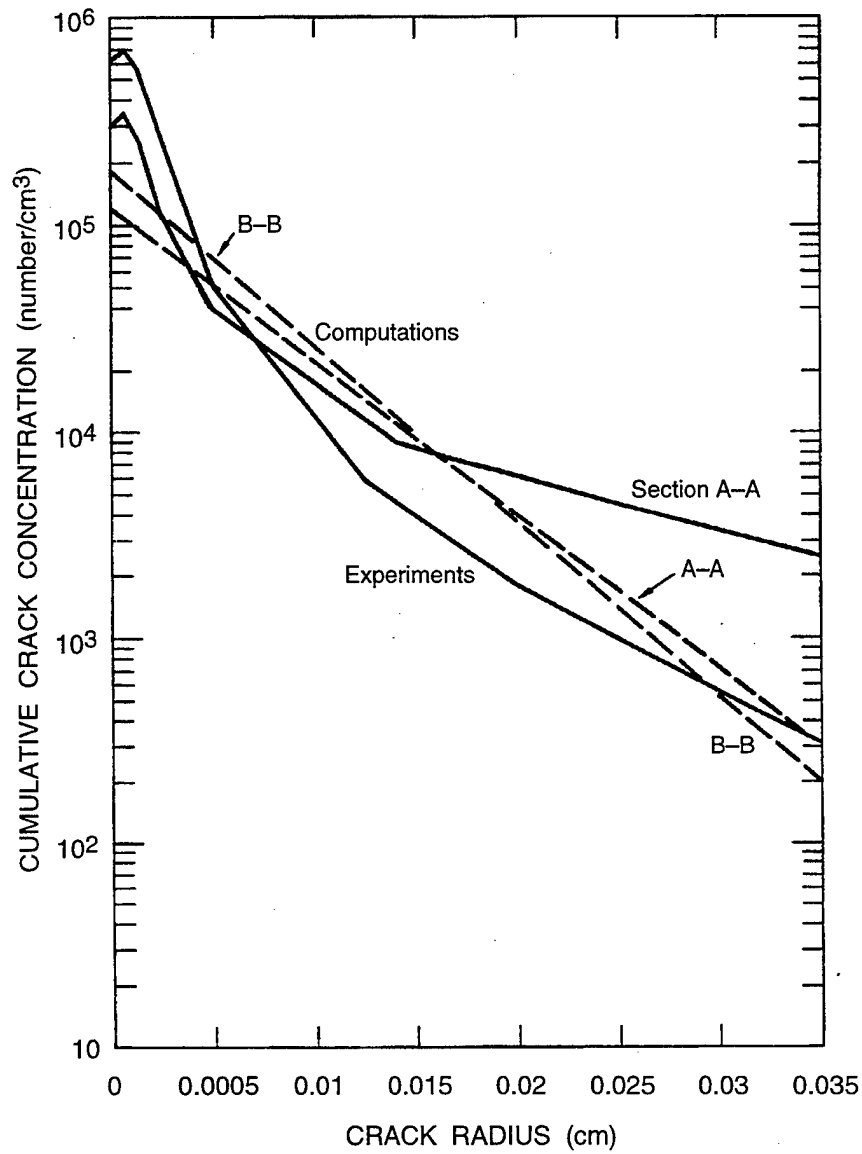
Figure 9-38. Comparison of measured and computed crack size distributions on the planes of maximum damage for tapered flyer impact 5 in XAR30.
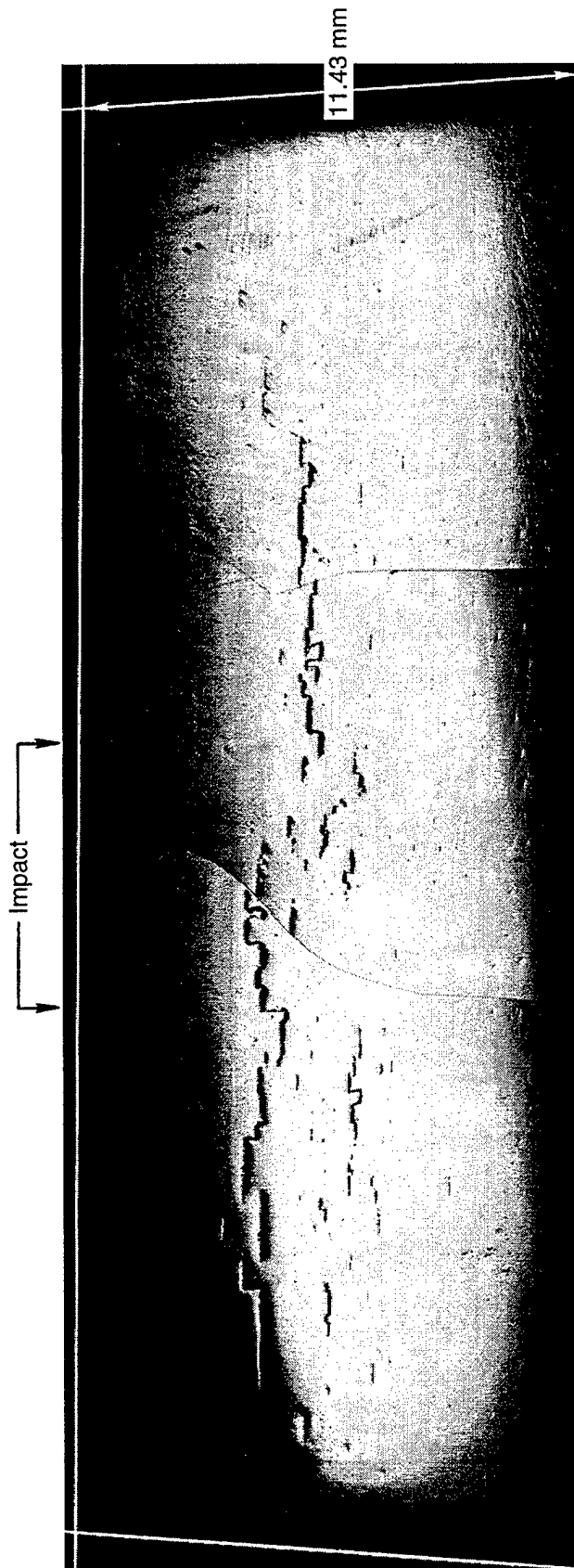
Figure 9-39. Polished cross section of section A–A in experiment 2 in MIL-S-12560B, showing fractures on the rolling plane.

298
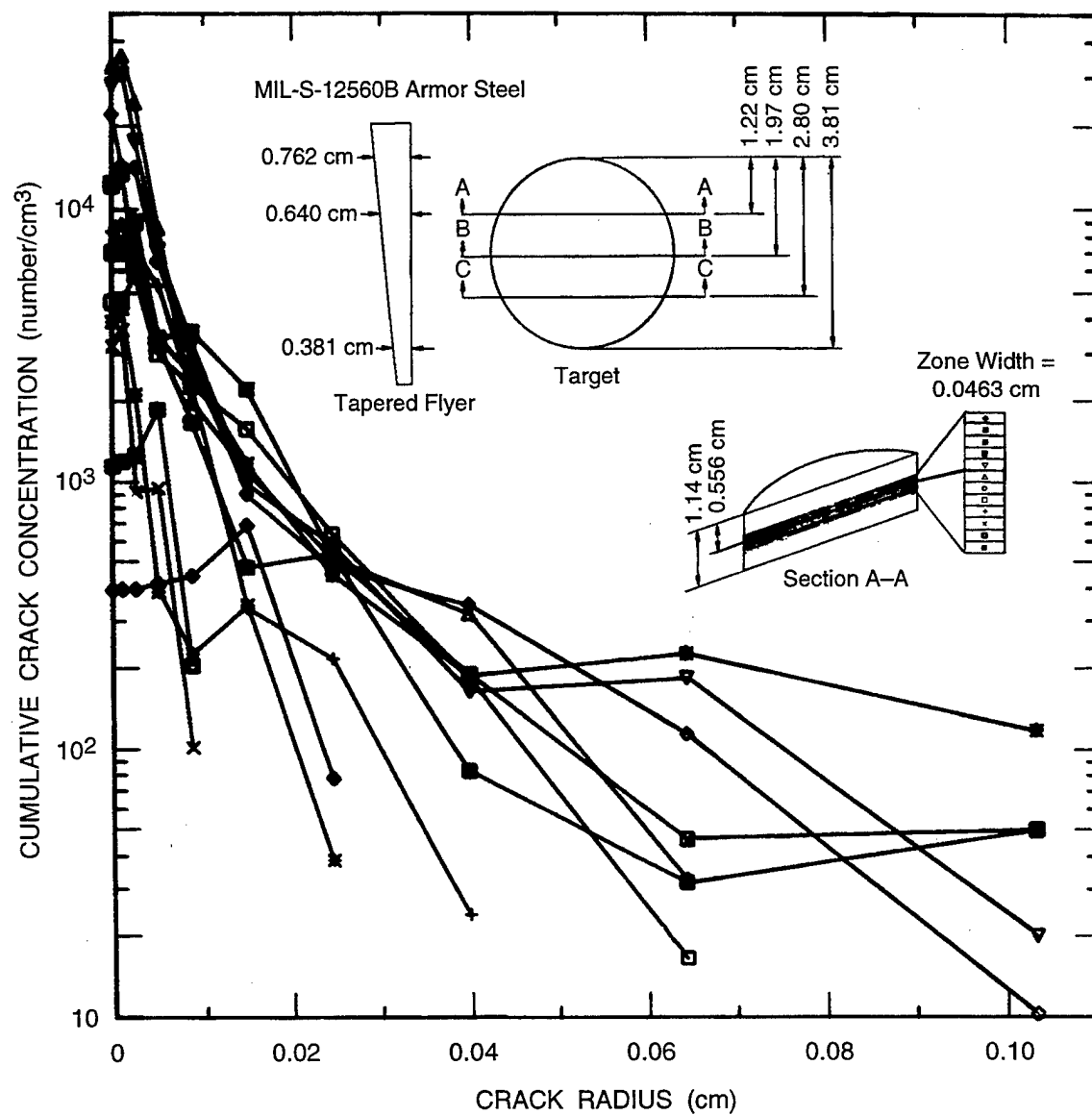
Figure 9-40.   Measured crack size distribution on section A–A of test 2 MIL-S-12560B.

299
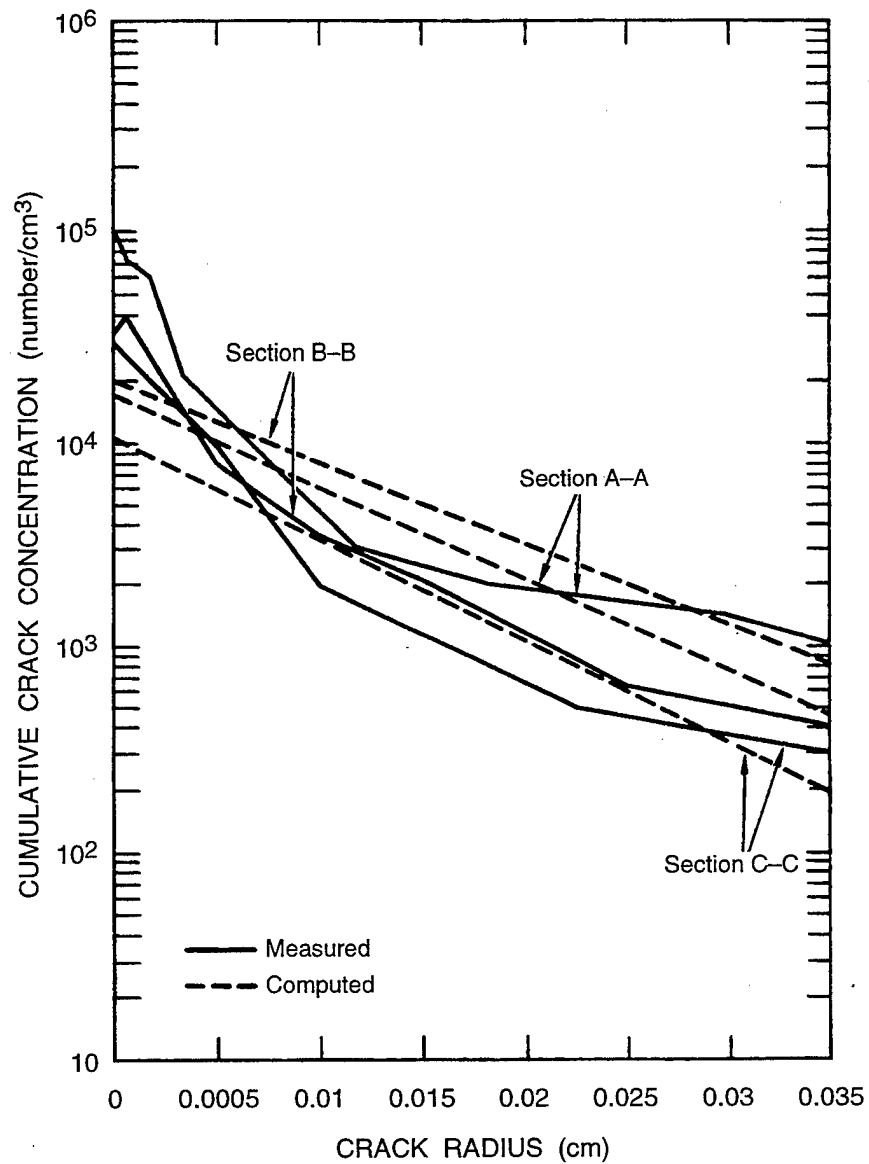
Figure 9-41. Comparison of measured and computed crack size
distributions on the planes of maximum damage
at three locations in specimen 2 of MIL-S-12560B.
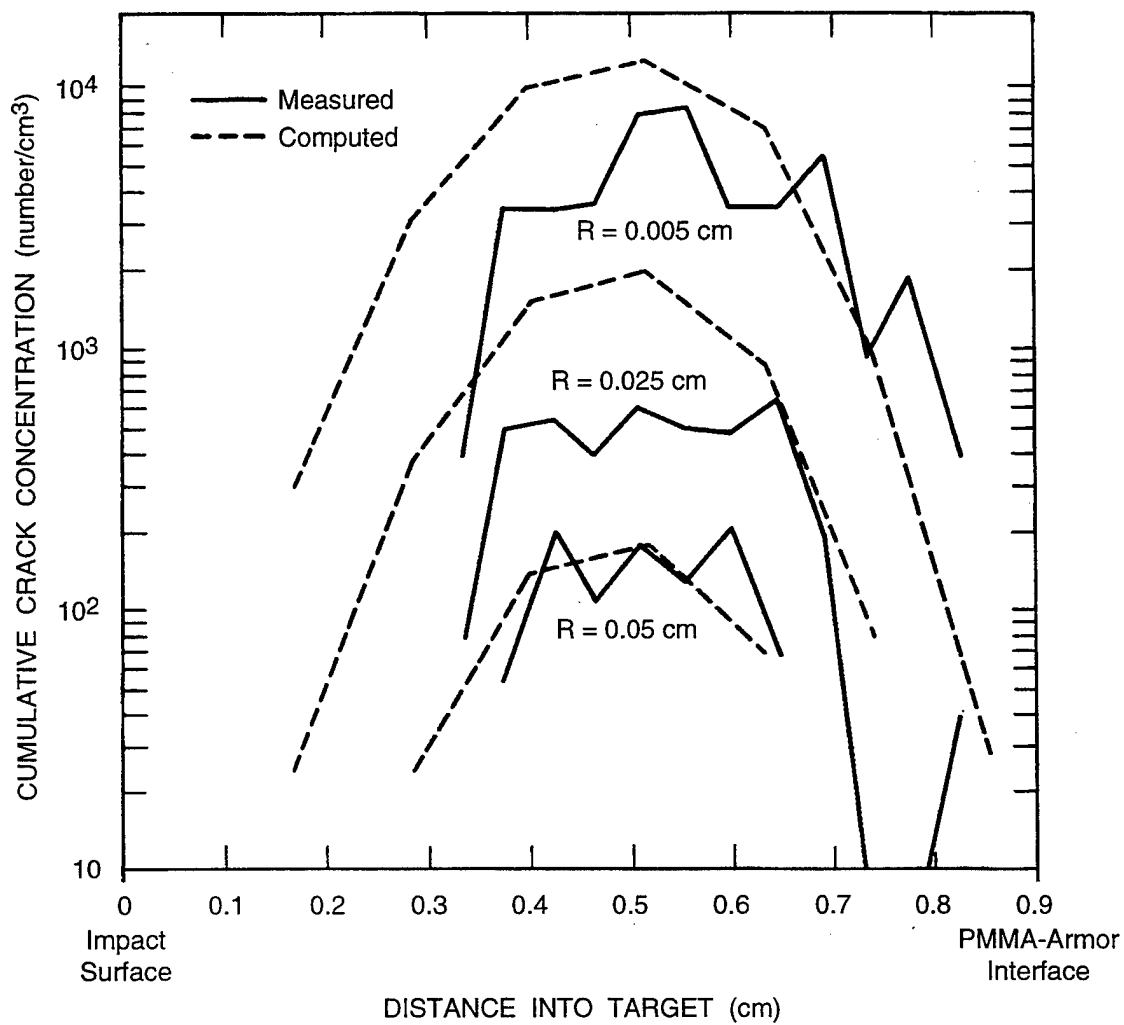
Figure 9-42. Comparison of measured and computed crack size distributions for three crack sizes as a function of depth in specimen 2 of MIL-S-12560B.
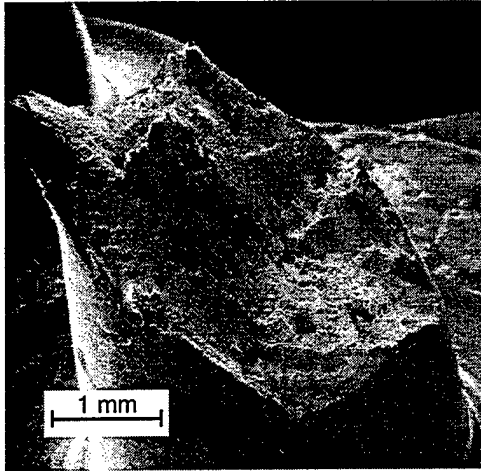
(a) Fracture surface produced at a strain rate of about 10-3 s⁻¹ in a short-transverse tensile specimen
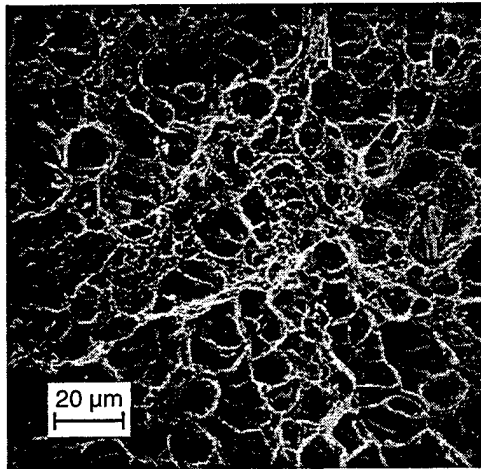
(b) Higher magnification view of (a), showing angular particles in the dimples
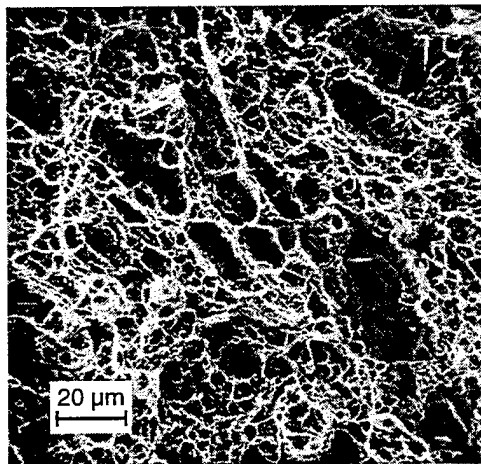
(c) Fracture surface of impact-loaded specimen 2151-4, showing similar dimple pattern as the quasi-static specimen in (b)

Figure 9-43. Scanning electron micrographs of fracture surfaces in MIL-S-12560B steel produced by quasi-static and dynamic loading.

of many dimples, and often the dimples contain the inclusion that we presume is the site of the crack initiation. For both loading rates, the largest dimples are 10 to 15 μm in diameter. For the dynamic loading, however, there is a great range of dimple sizes, and for the slow loading the dimples are nearly the same size. We conclude from this observation that in the high-rate test there was enough stress (13 GPa) to debond most of the inclusions, but in the slow test only the largest inclusions were debonded.

Armco Iron. Armco iron is a much softer material than the preceding steels, so the fracture behavior is different. The yield strength is 193.5 MPa, the ultimate tensile strength is 262 MPa, and the elongation is 35%. Again, tapered flyer experiments were conducted to survey the damage to be obtained. For one of these, conducted at an impact velocity of 103 m/s (impact stress of about 2.0 GPa), a section was made in the target parallel to the direction of taper in the flyer. Portions of this section are shown in Figure 9-44: in correspondence to the thickness of the flyer at that point are indications of the duration of the tensile stress. In this material, brittle cleavage cracks are nucleated and traverse individual metal grains, being arrested at grain boundaries. These cracks then coalesce by extension of ligaments between noncoplanar cracks, that is, by a ductile tearing along the grain boundaries. Therefore, the fracture process involves both brittle and ductile mechanisms.

In our study of Armco iron, we focused especially on test S25, which showed an intermediate level of damage spread over the central third of the specimen. The crack size distributions (obtained by counting and then transforming from areal to volume distributions with the BABS2 computer program) are shown in Figure 9-45 for the 3.156-mm-thick specimen. The impactor, also of Armco iron, was 1.138 mm thick and had a velocity of 196 m/s.

In this experiment S25, a manganin gage was placed between the Armco iron target and a PMMA buffer behind the target. The record from the manganin gage is compared with the computed stress history in Figure 9-46. To aid in understanding the modification of the stress history caused by the damage, a history from a no-damage simulation is also shown.

9.2.5.8 Discussion. In these samples of fracture obtained under high rate loading conditions we have seen a range of fracture types. In Armco iron, the microfractures occurred across grains and growth was actually a coalescence of many microcracks to form a longer crack. The polycarbonate behaved in a more glass-like manner, forming long cracks that probably extended by growth at the tips.

For the most ductile materials, there is an exponential cumulative crack size distribution, suggesting that the crack growth rate is not strongly size-dependent. For more brittle materials, such as the ceramic ZnS, the size distribution has two exponential portions connected by a nearly horizontal section, this shape is expected from linear elastic fracture mechanics.

(a) $t \cong 0.34 \ \mu s$ (b) $t \cong 0.45 \ \mu s$

Free Surface

Free Surface

(c) $t \cong 0.55 \ \mu s$ 0.5 mm   (d) $t \cong 0.63 \ \mu s$

Shock Direction

6.313 mm

3.156 mm

1.578 mm

103 m/s
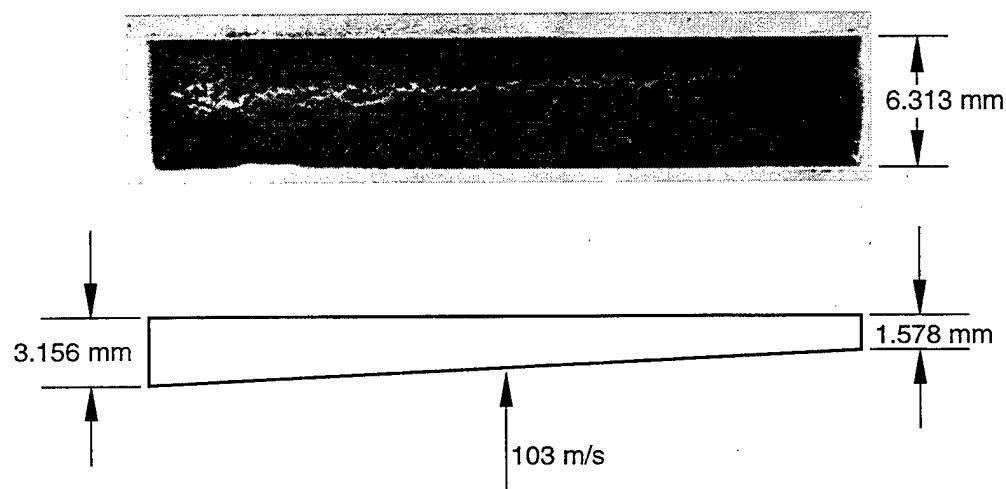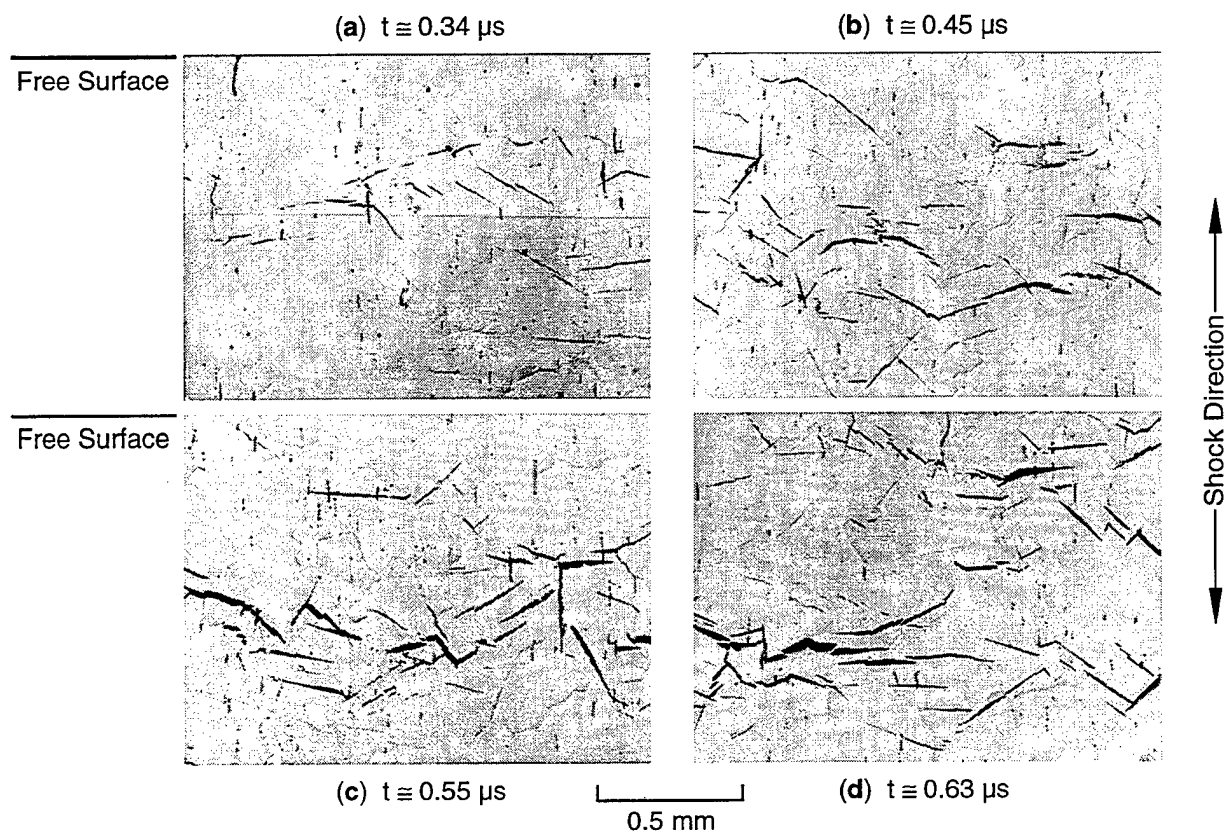
(e) Overall view of the experimental configuration and observed damage

Figure 9-44. Damage distributions observed in cross sections of the target
in a tapered flyer test S1 on Armco iron.
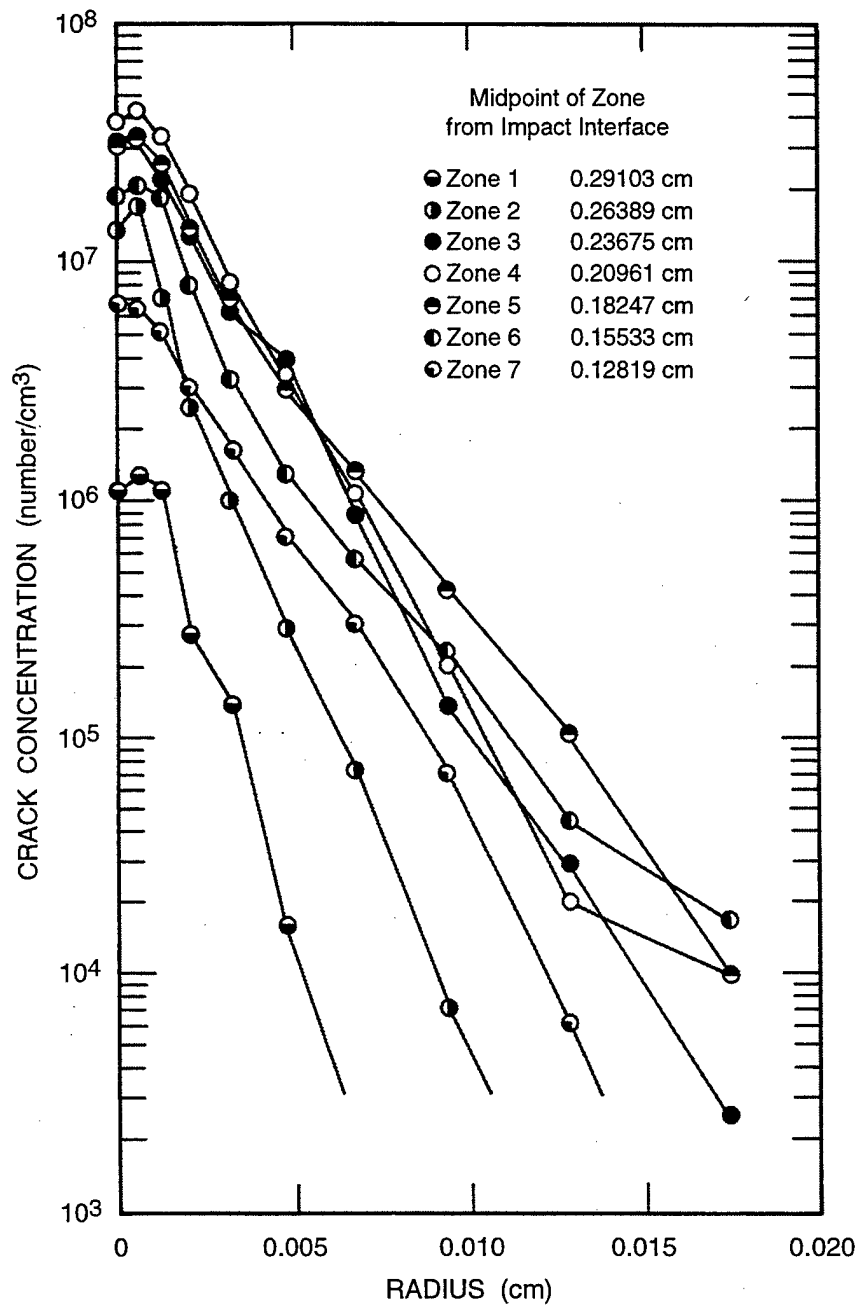
Figure 9-45. Crack size distributions for test S25 in Armco iron
from measurements (counted and transformed
by BABS2).

305
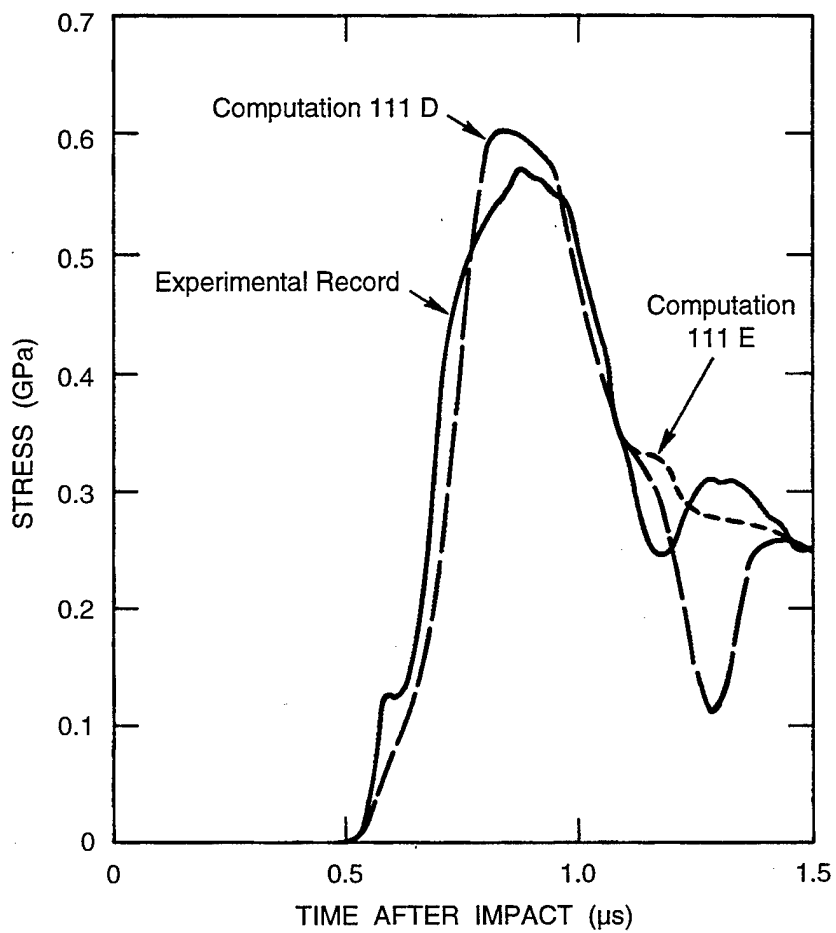
Figure 9-46. Comparison of the measured stress record behind the Armco iron target in test S25 with a simulated stress history computed using BFRACT.

When enough data were available, the number and size of cracks were measured and related to the imposed stresses and stress durations. In this way, we obtained approximate nucleation and growth rates for the cracks.

In several materials, we had difficulty causing incipient damage by plate impacts. This difficulty indicates that there may be a narrow range in tensile stress between no damage and a fairly high level of damage. For this reason, the brittle fracture experiments are much harder to perform and to control than similar experiments in more ductile materials.

SECTION 10

CONCLUSION AND NEW APPLICATIONS

10.1 SUMMARY.

Investigations of the spall phenomenon provide important information about the fracture properties of materials under short duration loading conditions unattainable with conventional quasi-static testing techniques. The one-dimensional strain state that prevails in spall experiments lends itself to straight forward interpretation, and the short duration, high amplitude stress pulses that can be produced with shock wave loading techniques make it possible to investigate the material behavior at stresses much higher than those attainable using other methods.

These factors contributed to the popularity of spall experiments as a mean of investigating dynamic fracture properties, and numerous spall investigations have been performed. Unfortunately, contradictory results of spall strength measurements have been reported in several instances, partly because all methods of measuring the dynamic tensile stress in materials during spalling are indirect. This lack of a direct spall strength measurement technique has led to several indirect methods. Each of the methods uses a different approach to determine the dynamic tensile stress, and in some cases, the measurements are based on primitive schemes that do not account for the wave dynamics during spall.

Meanwhile, detailed analyses have shown that the development of spall fracture influences the wave dynamics, and in turn, the wave dynamics influence the development of fracture. Thus, the choice of the measurement technique and the method of analyzing the experimental data are crucial in spall investigations. For this reason, we have devoted a great deal of attention to the theoretical background, experimental technique, and sources of errors associated with spall strength measurements.

Instrumental measurements made during shock wave loading provide the most accurate data about fracturing stresses under spalling. The free surface velocity profiles contain information not only about the spall strength of materials, but also about stress relaxation during fracture and the kinetics of damage evolution. More detailed information about the kinetics of the fracture process can be obtained by performing posttest microscopic examinations of impacted spall samples. Not only do such examinations provide information about the nature of damage, the damage nucleation sites, and the mode of fracture (i.e., brittle crack propagation versus ductile void growth), they also provide microstatistical data that can be used to develop quantitative estimates of the damage nucleation and growth processes.

The experimental and analytical tools for investigating the spall phenomenon are versatile and can be applied to study the response of practically all solid and liquid materials. The experiments described in this report illustrate this broad capability with applications to ductile and brittle materials, metals, ceramics, metal and inorganic single crystals, glasses, elastomers, and liquids in a wide range of temperatures, load intensities, and pulse durations.

One of the main goals of spall fracture investigations is to construct constitutive models for analyzing such phenomena as high velocity impacts, explosions, and laser and particle beam interactions with condensed targets. In this regard, two constitutive modeling approaches were discussed. In the first approach, the derivation of empirical constitutive relations is based on measurements of free surface velocity profiles over a wide range of load durations and is guided by an analysis of the influence of damage evolution on the wave profile during spalling. In the second approach, constitutive relationships of the nucleation and growth (NAG) type are constructed based on extensive microstructural observations of recovered spall samples subjected to a variety of predetermined loading conditions. NAG models are more complex than empirical models, and their calibration is more demanding. The trade-off to this relative complexity is that NAG models provide added insight into the damage process, and because the model is based on elementary physical processes, the material parameters are identifiable from experimental data and the results can be extrapolated with higher confidence outside the domain for which the model is calibrated.

Both types of constitutive descriptions are evolutionary and are computationally oriented. Choosing a constitutive model for a particular application depends to a large extent on the desired output. For applications where it is enough to characterize the response of the material in terms of kinematic variables (e.g., stress and strain), empirical models provide an adequate description of the resistance to fracture. Constitutive models of the NAG type, however, should be used when more detailed information about the state of the material is needed (e.g., flaw or fragment size distribution, response of partially damaged material).

Spall fracture is different from fracture under quasi-static loading conditions. Conventional quasi-static strength tests are always accompanied by complicating factors such as plastic flow preceding fracture, transition from a uniaxial stress state to a triaxial stress state with the development of necking, and surface and environment effects. In contrast, experiments with plane shock waves provide an unique base of information about the strength of solids under one-dimensional strain and stress states close to three-dimensional tension. Neither the surface of the body nor isolated coarse defects contribute to the main development of the spall fracture. The short duration of the applied stress makes possible the creation of large overstresses in the material near the minimum of the potential curve, $p(V)$, thus making it possible to study the conditions of elementary fracture events on a structural level close to that of the ideal crystal structure. In this sense, spall testing under shock wave loading conditions provides an opportunity for measuring the fundamental strength properties of matter.

10.2 NEW APPLICATIONS.

Spall strength measurements can also be useful for many engineering applications. For example, new technologies for treating materials using pulsed lasers are now being developed. For the success of such technologies, it is important to characterize the material behavior under conditions similar to those experienced during the laser treatment. In this way, the process can be optimized and undesirable fractures can be prevented. Spall studies can be used to aid in understanding the behavior of the material. When a pulsed laser is used as generator of shock load, spall strength measurements can be performed on very small samples obtained from different locations along the work piece. In this way a strength map can be constructed using a procedure similar to that used in microhardness mapping.

Spall studies can also be used to study the adhesion properties of coatings and to optimize processes ranging from laser cutting and drilling to laser surgery. Clinical studies have demonstrated that, for some applications, surgical lasers are superior to conventional surgical procedures. However, a fundamental understanding of the failure process in biological tissue, particularly when the tissue is irradiated by a laser, is not yet available. Such an understanding can be gained through carefully conceived spall experiments. The information could be used to develop and calibrate constitutive models for tissue failure, which could then be implemented in finite element and finite difference computer programs and used to optimize the laser surgery procedure.

Spall studies also have potential applications in the mining industry. The economy of many mining operations depends strongly on the fragment size distribution achieved during explosive blasting. Since fragmentation is the culmination of a crack nucleation, growth, and coalescence process, it is reasonable to expect that a fundamental understanding of this process would lead to practical algorithms that could be used to optimize explosive fragmentation and attain better control of the fragment size distribution. Spall studies could play a significant role in developing such algorithms because in a spall experiment, it is possible to produce damage under controlled conditions and characterize the damage in terms of flaw and fragment size distributions and in terms of material properties that affect the fragmentation process. The experiments could then be simulated using a suitable constitutive model. Once the fragmentation process is understood and characterized, appropriate fragmentation algorithms can be developed for use in mining operations.

Spall studies can be applied in still more areas. Potential areas of research where spall studies can be applied in the near future include studying the resistance to fracture in nanosecond and subnanosecond ranges of load duration, direct observations of fracture dynamics in transparent materials, and investigations of the dynamic fracture of composite materials, reinforced concrete, biological tissues, and other nonhomogeneous and nonmonolithic materials. Other areas of future research include investigating the tensor properties of the dynamic strength of anisotropic materials. This includes inherently anisotropic

materials like composites as well as materials that start out being isotropic, then become anisotropic as a result of cold work or directional deformation and damage.

Perhaps the most important area of future work is in establishing the link between classical fracture mechanics and microstatistical fracture mechanics. The existence of this link has been established by careful observations of the 'process zone' ahead of the macrocrack tip. In the process zone, microflaws nucleate and grow under the action of the amplified tensile stress field near the macrocrack tip, and the macrocrack grows by the coalescence of these microflaws. Thus, the processes that control macrocrack propagation are similar to those observed in spall experiments, and this fact provides the essential link between the classical fracture mechanics approach used to describe macrocrack propagation and the microstatistical fracture mechanics approach used to describe spall damage which is governed by the near-simultaneous nucleation and growth of many microcracks.

Bridging the gap between the classical fracture mechanics approach and the microstatistical approach offers the exciting possibility of relating material properties to underlying micromechanisms and hence material response to processing variable. If established, such a relationship could be used to design materials with superior fracture properties and response characteristics.

SECTION 11

REFERENCES

Al'tshuler, L. V., S. A. Novikov, and I. I. Divnov, *Dokl. Akad. Nauk. (USSR)* **21**, 67 (1966). (UNCLASSIFIED)

Al'tshuler, L. V., *Usp. Fiz. Nauk* **85**, 197 (1965). (UNCLASSIFIED)

Asay, J. R., L. C. Chhabildas, and D. P. Dandecar, *J. Appl. Phys.* **51**(9), 4774 (1980). (UNCLASSIFIED)

Asay, J. R., and L. M. Barker, "Interferometric Measurement of Shock-Induced Internal Particle Velocity and Spatial Variations of Particle Velocity," *J. Appl. Phys.* **45**(6), 2540-2544 (1974). (UNCLASSIFIED)

Barbee, T. W., Jr., L. Seaman, R. Crewdson, and D. R. Curran, "Dynamic Fracture Criteria for Ductile and Brittle Metals," *J. of Materials* **7**, 393-401 (1972). (UNCLASSIFIED)

Barbee, T. W., Jr., L. Seaman, and R. C. Crewdson, "Dynamic Fracture Criteria of Homogeneous Materials," Technical Report No. AFWL-TR-70-99, Air Force Weapons Laboratory, Kirtland Air Force Base, New Mexico (1970). (UNCLASSIFIED)

Barker, L. M., and K. W. Schuler, *J. Appl. Phys.* **45**, 3692-3693 (1974). (UNCLASSIFIED)

Barker, L. M., and R. E. Hollenbach. *J. Appl. Phys.* **43**, 4669 (1972). (UNCLASSIFIED)

Barker, L. M., and R. E. Hollenbach, *J. Appl. Phys.* **41**, 4208-4226 (1970). (UNCLASSIFIED)

Baumung, K., H. J. Bluhm, P. Hoppe, H. U. Kaow, D. Rush, O. Stoltz, . Singer, G. I. Kanel, A. V. Utkin, and S. V. Razorenov, "Hydrodynamic Beam-Target Interaction Experiments on the Karlsruhe Light Ion Facility KALIF," to be published in proceedings of the BEAMS-94 Conference (1994). (UNCLASSIFIED)

Bernstein, D., and D. D. Keough, "Piezoresistivity of Manganin," *J. Appl. Phys.* **35**, 1471 (1964). (UNCLASSIFIED)

Bless, S. J., and D. L. Paisley, In: *Shock Waves in Condensed Matter -1983*, ed. J. R.Asay, R. A. Graham, and G. K. Straub, Elsevier Science Publishers B.V., p. 163 (1984). (UNCLASSIFIED)

Blinkov, D. W., and D. W. Keller, *ASTM Spec. Tech. Publ.*, 252 (1962). (UNCLASSIFIED)

Bloomquist, D. D., and S. A. Sheffield, "Optically Recording Interferometer for Velocity Measurements with Subnanosecond Resolution," *J. Appl. Phys.* **54**, 1717 (1983). (UNCLASSIFIED)

Bourne, N. K., Z. Rozenberg, I. G. Crouch, and J. E. Field, "Microstructural Variations in Seven Aluminas and Their Effect on Impact Response," In: *High-Pressure Science and Technology -*

1993, Eds. S. C. Schmidt, J. W. Shaner, G. A. Samara and M. Ross, AIP Press, NY, 769-772 (1994). (UNCLASSIFIED)

Brar, N. S., Z. Rosenberg, and S. J. Bless, "Spall Strength and Failure Waves in Glass," *J. de Physique IV*, 1, p. C3-639 (1991). (UNCLASSIFIED)

Breed, B. R., C. L. Mader, and D. Venable, "Technique for the Determination of Dynamic-Tensile-Strength Characteristics," *J. Appl. Phys.* **38**(8), 3271-3275 (1967). (UNCLASSIFIED)

Bridgman, P., *Studies in Large Plastic Flow and Fracture.* Harvard University Press, Cambridge, MA (1964). (UNCLASSIFIED)

Bridgman, P. W., *Proc. Am. Acad. Arts and Sci.* **74**, 1 (1940). (UNCLASSIFIED)

Bridgman, P. W., *Proc. Am. Acad. Arts and Sci.* **47**, 321 (1911). (UNCLASSIFIED)

Bushman, A. V., G. I. Kanel, A. L. Ni, V. E. Fortov, *Intense Dynamic Loading of Condensed Matter*, Taylor and Francis, Washington, DC (1993). (UNCLASSIFIED)

Butcher, B. M., "Spallation in 4340 Steel," *J. Appl. Mech. (Trans. ASME, series E)* **34**, 209-210 (1967). (UNCLASSIFIED)

Butcher, B. M., L. M. Barker, D. E. Munson, C. D. Lundergan, "Influence of Stress History on Time-Dependent Spall in Metals," *AIAA J.* **2**(6), 977-995 (1964). (UNCLASSIFIED)

Caldirola, P., and H. Knoepfel (eds.), *Physics of High Energy Density*, Academic Press, New York, NY (1971). (UNCLASSIFIED)

Carroll, M. M., and A. C. Holt, "Static and Dynamic Pore-Collapse Relations for Ductile Porous Materials," *J. Appl. Phys.* **43**(4), 1626-1636 (1972a). (UNCLASSIFIED)

Carroll, M. M., and A. C. Holt, "Suggested Modification of the P–α Model for Porous Materials," *J. Appl. Phys.* **43**(2), 759-761 (1972b). (UNCLASSIFIED)

Chen, D. Y., Y. M. Gupta, and M. H. Miles, "Quasistatic Experiments to Determine Material Constants for the Piezoresistance Foils Used in Shock Wave Experiments," *J. Appl. Phys.* **55**(11), 3984-3993 (1984). (UNCLASSIFIED)

Chhabildas, L. C., and J. R. Asay, In: *Shock-Wave and High-Strain-Rate Phenomena in Materials*, eds., M. A. Meyers, L. E. Murr, K. P. Staudhammer, Marcel Dekker, Inc., 947 (1992). (UNCLASSIFIED)

Chhabildas, L. C., L. M. Barker, J. R. Asay, and T. G. Trucano, In: *Shock Compression of Condensed Matter - 1989*, eds., S. C. Schmidt, J. N. Johnson, L. W. Dawison, Elsevier Science Publishers B.V., 429 (1990). (UNCLASSIFIED)

Chhabildas, L. C., and R. A. Graham, "Development in Measurement Techniques for Shock Loaded Solids", In: Techniques and Theory of Stress Measurements for Shock Wave Applications, eds., R. R. Stout, E. R. Norwood, and M. E. Fourney, American Society of Mechanical Engineers, New York, AMD **83**, 1-18 (1987). (UNCLASSIFIED)

Chou, P. C., and A. K. Hopkins, *Dynamic Response of Materials to Intense Impulsive Loading*, Air Force Materials Laboratory, Wright Patterson Air Force Base, OH 45433 (1972). (UNCLASSIFIED)

Cochran, S., and D. Banner, *J. Appl. Phys.* **48**(7), 2729 (1977). (UNCLASSIFIED)

Cohen, L. J., H. M. Berkowitz, "Time-Dependent Fracture Criteria for 6061-T6 Aluminum Under Stress-Wave Loading in Uniaxial Strain," *Int. J. Fract. Mech.* **7**(2), 183-196 (1971). (UNCLASSIFIED)

Coleman, B. D., and M. E. Gurtin, "Thermodynamics with Internal State Variables," *J. Chem. Phys.* **47**(2), 597-613 (1967). (UNCLASSIFIED)

Courant, R., and K. O. Friedrichs, *Supersonic Flow and Shock Waves*, Interscience Publishers, Inc., New York (1948). (UNCLASSIFIED)

Couzens, D.C.F., and D. H. Trevena, *Nature* **222**(5192), 473-474 (1969). (UNCLASSIFIED)

Curran, D. R., L. Seaman, and D. A. Shockey, "Dynamic Failure of Solids," *Physics Reports* **147**(5&6), 253-388 (1987). (UNCLASSIFIED)

Curran, D. R., D. A. Shockey, and L. Seaman, "Dynamic Fracture Criteria for a Polycarbonate," *J. Appl. Phys.* **44**(9), 4025-4038 (1973). (UNCLASSIFIED)

Dandekar, D. P., and P. Bartkowski, "Shock Response of AD995 Alumina," In: *High-Pressure Science and Technology - 1993*, Eds., S. C. Schmidt, J. W. Shaner, G. A. Samara, and M. Ross, AIP Press, NY, 733-736 (1994). (UNCLASSIFIED)

Dandekar, D. P., "Response of Ceramics Under Shock Wave Loading," In: *High-Pressure Science and Technology - 1993*, Eds., S. C. Schmidt, J. W. Shaner, G. A. Samara, and M. Ross, AIP Press, NY, 729-732 (1994). (UNCLASSIFIED)

Davison, L., A. L. Stevens, and M. E. Kipp, "Theory of Spall Damage Accumulation in Ductile Metals," *J. Mech. Phys. Solids* **25**(1), 11-28 (1977). (UNCLASSIFIED)

DeCarli, P. S., "Stress Gage System for the Megabar (100 GPa) Range," Technical Report DNA 4066F, Defense Nuclear Agency, Washington, DC 20305 (1976). (UNCLASSIFIED)

Dremin, A. N., G. I. Kanel, and V. D. Glusman, "Experimental Investigation of the Pressure Profiles at Nonregular Reflection of Conical Shock Wave in PMMA Cylinders," *Fiz. Gorenia i Vzryva (in Russian)* **8**(1), 104-109 (1972). (UNCLASSIFIED)

Dremin, A. N., and A. M. Molodets, In: *Shock Compression of Condensed Matter -1989*, eds., S. C.Schmidt, J. N. Johnson, L. W. Dawison, Elsevier Science Publishers B.V., 415-418 (1990). (UNCLASSIFIED)

Dremin, A. N., and A. M. Molodets, "Kinetic Characteristics of Spall Fracture," *J. of Appl. Mech. and Tech. Phys.* **21**(6), 806 in Translation (1980). (UNCLASSIFIED)

Duffy, T. S., and T. J. Ahrens, "Free Surface Velocity Profiles in Molybdenum Shock Compressed at 1400°C," In: *High Pressure Science and Technology - 1993*, ed., S. C. Schmidt, J. W. Shaner, G. A. Samara, and M. Ross, AIP Press, Woodbury, NY, 1079-1082 (1994). (UNCLASSIFIED)

Durand, M., P. Laharrague, P. Lalle, A. Lebihan, J. Morvan, and H. Pujois, *Rev. Sci. Instrum.* **48**, 275-278 (1977). (UNCLASSIFIED)

Duval, G. E., and G. R. Fowles, "Shock Waves," in *High Pressure Physics and Chemistry* **2**, 209-291, edited by R. S. Bradley, Academic Press, London (1963). (UNCLASSIFIED)

Erlich, D. C., D. C. Wooten and R. C. Crewdson *J. Appl. Phys.* **42**, 5495-5502 (1971). (UNCLASSIFIED)

Ernsberger, F. M., "Role of Densification in Deformation of Glasses Under Point Loading," *J. Amer. Ceram. Soc.* **51**(10), 545-547 (1968). (UNCLASSIFIED)

Espinosa, H. D. and N. S. Brar, "Dynamic Failure Mechanisms of Ceramic Bars: Experiments and Numerical Simulations," *J. Mech. Phys. Solids* **43**(10), 1615-1638 (1995). (UNCLASSIFIED)

Evans, A. G., Y. M. Ito, and M. Rosenblatt, "Impact Damage Thresholds in Brittle Materials Impacted by Water Drops," *J. Appl. Phys.* **51**(5), 2473-2482 (1980). (UNCLASSIFIED)

Fowles, G. R., G. E. Duvall, J. Asay, P. Bellamy, F. Feistmann, D. Grady, T. Micheals, and R. Mitchell, "Gas Gun for Impact Studies," *Rev. Sci. Instr.* **41**, 984 (1970). (UNCLASSIFIED)

Fuller, J. A., and J. H. Price, "Dynamic Pressure Measurements to 300 Kilobars with a Resistance Transducer," *Brit. J. Appl. Phys.* **15**, 751 (1964). (UNCLASSIFIED)

Gent, A. N., and P. B. Lindley, "Internal Rupture of Bounded Rubber Cylinders in Tension," *Proc. Roy. Soc. (London), Series A*, **249**(1), (1959). (UNCLASSIFIED)

Gidon, S., and G. Behar, *Appl. Opt.* **25**, 1429 (1986). (UNCLASSIFIED)

Glusman, V. D., G. I.Kanel, V. F.Loskutov, V. E.Fortov, and I. E.Khorev, "The Resistance to Deformation and Fracture of Steel 35X3NM in the Shock Loading Conditions," *Problemy Prochnosti (USSR)*, No. 8, 52 (1985). (UNCLASSIFIED)

Golubev, V. K., A. I. Korshunov, S. A. Novikov, Yu. S. Sobolev, and N. A. Yukina, *J. Appl. Mech. and Tech. Phys. (USSR)*, No. 2, 121 (1988). (UNCLASSIFIED)

Golubev, V. K., S. A. Novikov, Yu. S. Sobolev, and N. A. Yukina, *Problems of Strength (USSR)*, No. 1, 63 (1985). (UNCLASSIFIED)

Golubev, V. K., and S. A. Novikov, "On an Influence of the Heat Treatment on the Strength of 40 kH Steel at Impact," *Problems of Strength (USSR)*, No. 4, 41 (1984). (UNCLASSIFIED)

Golubev, V. K., S. A. Novikov, Yu. S. Sobolev, and N. A. Yukina, *Problems of Strength (USSR)*, No. 2, 53 (1983). (UNCLASSIFIED)

Golubev, V. K., S. A.Novikov, and Yu. S. Sobolev, The Spall Fracture of PMMA, Teflon, and Polyethylene at Normal and Elevated Temperatures," *Problems of Strength (USSR)*, No.2, 88-91 (1982). (UNCLASSIFIED)

Golubev, V. K., S. A.Novikov, and Yu. S. Sobolev, "On the Temperature Influence on the Spall Strength of Polymer materials," *J. Appl. Mech. and Tech. Phys. (USSR)*, No. 1, 143-150 (1982). (UNCLASSIFIED)

Grady, D. E., "Shock-Wave Properties of High-Strength Ceramics," In: *Shock Compression of Condensed Matter 1991*, Eds., S. C. Schmidt, R. D. Dick, J. W. Forbes, and D. G. Tasker, Elsevier Science Publishers B.V., Amsterdam, The Netherlands, 455-458 (1992). (UNCLASSIFIED)

Grady, D. E., "The Spall Strength of Condensed Matter," *J. Mech. Phys. Solids* **36**(3), 353-384 (1988). (UNCLASSIFIED)

Grady, D. E., "Local Inertial Effects in Dynamic Fragmentation," *J. Appl. Phys.* **53**(1), 322-325 (1982). (UNCLASSIFIED)

Graham, R. A., *Solids under High-Pressure Shock Compression*, Springer-Verlag (1993). (UNCLASSIFIED)

Graham, R. A., and J. R. Asay, *High Temp. High Press.* **10**, 355 (1978). (UNCLASSIFIED)

Graham, R. A., "Shock-Wave Compression of X-Cut Quartz as Determined by Electrical Response Measurements," *J.Phys. Chem. Solids* **35**(3), 355-372 (1974). (UNCLASSIFIED)

Graham, R. A., and W. P. Brooks, "Shock-Wave Compression of Sapphire from 15 to 420 kbar. The Effects of Large Anisotropic Compression," *J. Phys. Chem. Solids* **32**, 2311-2330, (1971). (UNCLASSIFIED)

Griffith, A. A., "The Theory of Rupture," *First Int. Congress Appl. Mech. (1924)*, eds. Biezeno and Burgers, Waltman, 55-63 (1925). (UNCLASSIFIED)

Griffith, A. A., "The Phenomena of Rupture and Flow in Solids," *Phil. Trans. Roy. Soc. of London, Series A* **221**, 163-179 (1921). (UNCLASSIFIED)

Gupta, S. C., and Y. M. Gupta, "Experimental Measurements and Analysis of the Loading and unloading Response of Longitudinal and Lateral Manganin Gauges Shocked to 90 kbar," *J. Appl. Phys.* **62**(7), 2903-2609 (1987). (UNCLASSIFIED)

Gupta, Y. M., "Stress Measurements Using Piezoresistance Gauges: Modeling the Gauge as an Elastic-Plastic Inclusion," *J. Appl. Phys.* **54**(11), 6256-6266 (1983). (UNCLASSIFIED)

Hemsing, W. F., A. R. Mathews, R. H. Warnes, M. J. George, and G. R. Whittemore, "VISAR: Line Imaging Interferometer," In: Shock Compression of Condensed Matter 1991, Eds.: S. C. Schmidt, R. D. Dick, J. W. Forbes and D. G. Tasker, Elsevier Science Publishers B.V., Amsterdam, The Netherlands, 767-770 (1992). (UNCLASSIFIED)

Herrmann, W., "Constitutive Equations for Compaction of Porous Materials," *Symp. Appl. Mech. Aspects of Nuclear Effects in Materials*, ASME Winter Annual Meeting, Washington, D.C., November 28 - December 3 (1971). (UNCLASSIFIED)

Hopkinson, B., "A Method of Measuring the Pressure Produced in Detonation of High Explosives or by Impact of Bullets," *Proc. Roy. Soc.- Series A* **213**, 437-456 (1914). (UNCLASSIFIED)

Ivanov, A. G., "Spallation in the Quasiacoustic Approach," *Phys. Combustion and Explosion (USSR)*, No.3, 475-480 (1975). (UNCLASSIFIED)

Johnson, J. N., "Dynamic Fracture and Spallation in Ductile Solids," *J. Appl. Phys.* **52**(4), 2812-2825 (1981). (UNCLASSIFIED)

Johnson, P.M., and T. J. Burgess, *Rev. Sci. Instrum.* **39**, 1100-1103 (1968). (UNCLASSIFIED)

Kalmikov, Y. B., G. I. Kanel, I. P. Parchomenko, A. V. Utkin, and V. E. Fortov, "The Behaviour of Rubber in Shock and Rarefaction Waves, *J. Appl. Mechanics and Tech. Phys. (USSR)*, No. 1, 126-130, (1990). (UNCLASSIFIED)

Kanel, G. I., S. V. Razorenov, A. A. Bogatch, A. V. Utkin, V. E. Fortov, and D. E. Grady, "Spall Fracture Properties of Aluminum and Magnesium at High Temperatures," *J. Appl. Phys* **79**(11), 8310-8317 (1996a). (UNCLASSIFIED)

Kanel, G. I., S. V. Razorenov, A. V. Utkin and D.E. Grady, "The Spall Strength of Metals at Elevated Temperatures," In: *Shock Compression of Condensed Matter - 1995*, eds., S. C. Schmidt and W. C. Tao, AIP press, Woodbury, NY, 503-506 (1996b). (UNCLASSIFIED)

Kanel, G. I., S. V. Razorenov, A. V. Utkin, K. Baumung, H. U. Karow, and V. Licht, "Spallation Near the Ultimate Strength of Solids," In: *High-Pressure Science and Technology - 1993*, Eds.: S. C. Schmidt, J. W. Shaner, G. A. Samara and M. Ross, AIP Press, NY, 1043-1046 (1994). (UNCLASSIFIED)

Kanel, G. I., A. V. Utkin, and Z. G.Tolstikova, "Response of the High-Filled Elastomers to Shock-Wave Loading," In: *High-Pressure Science and Technology - 1993*, Eds., S. C. Schmidt, J. W. Shaner, G. A. Samara and M. Ross, AIP Press, NY, 1123-1126 (1994). (UNCLASSIFIED)

Kanel, G. I., S. V. Razorenov, A. V. Utkin, V. E. Fortov, K. Baumung, H. U. Karow, D. Rush, and V. Licht, "Spall Strength of Molybdenum Single Crystals," *J. Appl. Phys.*, **74**(12), 7162-7165 (1993). (UNCLASSIFIED)

Kanel, G. I., S. V. Rasorenov, and V. E. Fortov, "The Dynamic Strength of Copper Single Crystals," In: *Shock-Wave and High-Strain-Rate Phenomena in Material,*. Eds., M. A. Meyers, K. Murr and K. Staudhammer, Marcel Dekker, Inc., 775-782 (1992a). (UNCLASSIFIED)

Kanel, G. I., S. V. Razorenov, and V. E. Fortov, "The Failure Waves and Spallation in Homogeneous Brittle Materials," In: *Shock Compression of Condensed Matter 1991*, Eds., S. C. Schmidt, R. D. Dick, J. W. Forbes, and D. G. Tasker, Elsevier Science Publishers B.V., Amsterdam, The Netherlands, 451-454 (1992b). (UNCLASSIFIED)

Kanel, G. I., and A. V. Utkin, "Dynamics of o Cavitation Area at Reflection of a Compression Pulse from the Interface Between Two Media," *J. Appl. Mech. Tech. Phys. (USSR)* **32**(4), 23-26 (1991). (UNCLASSIFIED)

Kanel, G. I., S. V. Razorenov, and V. E. Fortov, "The Spall Strength of Metals in a Wide Range of Shock Load Amplitudes," *Academy of Sciences USSR - Doklady* **294**(2), 350-352 (1987). (UNCLASSIFIED)

Kanel, G. I., and A. N. Pityulin, *Phys. of Combustions and Explosions (USSR)*, No. 4, 85 (1984). (UNCLASSIFIED)

Kanel, G. I., S. V. Razorenov, and V. E. Fortov, "Kinetics of Spallation Rupture in the Aluminum Alloy AMg6M," *J. Appl. Mech. Tech. Phys.* **25**(5), 707-711 (1984a). (UNCLASSIFIED)

Kanel, G. I., S. V. Razorenov, and V. E. Fortov, "The Spall Strength of Metals in a Wide Range of the Load Duration," *Acad. of Sciences USSR - Doklady* **275**(2), 269-271 (1984b). (UNCLASSIFIED)

Kanel, G. I., and V. D. Glusman, *J. Appl. Mechanics and Technical Phys (USSR)*, No. 4, 146-150 (1983). (UNCLASSIFIED)

Kanel, G. I., "Resistance of Metals to Spall Fracture," *Combustions, Explosions and Shock Waves* **18**(3), 329-335 (1982a). (UNCLASSIFIED)

Kanel, G. I., "The Work of Spall Fracture," *Combustions, Explosions and Shock Waves* **18** (4) 461-464 (1982b). (UNCLASSIFIED)

Kanel, G. I., and E. N. Petrova, "The Strength of Titanium VT6 at Shock Wave Loading," In: II Workshop on Detonation, Chernogolovka, Russia, 136-142 (1981). (UNCLASSIFIED)

Kanel, G. I., and L. G. Chernych, *J. Appl. Mechanics and Technical Phys (USSR)*, No. 6, 78-84 (1980). (UNCLASSIFIED)

Kanel, G. I., and V. V. Shcherban, "Plastic Deformation and Cleavage Rupture of Armco Iron in a Shock Wave," *Combustion, Explosion, and Shock Waves* **16**(4), 439-446 (1980). (UNCLASSIFIED)

Kanel, G. I., G. G. Vakhitova, and A. N. Dremin, *Fiz. Goreniya i Vzryva*, No. 2, 130 (1978). (UNCLASSIFIED)

Kanel, G. I., and, A. M. Molodets, "Behavior of the K8 Glass at Dynamic Compression and Following Unloading, *Zh. Tehn. Fiz.* **46**, 398 (1976). (UNCLASSIFIED)

Keough, D. D., P. S. DeCarli, and T. Cooper, "Distant Mountain Test Series (Test Bed Designs and Flatpack Stress Gage Measurements)," Defense Nuclear Agency Technical Report DNA-TR-93-103, Alexandria, VA (1993). (UNCLASSIFIED)

Kipp, M. E., and D. E. Grady, "Elastic Wave Dispersion in High-Strength Ceramics," In: *Shock Compression of Condensed Matter 1991*, Eds., S. C. Schmidt, R. D. Dick, J. W. Forbes, and D. G. Tasker, Elsevier Science Publishers B.V., Amsterdam, The Netherlands, 459-462 (1992). (UNCLASSIFIED)

Kipp, M. E., D. E. Grady, and E. P. Chen, "Strain-Rate Dependent Fracture Initiation," *Int. J. of Fracture* **16**, 471-478 (1980). (UNCLASSIFIED)

Kornfeld, M., *Elasticity and Strength of Liquids*, State Publisher of Scientific and Technical Literature, Moscow-Leningrad, USSR (1951). (UNCLASSIFIED)

Krajcinovic, D., and G. U. Fonseka, "The Continuous Damage Theory of Brittle Materials, Part 1: General Theory," *J. of Appl. Mechanics* **48**, 809-815 (1981). (UNCLASSIFIED)

Kumano, A., and W. Goldsmith, "Analytical and Experimental Investigation of the Effect of Impact on Coarse Granular Rocks," *Rock Mechanics* **15**(2), (1982). (UNCLASSIFIED)

Landau, L. D., and E. M. Lifshitz, *Fluid Mechanics*, Pergamon Press, Oxford, UK (1959). (UNCLASSIFIED)

Lee, L. M., "Nonlinearity in the Piezoresistance Coefficient of Impact-Loaded Manganin," *J. Appl. Phys.* **44**, 4017-4022 (1973). (UNCLASSIFIED)

MacKenzie, J. K., "The Elastic Constants of a Solid Containing Spherical Holes," *Proc. of the Phys. Soc., Section B* **63**, 376 (1950). (UNCLASSIFIED)

Malvern, L. E., *Introduction to the Mechanics of a Continuous Medium*, Prentice-Hall, Englewood Cliffs, N.J. (1969). (UNCLASSIFIED)

Margolin, L. G., "Elastic Moduli of a Cracked Body," *Int. J. Fracture* **22**, 65-79 (1983). (UNCLASSIFIED)

Marston, P. L., and B. T. Unger, "Rapid Cavitation Induced by the Reflection of Shock Waves," In: *Shock Waves in Condensed Matter - 1985*, Plenum Press, NY, 401-405 (1986). (UNCLASSIFIED)

Mathews, A. R., R. M. Boat, W. F. Hemsing, R. H. Warnes, and G. R. Whittemore, "Full-Field Fabry-Perot Interferometer," In: Shock Compression of Condensed Matter 1991. Eds., S. C. Schmidt, R. D. Dick, J. W. Forbes, and D. G. Tasker, Elsevier Science Publishers B. V., Amsterdam, The Netherlands, 759-762 (1992). (UNCLASSIFIED)

McQueen, R. G., S. P. Marsh, J. W. Taylor, J. N. Fritz, and W. J. Carter, In: *High-Velocity Impact Phenomena*, Ed., Kinslow, New York, NY (1970). (UNCLASSIFIED)

McQueen, R. G., and S. P. Marsh, "Ultimate Yield Strength of Copper," *J. Appl. Phys.* **33**(2), 654-665 (1962). (UNCLASSIFIED)

McQueen, R. G., and S. P. Marsh, *J. Appl. Phys.* **31**, p.1253 (1960). (UNCLASSIFIED)

Me-Bar, Y., M. Boas, and Z. Rosenberg, *Mat. Sci. Eng.* **85**, 77 (1987). (UNCLASSIFIED)

Merzhievsky, L. A., and V. M. Titov, "The Criterion of Metal Lasting in Microsecond Range," *Acad. of Sciences USSR - Doklady (USSR)* **286**(1) 109-112 (1986). (UNCLASSIFIED)

Meyers, M. A., and C. T. Aimone, "Dynamic Fracture (Spalling) of Metals," Progress in Materials Science **28**, 1-96 (1983). (UNCLASSIFIED)

Murri, W. J., D. R. Curran, and L. Seaman, "Fracture Model for High Energy Propellant," *Proceedings of the American Physical Society Conference on Shock Waves in Condensed Matter*, 460-464 (1982). (UNCLASSIFIED)

Murri, W. J., C. Young, D. A. Shockey, R. E. Tokheim, and D. R. Curran, "Determination of Dynamic Fracture Parameters for Oil Shale," SRI International, Final Report to Sandia Laboratories, Albuquerque, New Mexico (1977). (UNCLASSIFIED)

Nahme, H., V. Hohler, and A. Stilp, "Determination of the Dynamic Material Properties of Shock Loaded Silicon-Nitride," In: *High-Pressure Science and Technology - 1993*, Eds., S. C. Schmidt, J. W. Shaner, G. A. Samara and M. Ross, AIP Press, NY, 765-768 (1994). (UNCLASSIFIED)

Novikov S. A., I. I. Divnov, and A. G. Ivanov, "The Study of Fracture of Steel, Aluminum, and Copper under Explosive Loading," *Phys. of Metals and Metal science (USSR)* **21**(4) 608-615 (1966). (UNCLASSIFIED)

Osher, J., G. Barnes, H. Chau et al.,. *Plasma Science* **17**(4), 392-403 (1989). (UNCLASSIFIED)

Paisley, D. L., R. H. Warnes, and R. A. Kopp, "Laser-Driven Flat Plate Impacts to 100 GPa with Sub-Nanosecond Pulse Radiation and Resolution for Material Property Studies," In: Shock Compression of Condensed Matter 1991. Eds., S. C. Schmidt, R. D. Dick, J. W. Forbes, and D. G. Tasker, Elsevier Science Publishers B.V., Amsterdam, The Netherlands, 825-828 (1992). (UNCLASSIFIED)

Poritsky, H., "The Collapse or Growth of a Spherical Bubble or Cavity in a Viscous Fluid," *Proceedings of the First U.S. National Congress of Applied Mechanics, ASME*, New York, 813 (1952). (UNCLASSIFIED)

Postnov V. I., In: Unsteady Problems of the Hydrodynamics, Novosobirsk **48**, 116 (1980) (in Russian). (UNCLASSIFIED)

Raiser, G., and R. J. Clifton, "Failure Waves in Uniaxial Compression of an Aluminosilicate Glass," In: *High-Pressure Science and Technology - 1993*, Eds., S. C. Schmidt, J. W. Shaner, G. A. Samara and M. Ross, AIP Press, NY, 1039-1042 (1994). (UNCLASSIFIED)

Razorenov, S. V., G. I. Kanel, and T. N. Yalovets, "Dynamic Strength of Ruby," *J. Chem. Phys. (USSR)* (1993). (UNCLASSIFIED)

Razorenov, S. V., and G. I. Kanel, "The Study of Edge Effects Under Spallation," *Problems of Strength (USSR)*, No. 9, 52-55 (1991). (UNCLASSIFIED)

Razorenov, S. V., G. I. Kanel, V. E. Fortov, and M. M. Abasehov, "The Fracture of Glass Under High-Pressure Impulsive Loading," *High Pressure Research* **6**, 225-232 (1991). (UNCLASSIFIED)

Read, H. E., and R. A. Cecil, "Rate-Dependent Constitutive Model for Shock-Loaded S-200 Beryllium," 3SR-949, Systems, Science, and Software, La Jolla, California, DNA 2845F (1972). (UNCLASSIFIED)

Rice, M. H., R. G. McQueen, and J. M. Walsh, "Compression of Solids by Strong Shock Waves", in *Solid State Physics* **6**, 1-63, edited by F. Seitz and D. Turnbull, Academic Press (1958).

Rinehart, J. S., "Some Quantitative Data Bearing on the Scabbing of Metals under Explosive Attack," *J. Appl. Phys.* **22**(3), 555-560 (1951a). (UNCLASSIFIED)

Rinehart, J. S., "Some Experimental Indications of the Stress Produced in a Body by an Exploding Charge," *J. Appl. Phys.* **22**(9), 1178-1185 (1951b). (UNCLASSIFIED)

Romanchenko, V. I., and G. V. Stepanov, *J. Appl. Mech. Tech. Phys.* **21**(4), 141 (1980). (UNCLASSIFIED)

Rozenberg, Z., "The Response of Ceramic Materials to Shock Loading," In: *Shock Compression of Condensed Matter 1991*, Eds., S. C. Schmidt, R. D. Dick, J. W. Forbes, and D. G. Tasker, Elsevier Science Publishers B.V., Amsterdam, The Netherlands, 439-444 (1992). (UNCLASSIFIED)

Rozenberg, Z., *J. Appl. Phys.* **62**(5), 1745 (1987). (UNCLASSIFIED).

Saltykov, S. A., *Stereometric Metallography*, 2nd Edition, Metallurgizdat, Moscow, 446 (1958). (UNCLASSIFIED)

Scheil, E., Statistische Gefügeuntersuchungen I, *Z. Metallk.* **27**, 199 (1935). (UNCLASSIFIED)

Scheil, E., "Die Berechnung der Anzahl und Grössenverteilung kugelförmiger Kristalle in undurchsichtigen Körpern mit Hilfe der durch einen ebenen Schnitt erhaltenen Schnittkreise," *Z. Anorg. Allgem. Chem..* **201**, 259 (1931). (UNCLASSIFIED)

Seaman, L., D. R. Curran, and W. J. Murri, "A Continuum Model for Dynamic Tensile Microfracture and Fragmentation," *J. Appl. Mech.* **107**, 593-600 (1985). (UNCLASSIFIED)

Seaman, L., "Development of Computational Models for Micro Structural Features," *Proceedings of the American Physical Society Conference on Shock Waves in Condensed Matter*, 118-129 (1982). (UNCLASSIFIED)

Seaman, L., and D. R. Curran, "SRI PUFF 8 Computer Program for One-Dimensional Stress Wave Propagation," SRI International Final Report (Volume II) Prepared for U.S. Army Ballistics Research Laboratory, Contract No. DAAK11-77-C-0083 (1978). (UNCLASSIFIED)

Seaman, L., and D. R. Curran, "SRI PUFF 8 Computer Program for One-Dimensional Stress Wave Propagation," Final Report, Volume II by SRI, for Ballistics Research Laboratory, Aberdeen Proving Ground, Maryland 21005 (1978a). (UNCLASSIFIED)

Seaman, L., D. R. Curran, and R. C. Crewdson, "Transformation of Observed Crack Traces on a Section to True Crack Density for Fracture Calculations," *J. Appl. Phys.* **49**, 5221 (1978b). (UNCLASSIFIED)

Seaman, L., D. R. Curran, and D. A. Shockey, "Computational Models for Ductile and Brittle Fracture," *J. Appl. Phys.* **47**(11), 4814 (1976). (UNCLASSIFIED)

Seaman, L., T. W. Barbee, Jr., and D. R. Curran, "Dynamic Fracture Criteria of Homogeneous Materials," Technical Report No. AFWL-TR-71-156, Air Force Weapons Laboratory, Kirtland Air Force Base, New Mexico (1971). (UNCLASSIFIED)

Sheffield, S. A., and G. A. Fisk, "Particle Velocity Measurements in Laser Irradiated Foils Using ORVIS," In: Shock Waves in Condensed Matter - 1983. Eds., J. R. Asay, R. A. Graham, and G. K. Straub, Elsevier Science Publishers B.V., Amsterdam, The Netherlands, 243-246 (1984). (UNCLASSIFIED)

Shockey, D. A., D. C. Erlich, and K. C. Dao, "Particle Impact Damage in Silicon Nitride at 1400°C," *J. Mater. Science* **16**, 477-482 (1981). (UNCLASSIFIED)

Shockey, D. A., L. Seaman, and D. R. Curran, "Microfracture Models and Their Applications to Nonlinear Dynamic Fracture Problems," *Nonlinear and Dynamic Fracture Mechanics, ASME, AMD-* **35**, 79 (1979). (UNCLASSIFIED)

Shockey, D. A., D. R. Curran, L. Seaman, J. T. Rosenberg, and C. F. Petersen, "Fracture of Rock Under Dynamic Loads," *Int. J. Rock. Mech. Sci. Geomech. Abstr.* **11**(1), 303-317 (1974). (UNCLASSIFIED)

Shockey, D. A., L. Seaman, D. R. Curran, P. S. DeCarli, M. Austin, and J. P. Wilhelm, "A Computational Model for Fragmentation of Armco Iron Under Ballistic Impact," Final Report,

prepared by SRI International for the U.S. Ballistic Research Laboratories, Aberdeen Proving Ground, Maryland 21005 (1973). (UNCLASSIFIED)

Shockey, D. A., L. Seaman, and D. R. Curran, "Dynamic Fracture of Beryllium Under Plate Impact and Correlation with Electron Beam and Underground Test Results," Final Rep. No. AFWL-TR-73-12, Kirtland Air Force Base, New Mexico (1973). (UNCLASSIFIED)

Skidmore, I. C., "An Introduction to Shock Waves in Solids," *Appl. Mater. Res.* **4**, 131 (1965). (UNCLASSIFIED)

Smith, J. H., "Three Low Pressure Spall Thresholds in Copper," *ASTM Spec. Tech. Publ. No. 336*, 264-281 (1962). (UNCLASSIFIED)

Sneddon, I. N., and M. Lowengrub, *Crack Problems in the Classical Theory of Elasticity*, John Wiley and Sons, New York (1969). (UNCLASSIFIED)

Speight, C. S., P. F. Taylor, and A. A. Wallace, "Observation of Spallation and Attenuation Effects in Aluminum and Berillium from Free-Surface Velocity Measurements," In: *Metallurgical Effects at High Strain Rates*, London, 429-442 (1973). (UNCLASSIFIED)

Staehler, J. M., W. W. Predeborn, and B. J. Pletka "The Response of High Purity Alumina to Plate-Impact Testing," In: *High-Pressure Science and Technology - 1993*, Eds., S. C. Schmidt, J. W. Shaner, G. A. Samara and M. Ross, AIP Press, NY, 745-748 (1994). (UNCLASSIFIED)

Sugiure, S. H., K. Kondo, and A. Sawaoka, "Dynamic Response of Fused Quartz in the Permanent Densification Region," *J. Appl. Phys.* **52**(5), 3375-3382 (1981). (UNCLASSIFIED)

Taylor, G. I., *Proc. Royal Soc.* **A200**, 235-247 (1950). (UNCLASSIFIED)

Taylor, J. W., In: *Dislocation Dynamics*, Ed., A. R. Rosenberg, New York, NY (1968). (UNCLASSIFIED)

Trevena, H. D., "The Behavior of Liquids Under Tension," *Contemp. Phys.* **8**, 185-191 (1967). (UNCLASSIFIED)

Tuler, F. R., and B. M. Butcher, "A Criterion for the Time Dependence of Dynamic Fracture," *Int. J. Fract. Mech.* **4**(4), 431-437 (1968). (UNCLASSIFIED)

Utkin, A. V., "Influence of the Initial Damage Rate on the Forming Spall Pulse," *J. Appl. Mech. Tech. Phys. (USSR)* **34** (4), 578-584 (1993). (UNCLASSIFIED)

Utkin, A.V., "Influence of the Damage Rate on the Dynamics of Interaction of Shock Load Pulse with a Body Surface," *J. Appl. Mech. Tech. Phys. (USSR)* **33**(6) , 82 (1992). (UNCLASSIFIED)

Winkler, W.-D., and A. J. Stilp, "Spallation Behavior of TiB_2, SiC, and B_4C Under Planar Impact Tensile Stresses, In: *Shock Compression of Condensed Matter 1991*, Eds., S. C. Schmidt, R. D. Dick, J. W. Forbes, and D. G. Tasker, Elsevier Science Publishers B.V., Amsterdam, The Netherlands, 475-478 (1992). (UNCLASSIFIED)

Zel'dovich, Ya. B., and Yu. P. Raizer, *Physics of Shock Waves and High-Temperature Hydrodynamic Phenomena*, edited by W. D. Hayes and R. F. Probstein, Vol. II, Academic Press, NY (1967). (UNCLASSIFIED)

DISTRIBUTION LIST
DSWA-TR-96-77-V1

DEPARTMENT OF DEFENSE

BALLISTIC MISSILE DEFENSE ORG
    ATTN: DOUG SCHAEFER

DEFENSE TECHNICAL INFORMATION CENTER
  2 CY ATTN: DTC/OCP

DEFENSE THREAT REDUCTION AGENCY
  2 CY ATTN: SWI

DEPARTMENT OF THE ARMY

US ARMY SPACE & MISSILE DEFENSE CMS
    ATTN: LIBRARY

US ARMY THAAD PROJECT OFFICE
  3 CY ATTN; CSSD-TC-W, R BECKER

DEPARTMENT OF THE NAVY

NAVAL SURFARE WARFARE CENTER
    ATTN: CODE G24, CHARLES R ELLINGTON

DEPARTMENT OF THE AIR FORCE

WRIGHT LABORATORY
    ATTN: RON HUNT

DEPARTMENT OF ENERGY

LAWRENCE LIVERMORE NATIONAL LAB
    ATTN: L-84, G POMYKAL

LOS ALAMOS NATIONAL LABORATORY
    ATTN: DOD PROG OFC, J V REPPA

SANDIA NATIONAL LABORATORIES
    ATTN: ERIC REECE

DEPARTMENT OF DEFENSE CONTRACTORS

ARES CORP
    ATTN: CHUCK MARTIN

BATTELLE MEMORIAL INSTITUTE
    ATTN: C ALEANDER

ITT INDUSTRIES
    ATTN: DASIAC
    ATTN: DASIAC/DARE

ITT SYSTEMS CORP
    ATTN: VERN SMITH

ITT SYSTEMS CORP
    ATTN: DENNIS JONES

JAYCOR
    ATTN: DR CYRUS P KNOOWLES

LOGICON RDA
    ATTN: DAVID GAKENHEIMER

LOGICON RDA
    ATTN: ED TOTON

MAXWELL TECHNOLOGIES INC
    ATTN: DR G GURTMAN

SRI INTERNATIONAL
  2 CY ATTN: D CURRAN
    ATTN: J COLTON
  2 CY ATTN: L SEAMAN
  2 CY ATTN: T ANTOUN

W J SCHAFER ASSOCIAES, INC.
    ATTN: J CHERNAULT